



Magneto-mechanical behavoirs of ferromagnetic shape memory alloys

Xue Chen, Ziad Moumni, Yong Jun He

► To cite this version:

Xue Chen, Ziad Moumni, Yong Jun He. Magneto-mechanical behavoirs of ferromagnetic shape memory alloys. Solid mechanics [physics.class-ph]. Ecole Polytechnique X, 2013. English. NNT: . pastel-00848630

HAL Id: pastel-00848630

<https://pastel.hal.science/pastel-00848630>

Submitted on 26 Jul 2013

HAL is a multi-disciplinary open access archive for the deposit and dissemination of scientific research documents, whether they are published or not. The documents may come from teaching and research institutions in France or abroad, or from public or private research centers.

L'archive ouverte pluridisciplinaire **HAL**, est destinée au dépôt et à la diffusion de documents scientifiques de niveau recherche, publiés ou non, émanant des établissements d'enseignement et de recherche français ou étrangers, des laboratoires publics ou privés.

ÉCOLE POLYTECHNIQUE
DEPARTMENT OF MECHANICAL ENGINEERING



DISSERTATION

submitted to the Graduate School of École Polytechnique in partial fulfillment of the
requirements for the degree of Doctor of Philosophy

by

Xue CHEN

Magneto-Mechanical Behaviors of Ferromagnetic Shape Memory Alloys

Thesis defended on the 25th of June 2013 with the committee composed of:

President:	Prof. Richard D. JAMES	University of Minnesota
Reviewers:	Prof. Oleg HECZKO	Institute of Physics of the ASCR
	Prof. Etienne PATOOR	Arts et Métiers ParisTech
Examinator:	Prof. Habibou MAITOURNAM	École Polytechnique
Co-advisor:	Prof. Yongjun HE	ENSTA ParisTech
Advisor:	Prof. Ziad MOUMNI	ENSTA ParisTech

To my parents

ACKNOWLEDGMENTS

This thesis is a summary of research work done in the past three years and a half. During this period of time, a lot of people have offered me help and support. It is my great pleasure to wholeheartedly express my gratitude to them.

I wish to express the most sincere gratitude towards my advisor Dr. Ziad Moumni for his continuous guidance, enthusiasm and encouragement, and what's more important, great confidence in me. His support helped me overcome all the difficulties during the Ph.D. period.

I wish to express the depth of my gratitude to my co-advisor Dr. Yongjun He. We have always worked together during the past years. For me, he is not only an advisor, but also a kind colleague and friend. I appreciated his guidance and his inspiration for research very much. It is him who helped me find the real happiness of research — discovering the truth and sharing it with the whole world.

I am grateful to Dr. Antoine Chaigne, dean of the mechanical engineering department, for accepting me as a Ph.D. student in his department.

I wish to thank Dr. Richard D. James, Dr. Oleg Heczkó, Dr. Etienne Patoor and Dr. Habibou Maitournam for kindly accepting as committee members in my thesis defense. Special thanks are given to Dr. Oleg Heczkó and Dr. Etienne Patoor for carefully reading the whole thesis and offering me valuable comments. I wish to express my gratitude again to Dr. Oleg Heczkó and Dr. Richard D. James for taking a long journey for the thesis defense.

I gratefully acknowledge the Materials and Structures research group, in which I have been involved. Many thanks to our researchers Anne-Lise, Corinne, Bertrand, Frédéric and Kim, to our technicians Patrice, Alain and Lahcène, and to our Ph.D. and post-doc students Claire, Lin, Alex, Abdel, Mohamed, Clément, Agathe, Ammar, Qianqiang, Oana and Qi. It is because of them that I enjoy the campus life far from the central city.

I gratefully acknowledge the Solid Mechanics Lab of École Polytechnique for kindly providing one of the loading apparatuses used in the experimental studies. Special thanks are given to Éva, Alexandre, Vincent and Jean-Christophe for their extremely kind technical assistance during the experiments.

I thank my boson friends Wenji and Yuan. Although we are separated either by the Atlantic Ocean or by the Himalaya Mountain, their mails full of consideration and encouragement always reach me.

I thank all of my family — my grandparents, my uncles and aunts, my cousins, and the most important, my parents. Family love and support is always my source of energy!

Abstract

Ferromagnetic Shape Memory Alloys (FSMA) are promising candidates for sensors and actuators for their high-frequency response and large reversible strain. The aim of this dissertation is the analysis of the magneto-mechanical behaviors of FSMA. In this regard, we study, both experimentally and theoretically, the martensite reorientation in FSMA. Firstly, a 2D/3D magneto-mechanical energy analysis is proposed and incorporated into phase diagrams for a graphic study of path-dependent martensite reorientation in FSMA under 3D loadings. Criteria and material requirements for obtaining reversible strain in cyclic loadings are derived. The energy analysis predicts that FSMA in 2D/3D configurations (multi-axial stresses) has much more advantages than that in 1D configuration, e.g., higher output stress and more application flexibility. Secondly, to validate the predictions of the energy analysis, 2D experiments are performed on FSMA and results reveal that the intrinsic dissipation and the transformation strain due to martensite reorientation are constant in all tested 2D stress states. Moreover, preliminary results validate that the output stress of FSMA in 2D configuration (magnetic field with biaxial stresses) is larger than that in 1D configuration, and the output stress can be increased by increasing the auxiliary stress. Finally, to predict the magneto-mechanical behaviors of FSMA in general multi-axial loadings, a 3D constitutive model is developed within the framework of thermodynamics of irreversible processes. All the martensite variants are considered and the temperature effect is also taken into account. Model simulations agree well with all the existing 1D/2D experiments. The model is further incorporated into finite element analysis for studying the non-linear bending behaviors of FSMA beams. The sample-geometry effect and the material anisotropic effect are systematically investigated.

Keywords: Ferromagnetic shape memory alloys; Martensite reorientation; Magneto-mechanical energy analysis; Phase diagram; Multi-axial experiments; Thermo-magneto-mechanical behaviors; Three-dimensional thermodynamics model; Finite element analysis.

Publications

Journal publications

- He, Y.J., **Chen, X.**, Moumni, Z., 2011. Two-dimensional analysis to improve the output stress in ferromagnetic shape memory alloys. *Journal of Applied Physics* 110, 063905.
- He, Y.J., **Chen, X.**, Moumni, Z., 2012. Reversible-strain criteria of ferromagnetic shape memory alloys under cyclic 3D magneto-mechanical loadings. *Journal of Applied Physics* 112, 033902.
- Chen, X.**, He, Y.J., Moumni, Z., 2013. Twin boundary motion in NiMnGa single crystals under biaxial compression. *Materials Letters* 90, 72–75.
- Chen, X.**, Moumni, Z., He, Y.J., Zhang, W. A three-dimensional model of thermo-magneto-mechanical behaviors of ferromagnetic shape memory alloys. *Journal of the Mechanics and Physics of Solids* (in revision).

Conference publications

- Chen, X.**, He, Y.J., Moumni, Z., 2012. Three-dimensional constitutive model of martensite reorientation in Ni-Mn-Ga ferromagnetic shape memory alloy. In: Proceedings of the 18th International Symposium on Plasticity & Its Current Applications, January 3–8, 2012, San Juan, Puerto Rico, pp. 289–291.
- He, Y.J., **Chen, X.**, Moumni, Z., 2013. 3D Energy analysis of magnetic-field induced martensite reorientation in magnetic shape memory alloys. *Materials Science Forum* 738–739, 400–404. (For the 9th European Symposium on Martensitic Transformations, September 9–16, 2012, Saint-Petersburg, Russia).
- Chen, X.**, He, Y.J., Moumni, Z., 2013. Energy dissipation of martensite reorientation in NiMnGa single crystals under biaxial compression. *Materials Science Forum* 738–739, 421–425. (For the 9th European Symposium on Martensitic Transformations, September 9–16, 2012, Saint-Petersburg, Russia).

Contents

Chapter 1 General introduction	16
1.1. Overview of ferromagnetic shape memory alloys	17
1.1.1. Background	17
1.1.2. Martensite reorientation	18
1.1.3. Research interests in ferromagnetic shape memory alloys	21
1.2. Research objectives and outline of dissertation	24
1.3. Notations	25
Chapter 2 Energy analysis of martensite reorientation under multi-axial magneto-mechanical loadings	27
2.1. 2D analysis to improve the output stress in ferromagnetic shape memory alloys	28
2.1.1. Introduction	28
2.1.2. Energy analysis	30
2.1.3. Phase diagrams and variant switching in different loading paths	35
2.1.4. Discussions	47
2.1.5. Conclusions	48
2.2. Reversible strain criteria of ferromagnetic shape memory alloys under cyclic 3D magneto-mechanical loadings	50
2.2.1. Introduction	50
2.2.2. Energy analysis and phase diagrams	52
2.2.3. Criterion for obtaining reversible strain under cyclic magneto-mechanical loadings	61
2.2.4. Discussions	72
2.2.5. Conclusions	73
2.3. Chapter conclusion	74
Chapter 3 Experimental analysis of martensite reorientation under multi-axial magneto-mechanical loadings	76
3.1. Biaxial compression tests	77
3.1.1. Introduction	77
3.1.2. Experiment	77
3.1.3. Results and discussions	80
3.1.4. Conclusions	85

3.2. Biaxial magneto-mechanical tests	86
3.2.1. Material and experimental procedures	86
3.2.2. Preliminary results	87
3.2.3. Structural external friction	88
3.2.4. Summary and prospect	91
3.3. Chapter conclusion	92
 Chapter 4 Three-dimensional constitutive model of thermo-magneto-mechanical behaviors of ferromagnetic shape memory alloys	93
4.1. Introduction	95
4.1.1. Literature review of models	95
4.1.2. Outline of chapter	99
4.2. Magneto-mechanical model of ferromagnetic shape memory alloys	100
4.2.1. Introduction of generalized standard materials with internal constraints	100
4.2.2. State variables and internal constraints	101
4.2.3. Formulation of Gibbs free energy density	102
4.2.4. State equations	107
4.2.5. Evolution laws of internal state variables	110
4.2.6. Identification of model parameters	114
4.3. Numerical simulations and model validations	119
4.3.1. Martensite reorientation induced by a non-rotating magnetic field	121
4.3.2. Martensite reorientation induced by a rotating magnetic field	126
4.3.3. Super-elasticity under biaxial compressions	128
4.3.4. Field-assisted super-elasticity	131
4.3.5. Thermo-magneto-mechanical behaviors of ferromagnetic shape memory alloys	135
4.4. Structural analysis of ferromagnetic shape memory beams	141
4.4.1. Simulation results	144
4.4.2. Specimen-geometry effect on bending deflection	145
4.4.3. Material anisotropic effect on bending deflection	148
4.5. Conclusions	150
 Chapter 5 General conclusion and future work	152
 Appendix A. Supplementary document for multi-axial experiments on ferromagnetic shape memory alloys	154
A.1. Biaxial compression tests	154
A.2. Biaxial magneto-mechanical tests	156

Appendix B. Finite element formulation for magneto-mechanical analysis of Ferromagnetic Shape Memory Alloys (FSMA)	157
B.1. Governing equations and boundary conditions for general magneto-mechanical analysis	157
B.1.1. Magnetic part	157
B.1.2. Mechanical part	159
B.1.3. Summary of fully coupled dynamic magneto-mechanical analysis	161
B.2. Weak form formulations	163
B.2.1. Magnetic part	164
B.2.2. Mechanical part	164
B.3. Finite element formulations	165
B.3.1. Magnetic part	165
B.3.2. Mechanical part	168
B.4. Summary	171
Appendix C. Non-symmetric stress tensor of magnetic materials in magnetic field	172
C.1. Introduction — origin of the non-symmetric stress tensor for magnetic materials	172
C.2. Non-symmetric stress tensor in ferromagnetic shape memory alloys	174
References	177

List of figures

Fig. 1. Schematic diagram of the austenite and the martensite variants of ferromagnetic shape memory alloys.	19
Fig. 2. Strain due to martensite reorientation induced by a magnetic field.	20
Fig. 3. FSMA under a single compressive stress (a) and two compressive stresses (b).	29
Fig. 4. The tetragonal martensite variants under two compressive stresses and a magnetic field.	31
Fig. 5. The dependence of the magnetization directions (in variant I and II) on the field direction at different field magnitudes.	33
Fig. 6. The dependence of the magnetization directions (in variant I and II) on the field magnitude at different field directions.	35
Fig. 7. Phase diagrams in terms of the stresses and the magnetic field direction (α) at different field magnitudes.	37
Fig. 8. Rotating-field-induced strain (c) and field-assisted superelasticity (b) derived from the stresses—field-direction phase diagram (a).	38
Fig. 9. The dependence of the time fraction z_1 of variant I on the applied stresses and the hysteretic effect (twinning stress).	40
Fig. 10. Phase diagrams in terms of the stresses and the magnetic field magnitude at the field direction $\alpha=0$.	43
Fig. 11. Non-rotating-field induced strain (c) and field-assisted superelasticity (b) derived from the stresses—field-magnitude phase diagram (a).	44
Fig. 12. Comparison between the analytic solution of switching fields/stresses and the experiments of magnetic field-induced strain (MFIS) and field-assisted superelasticity.	47
Fig. 13. Schematic diagram of the austenite and the martensite variants of Ferromagnetic Shape Memory Alloys (FSMA).	51
Fig. 14. (a) Schematic diagram of the equilibrium magnetization vector \vec{M} in the martensite variant I (short axis along x_1 -coordinate) under three-dimensional normal stresses $(\sigma_1, \sigma_2, \sigma_3)$ and a magnetic field \vec{H} . (b) The projection of the magnetic field \vec{H} on the x_2 - x_3 plane (with the magnitude $H \sin \alpha_1$) and the projection of the vector \vec{M} on the same plane (with the magnitude $M \sin \theta_1$).	53
Fig. 15. Phase diagram of the three martensite variants in terms of normalized deviatoric magneto-mechanical stresses without hysteresis.	58

Fig. 16. Phase diagram of the three martensite variants in terms of normalized deviatoric magneto-mechanical stresses S_i with hysteresis (normalized twinning stress is assumed). _____	60
Fig. 17. The loading paths of cyclic tension and compression along x_2 -direction ($\bar{\sigma}_2 = \frac{\sigma_2}{K_u / \epsilon_0} = -1 \sim 1$) while the other stresses are fixed._____	63
Fig. 18. The loading paths of the strong rotating magnetic fields ($H \cdot M / K_u \gg 1$) without mechanical stresses ($\sigma_1 = \sigma_2 = \sigma_3 = 0$)._____	66
Fig. 19. The loading paths of the non-rotating magnetic fields (with magnitudes cyclically changing between $H = 0$ and a large value $H \cdot M / K_u \gg 1$) in the phase diagram. _____	67
Fig. 20. The loading paths of the non-rotating magnetic fields along x_1 -axis (magnitudes cyclically changing between $H = 0$ and a large value $H \cdot M / K_u \gg 1$) with a constant mechanical stress $\bar{\sigma}_2$ along x_2 -axis. _____	71
Fig. 21. (a) Schematic diagram of the experimental setup for symmetric biaxial compression tests. (b) Friction occurs on the contact surfaces between the clamps and the sample's y-z surfaces. ____	78
Fig. 22. (a) Schematic diagram of measuring the friction coefficient. (b) Frictional force f_y at different levels of normal force F_x ._____	80
Fig. 23. Nominal stress-strain curves (σ_{yy} - ϵ_{yy}) at different levels of σ_{xx} . _____	81
Fig. 24. Force analysis of a half sample during loading._____	82
Fig. 25. (a) Nominal plateau stresses ($\sigma_{\text{upp-plat}}$, $\sigma_{\text{low-plat}}$) of the stress-strain curves (σ_{yy} - ϵ_{yy}). (b) Intrinsic plateau stresses (σ_f , σ_r). _____	84
Fig. 26. (a) Schematic diagram of the 2D magneto-mechanical setup. (b) Lever system for applying the compressive stress σ_{xx} . _____	87
Fig. 27. Magnetic-field-induced strain at different levels of constant compressive stresses (σ_{yy} and σ_{xx}). _____	88
Fig. 28. Lever movement at different weights of dead load._____	90
Fig. 29. Linear approximation (dashed line) of the magnetization curve (solid line) for martensite variant i ($i = 1, 2, 3$)._____	106
Fig. 30. Martensite reorientation among three variants (V1, V2, V3)._____	109
Fig. 31. (a) Martensite reorientation (from V1 to V2) induced by compressive stress σ_{yy} . (b) Stress-strain curve (σ_{yy} - ϵ_{yy}) of martensite reorientation under compression._____	115

Fig. 32. (a) Magnetization test along magnetic easy-axis. (b) Magnetization test along magnetic hard-axis.	116
Fig. 33. Magnetization curves (after linear approximation) of the magnetization along the magnetic easy-axis (dashed line) and that along the direction deviating from the easy-axis by an angle θ (solid line).	118
Fig. 34. FSMA used as an actuator driven by a non-rotating magnetic field (1D case: uniaxial stress).	121
Fig. 35. Comparison between simulations and experiments (Heczko, 2005) of the material's magneto-mechanical responses at different levels of compressive stress σ_{yy} .	124
Fig. 36. FSMA used as an actuator driven by a non-rotating magnetic field (2D case: biaxial compressions).	125
Fig. 37. Model predictions of the material's magneto-mechanical responses at different levels of compressive stress difference ($\sigma_{yy} - \sigma_{xx}$).	126
Fig. 38. FSMA used as an actuator driven by a rotating magnetic field.	126
Fig. 39. Evolution of strain ε_{yy} with the rotation of the magnetic field (with constant magnitude $\mu_0 H = 2$ T): results from the simulation (solid line) and experiment (crosses) are compared.	127
Fig. 40. (a) FSMA in a rotating magnetic field H and constant biaxial compressions σ_{xx} and σ_{yy} . (b) Model predictions of rotating-field-induced strain ε_{yy} at various levels of stress difference ($\sigma_{xx} - \sigma_{yy}$).	128
Fig. 41. (a) Schematic diagram of the experimental setup for symmetric biaxial compression tests. (b) Friction occurs on the contact surfaces between the clamps and the sample's y-z surfaces.	129
Fig. 42. Compressive stress-strain curves ($\sigma_{yy} - \varepsilon_{yy}$) at different levels of σ_{xx} .	131
Fig. 43. FSMA used as a sensor/generator/damper.	132
Fig. 44. Comparison between simulations and experiments (Heczko, 2005) of the material's magneto-mechanical responses at different levels of magnetic field $\mu_0 H_x$.	133
Fig. 45. (a) Illustration of the magneto-stress $\sigma_{mag}(H_x)$. (b) Magneto-stress σ_{mag} obtained from simulations and experiments.	134
Fig. 46. Linear approximations of the temperature-dependence of the material parameters ($\epsilon_0(T)$, $\sigma_{tw}(T)$, $M_s(T)$ and $K_u(T)$) in the working temperature range.	136
Fig. 47. Material's magneto-mechanical behaviors at different temperatures T .	138
Fig. 48. Model predictions of magnetic-field-induced strain under the constant compressive stress of 1.9 MPa at different temperatures.	139

Fig. 49. Rough estimations of the magnetic-field-induced strain under high-frequency dynamic loading.	140
Fig. 50. Clamped FSMA beam for numerical analysis of bending behaviors.	141
Fig. 51. (a) Force–deflection curve of FSMA beam. (b), (c) and (d) respectively show the evolutions of the deformed FSMA beam and the volume-fraction distributions for V2 (z_2) and V1 (z_1).	145
Fig. 52. Geometric effect on deflection D_{end} .	146
Fig. 53. Bending of an elastic beam.	147
Fig. 54. Force–deflection curves at different values of the beam thickness t .	148
Fig. 55. Illustration showing that for a fixed displacement u_x^{\max} on the top surface of the beam, the increase in the beam thickness from t_1 to t_2 reduces the slope of the beam from θ_1 to θ_2 .	148
Fig. 56. Geometric effect on deflection D_{end} for the FSMA beams in the initial states of martensite variant 1(V1), variant 2 (V2) and variant 3 (V3).	149
Fig. 57. (a) The bottom surface is expanded in x direction and compressed in y and z directions. (b) The shrinkage of the bottom surface along z-coordinate introduces a compression σ_{zz} on the top surface.	150

List of tables

Table 1. Notation used in the dissertation.	25
Table 2. Algorithm of simulation on material's behaviors.	119
Table 3. Parameter values from the uniaxial compression test and the magnetization tests.	120
Table 4. Algorithm of structural calculations.	141

Chapter 1 General introduction

1.1. Overview of ferromagnetic shape memory alloys	17
1.1.1. Background	17
1.1.2. Martensite reorientation	18
1.1.3. Research interests in ferromagnetic shape memory alloys	21
1.2. Research objectives and outline of dissertation	24
1.3. Notations	25

This opening chapter presents the overview of the ferromagnetic shape memory alloys, and the research interest and outline of this dissertation.

1.1. Overview of ferromagnetic shape memory alloys

1.1.1. Background

Ferromagnetic Shape Memory Alloys (FSMA) appeared as a new kind of smart (active) materials when a strain of 0.2% was first observed in Ni_2MnGa single crystals under a moderate magnetic field ($< 1 \text{ T}$) in 1996 (Ullakko et al., 1996). The observed Magnetic-Field-Induced Strain (MFIS) has the same order of magnitude as the highest magnetostriction obtained in giant magnetostrictive materials such as $\text{Tb}_{0.27}\text{Dy}_{0.73}$ and Terfenol-D (Ullakko et al., 1996). Later on, MFIS of FSMA has been increased to $6\% \sim 10\%$ in off-stoichiometric single crystalline Ni-Mn-Ga alloys (Heczko et al., 2000; Murray et al., 2000; Sozinov et al., 2002; Tickle and James, 1999). The large strain in FSMA is due to the martensite reorientation (switching among different martensite variants) driven by magnetic fields (Chopra et al., 2000; Likhachev and Ullakko, 2000; Ullakko et al., 1996). Therefore, in contrast to the conventional (traditional) temperature-driven shape memory alloys, FSMA can work in a large bandwidth up to 1~2 kHz (Henry et al., 2002; Marioni et al., 2003; Techapiesancharoenkij et al., 2009). The large reversible strain and the high-frequency response are the main advantages of FSMA, while its main limitations are brittleness (most materials are single crystals), and small working stress (usually smaller than 3 MPa, over this stress level the MFIS will be prohibited (Ganor et al., 2008; Gans et al., 2004; Heczko et al., 2000; Karaca et al., 2006; Kiefer and Lagoudas, 2005; Morito et al., 2007; Murray et al., 2000)). Improving the working stress is one of our objectives in this thesis. Details will be provided in the following chapters.

The most studied FSMA is Ni-Mn-Ga alloys. Webster et al. (1984) first studied the martensitic transformations in polycrystalline Ni_2MnGa alloy. Zasimchuk et al. (1990) and Martynov and Kokorin (1992) systematically investigated the crystal structure of the martensitic phases in Ni_2MnGa . Ullakko et al. (1996) first reported a strain of nearly 0.2% in

Ni_2MnGa single crystal under magnetic field and aroused a worldwide research interest in FSMA. Besides the Ni-Mn-Ga alloys, other important types of FSMA include Ni-Fe-Ga based alloys (e.g., Hamilton et al., 2006; Li et al., 2003; Oikawa et al., 2002; Sutou et al., 2004b), Fe-based alloys such as Fe-Pd (e.g., Cui et al., 2004; James and Wuttig, 1998; Liang et al., 2003; Wada et al., 2003; Yamamoto et al., 2004) and Fe-Pt (e.g., Kakeshita et al., 2000; Sakamoto et al., 2003), and Co-based alloys such as Co-Ni-Al (e.g., Karaca et al., 2003; Morito et al., 2002, 2010; Oikawa et al., 2001) and Co-Ni-Ga (e.g., Morito et al., 2009; Wuttig et al., 2001). These alloys usually have smaller magnetic-field-induced strains than Ni-Mn-Ga, but they may have other advantages, e.g., Fe-Pd alloys are more ductile than Ni-Mn-Ga; Co-Ni-Al alloys contain no expensive elements (Morito et al., 2010).

1.1.2. Martensite reorientation

Depending on the temperature and the material composition, the Ni-Mn-Ga single crystals have three different martensitic phases: i.e., tetragonal five-layered modulated martensite (5M), orthorhombic seven-layered modulated martensite (7M) and tetragonal non-modulated martensite (NMT) (Martynov and Kokorin, 1992). Magnetic-field-induced strain has been observed in both 5M and 7M martensites, and 5M martensite is the most studied martensitic phase in literature. For cubic to tetragonal (5M) martensitic transformation in Ni-Mn-Ga, there are three martensite variants (Tickle et al., 1999; Webster et al., 1984; Zasimchuk et al., 1990): V1, V2 and V3 with their short axes (c -axis) respectively parallel to the x -, y - and z -coordinate of the parent austenite lattice (see Fig. 1). Which variant is energetically preferred depends on the external loadings — mechanical stresses and magnetic fields: e.g., V1 is preferred by compression and magnetic field along x -coordinate (see a summary in Fig. 1 for other variants). So the magneto-mechanical loadings can induce the switching among variants (i.e., martensite reorientation).

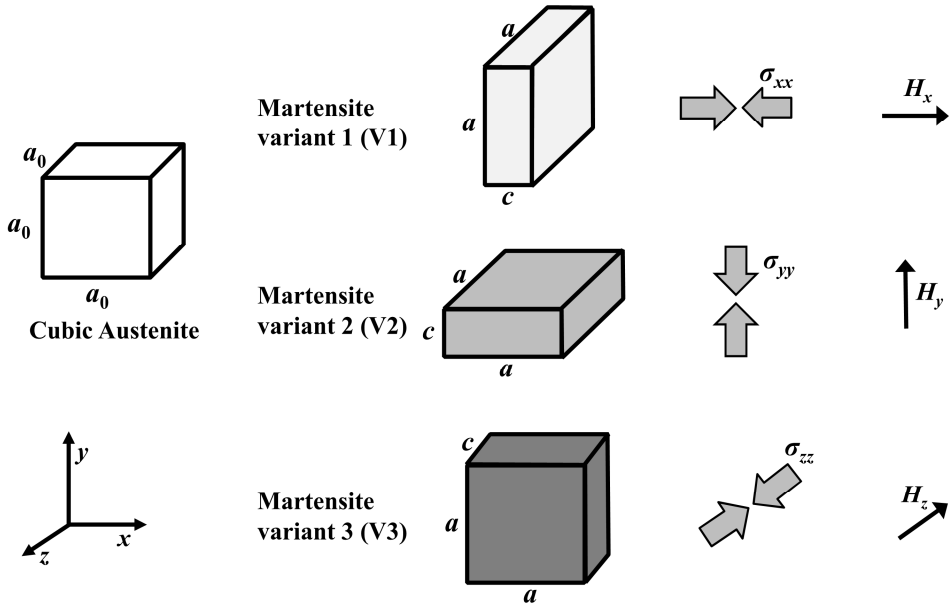


Fig. 1. Schematic diagram of the austenite and the martensite variants of ferromagnetic shape memory alloys. a_0 denotes the length of the austenite lattice; a and c respectively denote the lengths of the long (a -axis) and short (c -axis) axes of the martensite lattice (the difference between a and c is exaggerated in the schematic diagram). On the right of each variant, the compression (σ) and the magnetic field (H) which energetically prefer this variant are shown.

For a brief introduction here, we show by a simple example how a magnetic field can induce strain in FSMA. The material in the initial state of martensite variant 2 is in a magnetic field H_x along x -coordinate (see the insert of Fig. 2(a) for the loading condition and step ① in Fig. 2(b) for the initial state). With the increase of the magnetic field, the strain ε_{yy} first remains almost unchanged (steps ①→② in ε_{yy} - H_x curve of Fig. 2(a)), and then increases significantly (③→④ in Fig. 2(a)) when the magnetic-field-favored martensite variant (i.e., V1) nucleates and grows via the motion of twin boundaries (defined as the interface between the martensite variants, see ③→④ in Fig. 2(b)). The strain ε_{yy} saturates when the material is totally composed of V1 (see step ⑤ in Figs. 2(a) and 2(b)). Maximum strain due to martensite

reorientation ($V_2 \rightarrow V_1$ switching) induced by the magnetic field is around 6% for 5M martensite.

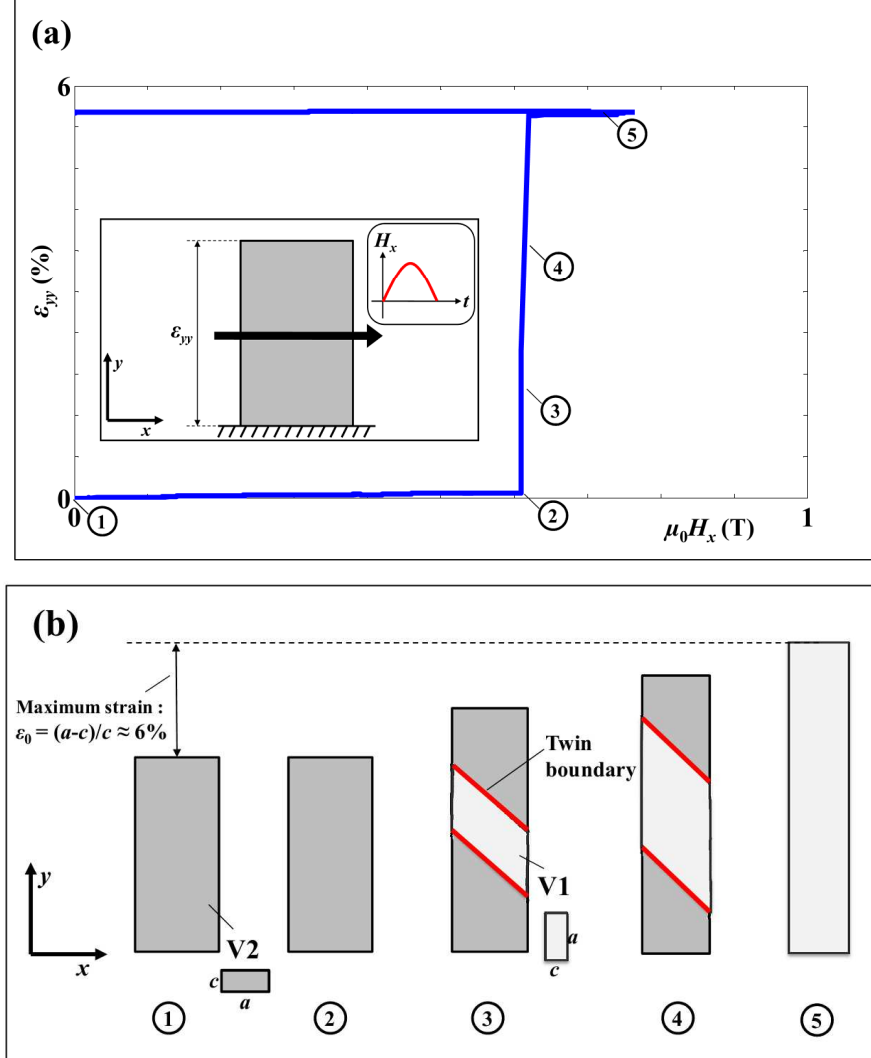


Fig. 2. Strain due to martensite reorientation induced by a magnetic field. (a) Strain–magnetic field curve. The loading condition is shown in the insert. (b) Schematic diagram of the micro-structural evolutions (i.e., distributions of martensite variants) during magnetic loading. The evolutions are simplified here just for illustration.

1.1.3. Research interests in ferromagnetic shape memory alloys

After the previous general introduction of FSMA, some interesting research topics are summarized below:

■ Theory and modeling

The magneto-mechanical behaviors of FSMA have been theoretically studied and a number of constitutive models have been proposed to quantitatively/qualitatively describe and predict the material's behaviors from microscopic to macroscopic scales. This thesis also concerns the constitutive model of FSMA. A detailed literature review of the existing models will be provided in Chapter 4.

■ Fundamental studies on FSMA

Martensite reorientation via twin boundary motion is the main mechanism in Magnetic-Field-Induced Strain (MFIS). A high mobility of twin boundary is essential for MFIS. Researches on the mechanism of twin boundary motion and the factors influencing the mobility of twin boundary are under development.

Twin microstructures were directly observed (e.g., Chulist et al., 2010b; Ge et al., 2004, 2006; Sullivan and Chopra, 2004), in order to better understand the twin boundary motion on the microscopic scale. Besides quasi-static loadings, the microscopic twin boundary motion in high-frequency dynamic loadings were also studied experimentally and theoretically (e.g., Faran and Shilo, 2011; Lai et al., 2008). Recently, a new twin (Type II, see (Jaswon and Dove, 1960) for the classification of twins) was observed and found to be much more mobile than the conventional twin (Type I) (Sozinov et al., 2011; Straka et al., 2010, 2011b). Studies on the different microstructures of the two twins and on how to produce Type II twin in the materials are still under way (e.g., Chulist et al., 2012, 2013; Heczko et al., 2013).

Factors influencing the mobility of the twin boundary have also been studied. The effects of temperature (e.g., Gavriljuk et al., 2003; Heczko and Straka, 2003; Straka et al., 2006, 2011a, 2012), training (mechanical and magnetic) (e.g., Chmielus et al., 2008; Chulist et al., 2010c; Straka et al., 2008), constraints (i.e., fixation of the ends of the sample) (e.g., Chmielus et al., 2008, 2011a) and surface conditions (e.g., Chmielus et al., 2010a, 2011b) were systematically investigated. One important finding in the temperature effects is that the twinning stress (related to the intrinsic dissipation of twin boundary motion) of Type I twin increases linearly with decreasing temperature, while that of Type II is temperature independent (Straka et al., 2012).

■ Magneto-caloric effects

Magneto-caloric effects are associated with the isothermal entropy change or adiabatic temperature change induced by an external magnetic field (Marcos et al., 2002; Planes et al., 2009). The magnetic refrigeration technology (utilizing the magneto-caloric effects) is a potential replacement of the traditional gas compression/expansion technology used today (Pecharsky and Gschneider, 1997). Large entropy change induced by magnetic field was discovered in Ni-Mn-Ga alloys (e.g., Hu et al., 2001; Marcos et al., 2002; Pareti et al., 2003). This entropy change is related to a first-order coupled magneto-structural transition (i.e., ferromagnetic austenite → ferromagnetic martensite, with the saturation magnetization of the martensite larger than that of the austenite).

Besides the Ni-Mn-Ga alloys, the entropy change induced by magnetic field were also discovered in Ni-Mn-X ($X=In,Sn,Sb$) alloys. The magnetic-field-induced martensitic transformations have been directly observed (Kainuma et al., 2006a, 2006b; Krenke et al., 2007; Oikawa et al., 2006; Yu et al., 2007). Different from Ni-Mn-Ga alloys whose two structural phases (i.e., martensite and austenite) are ferromagnetic, Ni-Mn-X ($X=In,Sn,Sb$) alloys has ferromagnetic austenite and antiferromagnetic/paramagnetic martensite. So

applying a magnetic field will induce the magneto-structural transition from the antiferromagnetic/paramagnetic martensite to the ferromagnetic austenite and cool down the material (so-called inverse magneto-caloric effect) (Khan et al., 2007; Krenke et al., 2007; Moya et al., 2007). By this mechanism, meta-magnetic shape memory effect (i.e., shape recovery by magnetic-field-induced reverse martensitic transformation from oriented martensite to austenite) is discovered in Ni-Mn-X ($X = \text{In, Sn}$) alloys (Kainuma et al., 2006a, 2006b). Since its discovery (Sutou et al., 2004a), Ni-Mn-X ($X=\text{In,Sn,Sb}$) seems to be a potential alternative to Ni-Mn-Ga for two important reasons: (1) it is cheaper (without the expensive element Ga), and (2) it has much larger working stress (as large as 100 MPa predicted by Kainuma et al. (2006b)). However, to induce the reverse martensitic transformation, a strong magnetic field is required, e.g., even for free-stress state, the required magnetic field should be larger than 3 T (Kainuma et al., 2006a, 2006b; Krenke et al., 2007).

■ Novel structures

Single crystalline FSMA shows large Magnetic-Field-Induced Strain (MFIS), but it is usually expensive, brittle and difficult to machine. Polycrystalline FSMA is a little more ductile, but it has little MFIS (Jeong et al., 2003; Ullakko et al., 2001) due to strain incompatibilities at grain boundaries. To overcome these problems, several solutions have been proposed: favorably textured FSMA polycrystals (e.g., Chulist et al., 2010a; Gaitzsch et al., 2007, 2009), polymer composites with FSMA particles (e.g., Feuchtwanger et al., 2003; Hosoda et al., 2004; Mahendran et al., 2011), polycrystalline FSMA foams (e.g., Boonyongmaneerat et al., 2007; Chmielus et al., 2010b; Zhang et al., 2011), etc. Moreover, for the potential applications of FSMA in micro-electro-mechanical systems, the FSMA micropillars and thin films have been intensely investigated (e.g., Auernhammer et al., 2008; Dong et al., 2004; Heczko et al., 2008; Ohtsuka et al., 2007, 2008; Reinhold et al., 2009; Thomas et al., 2008 among many others).

■ Applications

Linear actuators/motors (motion in a straight line) (e.g., Gauthier et al., 2006; Suorsa et al., 2002; Tellinen et al., 2002) using the materials' property of magnetic-field-induced martensite reorientation (accompanied by large strain change) were the first applications of FSMA. Later on, research interests have been drawn to the fabrication of micro- and nano- actuators (e.g., Khelfaoui et al., 2008; Kohl et al., 2010). Bending actuators (e.g., Kohl et al., 2004, 2007) were also proposed based on another mechanism: applying the gradient of a magnetic field introduces the attractive or repulsive force, which induce the martensite reorientation in the FSMA beam.

Besides actuators, sensors and energy harvesters based on the inverse effect of strain-induced magnetization change have been developed (e.g., Karaman et al., 2007; Kohl et al., 2013; Stephan et al., 2011; Suorsa et al., 2004); damping properties of the material have also been investigated for the possibility of damper applications (e.g., Wang et al., 2006; Zeng and al., 2010).

1.2. Research objectives and outline of dissertation

The material studied in this dissertation is the most important and the most utilized ferromagnetic shape memory alloys — single crystalline Ni-Mn-Ga alloys. The research is focused on the theoretical and experimental studies of martensite reorientation in Ni-Mn-Ga (5M martensite), and on developing a three-dimensional constitutive model to predict the magneto-mechanical behaviors of Ni-Mn-Ga in general loading conditions.

The remaining parts of the dissertation are organized as follows: Chapter 2 presents an energy analysis of martensite reorientation under 2D/3D loadings, in order to demonstrate the advantages of using the materials in multi-axial loading conditions and to verify the necessity

of developing a 3D constitutive model. In Chapter 3, 2D mechanical and magneto-mechanical experiments are reported, so as to study the martensite reorientation via twin boundary motion in 2D conditions and to validate the advantages of using the materials in multi-axial loadings. Chapter 4 is devoted to the development of a 3D constitutive model of the material's magneto-mechanical behaviors. A general conclusion is provided in Chapter 5.

1.3. Notations

The main notations used in the dissertation are summarized in Table 1.

Table 1. Notation used in the dissertation.

Notation	Meaning	Unit or Expression or Value
a, a_M	Length of long axis of tetragonal martensite unit cell	nm
a_0, a_A	Length of cubic austenite unit cell	nm
c, c_M	Length of short axis of tetragonal martensite unit cell	nm
\underline{H}, \vec{H}	Magnetic field strength	$A \cdot m^{-1}$
H_x	Magnetic field along x -coordinate of austenite lattice	$A \cdot m^{-1}$
K_u	Magneto-crystalline anisotropic energy	$J \cdot m^{-3}$
\underline{M}, \vec{M}	Magnetization vector	$A \cdot m^{-1}$
M_s	Saturation magnetization	$A \cdot m^{-1}$
M_x	Magnetization along x -coordinate of austenite lattice	$A \cdot m^{-1}$
MFIS	Magnetic-Field-Induced Strain	
MSMA	Magnetic Shape Memory Alloys	
T	Absolute temperature	K
V1, x-variant	martensite variant 1	
V2, y-variant	martensite variant 2	
V3	martensite variant 3	
z_1	Volume fraction of martensite variant 1	
z_2	Volume fraction of martensite variant 2	
z_3	Volume fraction of martensite variant 3	
z_{12}	Volume-fraction transformation between variant 1 and 2	

Notation	Meaning	Unit or Expression or Value
z_{23}	Volume-fraction transformation between variant 2 and 3	
z_{31}	Volume-fraction transformation between variant 3 and 1	
$\underline{\underline{\varepsilon}}$	Strain tensor	
ε_0	Strain change due to martensite reorientation	$(a-c)/a_0$
$\varepsilon_a, \varepsilon_2$	Strain change	$(a-a_0)/a_0$
$\varepsilon_c, \varepsilon_1$	Strain change	$(a_0-c)/a_0$
μ_0	Vacuum permeability	$4\pi \times 10^{-7} \text{ (V}\cdot\text{s}\cdot\text{A}^{-1}\cdot\text{m}^{-1}$
$\underline{\underline{\sigma}}$	Stress tensor	Pa
$\sigma_{tw}, \sigma_{twinning}$	Twinning stress (driving force for twin boundary motion)	Pa
$\sigma_{xx}, \sigma_x, \sigma_1$	Normal stress along x/x_1 -coordinate of austenite lattice	Pa
$\sigma_{yy}, \sigma_y, \sigma_2$	Normal stress along y/x_2 -coordinate of austenite lattice	Pa
$\sigma_{zz}, \sigma_z, \sigma_3$	Normal stress along z/x_3 -coordinate of austenite lattice	Pa

Chapter 2 Energy analysis of martensite reorientation

under multi-axial magneto-mechanical loadings

2.1. 2D analysis to improve the output stress in ferromagnetic shape memory alloys	28
2.1.1. Introduction	28
2.1.2. Energy analysis	30
2.1.3. Phase diagrams and variant switching in different loading paths	35
2.1.4. Discussions	47
2.1.5. Conclusions	48
2.2. Reversible strain criteria of ferromagnetic shape memory alloys under cyclic 3D magneto-mechanical loadings	50
2.2.1. Introduction	50
2.2.2. Energy Analysis and phase diagrams	52
2.2.3. Criterion for obtaining reversible strain under cyclic magneto-mechanical loadings	61
2.2.4. Discussions	72
2.2.5. Conclusions	73
2.3. Chapter conclusion	74

Most existing experiments investigating the martensite-variants reorientation (switching) of Ferromagnetic Shape Memory Alloys (FSMA) are in a simple 1D condition: an axial compressive stress and a transverse magnetic field. To obtain field-induced variant switching, however, the compressive stress (output stress) is limited by a small blocking stress (< 3 MPa). To overcome the stress limit, we suggest, in the first part of this chapter, using the materials in two-dimensional (2D) configurations: two (axial and transverse) compressive stresses and a magnetic field. Based on a 2D magneto-mechanical energy analysis, it is found that only the difference between the two stresses is limited; each of the two stresses can be larger than the blocking stress. The energy analysis is also incorporated into the field-stress phase diagrams (including hysteretic effect) to study the variant switching in different loading paths: rotating/non-rotating field-induced strain and field-assisted superelasticity. In the second part, the 2D magneto-mechanical energy analysis is extended to 3D and then incorporated into a phase diagram in terms of deviatoric stresses (including mechanical and magneto- stresses) to study the path-dependent (hysteretic) martensite reorientation in FSMA under 3D cyclic loadings. Based on the phase diagram (a plane graph), general criteria for obtaining reversible strain under cyclic magneto-mechanical loadings are derived, which provide basic guidelines for FSMA's applications under multi-axial loadings.

2.1. 2D analysis to improve the output stress in ferromagnetic shape memory alloys

2.1.1. Introduction

Ferromagnetic shape memory alloys (FSMA) are good candidates for actuators for their high-frequency response and large Magnetic-Field-Induced Strain (MFIS) (James and Wuttig, 1998; Murray et al., 2000; Straka and Heczko, 2005; Ullakko et al., 1996). MFIS is caused by the martensite variant reorientation (variant switching) in FSMA. In literature, there are two ways for obtaining magnetic-field induced variant switching: (i) changing the magnitude of a magnetic field with a fixed direction (non-rotating field) and (ii) changing the magnetic-field direction with a fixed magnitude (rotating magnetic field). Although most existing experiments belong to the loading method (i), method (ii) has advantages in some cases, for example in high-speed cyclic loadings (Boonyongmaneerat et al., 2007), sample-training (Chmielus et al., 2008), fatigue tests (Müllner et al., 2002) and some special actuators (Ganor et al., 2009; Suorsa et al., 2002). Moreover, a rotating field can induce reversible variant switching (i.e. reversible strain) without the assistance of mechanical stresses; but non-rotating field cannot solely induce reversible strain (Müllner et al., 2002).

Reversible variant switching (the two variants periodically switch to each other in cyclic loadings) is important in smart devices like actuators. Usually, a compressive mechanical stress is applied on FSMA (Fig. 3(a)) to help the non-rotating field induce the reversible strain, where the stress and the field are perpendicular to each other. When the FSMA works as an actuator, the stress represents the actuation stress (i.e. output working stress). However, the working stress is limited by a small blocking stress (< 3 MPa depending on the magnetic anisotropic energy), over which the MFIS is prohibited (Ganor et al., 2008; Gans et al., 2004; Heczko et al., 2000; Karaca et al., 2006; Kiefer and Lagoudas, 2005; Morito et al., 2007;

Murray et al., 2000). From energy point of view, it is possible to increase the working stress by applying a constant auxiliary force on the FSMA in another direction (Fig. 1(b)). In literature, there are no systematic experiments or modeling for this two-dimensional (2D) case (under two compressive stresses and a rotating/non-rotating magnetic field). In this section, based on a 2D energy model on the variant switching, we demonstrate that only the difference between the two stresses is limited by the magnetic anisotropic energy and the hysteretic effect — non-zero twinning stress (Eq. (14) for rotating field and Eq. (20) for non-rotating field). i.e., the working stresses can be larger than the blocking stress in 2D configurations.

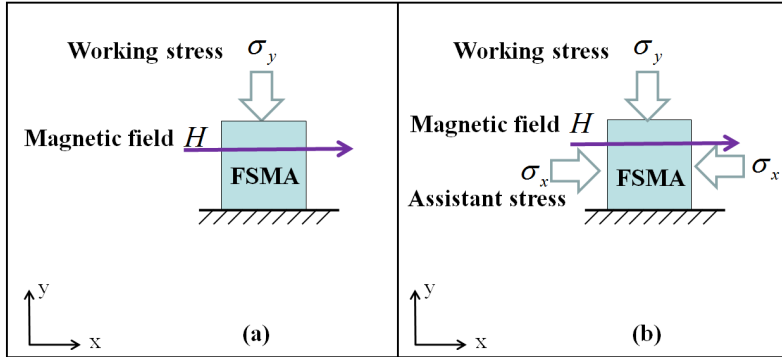


Fig. 3. FSMA under a single compressive stress (a) and two compressive stresses (b).

Several models have been proposed in literature, which are roughly classified into two categories: (1) micromagnetics models (e.g., Chernenko et al., 2004; James and Wuttig, 1998; Jin, 2009; Kiefer and Lagoudas, 2005, 2009; Paul et al., 2007; Tickle et al., 1999) can computationally determine microstructural evolutions; (2) energy models (e.g., Heczko and Straka, 2003; Heczko et al., 2006; Likhachev and Ullakko, 2000; Likhachev et al., 2004; Murray et al., 2001; Straka et al., 2006) focusing on macroscopic variables (e.g. switching stress/magnetic-field) can provide useful application guidelines (e.g. criterion of the existence of reversible actuation of FSMA in cyclic loadings). There are also some models (e.g., Marioni et al., 2002; O’Handley, 1998) in between the above two categories, which can

provide analytical expressions connecting macroscopic variables to the averaged (or effective) microstructures. In this section, an energy model is proposed to consider the 5M (five-layered modulated) martensite variant switching in Ni-Mn-Ga — the specimen transfers abruptly from one tetragonal-variant state to another (like the discontinuous model in (Murray et al., 2001)). In the 2D configuration (Fig. 4), we compare the energies of the two variants (I and II) under two compressive stresses and a magnetic field, and draw the phase diagrams (Fig. 7 and Fig. 10) (including hysteretic effects) to study the variant switching in different loading paths: rotating/non-rotating field-induced strain and field-assisted superelasticity (Fig. 8 and Fig. 11).

2.1.2. Energy analysis

2.1.2.1. Energy formulation

In the 2D configuration, the FSMA specimen is assumed to be composed of single variant (I or II in Fig. 4). The energy of each variant (which is assumed to consist of a single magnetic domain) includes the mechanical potential E_{mech} and the magnetic energy E_{mag} (Zeeman energy and the magnetic anisotropic energy) (Heczko et al., 2002; O'Handley, 1998; Straka and Heczko, 2003b).

$$E_{mech-V1} = -\boldsymbol{\sigma}_x \cdot \boldsymbol{\varepsilon}_1 + \boldsymbol{\sigma}_y \cdot \boldsymbol{\varepsilon}_2 \quad (1a)$$

$$E_{mech-V2} = -\boldsymbol{\sigma}_y \cdot \boldsymbol{\varepsilon}_1 + \boldsymbol{\sigma}_x \cdot \boldsymbol{\varepsilon}_2 \quad (1b)$$

$$\text{where } \boldsymbol{\varepsilon}_1 = 1 - \frac{c_M}{a_A} > 0, \quad \boldsymbol{\varepsilon}_2 = \frac{a_M}{a_A} - 1 > 0.$$

$$E_{mag-V1} = K_u \cdot \sin^2 \theta_1 - H \cdot M \cdot \cos(\alpha - \theta_1) \quad (2a)$$

$$E_{mag-V2} = K_u \cdot \sin^2 \theta_2 - H \cdot M \cdot \cos\left(\frac{\pi}{2} - \alpha - \theta_2\right) \quad (2b)$$

where a_A is the length of the austenite lattice; a_M and c_M are the lengths of the long (a-axis) and short (c-axis) axes of the martensite lattice; α is the angle between the magnetic field and x -coordinate; K_u , H and M are the uniaxial magnetic anisotropic energy, the magnitudes of the applied magnetic field (the unit is T) and the saturation magnetization, respectively; θ_1 and θ_2 are the equilibrium angles between the magnetization and the c-axis of the two variants, respectively (see the inserts in Figs. 5 and 6). The values of the compressive stresses (σ_x and σ_y) are positive here. Without losing generality, here we ignore the effects of elastic energy and magnetostriction, which will be discussed in sub-section 2.1.4. The energy difference (normalized by K_u) between the two variants is expressed as:

$$\begin{aligned} \frac{E_{V1} - E_{V2}}{K_u} &= \frac{(E_{mech-V1} + E_{mag-V1}) - (E_{mech-V2} + E_{mag-V2})}{K_u} \\ &= \frac{(\sigma_y - \sigma_x)}{K_u} \cdot \varepsilon_0 + (\sin^2 \theta_1 - \sin^2 \theta_2) - \frac{H \cdot M}{K_u} \cdot \left[\cos(\alpha - \theta_1) - \cos\left(\frac{\pi}{2} - \alpha - \theta_2\right) \right] \end{aligned} \quad (3)$$

where $\varepsilon_0 = \varepsilon_1 + \varepsilon_2 = (a_M - c_M)/a_A$. Eq. (3) indicates the energy preference of the two variants in the 2D configurations. Besides the material properties and the boundary conditions (ε_0 , M , K_u , H , α , σ_x , and σ_y), the equilibrium magnetization directions (θ_1 and θ_2) are needed to calculate the energy difference.

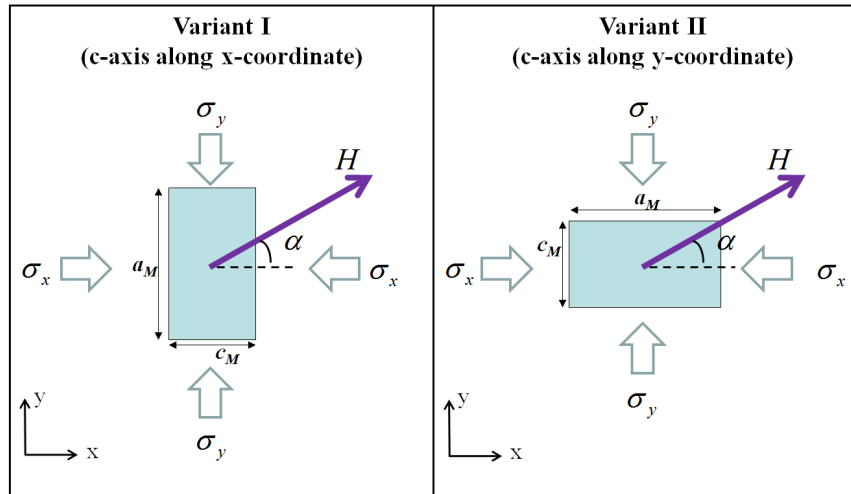


Fig. 4. The tetragonal martensite variants under two compressive stresses and a magnetic field.

2.1.2.2. Magnetization directions (θ_1 and θ_2)

Usually, the equilibrium magnetization direction can be determined by minimizing the magnetic energy (Müllner et al., 2002; Sasso et al., 2010) as:

$$\begin{aligned} 0 &= \frac{\partial E_{mag-V1}}{\partial \theta_1} = K_u \cdot \sin 2\theta_1 - H \cdot M \cdot \sin(\alpha - \theta_1) \\ 0 &= \frac{\partial E_{mag-V2}}{\partial \theta_2} = K_u \cdot \sin 2\theta_2 - H \cdot M \cdot \sin\left(\frac{\pi}{2} - \alpha - \theta_2\right) \end{aligned} \quad (4)$$

Normalized by K_u , Eq. (4) changes to:

$$\begin{aligned} \sin 2\theta_1 - \frac{H \cdot M}{K_u} \cdot \sin(\alpha - \theta_1) &= 0 \\ \sin 2\theta_2 - \frac{H \cdot M}{K_u} \cdot \sin\left(\frac{\pi}{2} - \alpha - \theta_2\right) &= 0 \end{aligned} \quad (5)$$

Equation (5) containing *sin* functions generally has no analytical solutions, except some special conditions. In the following, the analytical and numerical solutions are discussed in two magnetic loadings: a rotating field (with a fixed magnitude H) and a non-rotating field (with fixed direction α). Because of the symmetry of the system, we only need to study the angle range $\alpha \in [0, \pi/2]$.

Rotating magnetic field (with fixed field magnitude H)

In this case, Eq. (5) has some analytical solutions as:

$$\text{If } \frac{H \cdot M}{K_u} \approx 0, \quad \begin{cases} \sin 2\theta_1 = 0 \Rightarrow \theta_1 = 0 \\ \sin 2\theta_2 = 0 \Rightarrow \theta_2 = 0 \end{cases} \quad (6a)$$

$$\text{If } \frac{H \cdot M}{K_u} = 1, \quad \begin{cases} \theta_1 = \frac{\alpha}{3} \\ \theta_2 = \frac{\pi/2 - \alpha}{3} \end{cases} \quad (6b)$$

$$\text{If } \frac{H \cdot M}{K_u} \gg 1, \quad \begin{cases} \theta_1 = \alpha \\ \theta_2 = \frac{\pi}{2} - \alpha \end{cases} \quad (6c)$$

Equation (6) means that the magnetization is along the c-axis (which is the easy-axis of magnetization) when the applied field is weak ($\frac{H \cdot M}{K_u} \approx 0$); when H is strong ($\frac{H \cdot M}{K_u} \gg 1$), the magnetization is along the field; for other cases, the magnetization is in between c-axis and the field. The dependence of the magnetization orientations (θ_1 and θ_2) on the field direction α and the field magnitude $\frac{H \cdot M}{K_u}$ can be numerically determined (Fig. 5). Similar calculations of the magnetizations in a single magnetic domain of a single variant (Müllner et al., 2002; Sasso et al., 2010) and in twin structures of different specimen shapes (platelet and rod) with demagnetization (Chernenko et al., 2006) can be found in literature.

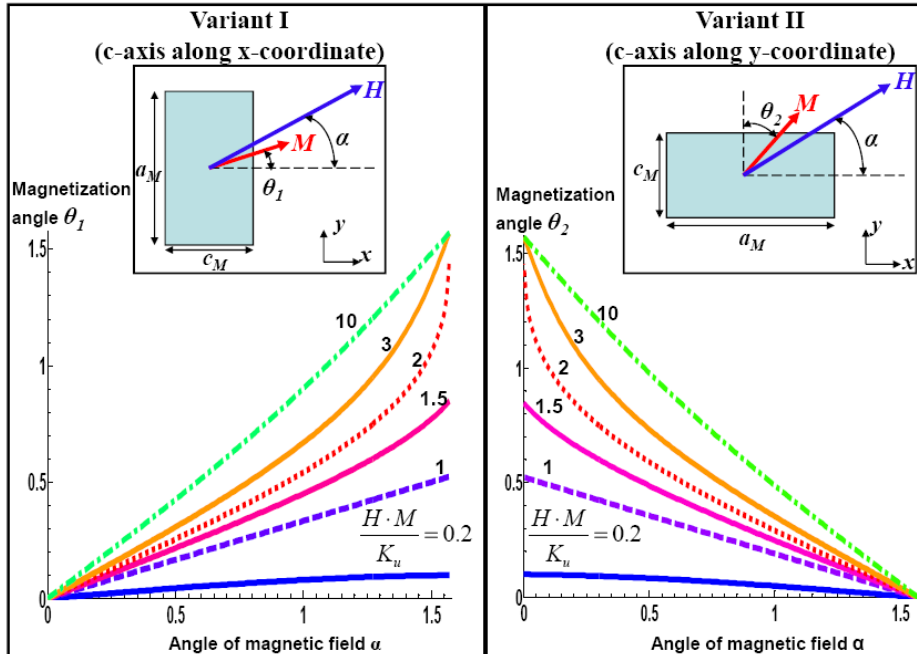


Fig. 5. The dependence of the magnetization directions (in variant I and II) on the field direction at different field magnitudes.

Non-rotating magnetic field (with fixed field direction α)

With basic knowledge of the magnetization in FSMA martensite variants, we can obtain the analytical solutions of Eq. (5) when α is equal to 0 or $\pi/2$ as:

$$\text{If } \alpha = 0, \left\{ \begin{array}{l} \sin \theta_1 \cdot \left(2 \cos \theta_1 + \frac{H \cdot M}{K_u} \right) = 0 \Rightarrow \theta_1 = 0 \quad \text{when } \frac{H \cdot M}{2K_u} > 0 \\ \cos \theta_2 \cdot \left(2 \sin \theta_2 - \frac{H \cdot M}{K_u} \right) = 0 \Rightarrow \begin{cases} \theta_2 = \arcsin \frac{H \cdot M}{2K_u} & \text{when } 0 \leq \frac{H \cdot M}{2K_u} \leq 1 \\ \theta_2 = \pi/2 & \text{when } \frac{H \cdot M}{2K_u} > 1 \end{cases} \end{array} \right. \quad (7a)$$

$$\text{If } \alpha = \frac{\pi}{2}, \left\{ \begin{array}{l} \cos \theta_1 \cdot \left(2 \sin \theta_1 - \frac{H \cdot M}{K_u} \right) = 0 \Rightarrow \begin{cases} \theta_1 = \arcsin \frac{H \cdot M}{2K_u} & \text{when } 0 \leq \frac{H \cdot M}{2K_u} \leq 1 \\ \theta_1 = \pi/2 & \text{when } \frac{H \cdot M}{2K_u} > 1 \end{cases} \\ \sin \theta_2 \cdot \left(2 \cos \theta_2 + \frac{H \cdot M}{K_u} \right) = 0 \Rightarrow \theta_2 = 0 \quad \text{when } \frac{H \cdot M}{2K_u} > 0 \end{array} \right. \quad (7b)$$

For other cases (i.e. $0 < \alpha < \pi/2$), solutions of Eq. (5) can be determined numerically. The dependence of the magnetization directions (θ_1 and θ_2) on the field magnitude H at different field directions is shown in Fig. 6. If the field direction coincides with the c-axis, the magnetization is always along the c-axis (no matter how large the field magnitude is). If they do not coincide, the magnetization direction rotates from the c-axis to the field direction when

the field magnitude increases from zero to a large value ($\frac{H \cdot M}{2K_u} > 1$).

With the magnetization directions, the energy difference between the two variants (Eq.(3)) can be calculated and incorporated into the field-stress phase diagrams to study the variant switching in different loading paths with the consideration of hysteresis.

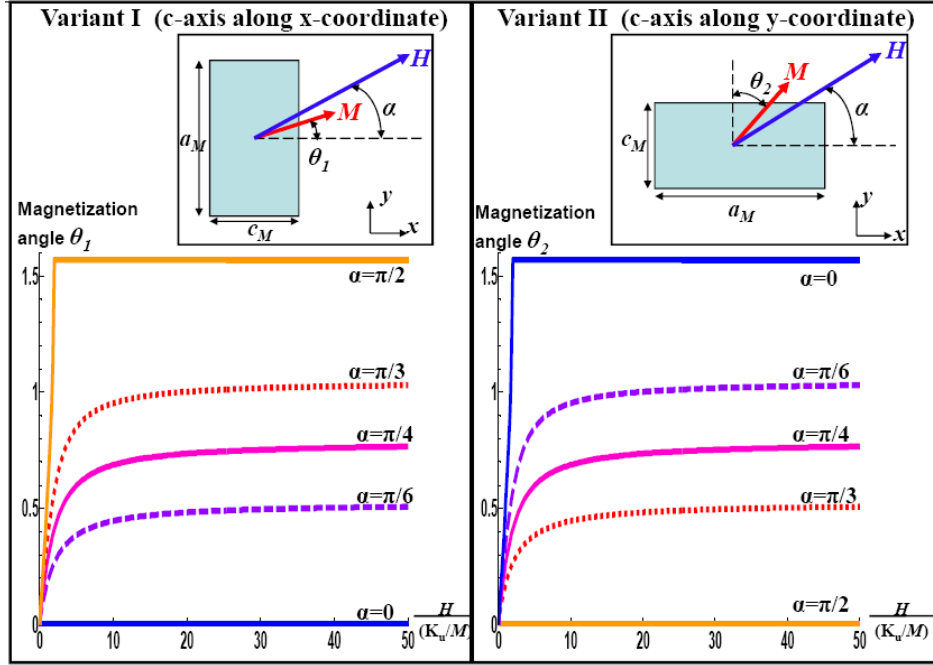


Fig. 6. The dependence of the magnetization directions (in variant I and II) on the field magnitude at different field directions.

2.1.3. Phase diagrams and variant switching in different loading paths

Substituting Eqs. (6) and (7) into Eq. (3), we can calculate the energy difference of the two variants and plot the phase diagrams (Figs. 7, 8, 10 and 11) to study the variant-switching induced by the rotating and non-rotating magnetic fields, respectively.

2.1.3.1. Rotating-field-induced variant switching

The dimensionless parameter $(\frac{H \cdot M}{K_u})$ characterizes three ranges of the field magnitude (low H , medium H and large H) where the energy difference between the two variants is obtained by substituting Eq. (6) into Eq. (3) as:

$$\text{when } \frac{H \cdot M}{K_u} \approx 0, \quad \frac{E_{V1} - E_{V2}}{K_u} = \frac{(\sigma_y - \sigma_x)}{K_u / \epsilon_0} \quad (8a)$$

$$\text{when } \frac{H \cdot M}{K_u} = 1, \quad \frac{E_{V1} - E_{V2}}{K_u} = \frac{(\sigma_y - \sigma_x)}{K_u / \epsilon_0} - \frac{3}{2} \sin\left(\frac{\pi}{6} - \frac{2\alpha}{3}\right) \quad (8b)$$

$$\text{when } \frac{H \cdot M}{K_u} \gg 1, \quad \frac{E_{V1} - E_{V2}}{K_u} = \frac{(\sigma_y - \sigma_x)}{K_u / \epsilon_0} - \cos(2\alpha) \quad (8c)$$

where $\alpha \in [0, \pi/2]$. From the symmetry of the system, the energy difference can be easily obtained for $\alpha \in [\pi/2, 2\pi]$: for low and large H , the forms of Eqs. (8a) and (8c) remain unchanged; for medium H , Eq. (8b) changes to:

$$\frac{E_{V1} - E_{V2}}{K_u} = \begin{cases} \frac{(\sigma_y - \sigma_x)}{K_u / \epsilon_0} + \frac{3}{2} \cos\left(\frac{2\alpha}{3}\right) & \alpha \in [\pi/2, \pi] \\ \frac{(\sigma_y - \sigma_x)}{K_u / \epsilon_0} - \frac{3}{2} \sin\left(\frac{\pi}{6} + \frac{2\alpha}{3}\right) & \alpha \in [\pi, 3\pi/2] \\ \frac{(\sigma_y - \sigma_x)}{K_u / \epsilon_0} - \frac{3}{2} \sin\left(\frac{\pi}{6} - \frac{2\alpha}{3}\right) & \alpha \in [3\pi/2, 2\pi] \end{cases} \quad (8d)$$

Equation (8) indicates the field-direction (α) dependence of the energy difference, which can be used to draw the phase diagrams in terms of the stresses and the field direction α as shown in Fig. 7. The figures on the left-hand side/right-hand side are without/with the hysteretic

effect (normalized twinning stress $\frac{\sigma_{twinning}}{K_u / \epsilon_0} = 0.5$ is assumed in Figs. 7(b), 7(d) and 7(f)). The

solid curves in Figs. 7(a), 7(c) and 7(e) are equal-energy curves with $\frac{E_{V1} - E_{V2}}{K_u} = 0$. The

equal-energy curves define the borders of the two regions for stable states of variant I and II:

when $\frac{E_{V1} - E_{V2}}{K_u} < 0$ ($\frac{E_{V1} - E_{V2}}{K_u} > 0$), variant I (variant II) is energetically preferred.

Considering the hysteretic effect where twinning stress is non-zero, the equal-energy curves are split into the switching thresholds (I→II and II→I switching thresholds in Figs. 7(b), 7(d) and 7(f)). The region between the switching thresholds is meta-stable, i.e., the variant state in this region depends on the loading history.

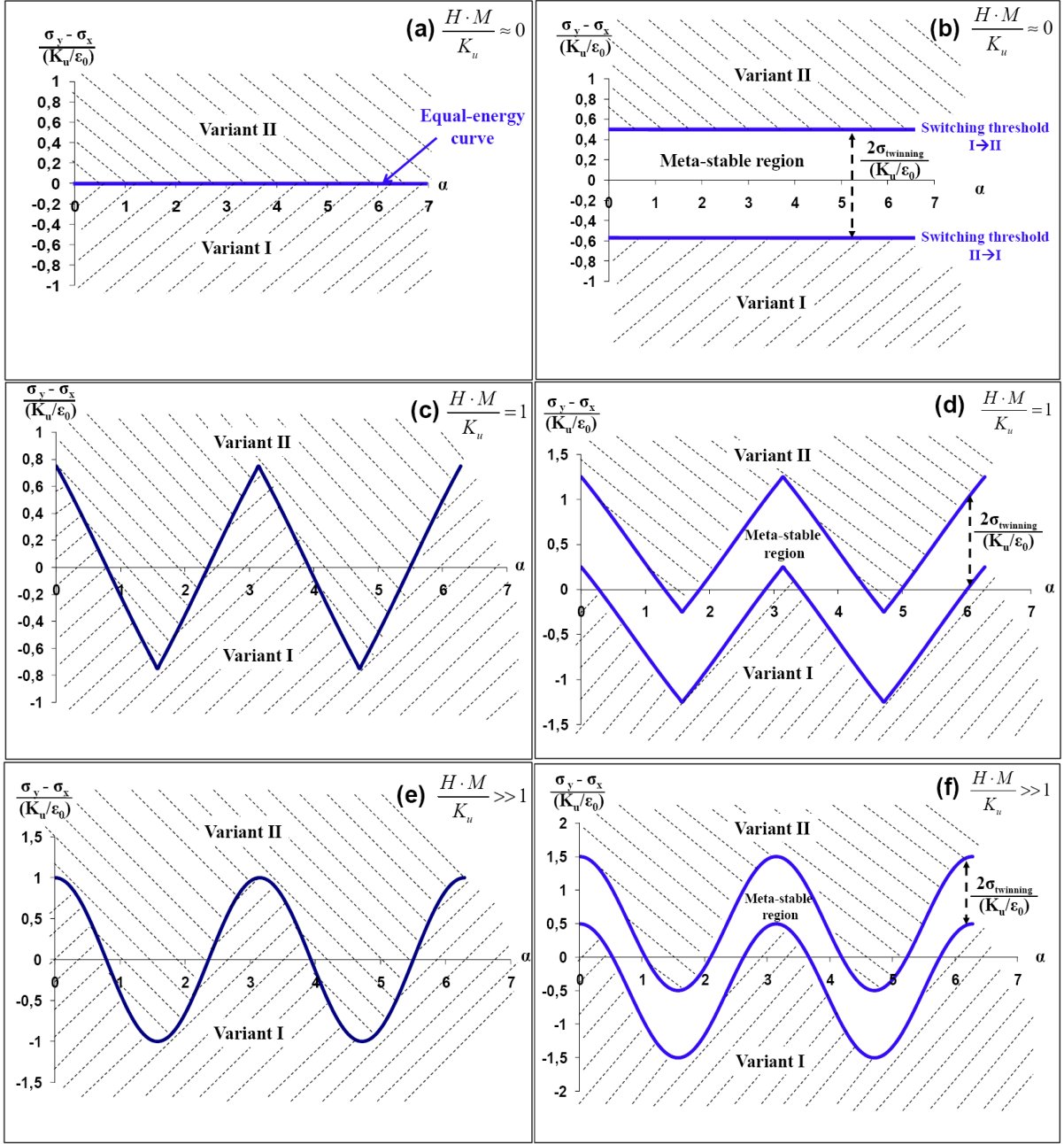


Fig. 7. Phase diagrams in terms of the stresses and the magnetic field direction (α) at different field magnitudes: $(H \cdot M) / K_u \approx 0$ ((a),(b)), $(H \cdot M) / K_u = 1$ ((c),(d)), $(H \cdot M) / K_u \gg 1$ ((e),(f)). The figures on the left-hand side (on the right-hand side) are without (with) hysteretic effect.

In Figs. 7(a) and 7(b) (when the applied field is low, $(H \cdot M) / K_u \approx 0$), the variant state is governed only by the mechanical stresses $((\sigma_y - \sigma_x) / (K_u / \varepsilon_0))$. When H is medium or large ($((H \cdot M) / K_u = 1$ or $(H \cdot M) / K_u \gg 1$ in Figs. 7(c)-(f)), the rotation of the magnetic field (changing α) can lead to the variant switching. For example, Fig. 8 shows the variant-

switching induced by a large H ($(H \cdot M) / K_u \gg 1$). In the loading path “R1” (a constant-rate rotating field with $\sigma_y = \sigma_x$), the two variants switch to each other periodically and the time fractions of the two variants in a loading cycle are equal due to the symmetry of the system. If $\sigma_y > \sigma_x$ (or $\sigma_y < \sigma_x$), variant II (or variant I) occupies a larger time fraction in a loading cycle as shown in the loading path “R2” (or “R3”). That means we can change the time fractions of the two variants in a cycle by properly setting the two stresses. Additionally, three important features are demonstrated by the phase diagram as follows.

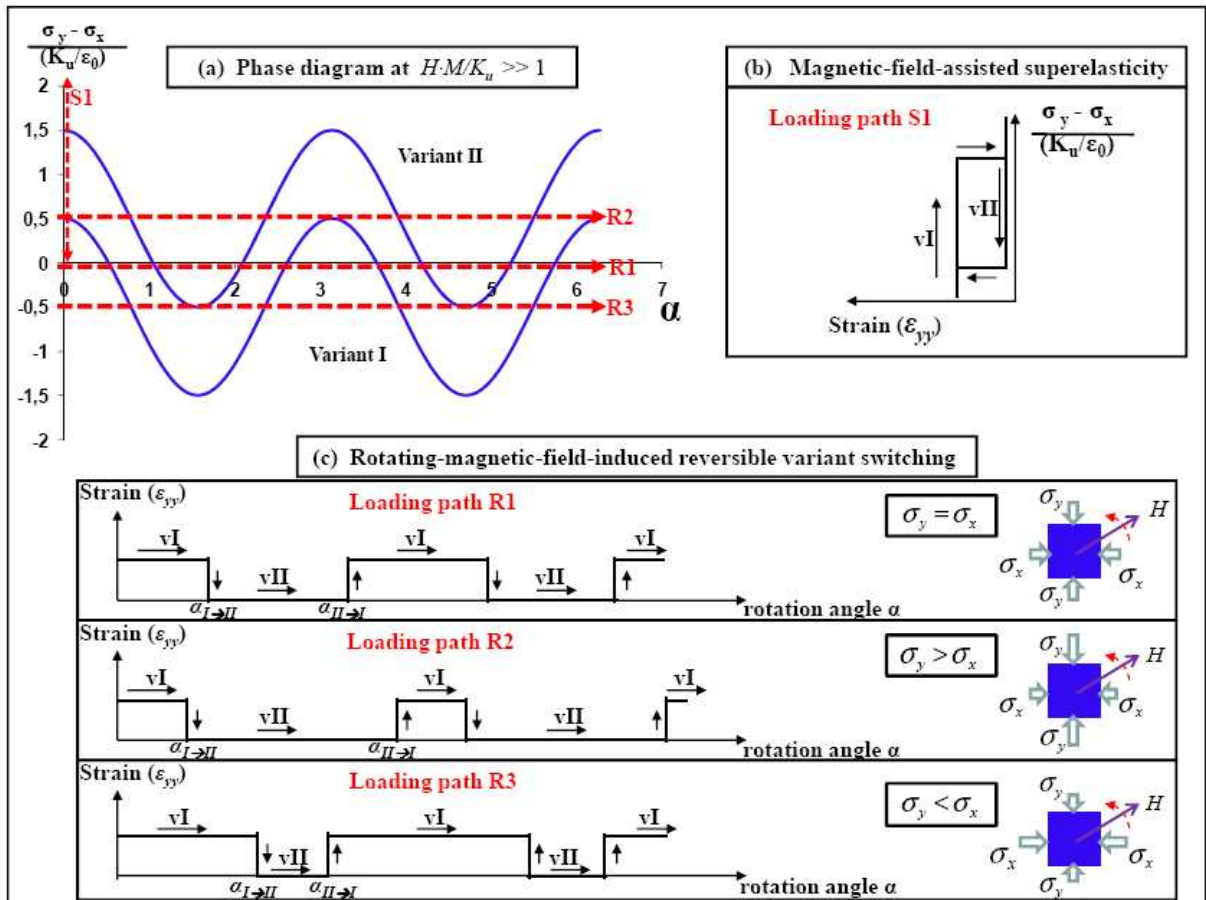


Fig. 8. Rotating-field-induced strain (c) and field-assisted superelasticity (b) derived from the stresses—field-direction phase diagram (a). The different loading paths (R1, R2 and R3 for rotating-field-induced strain and S1 for field-assisted superelasticity) are indicated on the phase diagram (a).

Switching angles and time fractions of the variants

Under a constant-rate rotating field ($\dot{\alpha} > 0$ and $(H \cdot M) / K_u \gg 1$), the FSMA specimen (initially in the state of variant I at $\alpha = 0$) switches to variant II at the angle $\alpha_{I \rightarrow II}$, and back to variant I at the angle $\alpha_{II \rightarrow I}$ (see Fig. 8). Such switching processes will be repeated in the following rotation, so we just study the first semi-cycle (i.e. the rotating angle $\alpha \in [0, \pi]$).

With the hysteretic effect ($\frac{E_{V1} - E_{V2}}{K_u} = \pm \frac{\sigma_{twinning}}{K_u / \epsilon_0}$) and Eq. (8c), the two typical switching angles

can be determined as

$$\alpha_{I \rightarrow II} = \frac{1}{2} \arccos\left(\frac{\sigma_y - \sigma_x}{K_u / \epsilon_0} - \frac{\sigma_{twinning}}{K_u / \epsilon_0}\right) \quad (9)$$

$$\alpha_{II \rightarrow I} = \pi - \frac{1}{2} \arccos\left(\frac{\sigma_y - \sigma_x}{K_u / \epsilon_0} + \frac{\sigma_{twinning}}{K_u / \epsilon_0}\right) \quad (10)$$

For the loading path “R1” in Fig. 8 ($\sigma_y = \sigma_x$ and $\frac{\sigma_{twinning}}{K_u / \epsilon_0} = 0.5$), the switching angles

determined by Eq. (9) and (10) are: $\alpha_{I \rightarrow II} = 60^\circ$ and $\alpha_{II \rightarrow I} = 150^\circ$, which agree with the experimental observations (Müllner et al., 2002). It is noted that the specimen is in the state of variant I at the angle range of $[0, \alpha_{I \rightarrow II}] \cup [\alpha_{II \rightarrow I}, \pi]$. So the time fraction z_1 of variant I in the constant-rate rotation cycle is:

$$z_1 = \frac{1}{\pi} (\alpha_{I \rightarrow II} + (\pi - \alpha_{II \rightarrow I})) \quad (11)$$

With Eqs. (9) and (10), Eq.(11) becomes:

$$z_1 = \frac{1}{2\pi} \left(\arccos\left(\frac{\sigma_{yy} - \sigma_{xx}}{K_u / \epsilon_0} - \frac{\sigma_{twinning}}{K_u / \epsilon_0}\right) + \arccos\left(\frac{\sigma_{yy} - \sigma_{xx}}{K_u / \epsilon_0} + \frac{\sigma_{twinning}}{K_u / \epsilon_0}\right) \right) \quad (12)$$

Equation (12) is plotted in Fig. 9 to show the dependence of the time fraction of variant I on the applied stresses ($\frac{\sigma_y - \sigma_x}{K_u / \epsilon_0}$) and the twinning stress ($\frac{\sigma_{twinning}}{K_u / \epsilon_0}$). When $\sigma_y = \sigma_x$, the time

fraction of variant I is always the same as that of variant II ($z_1=0.5$), due to the symmetry of the system. If variant I occupies a larger time fraction than variant II ($z_1>0.5$), Eq.(12) predicts:

$$\sigma_y < \sigma_x \quad (13)$$

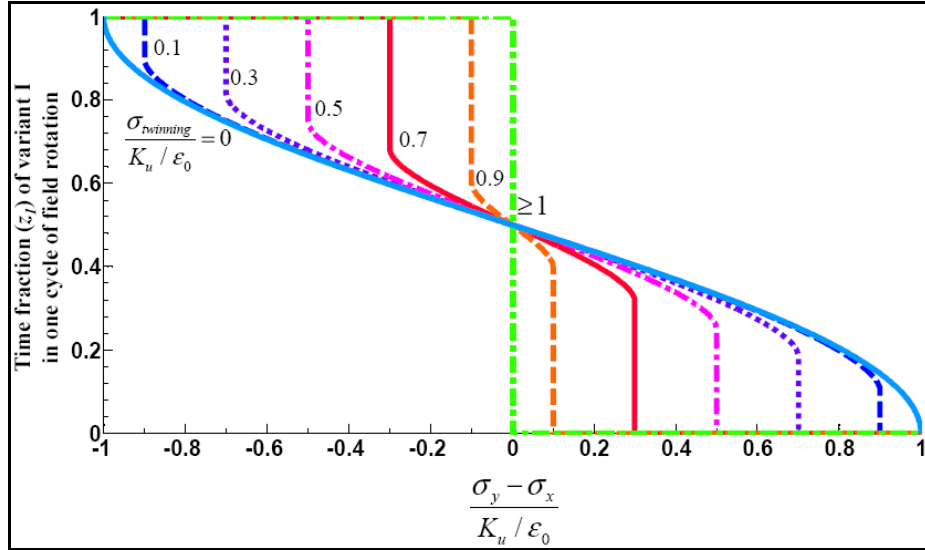


Fig. 9. The dependence of the time fraction z_1 of variant I on the applied stresses and the hysteretic effect (twinning stress).

From Fig. 9, it is also noted that, for obtaining reversible variant switching (two variants switch to each other in cyclic loadings, i.e., z_1 is not equal to 1 or 0), the stress difference $(\frac{\sigma_y - \sigma_x}{K_u / \epsilon_0})$ must be in a certain range, which depends on the hysteretic effect $(\frac{\sigma_{twinning}}{K_u / \epsilon_0})$. This issue is related to the second feature included in the phase diagrams as follows.

Criterion of reversible variant switching

If $\sigma_y \gg \sigma_x$ or $\sigma_y \ll \sigma_x$, the rotating field cannot induce reversible switching because the loading path cannot intersect the two switching thresholds in the phase diagram. The criterion for obtaining the rotating-field-induced reversible switching is

$$-\left(1 - \frac{\sigma_{\text{twinning}}}{K_u / \varepsilon_0}\right) \leq \frac{\sigma_y - \sigma_x}{K_u / \varepsilon_0} \leq 1 - \frac{\sigma_{\text{twinning}}}{K_u / \varepsilon_0} \quad (14)$$

The criterion (Eq. (14)) is possible only when

$$1 - \frac{\sigma_{\text{twinning}}}{K_u / \varepsilon_0} > 0 \Rightarrow K_u / \varepsilon_0 > \sigma_{\text{twinning}} \quad (15)$$

Equation (15) is the well-known basic requirement of the Magnetic-Field-Induced-Strain (MFIS) in FSMA (Heczko and Straka, 2003; Söderberg et al., 2005).

If only one mechanical stress is applied (i.e., $\sigma_y \neq 0$ and $\sigma_x = 0$), the magnitude of the working stress (σ_y) can be estimated by expressing Eq. (14) as:

$$\frac{\sigma_y}{K_u / \varepsilon_0} \leq 1 - \frac{\sigma_{\text{twinning}}}{K_u / \varepsilon_0} < 1 \quad (16)$$

It is noted that σ_{twinning} , K_u and ε_0 have positive values. Eq. (16) means, if the single compressive stress (σ_y) is larger than K_u/ε_0 (so called blocking stress (Heczko et al., 2000)), the magnetic field cannot induce the reversible variant switching. From the existing experiments, K_u/ε_0 is less than 3 MPa (Heczko et al., 2000, 2002; Murray et al., 2000). Therefore, the working stress σ_y (or the output stress limit of FSMA actuators) is low. By contrast, in obtaining the reversible variant switching in 2D configurations (both σ_y and σ_x are non-zero), the output stress σ_y can be larger than K_u/ε_0 as long as these two stresses satisfy the criterion of Eq. (14).

Equation (14) is derived for the case of a large H (i.e., $\frac{H \cdot M}{K_u} \gg 1$). With the same approach, the criterion for other cases can be obtained analytically or numerically (graphically). For example, the criterion for the rotating-field-induced reversible switching for medium H ($\frac{H \cdot M}{K_u} = 1$) is obtained (by substituting $\alpha = \pi/2$ into Eq. (8b) and using phase diagram Fig. 7(d)) as:

$$-\left(\frac{3}{4} - \frac{\sigma_{\text{twinning}}}{K_u / \epsilon_0}\right) \leq \frac{\sigma_y - \sigma_x}{K_u / \epsilon_0} \leq \frac{3}{4} - \frac{\sigma_{\text{twinning}}}{K_u / \epsilon_0} \quad (17)$$

Field-assisted superelasticity

From the phase diagram, we can study not only the field-induced variant switching, but also the field-assisted superelasticity (another important feature of FSMA), as shown in the loading path “S1” in Fig. 8. It is noted that, besides the material properties (K_u , M , σ_{twinning} and ϵ_0), the switching stresses (the stresses triggering the variant switching I→II or II→I) depend on the magnetic field. In other words, the switching stresses of the superelasticity can be changed by properly setting the field direction α and the field magnitude H . For a large H ($\frac{H \cdot M}{K_u} \gg 1$), the switching stresses for variant I→II and II→I can be determined with Eq. (8c)

and the phase diagram in Fig. 8:

$$\begin{aligned} \left(\frac{\sigma_y - \sigma_x}{K_u / \epsilon_0} \right)_{I \rightarrow II} &= \cos(2\alpha) + \frac{\sigma_{\text{twinning}}}{K_u / \epsilon_0} \\ \left(\frac{\sigma_y - \sigma_x}{K_u / \epsilon_0} \right)_{II \rightarrow I} &= \cos(2\alpha) - \frac{\sigma_{\text{twinning}}}{K_u / \epsilon_0} \end{aligned} \quad (18a)$$

For example in loading path “S1” in Fig. 8 ($\alpha = 0$), the switching stresses are:

$$\begin{aligned} \left(\frac{\sigma_y - \sigma_x}{K_u / \epsilon_0} \right)_{I \rightarrow II} &= 1 + \frac{\sigma_{\text{twinning}}}{K_u / \epsilon_0} \\ \left(\frac{\sigma_y - \sigma_x}{K_u / \epsilon_0} \right)_{II \rightarrow I} &= 1 - \frac{\sigma_{\text{twinning}}}{K_u / \epsilon_0} \end{aligned} \quad (18b)$$

2.1.3.2. Non-rotating-field-induced variant switching

Substituting Eq. (7) into Eq. (3), we obtain the energy difference with a fixed α .

$$\text{If } \alpha = 0, \frac{E_{V1} - E_{V2}}{K_u} = \begin{cases} \frac{(\sigma_y - \sigma_x)}{K_u / \epsilon_0} + \left(\frac{H \cdot M}{2K_u} \right)^2 - \frac{H \cdot M}{K_u} & 0 \leq \frac{H \cdot M}{K_u} \leq 2 \\ \frac{(\sigma_y - \sigma_x)}{K_u / \epsilon_0} - 1 & \frac{H \cdot M}{K_u} > 2 \end{cases} \quad (19a)$$

$$\text{If } \alpha = \frac{\pi}{2}, \frac{E_{V1} - E_{V2}}{K_u} = \begin{cases} \frac{(\sigma_y - \sigma_x)}{K_u / \epsilon_0} - \left(\frac{H \cdot M}{2K_u} \right)^2 + \frac{H \cdot M}{K_u} & 0 \leq \frac{H \cdot M}{K_u} \leq 2 \\ \frac{(\sigma_y - \sigma_x)}{K_u / \epsilon_0} + 1 & \frac{H \cdot M}{K_u} > 2 \end{cases} \quad (19b)$$

With these energy expressions, the phase diagrams in terms of the stresses and the field magnitude H are plotted in Fig. 10 (where $\alpha = 0$). The non-rotating-field induced variant switching can be demonstrated by the phase diagram (Fig. 11). Similarly, some important features can be obtained from the phase diagram.

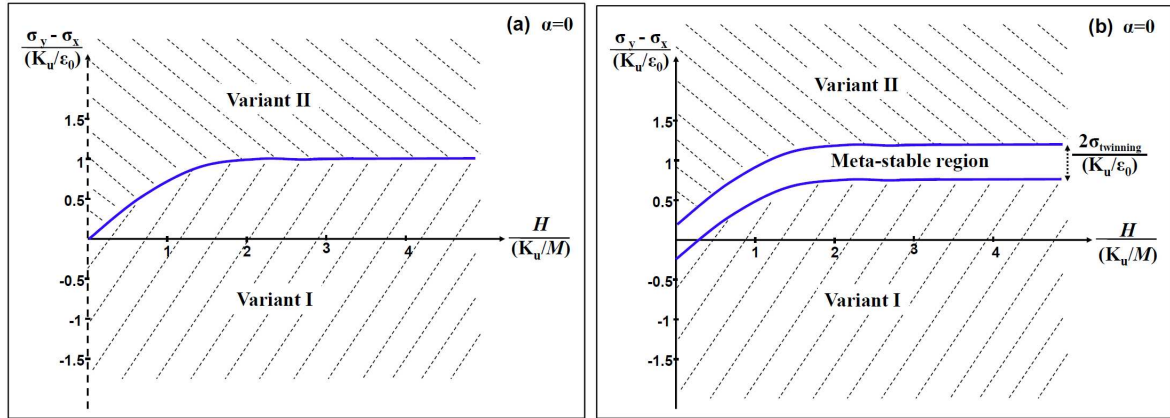


Fig. 10. Phase diagrams in terms of the stresses and the magnetic field magnitude at the field direction $\alpha=0$. The figure on the left-hand side (on the right-hand side) is without (with) hysteretic effect.

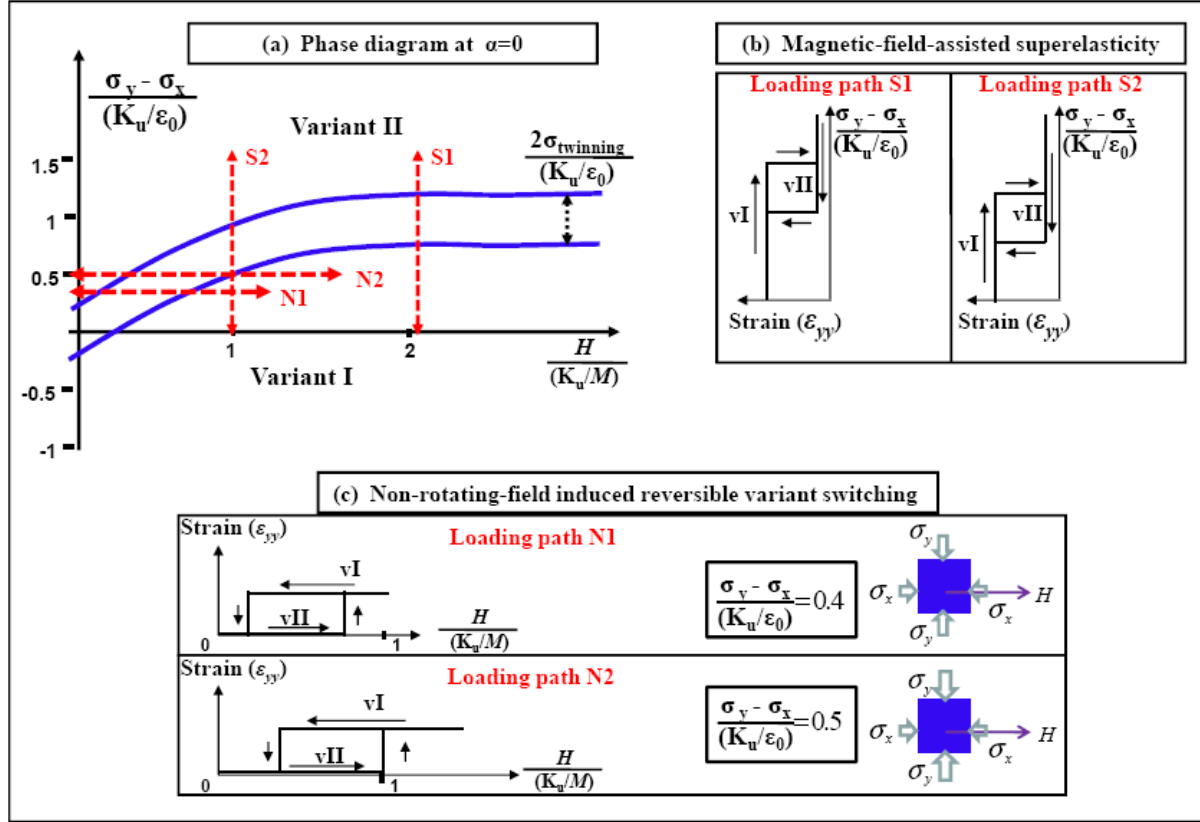


Fig. 11. Non-rotating-field induced strain (c) and field-assisted superelasticity (b) derived from the stresses—field-magnitude phase diagram (a). The different loading paths (N1 and N2 for non-rotating-field induced strain; S1 and S2 for field-assisted superelasticity) are indicated on the phase diagram (a).

Criterion of reversible variant switching

The criterion of setting stresses for obtaining the non-rotating-field induced reversible switching ($\alpha=0$) is:

$$\frac{\sigma_{\text{twinning}}}{K_u / \epsilon_0} \leq \frac{\sigma_y - \sigma_x}{K_u / \epsilon_0} \leq 1 - \frac{\sigma_{\text{twinning}}}{K_u / \epsilon_0} \quad (20)$$

This criterion is similar to (Heczko and Straka, 2003; Heczko et al., 2006; O’Handley, 1998) where a single stress is used. The solution of $(\sigma_y - \sigma_x)$ to Eq. (20) exists only when the material’s properties satisfy:

$$\frac{\sigma_{\text{twinning}}}{K_u / \epsilon_0} < 1 - \frac{\sigma_{\text{twinning}}}{K_u / \epsilon_0} \Rightarrow K_u / \epsilon_0 > 2\sigma_{\text{twinning}} \quad (21)$$

The condition in Eq. (21) was also pointed out in (Heczko, 2005; Straka and Heczko, 2005). It is noted that the requirement of the material properties is stricter in the non-rotating field (Eq. (21)) than in the rotating field (Eq. (15)). In other words, for FSMA with the material properties $\sigma_{twinning} < K_u/\epsilon_0 < 2\sigma_{twinning}$, it is the rotating field rather than non-rotating field that can induce reversible variant switching.

Switching magnetic field

It is also noted that the switching fields for variant I \rightarrow II (or II \rightarrow I) depend on the stresses and the hysteretic effect. They can be obtained from Eq. (19a) and the phase diagram with hysteretic effect (twinning stress) as:

$$\begin{aligned}\left(\frac{H}{K_u/M}\right)_{II \rightarrow I} &= 2\sqrt{1 - \left(1 - \left(\frac{\sigma_y - \sigma_x}{K_u/\epsilon_0} + \frac{\sigma_{twinning}}{K_u/\epsilon_0}\right)\right)} \\ \left(\frac{H}{K_u/M}\right)_{I \rightarrow II} &= 2\sqrt{1 - \left(1 - \left(\frac{\sigma_y - \sigma_x}{K_u/\epsilon_0} - \frac{\sigma_{twinning}}{K_u/\epsilon_0}\right)\right)}\end{aligned}\quad (22a)$$

For example, when $\frac{\sigma_y - \sigma_x}{K_u/\epsilon_0} = 0.5$ and $\frac{\sigma_y - \sigma_x}{K_u/\epsilon_0} = 0.25$ (loading path “N2” in Fig. 11), the switching fields are:

$$\begin{aligned}\left(\frac{H}{K_u/M}\right)_{II \rightarrow I} &= 1 \\ \left(\frac{H}{K_u/M}\right)_{I \rightarrow II} &= 2\left(1 - \frac{\sqrt{3}}{2}\right) \approx 0.27\end{aligned}\quad (22b)$$

Field-assisted superelasticity

The switching stresses for the field-assisted superelasticity depend on the field magnitude H and the hysteretic effect. With Eq. (19a) and the phase diagram (Fig. 11), the switching stresses can be determined as:

$$\left[\frac{(\sigma_y - \sigma_x)}{K_u / \epsilon_0} \right]_{I \rightarrow II} = \begin{cases} \frac{H \cdot M}{K_u} - \left(\frac{H \cdot M}{2K_u} \right)^2 + \frac{\sigma_{twinning}}{K_u / \epsilon_0} & 0 \leq \frac{H \cdot M}{K_u} \leq 2 \\ 1 + \frac{\sigma_{twinning}}{K_u / \epsilon_0} & \frac{H \cdot M}{K_u} > 2 \end{cases} \quad (23a)$$

$$\left[\frac{(\sigma_y - \sigma_x)}{K_u / \epsilon_0} \right]_{II \rightarrow I} = \begin{cases} \frac{H \cdot M}{K_u} - \left(\frac{H \cdot M}{2K_u} \right)^2 - \frac{\sigma_{twinning}}{K_u / \epsilon_0} & 0 \leq \frac{H \cdot M}{K_u} \leq 2 \\ 1 - \frac{\sigma_{twinning}}{K_u / \epsilon_0} & \frac{H \cdot M}{K_u} > 2 \end{cases} \quad (23b)$$

For example in the loading path “S2” in Fig. 11 ($\frac{\sigma_y - \sigma_x}{K_u / \epsilon_0} = 0.5$ and $\frac{\sigma_y - \sigma_x}{K_u / \epsilon_0} = 0.25$), the switching stress are:

$$\left[\frac{(\sigma_y - \sigma_x)}{K_u / \epsilon_0} \right]_{I \rightarrow II} = 1 \quad (24a)$$

$$\left[\frac{(\sigma_y - \sigma_x)}{K_u / \epsilon_0} \right]_{II \rightarrow I} = \frac{1}{2} \quad (24b)$$

For a large H ($\frac{H \cdot M}{K_u} > 2$, loading path “S1” in Fig. 11), the switching stresses in Eq. (23) are

the same as Eq. (18b) since the loading path “S1” in Fig. 11 is the same as “S1” in Fig. 8.

Unified description of switching fields/stresses and experimental verification

Since both the switching field (Eq. (22a) for field-induced switching) and switching stress (Eq. (23) for field-assisted superelasticity) are determined based on the energy difference (Eq. (19a)) and the hysteretic effect ($\frac{E_{V1} - E_{V2}}{K_u} = \pm \frac{\sigma_{twinning}}{K_u / \epsilon_0}$), there is a unified expression connecting these magneto-mechanical parameters:

$$\bar{\sigma} = \begin{cases} -\frac{1}{4} \cdot \bar{H}^2 + \bar{H} & 0 < \bar{H} \leq 2 \\ 1 & \bar{H} > 2 \end{cases} \quad (25)$$

where $\bar{\sigma} = \frac{(\sigma_y - \sigma_x) \mp \sigma_{twinning}}{K_u / \varepsilon_0}$ and $\bar{H} = \frac{H}{K_u / M}$. This formula of the switching parameters (switching fields/stresses) can be compared with the existing experiments ($\sigma_y \neq 0$ and $\sigma_x = 0$) of the field-induced switching and the field-assisted superelasticity in Fig. 12, where the solid line represents the analytic solution (Eq. (25)) and the points are experimental measurements. It is seen that the theoretical prediction agree with the experiments.

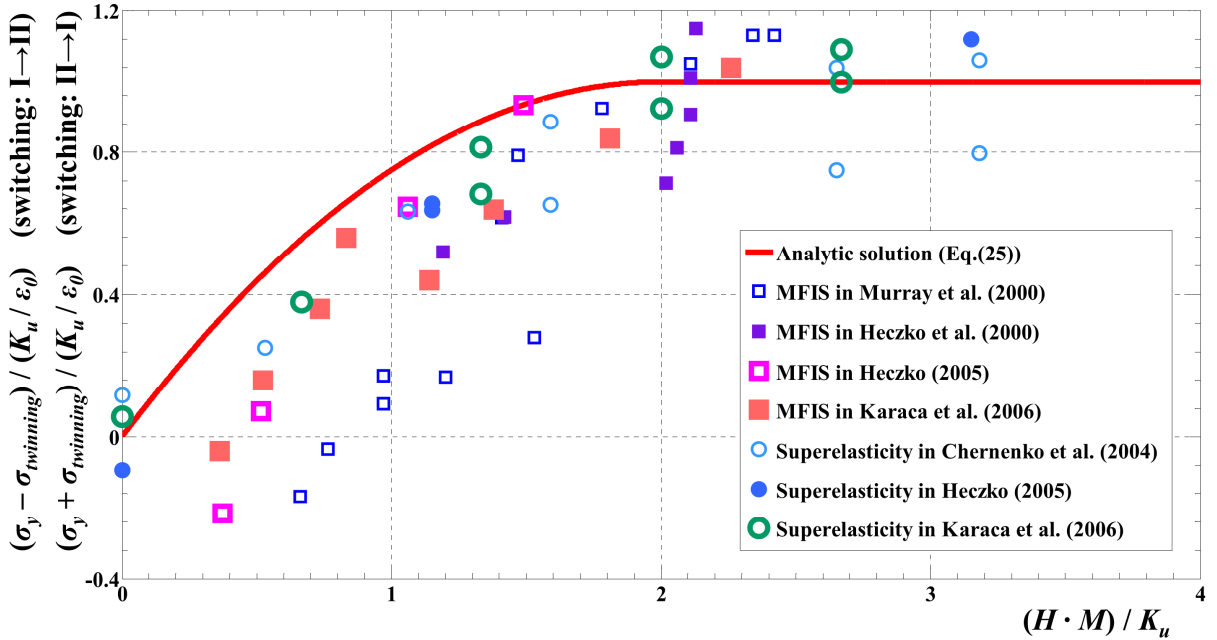


Fig. 12. Comparison between the analytic solution of switching fields/stresses and the experiments of magnetic field-induced strain (MFIS) and field-assisted superelasticity.

2.1.4. Discussions

Although the analytical results obtained above are only for some special conditions (e.g.,

$\frac{H \cdot M}{K_u} \gg 1$ and $\frac{H \cdot M}{K_u} = 1$ for the rotating field and $\alpha = 0$ for the non-rotating field), the

approach (the energy preference and the phase diagram with hysteretic effect) can give numerical solutions for other 2D cases. The motivation of this section is to provide a simple approach to understand and predict the main features of the variant switching in 2D configurations. Although the experimental implementation of the 2D configurations (Fig. 3(b)) will be more complicated than that of the simple loading (Fig. 3(a)), the 2D configurations have many potential applications for their advantages: higher working stress, controllable switching field/angle/stress and controllable time fractions of the two variants in a cyclic loading, etc.

For simplicity, only two variants are considered in the current model. That leads to a limitation of the model: the mechanical stresses must be compressive; otherwise the third variant (with c-axis along z-coordinate) must be considered. For example, the third variant might be energetically preferred in 2D tensile stresses (tensile σ_x and σ_y). In addition, the elastic energy, magnetostriction, demagnetization, magnetic-domain structures are ignored in current model. Detailed discussions on these factors can be found in literature (Chernenko et al., 2006; Heczko, 2005; Jin, 2009; O’Handley et al., 2000). Including these factors may enable the model to describe the continuous variant reorientation (i.e., the variant reorientation is not abrupt) (Murray et al., 2001; O’Handley et al., 2000). Moreover, the statistical model in (Glavatska et al., 2003) also predicted a significant dependence of the field-induced reversible strain on the 2D compressive stresses.

2.1.5. Conclusions

Graphical representation of energy preference (phase diagram with hysteretic effects) is a good tool to study the behaviors of FSMA under various loading conditions: rotating/non-rotating Magnetic Field-Induced Strain (MFIS) and field-assisted superelasticity. Due to the

hysteretic effect (non-zero twinning stress), there is a meta-stable region in the phase diagram, in which the material state (variant state) depends on the loading history.

Reversible MFIS (reversible variant switching) is obtained only when the difference between the two mechanical stresses ($\sigma_y - \sigma_x$) is in a range governed by the material properties (magnetic anisotropic energy K_u and lattice strain ε_0) and the hysteretic effect — twinning stress $\sigma_{twinning}$. The criterion and the related material requirement are different for the rotating field (Eqs. (14), (15)) and for the non-rotating field (Eqs. (20), (21)). Such criteria and material requirements for reversible MFIS provide design guidelines for FSMA actuators working in multiple cycles with reversible strains.

The output stress (σ_y) of a FSMA actuator can be larger than the blocking stress (K_u/ε_0) when an assistant stress (σ_x) is applied. By setting the difference between these stresses, we can also control the switching angles (Eqs. (9) and (10) for rotating field), the switching fields (Eq. (22a) for non-rotating field) and the time fractions of the martensite variants in cyclic rotating fields (Eq. (12)). Such 2D configurations can give much flexibility of FSMA applications in various situations.

2.2. Reversible strain criteria of ferromagnetic shape memory alloys under cyclic 3D magneto-mechanical loadings

2.2.1. Introduction

Recent researches (Glavatska et al., 2003; He et al., 2011) revealed that FSMA in 2D/3D configurations (with multi-axial stresses) had much more advantages than that in 1D configuration (with uniaxial stress). For example, in the 2D/3D configurations, higher working stress (higher output energy) can be provided, and the critical stress or magnetic field triggering the martensite reorientation can be tuned to satisfy various applications (He et al., 2011). Therefore, there are increasing theoretical researches on FSMA's behaviors under multi-axial loadings (2D/3D configurations) (e.g., Glavatska et al., 2003; He et al., 2011; Kiang and Tong, 2007; Kiefer and Lagoudas, 2009; L'vov et al., 2002).

Reversible strain (with martensite variants periodically switching to each other during cyclic loadings) is a basic requirement in most FSMA devices under magneto-mechanical loadings of multiple cycles. The criteria for obtaining the reversible strain in 1D (a uniaxial stress plus a non-rotating magnetic field) (Heczko and Straka, 2003; Heczko et al., 2006; Straka et al., 2006) and 2D configurations (biaxial compression plus a rotating/non-rotating magnetic field) (He et al., 2011) have been derived recently. However, the 3D criteria of reversible strain for general cyclic magneto-mechanical loadings are seldom reported. In this section, we extend our previous energy analysis (He et al., 2011) to study the switching among all the three tetragonal martensite variants of FSMA (i.e., five-layered modulated martensite variants in Ni-Mn-Ga single crystals (see Fig. 13)) under 3D magneto-mechanical cyclic loadings. Our aim is to provide a global picture (by a phase diagram) of the variant switching in FSMA and to derive general criteria for obtaining reversible strain under various 3D cyclic loadings.

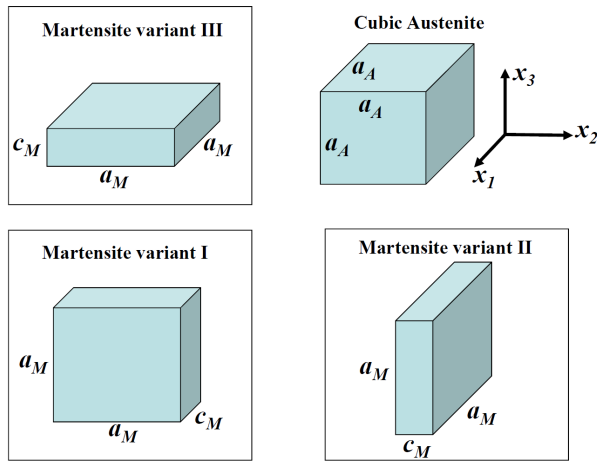


Fig. 13. Schematic diagram of the austenite and the martensite variants of Ferromagnetic Shape Memory Alloys (FSMA). a_A denotes the length of the austenite lattice; a_M and c_M denote the lengths of the long (a -axis) and short (c -axis) axes of the martensite lattice (the difference between a_M and c_M are exaggerated in the schematic diagram).

In the following paragraphs, the mechanical and magnetic energies of the three tetragonal martensite variants are formulated and compared to determine the energy preference of the variants under 3D magneto-mechanical loadings (Fig. 14(a)). For a clear comparison of the energy preference among the three variants, deviatoric magneto-mechanical stresses (Eq. (38)) are defined from the energy formulation and utilized in a phase diagram (a plane graph, Fig. 15 without hysteresis and Fig. 16 with hysteresis). In the phase diagram, various cyclic magneto-mechanical loadings can be conveniently studied (Figs. 17~20). Based on the phase diagram, the general criteria for obtaining the reversible strain under various 3D cyclic loadings are formulated (Eq. (43)). Particularly for actuators driven by cyclic magnetic fields, the criteria of setting the mechanical stresses to allow field-induced reversible strain are derived (Eq. (51) for rotating magnetic fields and Eq. (54) for non-rotating magnetic fields).

2.2.2. Energy analysis and phase diagrams

2.2.2.1. Energy formulation

In order to determine the energy preference of the martensite variants, we formulate and compare the energy of the variants under three-dimensional normal stresses and a magnetic field. For example in Fig. 14(a), the energy of variant I (which is assumed to consist of a single magnetic domain) includes mechanical energy $E_{mech-vI}$ and magnetic energy E_{mag-vI} (magnetic anisotropic energy ($K_u \cdot \sin^2 \theta_1$) and Zeeman energy ($-\vec{H} \cdot \vec{M}$)), which can be expressed as:

$$E_{mech-vI} = -\sigma_1 \cdot \varepsilon_1 + \sigma_2 \cdot \varepsilon_2 + \sigma_3 \cdot \varepsilon_3, \quad \text{where } \varepsilon_1 = 1 - \frac{c_M}{a_A} > 0, \quad \varepsilon_2 = \frac{a_M}{a_A} - 1 > 0 \quad (26)$$

$$E_{mag-vI} = K_u \cdot \sin^2 \theta_1 - \vec{H} \cdot \vec{M} \quad (27)$$

where a_A is the length of the austenite lattice; a_M and c_M are the lengths of the long (a -axis) and short (c -axis) axes of the martensite lattice; α_1 , α_2 and α_3 are respectively the angles between the magnetic field \vec{H} and x_1 -, x_2 - and x_3 -coordinates (Fig. 14(a)); θ_1 is the angle between the equilibrium magnetization \vec{M} and x_1 -coordinate; K_u , H and M are the uniaxial magnetic anisotropic energy, the magnitudes of the applied magnetic field (the unit is T) and the saturation magnetization, respectively. The values of the stresses (σ_1 , σ_2 and σ_3) are positive for compression and negative for tension in this section. Without losing generality, we ignore the effects of elastic energy and magneto-striction here. This simple energy formulation is adopted to facilitate the discussions and predictions of the martensite variant reorientation (He et al., 2011; Heczko et al., 2002; O'Handley, 1998; Straka and Heczko, 2003b).

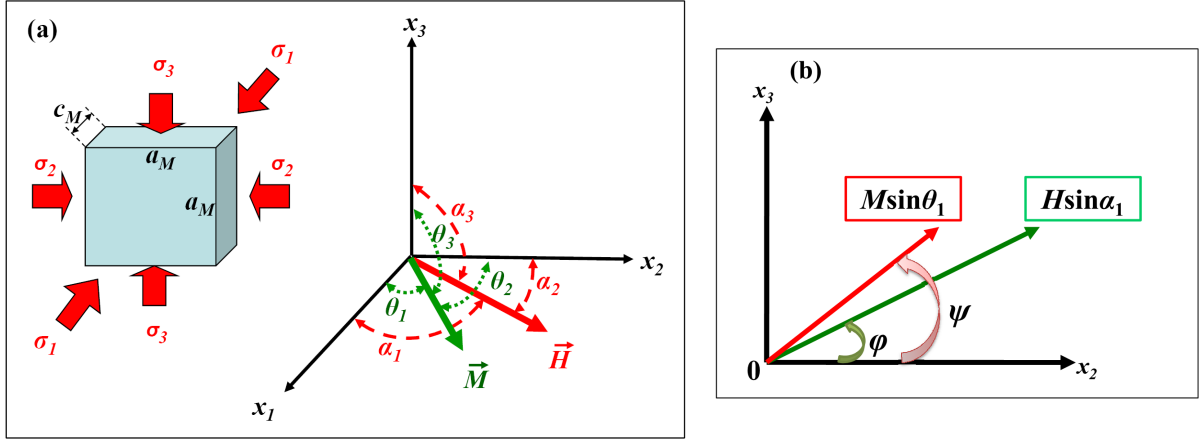


Fig. 14. (a) Schematic diagram of the equilibrium magnetization vector \vec{M} in the martensite variant I (short axis along x_1 -coordinate) under three-dimensional normal stresses ($\sigma_1, \sigma_2, \sigma_3$) and a magnetic field \vec{H} . α_1, α_2 and α_3 (θ_1, θ_2 and θ_3) are, respectively, the angles between the coordinates and the magnetic field \vec{H} (magnetization \vec{M}). (b) The projection of the magnetic field \vec{H} on the x_2 - x_3 plane (with the magnitude $H \sin \alpha_1$) and the projection of the vector \vec{M} on the same plane (with the magnitude $M \sin \theta_1$).

It is noted that the angles (defining the directions of the applied magnetic field \vec{H} and the equilibrium magnetization \vec{M}) have the following geometric relations:

$$\cos^2 \alpha_1 + \cos^2 \alpha_2 + \cos^2 \alpha_3 = 1 \quad (28a)$$

$$\cos^2 \theta_1 + \cos^2 \theta_2 + \cos^2 \theta_3 = 1 \quad (28b)$$

where θ_1, θ_2 and θ_3 are the angles between the equilibrium magnetization \vec{M} and x_1 -, x_2 - and x_3 -coordinates, respectively (see Fig. 14(a)). In order to determine the equilibrium magnetic energy, the direction of the magnetization \vec{M} (θ_1, θ_2 and θ_3) needs to be determined through the energy minimization principle. Take the case of variant I for example (Fig. 14(a)). By Eq. (28b), only two of θ_1, θ_2 and θ_3 are independent. Therefore, instead of using θ_1, θ_2 and θ_3 , we can describe the magnetization direction by θ_1 and ψ (ψ is the angle between x_2 -coordinate and the projection of the magnetization vector \vec{M} on the x_2 - x_3 plane, see Fig. 14(b)).

Similarly, we can use α_1 and ϕ to describe the direction of \vec{H} . Therefore, the magnetic energy of the martensite variant I in Eq. (27) can be expressed as:

$$E_{mag-vI} = K_u \cdot \sin^2 \theta_1 - H \cdot M (\cos \alpha_1 \cos \theta_1 + \sin \alpha_1 \sin \theta_1 \cos(\phi - \psi)) \quad (29)$$

The equilibrium magnetization direction (θ_1, ψ) can be determined by minimizing the magnetic energy as:

$$\frac{\partial E_{mag-vI}}{\partial \psi} = 0 \rightarrow \sin \alpha_1 \cdot \sin \theta_1 \cdot \sin(\phi - \psi) = 0 \rightarrow \psi = \phi \text{ (also making } \frac{\partial^2 E_{mag-vI}}{\partial \psi^2} \geq 0) \quad (30a)$$

$$\frac{\partial E_{mag-vI}}{\partial \theta_1} = 0 \rightarrow K_u \sin(2\theta_1) - H \cdot M [\sin \alpha_1 \cdot \cos \theta_1 \cdot \cos(\phi - \psi) - \sin \theta_1 \cdot \cos \alpha_1] = 0 \quad (30b)$$

Equation (30a) means that the projections of \vec{M} and \vec{H} have the same direction in the x_2 - x_3 plane. By Eq. (30a), Eq. (29) is reduced to Eq. (31a) to calculate the magnetic energy of variant I.

$$E_{mag-vI} = K_u \cdot \sin^2 \theta_1 - H \cdot M \cdot \cos(\alpha_1 - \theta_1) \quad (31a)$$

The first term on the right-hand side of Eq. (31a) is the magnetic anisotropic energy while the second term is the Zeeman energy. Similarly, the magnetic energy of variant II and III can be obtained as

$$E_{mag-vII} = K_u \cdot \sin^2 \theta_2 - H \cdot M \cdot \cos(\alpha_2 - \theta_2) \quad (31b)$$

$$E_{mag-vIII} = K_u \cdot \sin^2 \theta_3 - H \cdot M \cdot \cos(\alpha_3 - \theta_3) \quad (31c)$$

Using Eq. (30a), Eq. (30b) can be reduced to Eq. (32a) for determining the direction θ_1 of equilibrium magnetization in variant I:

$$K_u \cdot \sin 2\theta_1 - H \cdot M \cdot \sin(\alpha_1 - \theta_1) = 0 \quad \text{for variant I} \quad (32a)$$

Similarly, the equilibrium magnetization angles in variant II and III can be determined by:

$$K_u \cdot \sin 2\theta_2 - H \cdot M \cdot \sin(\alpha_2 - \theta_2) = 0 \quad \text{for variant II} \quad (32b)$$

$$K_u \cdot \sin 2\theta_3 - H \cdot M \cdot \sin(\alpha_3 - \theta_3) = 0 \quad \text{for variant III} \quad (32c)$$

Normalized by K_u , Eq. (32) changes to:

$$\sin 2\theta_i - \frac{H \cdot M}{K_u} \cdot \sin(\alpha_i - \theta_i) = 0 \quad \text{for variant i (i = 1, 2, 3)} \quad (33)$$

The above equations containing *sin* functions generally have no analytical solutions, except some special conditions. For example, Eq. (33) for minimizing the magnetic energy have the analytical solutions as:

$$\text{If } \frac{H \cdot M}{K_u} \approx 0, \quad \sin 2\theta_i = 0 \Rightarrow \theta_i = 0 \quad \text{for variant i (i = 1, 2, 3)} \quad (34a)$$

$$\text{If } \frac{H \cdot M}{K_u} = 1, \quad \theta_i = \frac{\alpha_i}{3} \quad \text{for variant i (i = 1, 2, 3)} \quad (34b)$$

$$\text{If } \frac{H \cdot M}{K_u} \gg 1, \quad \theta_i = \alpha_i \quad \text{for variant i (i = 1, 2, 3)} \quad (34c)$$

Equation (34) means that the magnetization is along the c-axis (the easy-axis of magnetization) when the applied field is weak ($H \cdot M / K_u \approx 0$); when H is strong ($H \cdot M / K_u \gg 1$), the magnetization is along the field; for other cases, the magnetization is in between the c-axis and the field. Detailed discussion about the dependences of the equilibrium magnetization angles on the direction and amplitude of the magnetic field can be found in (He et al., 2011).

With Eqs. (26) and (31a), the total energy of variant I, combining mechanical energy and magnetic energy can be expressed as

$$E_{vI} = E_{mech-vI} + E_{mag-vI} = -\sigma_1 \cdot \epsilon_1 + \sigma_2 \cdot \epsilon_2 + \sigma_3 \cdot \epsilon_2 + K_u \cdot \sin^2 \theta_1 - H \cdot M \cdot \cos(\alpha_1 - \theta_1) \quad (35a)$$

Similarly, the energy of variants II and III can be obtained respectively as

$$\begin{aligned} E_{vII} &= E_{mech-vII} + E_{mag-vII} \\ &= -\sigma_2 \cdot \epsilon_1 + \sigma_3 \cdot \epsilon_2 + \sigma_1 \cdot \epsilon_2 + K_u \cdot \sin^2 \theta_2 - H \cdot M \cdot \cos(\alpha_2 - \theta_2) \end{aligned} \quad (35b)$$

$$\begin{aligned} E_{vIII} &= E_{mech-vIII} + E_{mag-vIII} \\ &= -\sigma_3 \cdot \epsilon_1 + \sigma_1 \cdot \epsilon_2 + \sigma_2 \cdot \epsilon_2 + K_u \cdot \sin^2 \theta_3 - H \cdot M \cdot \cos(\alpha_3 - \theta_3) \end{aligned} \quad (35c)$$

Normalized by K_u , the energy of the variants is expressed as

$$\bar{E}_{vl} \equiv \frac{E_{vl}}{K_u} = -\frac{\sigma_1}{K_u} \cdot \varepsilon_1 + \frac{\sigma_2}{K_u} \cdot \varepsilon_2 + \frac{\sigma_3}{K_u} \cdot \varepsilon_3 + \sin^2 \theta_1 - \frac{H \cdot M}{K_u} \cdot \cos(\alpha_1 - \theta_1) \quad (36a)$$

$$\bar{E}_{vll} \equiv \frac{E_{vll}}{K_u} = -\frac{\sigma_2}{K_u} \cdot \varepsilon_1 + \frac{\sigma_3}{K_u} \cdot \varepsilon_2 + \frac{\sigma_1}{K_u} \cdot \varepsilon_3 + \sin^2 \theta_2 - \frac{H \cdot M}{K_u} \cdot \cos(\alpha_2 - \theta_2) \quad (36b)$$

$$\bar{E}_{vlll} \equiv \frac{E_{vlll}}{K_u} = -\frac{\sigma_3}{K_u} \cdot \varepsilon_1 + \frac{\sigma_1}{K_u} \cdot \varepsilon_2 + \frac{\sigma_2}{K_u} \cdot \varepsilon_3 + \sin^2 \theta_3 - \frac{H \cdot M}{K_u} \cdot \cos(\alpha_3 - \theta_3) \quad (36c)$$

2.2.2.2. Phase diagrams

In order to compare the variants' energy to determine their energy preference in the given mechanical stresses (σ_1 , σ_2 and σ_3) and a magnetic field (\vec{H}), we calculate the mean (\bar{E}_{mean}) and the deviatoric parts (S_i ($i = 1, 2$ and 3)) of the variants' energy as:

$$\begin{aligned} \bar{E}_{mean} \equiv \frac{\bar{E}_{vl} + \bar{E}_{vll} + \bar{E}_{vlll}}{3} &= \frac{1}{3} \left\{ \frac{(2\varepsilon_2 - \varepsilon_1)}{K_u} (\sigma_1 + \sigma_2 + \sigma_3) + \sin^2 \theta_1 + \sin^2 \theta_2 + \sin^2 \theta_3 \right. \\ &\quad \left. - \frac{H \cdot M}{K_u} \cdot [\cos(\alpha_1 - \theta_1) + \cos(\alpha_2 - \theta_2) + \cos(\alpha_3 - \theta_3)] \right\} \end{aligned} \quad (37)$$

$$\begin{aligned} S_1 &\equiv \bar{E}_{mean} - \bar{E}_{vl} \\ &= \frac{1}{3} \left\{ \frac{(2\sigma_1 - \sigma_2 - \sigma_3)}{K_u / \varepsilon_0} - 2\sin^2 \theta_1 + \sin^2 \theta_2 + \sin^2 \theta_3 \right. \\ &\quad \left. + \frac{H \cdot M}{K_u} \cdot [2\cos(\alpha_1 - \theta_1) - \cos(\alpha_2 - \theta_2) - \cos(\alpha_3 - \theta_3)] \right\} \\ &= S_{1-mech} + S_{1-mag} \end{aligned} \quad (38a)$$

$$\begin{aligned} S_2 &\equiv \bar{E}_{mean} - \bar{E}_{vll} \\ &= \frac{1}{3} \left\{ \frac{(2\sigma_2 - \sigma_3 - \sigma_1)}{K_u / \varepsilon_0} - 2\sin^2 \theta_2 + \sin^2 \theta_3 + \sin^2 \theta_1 \right. \\ &\quad \left. + \frac{H \cdot M}{K_u} \cdot [2\cos(\alpha_2 - \theta_2) - \cos(\alpha_3 - \theta_3) - \cos(\alpha_1 - \theta_1)] \right\} \\ &= S_{2-mech} + S_{2-mag} \end{aligned} \quad (38b)$$

$$\begin{aligned}
S_3 &\equiv \bar{E}_{mean} - \bar{E}_{vIII} \\
&= \frac{1}{3} \left\{ \frac{(2\sigma_3 - \sigma_1 - \sigma_2)}{K_u / \epsilon_0} - 2\sin^2 \theta_3 + \sin^2 \theta_1 + \sin^2 \theta_2 \right. \\
&\quad \left. + \frac{H \cdot M}{K_u} \cdot [2\cos(\alpha_3 - \theta_3) - \cos(\alpha_1 - \theta_1) - \cos(\alpha_2 - \theta_2)] \right\} \\
&= S_{3-mech} + S_{3-mag}
\end{aligned} \tag{38c}$$

where:

$$\left\{
\begin{aligned}
\epsilon_0 &= \epsilon_1 + \epsilon_2 = \frac{a_M - c_M}{a_A} \\
S_{1-mech} &= \frac{1}{3} \cdot \frac{(2\sigma_1 - \sigma_2 - \sigma_3)}{K_u / \epsilon_0} \\
S_{2-mech} &= \frac{1}{3} \cdot \frac{(2\sigma_2 - \sigma_1 - \sigma_3)}{K_u / \epsilon_0} \\
S_{3-mech} &= \frac{1}{3} \cdot \frac{(2\sigma_3 - \sigma_2 - \sigma_1)}{K_u / \epsilon_0} \\
S_{1-mag} &= \frac{1}{3} \left\{ -2\sin^2 \theta_1 + \sin^2 \theta_2 + \sin^2 \theta_3 + \frac{H \cdot M}{K_u} \cdot [2\cos(\alpha_1 - \theta_1) - \cos(\alpha_2 - \theta_2) - \cos(\alpha_3 - \theta_3)] \right\} \\
S_{2-mag} &= \frac{1}{3} \left\{ -2\sin^2 \theta_2 + \sin^2 \theta_1 + \sin^2 \theta_3 + \frac{H \cdot M}{K_u} \cdot [2\cos(\alpha_2 - \theta_2) - \cos(\alpha_1 - \theta_1) - \cos(\alpha_3 - \theta_3)] \right\} \\
S_{3-mag} &= \frac{1}{3} \left\{ -2\sin^2 \theta_3 + \sin^2 \theta_2 + \sin^2 \theta_1 + \frac{H \cdot M}{K_u} \cdot [2\cos(\alpha_3 - \theta_3) - \cos(\alpha_2 - \theta_2) - \cos(\alpha_1 - \theta_1)] \right\}
\end{aligned}
\right.$$

$\epsilon_0 (> 0)$ is the strain change due to variant switching; S_{i-mech} and S_{i-mag} ($i = 1, 2$ and 3) are the normalized deviatoric mechanical stresses and magneto-stresses (magnetic driving force for variant switching), respectively. It is noted that there are simple relations between these deviatoric parts:

$$\left\{
\begin{aligned}
S_1 + S_2 + S_3 &= 0 \\
S_{1-mech} + S_{2-mech} + S_{3-mech} &= 0 \\
S_{1-mag} + S_{2-mag} + S_{3-mag} &= 0
\end{aligned}
\right. \tag{39}$$

Therefore, a phase diagram (a plane graph) of the martensite variants under three-dimensional mechanical stresses and a magnetic field can be obtained in terms of the deviatoric parts S_i (see a simple example in Fig. 15, where $H \cdot M / K_u \approx 0$ is assumed, i.e., $S_{i-mag} = 0$). It is noted that when there is a larger compression (i.e., larger positive stress value) along x_1 direction (or x_2, x_3 directions), S_1 (or S_2, S_3) will be larger (according to Eq. (38)) so that variant I (or II, III) will be more energetically preferred. For example, variant II is energetically preferred under the single compressive stress along x_2 -coordinate with $\bar{\sigma}_2 = \frac{\sigma_2}{K_u / \epsilon_0} = 1$ and $\bar{\sigma}_1 = \bar{\sigma}_3 = 0$, which is represented by point A (with the coordinates: $S_2 = 2/3$, $S_1 = S_3 = -1/3$) in Fig. 15. The coordinates of point A are determined by the perpendicular projections of the vector OA onto the three axes (S_i). It is noted that the phase diagram is a planar diagram (plane graph) because only two of the S_i coordinates are independent (see Eq. (39)).

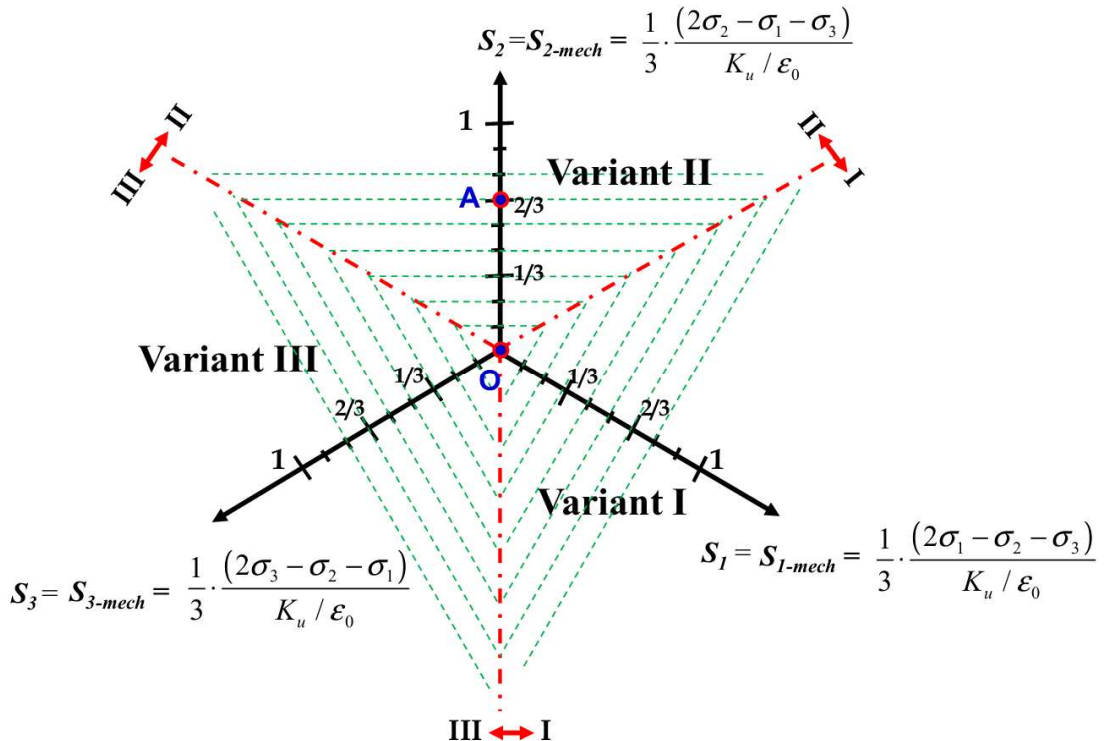


Fig. 15. Phase diagram of the three martensite variants in terms of normalized deviatoric magneto-mechanical stresses without hysteresis. The phase diagram (a plane graph) consists of three regions

where the variants I, II and III are energetically preferred, respectively. When no magnetic field is applied, the deviatoric magneto-mechanical stresses S_i (defined by Eq. (38)) only have the mechanical parts ($S_i=S_{i-mech}$). The coordinates (S_1, S_2, S_3) of a point (e.g, point A) are determined by the perpendicular projections of the vector OA onto the three axes. Here, point A has the coordinates: $S_2 = 2/3$, $S_1 = S_3 = -1/3$.

The phase diagram in Fig. 15 is equally divided into three regions for the energetically preferred states — variant I, II and III. A border between any two of these regions is the equal-energy line signifying the reorientation between the two martensite variants. In the phase diagram, there are three borders (switching lines I↔II, II↔III and III↔I) defined as:

$$\text{Switching I} \leftrightarrow \text{II} \quad S_1 = S_2 \quad (S_3 < 0) \quad (40\text{a})$$

$$\text{Switching I} \leftrightarrow \text{III} \quad S_1 = S_3 \quad (S_2 < 0) \quad (40\text{b})$$

$$\text{Switching II} \leftrightarrow \text{III} \quad S_2 = S_3 \quad (S_1 < 0) \quad (40\text{c})$$

This kind of phase diagram has been shown to be useful in studying the martensite phase transformation and variant switching under three-dimensional mechanical loadings (Levitin and Preston, 2002a, 2002b).

In real experiments, martensite variant reorientation (switching) needs extra energy to overcome some frictional force (known as twinning stress $\sigma_{twinning}$) (Heczko, 2005; Heczko and Straka, 2003; Heczko et al., 2006; Likhachev and Ullakko, 2000; Straka et al., 2011). Therefore, the switching lines with hysteresis are determined (using the definitions of S_i in Eq. (38)) as:

$$\left\{ \begin{array}{l} \text{Line I} \rightarrow \text{II: } S_2 - S_1 = (\bar{E}_{mean} - \bar{E}_{vII}) - (\bar{E}_{mean} - \bar{E}_{vI}) = \bar{E}_{vI} - \bar{E}_{vII} = \frac{\sigma_{twinning}}{K_u / \epsilon_0} \text{ and } S_2 > S_3 \\ \text{Line I} \leftarrow \text{II: } S_1 - S_2 = (\bar{E}_{mean} - \bar{E}_{vI}) - (\bar{E}_{mean} - \bar{E}_{vII}) = \bar{E}_{vII} - \bar{E}_{vI} = \frac{\sigma_{twinning}}{K_u / \epsilon_0} \text{ and } S_1 > S_3 \end{array} \right. \quad (41\text{a})$$

$$\left\{ \begin{array}{l} \text{Line I} \rightarrow \text{III}: S_3 - S_1 = \frac{\sigma_{\text{twinning}}}{K_u / \varepsilon_0} \text{ and } S_3 > S_2 \\ \text{Line I} \leftarrow \text{III}: S_1 - S_3 = \frac{\sigma_{\text{twinning}}}{K_u / \varepsilon_0} \text{ and } S_1 > S_2 \end{array} \right. \quad (41\text{b})$$

$$\left\{ \begin{array}{l} \text{Line II} \rightarrow \text{III}: S_3 - S_2 = \frac{\sigma_{\text{twinning}}}{K_u / \varepsilon_0} \text{ and } S_3 > S_1 \\ \text{Line II} \leftarrow \text{III}: S_2 - S_3 = \frac{\sigma_{\text{twinning}}}{K_u / \varepsilon_0} \text{ and } S_2 > S_1 \end{array} \right. \quad (41\text{c})$$

It is seen that the three equal-energy lines (lines $\text{I} \leftrightarrow \text{II}$, $\text{II} \leftrightarrow \text{III}$ and $\text{III} \leftrightarrow \text{I}$) are replaced by six switching lines (considering hysteresis) as shown in Fig. 16, where the normalized twinning stress is assumed: $\frac{\sigma_{\text{twinning}}}{K_u / \varepsilon_0} = \frac{1}{3}$.

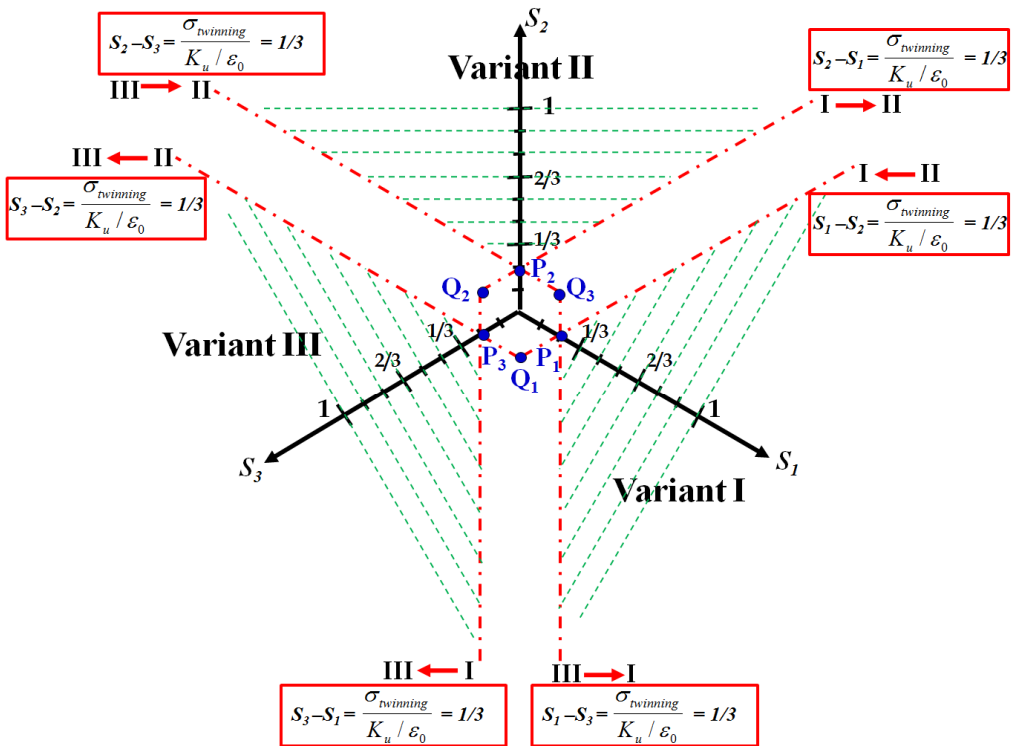


Fig. 16. Phase diagram of the three martensite variants in terms of normalized deviatoric magneto-mechanical stresses S_i (defined in Eq. (38)) with hysteresis (normalized twinning stress is assumed:

$\frac{\sigma_{\text{twinning}}}{K_u / \varepsilon_0} = \frac{1}{3}$). The phase diagram consists of stable regions (the shaded area where only one variant can exist) and meta-stable regions (un-shaded area where the variant state depends on loading history).

The phase diagram (with hysteresis) is divided into several parts: three stable regions (for variant I, II and III, respectively) and some meta-stable regions. The three stable regions are defined as

$$\text{Variant I} \quad S_1 - S_2 \geq \frac{\sigma_{\text{twinning}}}{K_u / \epsilon_0} \quad \text{and} \quad S_1 - S_3 \geq \frac{\sigma_{\text{twinning}}}{K_u / \epsilon_0} \quad (42\text{a})$$

$$\text{Variant II} \quad S_2 - S_1 \geq \frac{\sigma_{\text{twinning}}}{K_u / \epsilon_0} \quad \text{and} \quad S_2 - S_3 \geq \frac{\sigma_{\text{twinning}}}{K_u / \epsilon_0} \quad (42\text{b})$$

$$\text{Variant III} \quad S_3 - S_1 \geq \frac{\sigma_{\text{twinning}}}{K_u / \epsilon_0} \quad \text{and} \quad S_3 - S_2 \geq \frac{\sigma_{\text{twinning}}}{K_u / \epsilon_0} \quad (42\text{c})$$

In the meta-stable regions, the material's state depends on the loading history. With this phase diagram, we can study the path-dependent martensite variant reorientation and derive the criterion for obtaining reversible strain under cyclic magneto-mechanical loadings as shown in the following sub-section.

2.2.3. Criterion for obtaining reversible strain under cyclic magneto-mechanical loadings

With the phase diagram (Fig. 16) and Eq. (42), a general criterion for obtaining reversible strain can be obtained: when a cyclic-loading path touches any two of the three stable regions, the cyclic switching between these two variants (denoted by i and j , $i \neq j$) will occur and lead to reversible strain. Mathematically, we can express this criterion as:

$$(S_i - S_j)_{\max} \geq \frac{\sigma_{\text{twinning}}}{K_u / \epsilon_0} \quad \text{at that time} \quad S_i - S_k \geq \frac{\sigma_{\text{twinning}}}{K_u / \epsilon_0} \quad (43\text{a})$$

$$(S_i - S_j)_{\min} \leq -\frac{\sigma_{\text{twinning}}}{K_u / \epsilon_0} \quad \text{at that time} \quad S_j - S_k \geq \frac{\sigma_{\text{twinning}}}{K_u / \epsilon_0} \quad (43\text{b})$$

where k represents the variant other than i or j (i.e., $k \neq i, k \neq j$). That means, when the two extreme points ($(S_i - S_j)_{\max}$ and $(S_i - S_j)_{\min}$) of the loading path are respectively in the stable regions for variants i and j , the reversible strain due to the cyclic switching between these two variants can be obtained.

In the remaining parts of this section, typical examples are demonstrated for the applications of the general criterion (Eq. (43)) in different kinds of cyclic loadings: (1) pure mechanical stresses, (2) pure magnetic field (rotating or non-rotating) and (3) proper stresses setting for obtaining reversible strain with a cyclic magnetic field.

2.2.3.1. Pure mechanical stresses (ignorable magnetic field $H \cdot M / K_u \approx 0$)

The case of pure mechanical stresses is obtained by substituting Eq. (34a) into Eq. (38):

$$\begin{cases} S_{1-mag} = 0 \\ S_{2-mag} = 0 \\ S_{3-mag} = 0 \end{cases} \quad \text{and} \quad \begin{cases} S_1 = S_{1-mech} = \frac{1}{3} \cdot \frac{(2\sigma_1 - \sigma_2 - \sigma_3)}{K_u / \epsilon_0} \\ S_2 = S_{2-mech} = \frac{1}{3} \cdot \frac{(2\sigma_2 - \sigma_1 - \sigma_3)}{K_u / \epsilon_0} \\ S_3 = S_{3-mech} = \frac{1}{3} \cdot \frac{(2\sigma_3 - \sigma_2 - \sigma_1)}{K_u / \epsilon_0} \end{cases} \quad (44)$$

That means, when the magnetic field is weak ($H \cdot M / K_u \approx 0$), the mechanical stresses are the dominant driving forces for the variant switching. In Fig. 17, it is convenient to use Eq. (44) to determine the loading paths of the two examples (Eqs. (45a) and (45b)) for the pure-mechanical cyclic loadings of compression and tension.

$$\left\{ \begin{array}{l} \text{fixed } \bar{\sigma}_1 = \frac{\sigma_1}{K_u / \epsilon_0} = \frac{1}{3} \\ \bar{\sigma}_2 = \frac{\sigma_2}{K_u / \epsilon_0} \text{ changes between } -1 \text{ and } +1 \\ \text{fixed } \bar{\sigma}_3 = \frac{\sigma_3}{K_u / \epsilon_0} = 0 \end{array} \right. \quad (45a)$$

$$\begin{cases} \text{fixed } \bar{\sigma}_1 = 1 \\ \bar{\sigma}_2 \text{ changes between } -1 \text{ and } +1 \\ \text{fixed } \bar{\sigma}_3 = 0 \end{cases} \quad (45b)$$

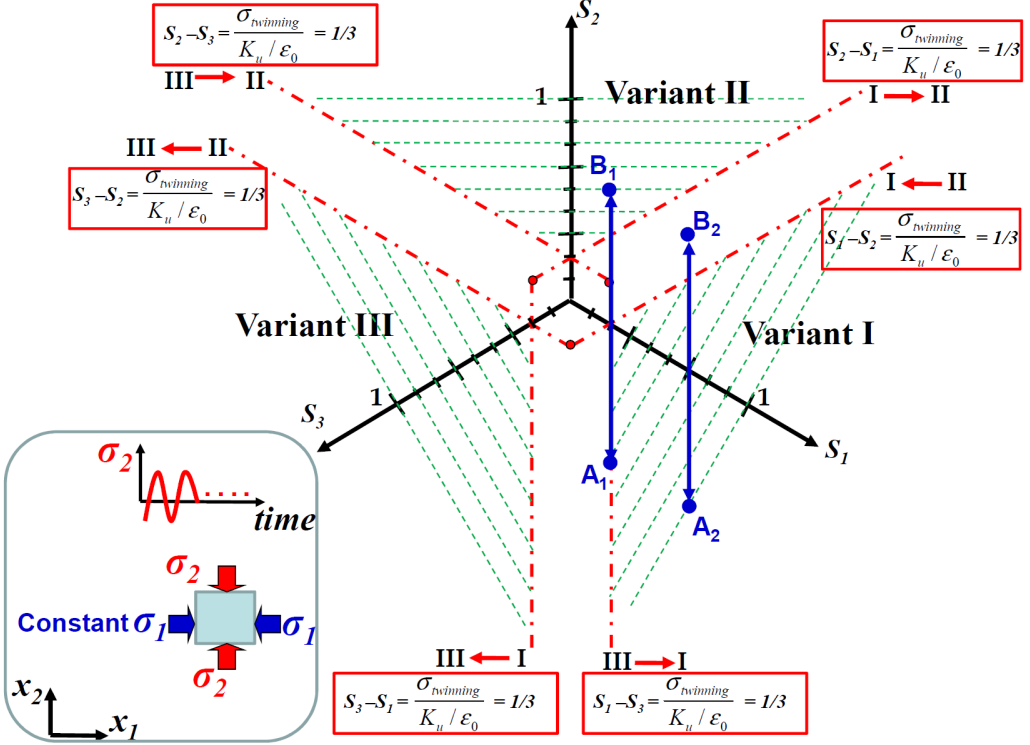


Fig. 17. The loading paths of cyclic tension and compression along x_2 -direction ($\bar{\sigma}_2 = \frac{\sigma_2}{K_u / \varepsilon_0} = -1 \sim 1$) while the other stresses are fixed: ($\bar{\sigma}_1 = 1/3$, $\bar{\sigma}_3 = 0$) for path A_1B_1 , and ($\bar{\sigma}_1 = 1$, $\bar{\sigma}_3 = 0$) for path A_2B_2 . The loading path A_1B_1 touching two stable regions have reversible strain via cyclic switching between variants I and II; the loading path A_2B_2 touching only one stable region cannot have cyclic variant switching.

In the first example (Eq. (45a)), the normalized stress ($\bar{\sigma}_2$) along x_2 -direction cyclically changes between -1 (tension) and $+1$ (compression), while the other two stresses are fixed ($\bar{\sigma}_1=1/3$ and $\bar{\sigma}_3=0$). It is seen that the loading path (A_1B_1) for this example touches the two stable regions of variants I and II so that the material will cyclically switch between variant II and variant I (see Fig. 17). If the stress along x_1 -direction increases (e.g., $\bar{\sigma}_1=1$), the loading

path A₂B₂ (Eq. (45b)) can touch only one stable region; that means the material will stay in variant I without martensite reorientation or reversible strain. According to the general criterion Eq. (43), when the cyclic mechanical-loading path satisfies Eq. (46), the reversible strain of the cyclic switching between variants I and II can be obtained.

$$(S_1 - S_2)_{\max} \geq \frac{\sigma_{\text{twinning}}}{K_u / \epsilon_0} \quad \text{at that time} \quad S_1 - S_3 \geq \frac{\sigma_{\text{twinning}}}{K_u / \epsilon_0} \quad (46a)$$

$$(S_1 - S_2)_{\min} \leq -\frac{\sigma_{\text{twinning}}}{K_u / \epsilon_0} \quad \text{at that time} \quad S_2 - S_3 \geq \frac{\sigma_{\text{twinning}}}{K_u / \epsilon_0} \quad (46b)$$

It is easy to verify that, the loading path's extreme points of the first example (points A₁ and B₁) satisfy respectively Eqs. (46a) and (46b), while the point B₂ of the second example cannot satisfy Eq. (46b). From these simple examples, it is shown that the reversible strain can be obtained with cyclic compression and/or cyclic tension as long as the mechanical stresses satisfy the general criterion Eq. (43), or particularly Eq. (46) for cyclic switching between variants I and II.

2.2.3.2. Pure magnetic field ($\sigma_1 = \sigma_2 = \sigma_3 = 0$)

Substituting Eq. (34c) into Eq. (38), we obtain the deviatoric stresses S_i for the strong magnetic field ($H \cdot M / K_u \gg 1$):

$$S_1 = S_{1-\text{mech}} + \cos^2 \alpha_1 - \frac{1}{3}, \quad S_2 = S_{2-\text{mech}} + \cos^2 \alpha_2 - \frac{1}{3}, \quad S_3 = S_{3-\text{mech}} + \cos^2 \alpha_3 - \frac{1}{3} \quad (47a)$$

where the geometric relation of Eq. (28a) has been used. When no mechanical stress is applied ($\sigma_1 = \sigma_2 = \sigma_3 = 0$, i.e., $S_{1-\text{mech}} = S_{2-\text{mech}} = S_{3-\text{mech}} = 0$), Eq. (47a) can be simplified to:

$$S_1 = \cos^2 \alpha_1 - \frac{1}{3}, \quad S_2 = \cos^2 \alpha_2 - \frac{1}{3}, \quad S_3 = \cos^2 \alpha_3 - \frac{1}{3} \quad (47b)$$

There are usually two types of magnetic loadings: (1) rotating magnetic field (changing the magnetic-field direction with a fixed magnitude) (e.g., Boonyongmaneerat et al., 2007; Chmielus et al., 2008; Müllner et al., 2002); (2) non-rotating magnetic field (changing the magnitude of a magnetic field with a fixed direction) (e.g., Murray et al., 2000; Straka and Heczko, 2005; Ullakko et al., 1996).

Rotating magnetic field

In literature, there are some experiments with a magnetic field rotating around a certain axis of the single crystal FSMA (e.g., Boonyongmaneerat et al., 2007; Chmielus et al., 2008; Müllner et al., 2002). For example, a strong magnetic field rotates around x_3 -axis (i.e., fixed $\alpha_3 = 90^\circ$ and the field rotates in the x_1 - x_2 plane, see the insert of Fig. 18) can induce reversible strain (cyclic variant switching) without mechanical stresses. Using Eq. (47b), the loading path AB (in Fig. 18) representing a strong magnetic field rotating around x_3 -axis can be plotted, which touches the two stable regions for variants I and II. It is noted that, for the rotating field around x_3 -axis, the angle α_3 is fixed ($= 90^\circ$) and S_3 is also fixed ($S_3 = -1/3$ according to Eq. (47b)); therefore, the line AB is perpendicular to the coordinate S_3 in Fig. 18. Similarly, lines BC and CA in Fig. 18 represent the paths of a strong rotating field around x_1 -axis and x_2 -axis respectively.

To obtain the reversible strain with cyclic switching between variants i and j , the criterion Eq. (43) must be satisfied. It is easy to verify that the strong rotating field without mechanical stresses (Eq. (47b)) satisfies the criterion because $(S_i - S_j)$ cyclically changes between -1 and $+1$, and the normalized twinning stress is always positive and less than 1:

$$S_i - S_j \in [-1, +1] \quad (48a)$$

$$0 < \frac{\sigma_{twinning}}{K_u / \varepsilon_0} < 1 \quad (48b)$$

Equation (48b) is the basic requirement of the material properties for the Magnetic-Field-Induced-Strain (MFIS) in FSMA (He et al., 2011; Heczko and Straka, 2003; Söderberg et al., 2005).

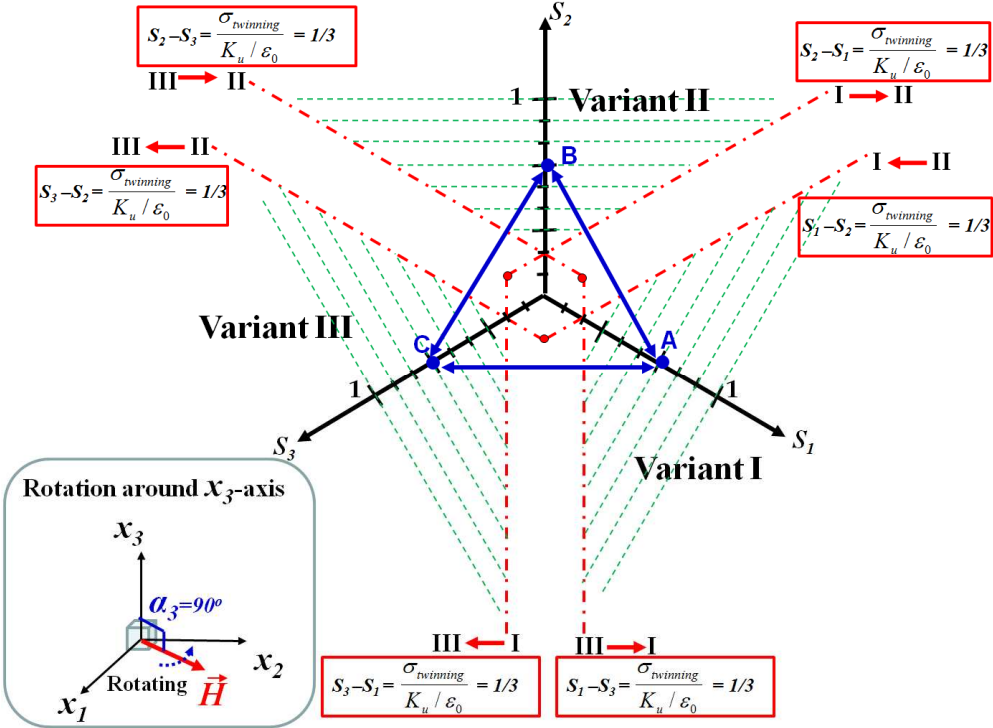


Fig. 18. The loading paths of the strong rotating magnetic fields ($H \cdot M / K_u \gg 1$) without mechanical stresses ($\sigma_1 = \sigma_2 = \sigma_3 = 0$): BC for rotation around x_1 -axis ($\alpha_1 = 90^\circ$), CA for rotation around x_2 -axis ($\alpha_2 = 90^\circ$), AB for rotation around x_3 -axis ($\alpha_3 = 90^\circ$). Each loading path can touch two stable regions leading to cyclic switching between the two variants of the stable regions.

Non-rotating magnetic field

Usually, non-rotating magnetic fields are applied along a certain axis of the single crystal. For example, the direction of the applied magnetic field is fixed in x_1 -direction (i.e., $\alpha_1 = 0^\circ$, $\alpha_2 = 90^\circ$ and $\alpha_3 = 90^\circ$) while the magnitude of the magnetic field cyclically changes between zero ($H = 0$) and a large value ($H \cdot M / K_u \gg 1$). With Eq. (44) for weak fields, Eq. (47a) for

strong fields and $S_{i-mech} = 0$ (no mechanical stress), the two extreme points of the loading path (in Fig. 19) corresponding to $H = 0$ and $H \cdot M / K_u \gg 1$ are point O ($S_1 = S_2 = S_3 = 0$) and point A ($S_1 = 2/3$, $S_2 = S_3 = -1/3$), respectively. Based on the symmetry of Eq. (38), the loading path of the non-rotating field along x_1 -axis is represented by the line OA. Similarly, the loading paths for the cyclic non-rotating magnetic fields along x_2 -axis and x_3 -axis can be represented by OB and OC, respectively, in Fig. 19. It is seen that a non-rotating cyclic magnetic field cannot induce reversible variant switching because its loading path cannot touch two stable regions of the phase diagram. In real applications of non-rotating magnetic fields, mechanical stresses are needed to obtain reversible strain. Thus, an important question arises: how to set the mechanical stresses to allow the cyclic magnetic field to induce reversible strain? This question is answered in the following sub-section.

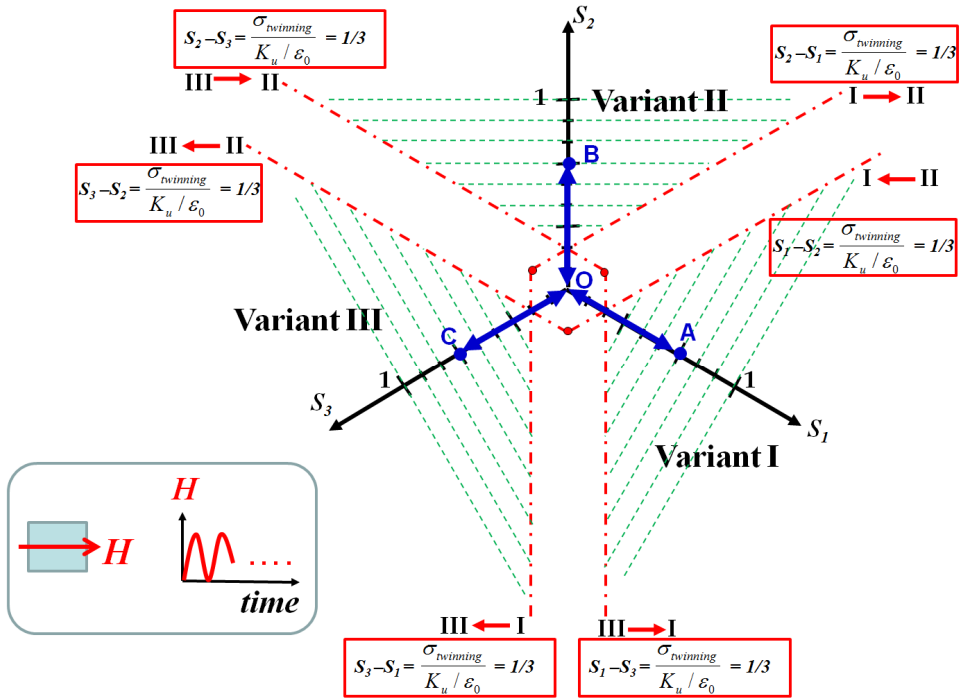


Fig. 19. The loading paths of the non-rotating magnetic fields (with magnitudes cyclically changing between $H = 0$ and a large value $H \cdot M / K_u \gg 1$) in the phase diagram: OA, OB and OC are the loading paths of the magnetic field along x_1 -axis, x_2 -axis and x_3 -axis, respectively. Each loading path

can touch only one stable region; therefore, the non-rotating magnetic field cannot solely induce cyclic variant switching.

2.2.3.3. Stress-setting for reversible MFIS (Magnetic-Field-Induced-Strain)

In most of the FSMA actuators, the mechanical stresses are properly designed (fixed) and a changing magnetic field is used to achieve high-frequency control of the deformation. In this subsection, from the general criterion Eq. (43), we derive the criterion of setting the mechanical stresses to allow the reversible strain induced by a strong rotating/non-rotating magnetic field.

Rotating magnetic field

For a strong magnetic field rotating around x_k -axis ($\alpha_k = 90^\circ$ and $H \cdot M / K_u \gg 1$), the range of the values of $(S_i - S_j)$ can be obtained from Eqs. (47a), (38) and (28a) as

$$S_i - S_j = S_{i-mech} - S_{j-mech} + \cos^2 \alpha_i - \cos^2 \alpha_j = \left[\frac{(\sigma_i - \sigma_j)}{K_u / \varepsilon_0} - 1 \right] \sim \left[\frac{(\sigma_i - \sigma_j)}{K_u / \varepsilon_0} + 1 \right] \quad (49)$$

Equation (49) means that $(S_i - S_j)$ cyclically changes between $\left[(\sigma_i - \sigma_j) / (K_u / \varepsilon_0) - 1 \right]$ and $\left[(\sigma_i - \sigma_j) / (K_u / \varepsilon_0) + 1 \right]$ during the field rotation. To satisfy the general criterion (Eq. (43)) to obtain rotating-field-induced reversible strain by variant switching between i and j , the loading path must touch the two stable regions as:

$$\left[\frac{(\sigma_i - \sigma_j)}{K_u / \varepsilon_0} + 1 \right] \geq \frac{\sigma_{twinning}}{K_u / \varepsilon_0} \quad \text{and} \quad \frac{\sigma_i}{K_u / \varepsilon_0} + 1 \geq \frac{\sigma_k}{K_u / \varepsilon} + \frac{\sigma_{twinning}}{K_u / \varepsilon_0} \quad (50a)$$

$$\left[\frac{(\sigma_i - \sigma_j)}{K_u / \varepsilon_0} - 1 \right] \leq -\frac{\sigma_{twinning}}{K_u / \varepsilon_0} \quad \text{and} \quad \frac{\sigma_j}{K_u / \varepsilon_0} + 1 \geq \frac{\sigma_k}{K_u / \varepsilon_0} + \frac{\sigma_{twinning}}{K_u / \varepsilon_0} \quad (50b)$$

That means the mechanical stresses need to satisfy

$$-\left(1 - \frac{\sigma_{\text{twinning}}}{K_u / \varepsilon_0}\right) \leq \frac{(\sigma_i - \sigma_j)}{K_u / \varepsilon_0} \leq 1 - \frac{\sigma_{\text{twinning}}}{K_u / \varepsilon_0} \quad (51\text{a})$$

$$\frac{\sigma_i}{K_u / \varepsilon_0} + 1 \geq \frac{\sigma_k}{K_u / \varepsilon_0} + \frac{\sigma_{\text{twinning}}}{K_u / \varepsilon_0} \quad (51\text{b})$$

$$\frac{\sigma_j}{K_u / \varepsilon_0} + 1 \geq \frac{\sigma_k}{K_u / \varepsilon_0} + \frac{\sigma_{\text{twinning}}}{K_u / \varepsilon_0} \quad (51\text{c})$$

It is seen that, as long as the mechanical stresses satisfy Eq. (51), a strong rotating field (around x_k -axis) can induce reversible strain via the cyclic switching between variants i and j . Particularly, for the cases of two-dimensional compression (i.e., $\sigma_k = 0$, $\sigma_i > 0$ and $\sigma_j > 0$), the requirements of Eqs. (51b) and (51c) are automatically satisfied (note Eq. (48b)) and only Eq. (51a) need to be taken care of. This criterion for 2D compression (Eq. (51a)) was also obtained with simple 2D energy analysis in (He et al., 2011). It is also noted that the trivial case — a pure rotating field without mechanical stress ($\sigma_1 = \sigma_2 = \sigma_3 = 0$) can satisfy Eq. (51); that means a pure rotating field can induce reversible strain as discussed in Fig. 18.

Non-rotating magnetic field

For a non-rotating magnetic field along x_i -axis ($\alpha_i = 0^\circ$, $\alpha_j = 90^\circ$ and $\alpha_k = 90^\circ$), whose amplitude cyclically changes between zero ($H = 0$) and a large value ($H \cdot M / K_u \gg 1$), ($S_i - S_j$) cyclically changes between $\left[(\sigma_i - \sigma_j)/(K_u / \varepsilon_0)\right]$ and $\left[(\sigma_i - \sigma_j)/(K_u / \varepsilon_0) + 1\right]$:

$$S_i - S_j = \left[\frac{(\sigma_i - \sigma_j)}{K_u / \varepsilon_0} \right] \sim \left[\frac{(\sigma_i - \sigma_j)}{K_u / \varepsilon_0} + 1 \right] \quad (52)$$

For obtaining reversible strain, similar to Eq. (50), the loading path should touch the two stable regions as

$$\left[\frac{(\sigma_i - \sigma_j)}{K_u / \epsilon_0} + 1 \right] \geq \frac{\sigma_{twinning}}{K_u / \epsilon_0} \quad \text{and} \quad \frac{\sigma_i}{K_u / \epsilon_0} + 1 \geq \frac{\sigma_k}{K_u / \epsilon_0} + \frac{\sigma_{twinning}}{K_u / \epsilon_0} \quad (53a)$$

$$\frac{(\sigma_i - \sigma_j)}{K_u / \epsilon_0} \leq -\frac{\sigma_{twinning}}{K_u / \epsilon_0} \quad \text{and} \quad \frac{\sigma_j}{K_u / \epsilon_0} \geq \frac{\sigma_k}{K_u / \epsilon_0} + \frac{\sigma_{twinning}}{K_u / \epsilon_0} \quad (53b)$$

Thus, the criteria of setting the mechanical stresses to allow the reversible strain (induced by a non-rotating cyclic magnetic field along x_i -axis) are

$$\frac{\sigma_{twinning}}{K_u / \epsilon_0} \leq \frac{(\sigma_j - \sigma_i)}{K_u / \epsilon_0} \leq 1 - \frac{\sigma_{twinning}}{K_u / \epsilon_0} \quad (54a)$$

$$\frac{\sigma_i}{K_u / \epsilon_0} + 1 \geq \frac{\sigma_k}{K_u / \epsilon_0} + \frac{\sigma_{twinning}}{K_u / \epsilon_0} \quad (54b)$$

$$\frac{\sigma_j}{K_u / \epsilon_0} \geq \frac{\sigma_k}{K_u / \epsilon_0} + \frac{\sigma_{twinning}}{K_u / \epsilon_0} \quad (54c)$$

Particularly, for the cases of two-dimensional compressions (i.e., $\sigma_k = 0$, $\sigma_i > 0$ and $\sigma_j > 0$), Eq. (54b) is automatically satisfied (note Eq. (48b)) and Eq. (54c) is included in Eq. (54a); therefore, only Eq. (54a) needs to be taken care of. This criterion for 2D compressions (Eq. (54a)) was also obtained in (He et al., 2011). The trivial case — a pure non-rotating field without mechanical stress ($\sigma_i = \sigma_j = \sigma_k = 0$) cannot satisfy Eq. (54a) because the twinning stress (frictional force) is always positive (Eq. (48b)). That means pure non-rotating field cannot induce reversible strain as discussed in Fig. 19. In most existing experiments with the non-rotating field, a uniaxial mechanical stress σ_j is applied (perpendicular to the magnetic field along x_i -axis) to obtain the field-induced reversible strain (see the insert of Fig. 20). In the uniaxial-mechanical cases ($\sigma_i = \sigma_k = 0$ and $\sigma_j \neq 0$), the requirements of Eq. (54) are simplified to

$$\frac{\sigma_{twinning}}{K_u / \epsilon_0} \leq \frac{\sigma_j}{K_u / \epsilon_0} \leq 1 - \frac{\sigma_{twinning}}{K_u / \epsilon_0} \quad (55)$$

Figure 20 shows some typical loading paths of the non-rotating magnetic field along x_1 -axis and the uniaxial mechanical stress along x_2 -axis. The paths O_1A_1 , O_2A_2 and O_3A_3 are for

$\bar{\sigma}_2 = \sigma_2 / (K_u / \varepsilon_0) = 1/3, 2/3$ and 1 , respectively; and the twinning stress is assumed to be $\sigma_{\text{twinning}} / (K_u / \varepsilon_0) = 1/3$. It is seen that the first two paths (O_1A_1 and O_2A_2) satisfying Eq. (55) can touch two stable regions leading to cyclic variant switching and reversible strain, while the last path (O_3A_3) cannot. The criterion (Eq. (55)) of setting the uniaxial mechanical stress for allowing non-rotating-field-induced reversible strain has been verified in experiments (Karaca et al., 2006; Heczko, 2005; Heczko et al., 2000, 2006).

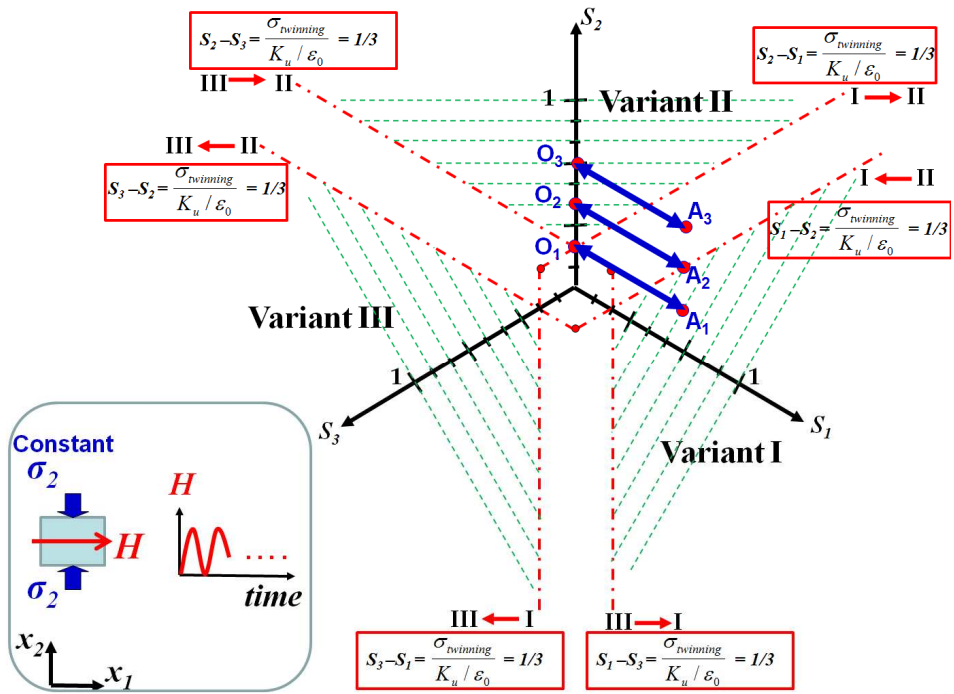


Fig. 20. The loading paths of the non-rotating magnetic fields along x_1 -axis (magnitudes cyclically changing between $H = 0$ and a large value $H \cdot M / K_u \gg 1$) with a constant mechanical stress $\bar{\sigma}_2$ along x_2 -axis: O_1A_1 , O_2A_2 and O_3A_3 are the loading paths of $\bar{\sigma}_2 = \frac{\sigma_2}{K_u / \varepsilon_0} = 1/3, 2/3$ and 1 , respectively.

Paths O_1A_1 and O_2A_2 touching two stable regions can lead to cyclic switching between variants I and II; path O_3A_3 touching only one stable region cannot lead to cyclic variant switching.

2.2.4. Discussions

The deviatoric stresses S_i consisting of the mechanical stresses and the magneto-stresses have the simple superposition form ($S_i = S_{i-mech} + S_{i-mag}$ in Eq. (38)) because the detailed magneto-mechanical couplings (e.g., magnetostriction, elastic energy and magnetic-domain structures) are ignored here. Including these factors in the analysis may enable the model to describe the continuous martensite reorientation (i.e., the martensite reorientation is not abrupt) (Murray et al., 2001; O'Handley et al., 2000). As the aim of this section is to provide a simple global picture of the variant switching under 3D cyclic loadings, the derived formulae of S_i and the associated phase diagrams facilitate the analytical predictions and graphical representations of the magneto-mechanical effects on the variant switching (martensite reorientation).

Although the previous parts discussing the analytical solutions and the associated loading paths in the phase diagrams are only for some typical cases $H = 0$ and $H \cdot M / K_u \gg 1$, it is not difficult to use the same approach to analytically or numerically determine the loading paths for other magneto-mechanical loadings. After the loading paths in the phase diagram are obtained, the switching parameters (switching stress or switching magnetic field or switching rotation angle) triggering the martensite reorientation can be determined (He et al., 2011), from which the time fractions of the variants in a cycle can be controlled by properly setting the mechanical stresses and/or the magnetic field.

The above analysis is focused on the stable regions of the phase diagrams to derive simple criteria for obtaining reversible strain. In fact, the material's behaviour in the meta-stable regions of the phase diagram is more complex. For example, some cyclic-loading paths within the meta-stable regions can still cross the switching lines (e.g., crossing the lines P_1Q_1 and P_2Q_2 in Fig. 16), which might lead to reversible strain if the material's initial state is properly set. In this sense, the criteria derived in this paper are just sufficient conditions for obtaining

reversible strain, rather than necessary conditions. Nevertheless, for reliable designs of FSMA devices (e.g., actuators), the criteria (sufficient conditions) are preferred.

As the martensite variants are tetragonal (Fig. 13), the anisotropy of the magnetization energy should be better described by tetragonal symmetry. Thus, two or more material parameters would be needed to characterize the anisotropic magnetic energy. So, the energy formulation above would be more complex; but the approach is still useful: expressing the loading path in the phase diagram in terms of the deviatoric stresses S_i to study the hysteretic martensite reorientation. Instead of the tetragonal symmetry, the assumption of uniaxial magnetic anisotropy (with one material parameter, K_u , in Eq. (27)) is adopted in the section in order to make the energy formulation simpler and to facilitate the derivation of some analytical solutions and the key physical concepts.

It is also noted in recent publications (Straka et al., 2011b) that different twin microstructures with different values of twinning stress ($\sigma_{twinning}$) can be formed in the material. But, the dependence of the twinning microstructures on the 3D magneto-mechanical loading conditions is still unknown. In our 3D macroscopic model, the twinning stress $\sigma_{twinning}$ is treated as a constant for an FSMA material with a given twin microstructure (i.e., $\sigma_{twinning}$ does not change with the loading conditions).

2.2.5. Conclusions

Phase diagrams in terms of the deviatoric stresses S_i (including mechanical stresses and magneto-stresses) are useful in studying path-dependent (hysteretic) martensite variant reorientation in Ferromagnetic Shape Memory Alloys (FSMA) under complex three-dimensional magneto-mechanical loadings. The superposition form of the deviatoric stresses ($S_i = S_{i-mech} + S_{i-mag}$ in Eq. (38)) facilitates the analytical predictions and graphical

representations of the magneto-mechanical effects on the variant switching (martensite reorientation).

General criteria (Eq. (43)) for obtaining reversible strain under cyclic magneto-mechanical loadings are obtained. As long as the criteria are satisfied, all kinds of mechanical stresses (cyclic tension and/or cyclic compression) and magnetic fields (rotating or non-rotating) can induce a large reversible strain by the stress-induced and/or field-induced cyclic martensite reorientation between two or more variants.

For magnetic-field-driven actuators, the criteria of setting the mechanical stresses to allow the magnetic-field-induced reversible strain are derived (Eq. (51) for rotating fields and Eq. (54) for non-rotating fields), which provide guidelines for designing FSMA actuators in various applications.

2.3. Chapter conclusion

In this chapter, a 2D/3D energy analysis of martensite reorientation between/among two/three tetragonal martensite variants is presented. Based on this analysis, phase diagrams are drawn to graphically study the path-dependent martensite reorientation of FSMA in general multi-axial magneto-mechanical loading conditions. Criteria and the related material requirements for obtaining the reversible strain in cyclic loadings are also derived.

In the 2D/3D energy analysis, we assume that the loading conditions (i.e., uni-/multi-axial loading) have no influence on the twin microstructures of the material so that the twinning stress $\sigma_{twinning}$ is supposed to be constant in all loading conditions. But this assumption needs the experimental support. Moreover, shown by the 2D/3D energy analysis, the most important advantage of using FSMA in multi-axial loadings is that a higher working stress can be obtained (higher than the blocking stress in 1D configuration). And this theoretical prediction

also needs the experimental verifications. Based on these objectives, the following chapter (Chapter 3) is devoted to the experimental study of martensite reorientation in FSMA under multi-axial loading conditions.

Chapter 3

Experimental analysis of martensite

reorientation under multi-axial magneto-mechanical loadings

3.1. Biaxial compression tests	77
3.1.1. Introduction	77
3.1.2. Experiment	77
3.1.3. Results and discussions	80
3.1.4. Conclusions	85
3.2. Biaxial magneto-mechanical tests	86
3.2.1. Material and experimental procedures	86
3.2.2. Preliminary results	87
3.2.3. Structural external friction	88
3.2.4. Summary and prospect	91
3.3. Chapter conclusion	92

Martensite reorientation via twin boundary motion in Ni-Mn-Ga single crystals was experimentally studied under biaxial compressions. The threshold driving force (i.e., twinning stress σ_{twinning} , related to the intrinsic energy dissipation) of the twin boundary motion, and the transformation strain due to martensite reorientation are found to be constant in all tested 2D stress states. These findings imply that the materials can work at high levels of multi-axial stresses while keeping their advantages — low intrinsic dissipation and large reversible strain. Followed by the 2D compression tests, the 2D magneto-mechanical tests (i.e., magnetic field with biaxial compressions) are reported. Preliminary results show that the working stress increases with the auxiliary stress.

3.1. Biaxial compression tests

3.1.1. Introduction

The large strain of Ferromagnetic Shape Memory Alloys (FSMA) is due to the martensite reorientation via twin boundary motion driven by mechanical stresses and/or magnetic fields. In literature, all of the experiments studying the martensite reorientation of FSMA were focused on a simple loading condition: a uniaxial mechanical stress and/or a magnetic field (e.g., Heczko et al., 2000; Karaca et al., 2006; Müllner et al., 2002, 2003, 2004; Murray et al., 2000; Straka and Heczko, 2005). However, the uniaxial stress cannot exceed a critical value (called blocking stress), otherwise the magnetic field cannot induce the martensite reorientation. The small blocking stress (usually smaller than 3 MPa (Heczko et al., 2000; Murray et al., 2000)) leads to the low working stresses of FSMA-based actuators. Recent 2D/3D energy analysis (He et al., 2011, 2012) and constitutive models (Glavatska et al., 2003; Hirsinger and LExcellent, 2003a; Kiefer and Lagoudas, 2009) implied that FSMA can work at high stress levels in 2D/3D configurations (multi-axial stresses with a magnetic field). But, all the existing theories assumed the kinetics of twin boundary motion in 2D/3D configurations based on the existing uniaxial experiments. This section experimentally studies the twin boundary motion in NiMnGa FSMA single crystals under various biaxial-loading conditions, in order to explore the possibility of using FSMA in multi-axial stresses of high levels.

3.1.2. Experiment

3.1.2.1. Material and experimental procedures

Single crystal Ni_{50.0}Mn_{28.5}Ga_{21.5} (at. %) samples of the dimensions 1×2.5×20 mm³ (with faces parallel to the {100} planes of the parent austenite) supplied by Adaptamat Ltd. are used in the quasi-static tests at room temperature, where the material is in the state of tetragonal

five-layered modulated martensite (5M). From the DSC test (Differential Scanning Calorimeter), the temperatures of martensite start (M_s), martensite finish (M_f), austenite start (A_s) and austenite finish (A_f) are respectively 50.5 °C, 48.5 °C, 57 °C, 58.5 °C, and the latent heat of martensitic transformation is 7.7 J/g.

The lab-built experimental setup for symmetric biaxial loadings is shown in Fig. 21(a). Biaxial compressive stresses (σ_{xx} along x -coordinate and σ_{yy} along y -coordinate) are applied by four loading heads and measured by load cells SCAIME K1563 (resolution: ± 0.1 N within ± 100 N). To reduce the friction, the clamps (see Fig. 21(a)) were polished by 5 μm SiC paper and graphite powder was spread on them.

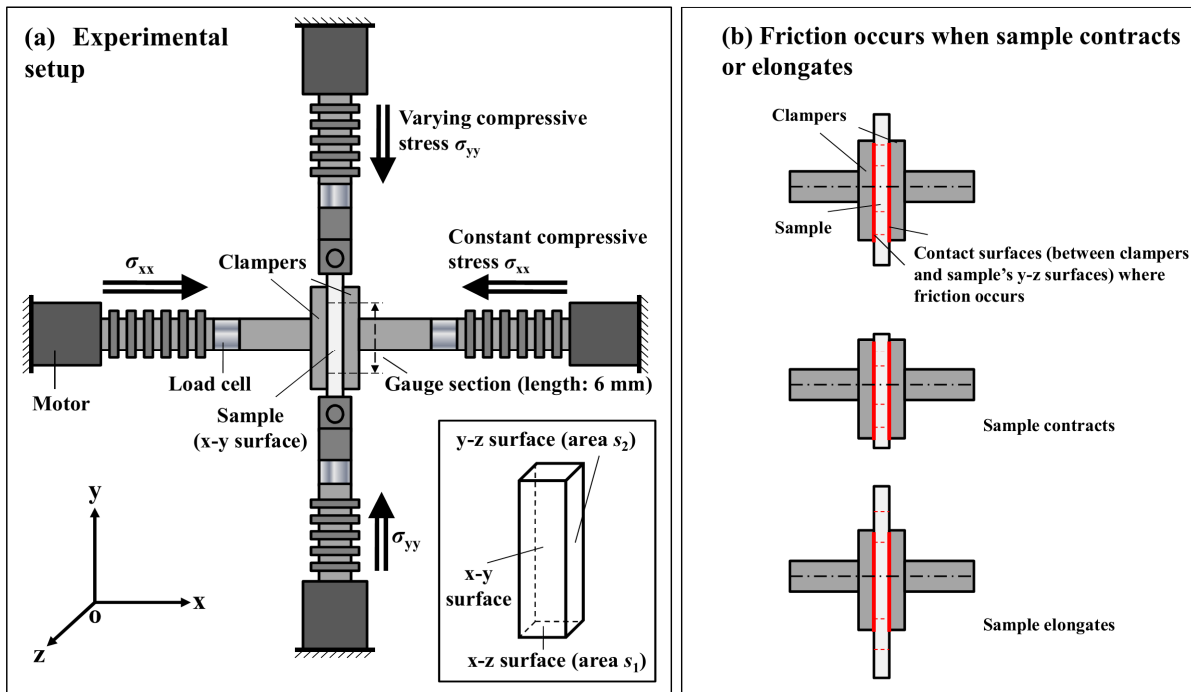


Fig. 21. (a) Schematic diagram of the experimental setup for symmetric biaxial compression tests. (b) Friction occurs on the contact surfaces between the clamps and the sample's $y-z$ surfaces. Dotted lines are marked on the sample for reference showing the relative motion between the sample and the clamps.

To observe the motion of twin boundaries (identified as the boundaries separating low-strain and high-strain regions), the local strain is measured using Digital Image Correlation

(DIC) technique — an *in situ* optical correlation method to measure the displacement of the sample surface (x - y surface in Fig. 21(a)) by a CCD camera (Allied Vision Technologies PIKE F-505: 2452 × 2054 pixels). The nominal strain is calculated as the average strain in the gauge section.

Before each test, uniaxial compressive stress ($\sigma_{xx} = 9$ MPa) is applied on the sample to make it back to the initial state — single martensite variant with its short-axis along x -coordinate (energetically preferred by σ_{xx}), so-called x -variant. During each test, σ_{xx} is fixed at a certain level by a feed-back control system (error < 1%), while the compressive loading and unloading along y -coordinate is displacement-controlled (nominal strain rate: 7.7×10^{-5} /s). Loading stops when σ_{yy} increases to 24 MPa, and then unloading takes place until σ_{yy} returns to zero. The values of stresses and strains are positive for compression here.

3.1.2.2. Characterization of experimental setup

During the experiments, the sample contracts or elongates, leading to the external friction between the clamps and the sample's surfaces (see Fig. 21(b)). To estimate the effects of the external friction, the friction coefficient μ is measured. Fig. 22(a) shows the schematic diagram of the experimental setup for measuring μ . A displacement u_y along y -coordinate is applied by a stepper motor (constant velocity: 1×10^{-6} m/s), while a constant normal force F_x along x -coordinate is applied on the sample's y - z surfaces. The total frictional force ($2f_y$) is measured by a load cell at the end of the sample where u_y is applied (the other end is stress free). It is assumed that the frictional force is uniformly distributed. Then the friction coefficient μ can be calculated as: $\mu = (2f_y) / (2F_x) = f_y / F_x$. Fig. 22(b) shows the frictional force f_y measured at different levels of normal force F_x , where μ is determined to be 0.095.

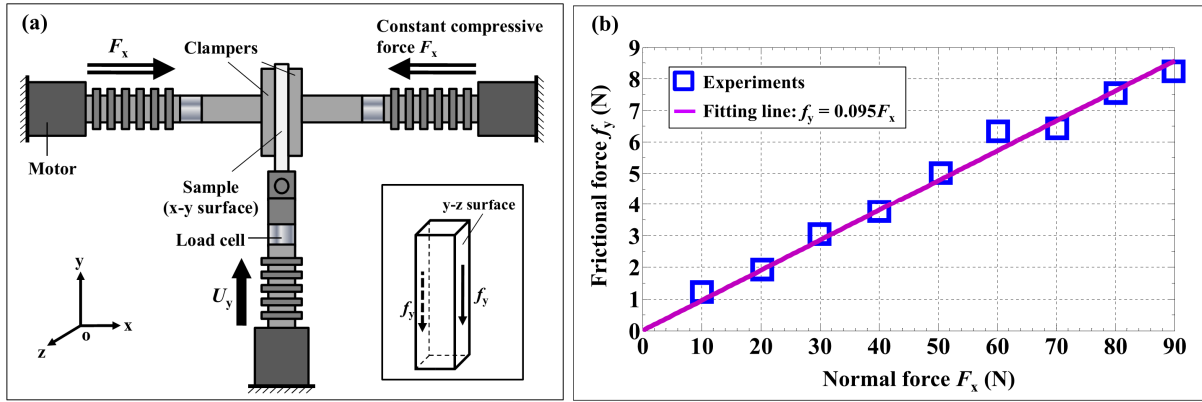


Fig. 22. (a) Schematic diagram of measuring the friction coefficient. (b) Frictional force f_y at different levels of normal force F_x : squares are the experimental results and the solid line is the fitting line: $f_y = 0.095F_x$.

3.1.3. Results and discussions

3.1.3.1. Experimental observations

Fig. 23 shows three typical nominal stress–strain curves (σ_{yy} – ε_{yy}) among our 17 tests at different levels of σ_{xx} (0 ~ 9 MPa). For all of the σ_{yy} – ε_{yy} curves, please refer to Appendix A.1.

Fig. 23(a) is for the martensite reorientation under uniaxial compression σ_{yy} ($\sigma_{xx} = 0$), where the sample's initial state is x -variant. After a very small elastic loading, martensite reorientation from x -variant to y -variant (with short-axis along y -coordinate, energetically preferred by σ_{yy}) starts. During the reorientation, with increasing nominal strain ε_{yy} , the nominal stress σ_{yy} remains nearly constant (stress plateau) while y -variant (with large local strain ε_{yy}) nucleates and grows via the interface (twin boundary) propagation (see the DIC images accompanying the curve). After the reorientation, the elastic deformation of y -variant leads to significant stress increase. Transformation strain ε_{tr} due to martensite reorientation is determined as the strain change between the two elastic loading parts. During unloading, only the small elastic deformation is recovered. Residual strain of 5.7% appears because the

material's state at the end of unloading is y-variant rather than x-variant (initial state). In this uniaxial test, the residual strain represents the transformation strain.

For biaxial compressions ($\sigma_{xx} \neq 0$ in Figs. 23(b) and 23(c)), the transformation strain ε_{tr} changes little ($\varepsilon_{tr} = 5\% \sim 5.7\%$) while the residual strain decreases significantly with increasing σ_{xx} because reverse martensite reorientation from y-variant to x-variant is induced during unloading. At high levels of σ_{xx} (e.g., 9 MPa in Fig. 23(c)), super-elasticity can be obtained (zero residual strain), where the evolutions of the deformation patterns (strain distributions shown by the DIC images) are reversible. Compared with Fig. 23(a), the deformation patterns in Figs. 23(b) and 23(c) are not sharp (x-variant and y-variant are not clearly separated). The reason might be due to the 2D elastic effects of the kink at the twin boundary and 2D geometric compatibility (He and Sun, 2010; Straka et al., 2010).

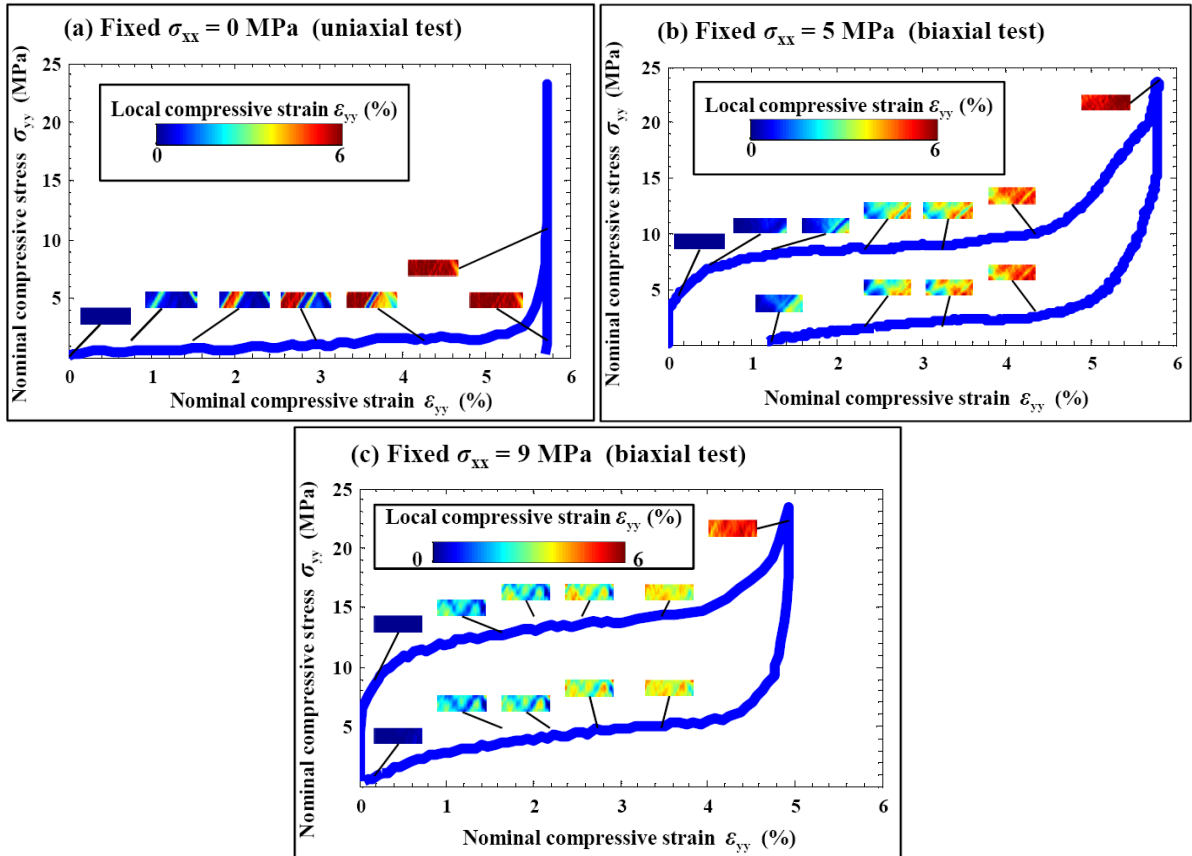


Fig. 23. Nominal stress–strain curves (σ_{yy} – ε_{yy}) at different levels of σ_{xx} : (a) $\sigma_{xx} = 0$ MPa, (b) $\sigma_{xx} = 5$ MPa, (c) $\sigma_{xx} = 9$ MPa. The DIC images show the distributions of local strain ε_{yy} .

It is also seen in Fig. 23 that the upper/lower plateau stress σ_{yy} for forward/reverse martensite reorientation increases with increasing σ_{xx} . The two plateaus (denoted respectively by $\sigma_{\text{upp-plat}}$ and $\sigma_{\text{low-plat}}$) are estimated from the $\sigma_{yy}-\varepsilon_{yy}$ curve (σ_{yy} at $\varepsilon_{yy} = 3\%$). The dependence of $\sigma_{\text{upp-plat}}$ and $\sigma_{\text{low-plat}}$ on σ_{xx} is shown in Fig. 25(a). It is found that the nominal stress-hysteresis (difference between the two nominal plateau stresses ($\sigma_{\text{upp-plat}} - \sigma_{\text{low-plat}}$)) increases with increasing σ_{xx} . In fact, this observed stress-hysteresis consists of two parts (i.e., the material intrinsic hysteresis and the structural external friction), which will be discussed in the following sub-section.

3.1.3.2. Intrinsic plateau stresses (σ_f and σ_r) for forward and reverse martensite reorientations

The compressive stress σ_{yy} is applied by two stepper motors at each end of the sample (see Fig. 21(a)). By symmetry, the center of the sample (point ‘O’ in Fig. 24) can be taken to be fixed, and we only need to consider a half of the sample for the force analysis.

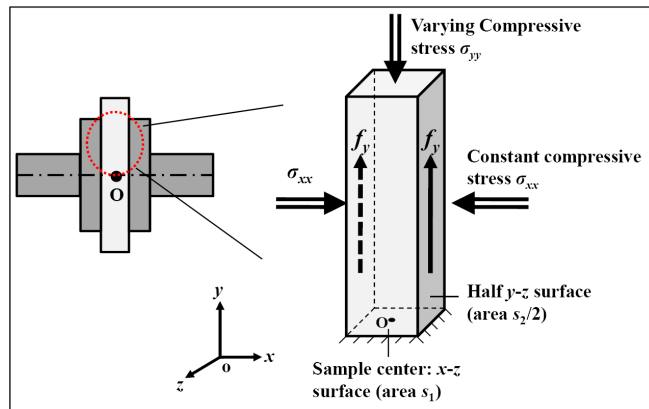


Fig. 24. Force analysis of a half sample during loading. f_y is the frictional force on each contact surface.

When the sample contracts during loading, the total frictional force ($2f_y$) on the contact surfaces is opposite to the applied compressive stress σ_{yy} . Then the compressive stress σ_{yy}^{center} at the sample center is calculated as:

$$\sigma_{yy}^{center} = \sigma_{yy} - \frac{2}{s_1} f_y \quad (56)$$

where s_1 is the cross section area of x - z surface ($1 \times 2.5 \text{ mm}^2$, see Figs. 24 and 21(a)). With the measured friction coefficient μ , the total frictional force is obtained:

$$2f_y = 2\mu(\sigma_{xx} \cdot \frac{s_2}{2}) = \mu\sigma_{xx}s_2 \quad (57)$$

where s_2 is the contact area of y - z surface between the sample and the clamps ($1 \times 10 \text{ mm}^2$ with the clamp length of 10 mm, see Figs. 24 and 21(a)). Substituting Eq. (57) into Eq. (56), we obtain the compressive stress at the sample center (intrinsic stress without external friction):

$$\sigma_{yy}^{center} = \sigma_{yy} - \frac{s_2}{s_1} \mu\sigma_{xx} \quad (58)$$

With Eq. (58), the intrinsic plateau stress for forward martensite reorientation (denoted by σ_f) can be calculated from the nominal plateau stress $\sigma_{upp-plat}$:

$$\sigma_f = \sigma_{upp-plat} - \frac{s_2}{s_1} \mu\sigma_{xx} \quad (59)$$

During unloading, the sample elongates. So the frictional force is in the same direction as the applied stress σ_{yy} . By similar analysis, the intrinsic plateau stress σ_r for reverse martensite reorientation is obtained

$$\sigma_r = \sigma_{low-plat} + \frac{s_2}{s_1} \mu\sigma_{xx} \quad (60)$$

With Eqs. (59) and (60), we can obtain Eq. (61)

$$\sigma_{upp-plat} - \sigma_{low-plat} = 2 \frac{s_2}{s_1} \mu\sigma_{xx} + (\sigma_f - \sigma_r) \quad (61)$$

where the two contributions to the nominal stress-hysteresis ($\sigma_{\text{upp-plat}} - \sigma_{\text{low-plat}}$) can be distinguished: one is related to the energy dissipation of the external friction ($2 \frac{s_2}{s_1} \mu \sigma_{\text{xx}}$) and it is proportional to σ_{xx} ; the other is the material intrinsic stress-hysteresis ($\sigma_f - \sigma_r$), which is related to the intrinsic dissipation of martensite reorientation. Fig. 25(b) shows the σ_{xx} -dependence of σ_f and σ_r . It is seen that the intrinsic stress-hysteresis ($\sigma_f - \sigma_r$) is almost a constant: $2\sigma_{\text{twinning}} = 2.4$ MPa, where the threshold driving force for twin boundary motion σ_{twinning} (so-called twinning stress, related to the intrinsic energy dissipation) can be determined as: $\sigma_{\text{twinning}} = (\sigma_f - \sigma_r)/2 = 1.2$ MPa.

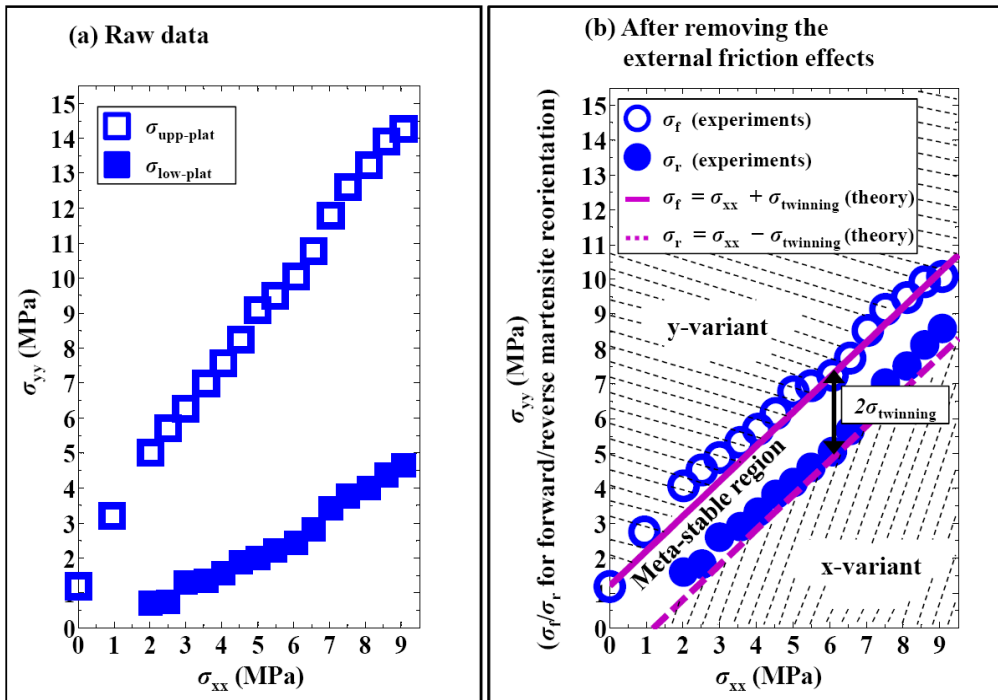


Fig. 25. (a) Nominal plateau stresses ($\sigma_{\text{upp-plat}}, \sigma_{\text{low-plat}}$) of the stress-strain curves ($\sigma_{\text{yy}}-\varepsilon_{\text{yy}}$). (b) Intrinsic plateau stresses (σ_f, σ_r) calculated with Eqs. (59) and (60) to remove the external friction effects. The theoretical predictions for forward and reverse martensite reorientations (two lines) are, respectively, $\sigma_f = \sigma_{\text{xx}} + \sigma_{\text{twinning}}$ and $\sigma_r = \sigma_{\text{xx}} - \sigma_{\text{twinning}}$, where $\sigma_{\text{twinning}} = 1.2$ MPa.

Fig. 25(b) is actually a phase diagram of the martensite reorientation in NiMnGa single crystal under 2D compressive stresses. It is divided into three regions: two stable regions

respectively for x-variant and y-variant, and one meta-stable region where the material's state depends on the loading history.

The effects of the auxiliary compression σ_{xx} on the material's mechanical behavior ($\sigma_{yy}-\varepsilon_{yy}$ curve) are similar to that of a magnetic field H_x along x-coordinate. In the experiments of field-assisted super-elasticity (compression σ_{yy} with a constant magnetic field H_x), the threshold driving force σ_{twinning} (≈ 1.4 MPa) for twin boundary motion and the transformation strain ε_{tr} ($\approx 6\%$) due to martensite reorientation are also found to be constant (Straka and Heczko, 2003a). While the microscopic structures of twin boundaries would have a significant influence on σ_{twinning} (Straka et al., 2011b), the macroscopic twin structures (i.e., the deformation patterns: ‘//’ in Fig. 23(a) and ‘M’ in Fig. 23(c)) have little influence on σ_{twinning} in our biaxial tests. Besides 2D compression, the discussion on 2D tension and general 3D magneto-mechanical loadings can be found in (He et al., 2012).

3.1.4. Conclusions

From the 2D compression tests on single crystal NiMnGa 5M martensite, it is found that the material can work at high stress levels (plateau stress > 12 MPa), which are much larger than the blocking stress (< 3 MPa) in 1D configuration. At high levels of biaxial loadings, super-elasticity was observed. Based on the experiments, a phase diagram of martensite reorientation is obtained, which helps us easily determine the material's state under various 2D stresses. The energy dissipation due to the structural external friction is proportional to the stress levels, while the material intrinsic energy dissipation for twin boundary motion is found to be constant in all tested 2D stress states and the variation of the transformation strain due to martensite reorientation is negligible ($< 15\%$). These findings imply the possibility of using FSMA in multi-axial magneto-mechanical loading conditions.

3.2. Biaxial magneto-mechanical tests

3.2.1. Material and experimental procedures

Recent 2D/3D energy analysis (He et al., 2011, 2012) shows that FSMA in multi-axial loadings can have high levels of working stress (higher than the blocking stress in 1D configuration). To verify this theoretical prediction, the 2D magneto-mechanical tests are reported in this section.

The samples of single crystalline $\text{Ni}_{50.0}\text{Mn}_{28.5}\text{Ga}_{21.5}$ alloy used in the previous 2D compression tests are also used here. Fig. 26 shows the experimental setup of 2D magneto-mechanical tests at room temperature. Two constant compressive stresses (i.e., σ_{yy} along y -coordinate and σ_{xx} along x -coordinate) are applied respectively by a dead load (see Fig. 26(a)) and a lever system (Fig. 26(b)). The strain ε_{yy} along y -coordinate is determined as: $\varepsilon_{yy} = \Delta l/l_0$, where l_0 is the gauge length of the sample, and Δl is the vertical displacement of a plate fixed to the top of the sample (see Fig. 26(a)). Δl is measured by a laser displacement sensor (Keyence LK-G37: $\pm 0.005\text{ }\mu\text{m}$ within $\pm 5\text{ mm}$). All the mechanical loading systems are made up of non-magnetic materials (aluminum or brass). An electromagnet (Varian Associates Model V3400-260) is used to generate a uniform magnetic field H_x along x -coordinate in the volume of $35 \times 35 \times 35\text{ mm}^3$. The applied magnetic field strength is monitored by the electric current passing through the wire of the electromagnet.

Before each test, a dead load of 1 kg (compressive stress of 4 MPa) is applied along y -coordinate in order to guarantee that the sample is in the initial state of σ_{yy} -preferred martensite variant. During the test, σ_{xx} and σ_{yy} are fixed at certain levels, while the magnetic field $\mu_0 H_x$ is cycled between $\pm 0.75\text{ T}$ at a rate of $6 \times 10^{-3}\text{ T/s}$ (i.e., frequency: 0.002 Hz).

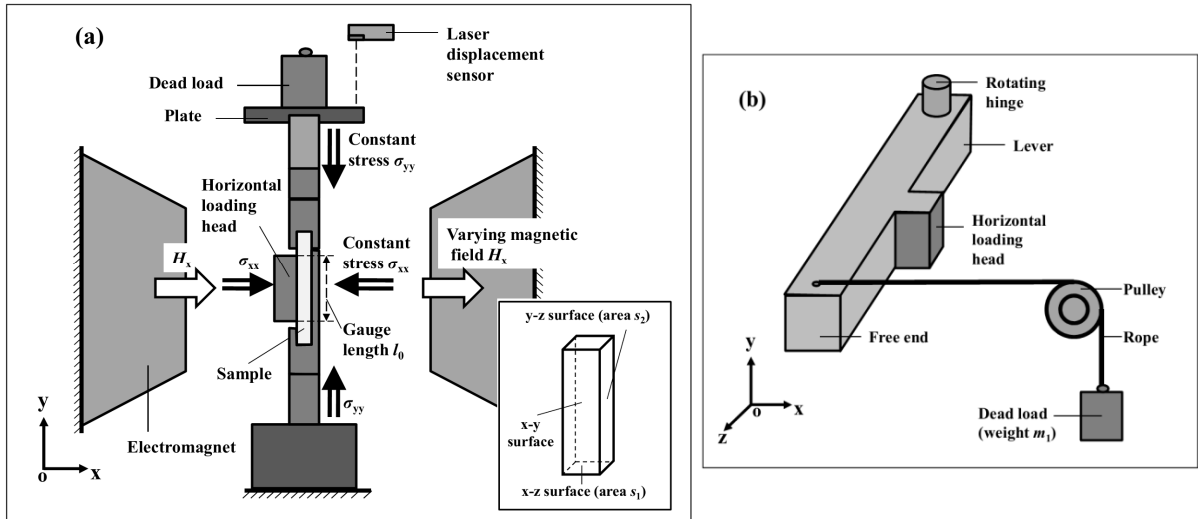


Fig. 26. (a) Schematic diagram of the 2D magneto-mechanical setup. (b) Lever system for applying the compressive stress σ_{xx} .

3.2.2. Preliminary results

Figure 27 shows the magnetic-field-induced strains at different levels of compressive stresses (σ_{xx} and σ_{yy}). It is seen that the maximum working stress σ_{yy}^{\max} (stress over which no strain change is observed) increases with increasing σ_{xx} : $\sigma_{yy}^{\max} = 1.6$ MPa at $\sigma_{xx} = 0$ MPa (Fig. 27(a)), $\sigma_{yy}^{\max} = 4$ MPa at $\sigma_{xx} = 5$ MPa (Fig. 27(b)), $\sigma_{yy}^{\max} = 5.5$ MPa at $\sigma_{xx} = 10$ MPa (Fig. 27(c)). As predicted by the recent 2D/3D energy analysis (He et al., 2011, 2012), the auxiliary stress σ_{xx} helps increase the working stress σ_{yy} .

It is also seen from Fig. 27 that there is little reversible strain in the 2D configurations. The main problem for obtaining reversible martensite reorientation (leading to reversible strain) is the structural external friction, which will be discussed in the next sub-section.

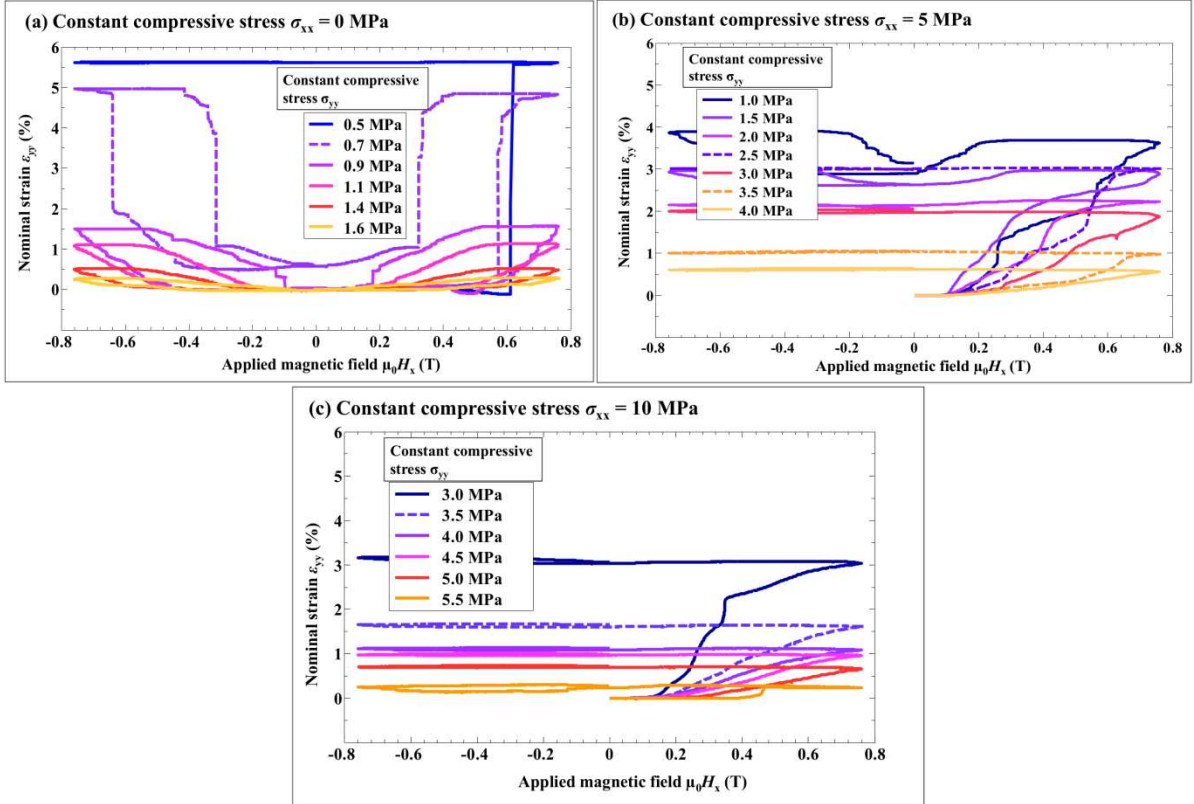


Fig. 27. Magnetic-field-induced strain at different levels of constant compressive stresses (σ_{yy} and σ_{xx}).

3.2.3. Structural external friction

The material requirement for obtaining the non-rotating-field induced reversible martensite reorientation has been derived in Chapter 2 by Eq. (21): $K_u / \varepsilon_0 > 2\sigma_{\text{twinning}}$, which means that the maximum magneto-stress (i.e., ratio of the magnetic anisotropic energy K_u to the strain change ε_0 due to martensite reorientation) must be larger than the material intrinsic hysteresis (i.e., $2\sigma_{\text{twinning}}$ due to martensite reorientation). If the structural external friction in 2D configurations is also considered, the material requirement can be modified as:

$$K_u / \varepsilon_0 > 2\sigma_{\text{twinning}} + \sigma_{\text{hysteresis}}^{\text{external}} \quad (62)$$

The external stress hysteresis $\sigma_{\text{hysteresis}}^{\text{external}}$ has the following two contributions:

(1) $\sigma_{hysteresis,1}^{external}$ due to the friction between the horizontal loading head and the sample's y-z surfaces (see the insert of Fig. 26(a)).

This contribution has already been identified by Eq. (61) in the previous 2D compression tests:

$$\sigma_{hysteresis,1}^{external} = 2 \frac{s_2}{s_1} \mu \sigma_{xx} \quad (63)$$

where μ is the friction coefficient (uniform distribution of the frictional force is assumed), s_1 ($= 1 \times 2.5 \text{ mm}^2$) is the cross section area of x-z surface and s_2 ($= 1 \times 10 \text{ mm}^2$) is the contact area of y-z surface between the sample and the horizontal loading head (with the head length of 10 mm, see Fig. 26(a)).

(2) $\sigma_{hysteresis,2}^{external}$ due to the friction in the lever system (e.g., between the rotating hinge and the lever, the pulley and the rope (see Fig. 26(b)), the lever-supporter and the lever, etc.)

To measure the total frictional moment M_y against the lever motion, additional test is done: in the pure lever system (Fig. 26(b)), dead load m_1 are successively added until a critical weight m_c when the free end of the lever rotates. Fig. 28 shows the results, from which m_c is obtained ($= 156 \text{ g}$) and the frictional moment M_y can be determined as:

$$M_y = m_c \cdot g \cdot L_{lever}, \text{ with } L_{lever} \text{ length of the lever}$$

Then the frictional stress $\sigma_{friction}^{lever-moment}$ applied by the frictional moment M_y on the sample's y-z contact surface (area = s_2 , located in the middle of the lever) is:

$$\sigma_{friction}^{lever-moment} = \frac{1}{s_2} \cdot \frac{M_y}{L_{lever}/2} = 2 \frac{m_c g}{s_2}$$

From which the stress hysteresis (two times the frictional stress) can be obtained:

$$\sigma_{hysteresis,2}^{external} = 4 \frac{m_c g}{s_2} \quad (64)$$

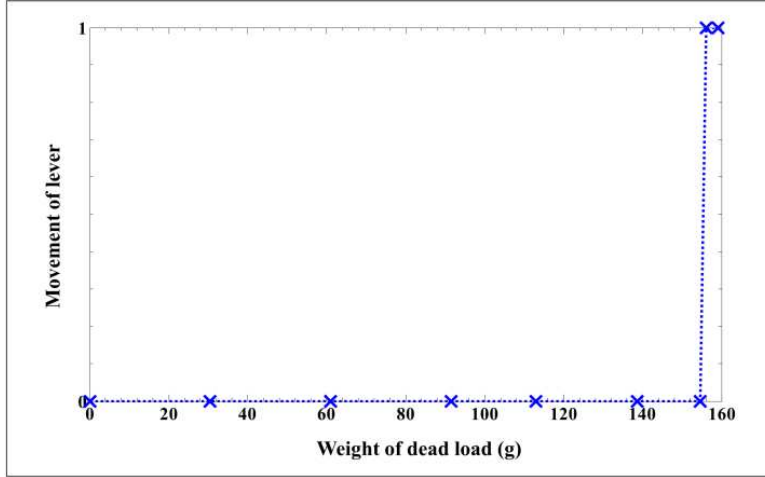


Fig. 28. Lever movement at different weights of dead load. ‘0’ means the lever stays; ‘1’ means it moves.

Based on Eqs. (62), (63) and (64), the material requirement for obtaining magnetic-field-induced reversible martensite reorientation in 2D configurations is:

$$K_u / \varepsilon_0 > 2\sigma_{\text{twinning}} + 2\frac{s_2}{s_1} \mu \sigma_{xx} + 4\frac{m_c g}{s_2} \quad (65)$$

For our 2D magneto-mechanical tests, we calculate each term in Eq. (65) as follows:

- From the material property (Heczko et al., 2000; Murray et al., 2000), $K_u/\varepsilon_0 \approx 3$ MPa.
- From the previous biaxial compression tests, $2\sigma_{\text{twinning}} \approx 2.4$ MPa.
- With the known parameters, $(2\frac{s_2}{s_1} \mu \sigma_{xx} + 4\frac{m_c g}{s_2})$ is calculated at $\sigma_{xx} = 5$ MPa:

$$2\frac{s_2}{s_1} \mu \sigma_{xx} + 4\frac{m_c g}{s_2} = 2 \times \frac{1 \times 10}{1 \times 2.5} \times 0.095 \times 5 + 4 \times \frac{156/1000 \times 9.8}{1 \times 10} = 4.4 \text{ MPa}$$

where μ is assumed to be the same ($= 0.095$) as the friction coefficient measured in the previous 2D compression tests, because the clampers used in the previous tests (see Fig. 21(a)) and the horizontal loading head used in the current tests (see Fig. 26(a)) are made of the same material (brass).

It is seen that Eq. (65) (i.e., $3 > 2.4 + 4.4$) does not stand, so there is no reversible strain in the 2D magneto-mechanical tests. We can try to lower the total external friction by changing the length of the horizontal loading head (so s_2 is changed):

$$\left(2 \frac{s_2}{s_1} \mu \sigma_{xx} + 4 \frac{m_c g}{s_2} \right)_{\min} = 4 \sqrt{2 \frac{\mu m_c g}{s_1} \sigma_{xx}} \quad \text{at} \quad s_2 = \sqrt{2 \frac{m_c g s_1}{\mu \sigma_{xx}}}$$

With $\sigma_{xx} = 5$ MPa, we have: $\left(2 \frac{s_2}{s_1} \mu \sigma_{xx} + 4 \frac{m_c g}{s_2} \right)_{\min} = 3.0$ MPa at $s_2 = 1 \times 4 \text{ mm}^2$ (with length of the horizontal loading head: 4 mm). Still Eq. (65) (i.e., $3 > 2.4 + 3.0$) does not stand.

3.2.4. Summary and prospect

2D magneto-mechanical tests (magnetic field with biaxial compressions) are reported. Preliminary results (Fig. 27) show that the working stress of FSMA increases with increasing the auxiliary stress.

The material requirement (Eq. (65)) for obtaining the reversible magnetic-field-induced strain in the current 2D configurations is derived. It is found that the reversible strain cannot be obtained in the current 2D magneto-mechanical tests. Two possible solutions are proposed:

(1) Change the 2D mechanical loading system to reduce the external friction

The external friction of the current 2D mechanical loading system has been reduced to its minimum by surface polishing, graphite lubricating, Telfon sticking to some contact surfaces, etc. However the external friction is still too large to allow the reversible strain. So it is suggested to change the mechanical loading system with much smaller external friction.

(2) Change the FSMA sample to reduce the intrinsic hysteresis

The samples used in the experiments contain Type I twin with twinning stress σ_{twinning} around 1.2 MPa. Recently, Type II twin with σ_{twinning} around 0.1 MPa was discovered (Sozinov et al., 2011; Straka et al., 2010, 2011b). Samples with Type II twin will have much

smaller intrinsic hysteresis ($2\sigma_{\text{twinning}}$), so at some stress levels they can satisfy the material requirement (Eq. (65)) for reversible strain.

3.3. Chapter conclusion

2D mechanical and magneto-mechanical tests are reported in this chapter. It is found that the twinning stress σ_{twinning} for twin boundary motion and the transformation strain due to martensite reorientation are constant in all tested 2D stress states. Moreover, preliminary results show that the working stress of FSMA can be increased by the increase of the assistant stress. These experimental findings imply the possibility of using FSMA in multi-axial loading conditions. To predict the magneto-mechanical behaviors of FSMA under multi-axial loadings, a 3D constitutive model must be developed, which is the topic of the next chapter (Chapter 4).

Chapter 4

Three-dimensional constitutive model of thermo-magneto-mechanical behaviors of ferromagnetic shape memory alloys

4.1. Introduction	95
4.1.1. Literature review of models	95
4.1.2. Outline of chapter	99
4.2. Magneto-mechanical model of ferromagnetic shape memory alloys	100
4.2.1. Introduction of generalized standard materials with internal constraints	100
4.2.2. State variables and internal constraints	101
4.2.3. Formulation of Gibbs free energy density	102
4.2.4. State equations	107
4.2.5. Evolution laws of internal state variables	110
4.2.6. Identification of model parameters	114
4.3. Numerical simulations and model validations	119
4.3.1. Martensite reorientation induced by a non-rotating magnetic field	121
4.3.2. Martensite reorientation induced by a rotating magnetic field	126
4.3.3. Super-elasticity under biaxial compressions	128
4.3.4. Field-assisted super-elasticity	131
4.3.5. Thermo-magneto-mechanical behaviors of ferromagnetic shape memory alloys	135
4.4. Structural analysis of ferromagnetic shape memory beams	141
4.4.1. Simulation results	144
4.4.2. Specimen-geometry effect on bending deflection	145
4.4.3. Material anisotropic effect on bending deflection	148
4.5. Conclusions	150

The large strain in Ferromagnetic Shape Memory Alloys (FSMA) is due to the martensite reorientation driven by mechanical stresses and/or magnetic fields. Although most experiments studying the martensite reorientation in FSMA are under 1D condition (uniaxial stress plus a perpendicular magnetic field), the energy and experimental analyses of the previous chapters have shown that the

2D/3D configurations can improve the working stress and give much flexibility of the material's applications. To predict the material's behaviors in 3D loading conditions, a constitutive model is developed in this chapter, based on the thermodynamics of irreversible processes with internal variables. All the tetragonal martensite variants are considered in the model and the temperature effect is also taken into account. The model is able to describe all the behaviors of FSMA in the existing experiments: rotating/non-rotating magnetic-field-induced martensite reorientation, magnetic-field-assisted super-elasticity, super-elasticity under biaxial compressions and temperature-dependence of martensite reorientation. The model is further used to study the nonlinear bending behaviors of FSMA beams and provides some basic guidelines for designing the FSMA-based bending actuators.

4.1. Introduction

In literature, most of the experiments studying the martensite reorientation in FSMA were conducted in a simple loading condition: a uniaxial mechanical stress plus a non-rotating magnetic field or a rotating magnetic field (e.g., Karaca et al., 2006; Müllner et al., 2002; Straka and Heczko, 2005). However, the uniaxial stress is limited to a few MPa (Heczko et al., 2000; Murray et al., 2000), which leads to the low stress output of FSMA-based actuators. Recent 2D/3D energy analysis (He et al., 2011, 2012) showed that FSMA can work at high stress levels in 2D/3D configurations (multi-axial stresses with a magnetic field). In the recent experiments of biaxial compressions on FSMA (Chen et al., 2013), it is found that the material intrinsic hysteresis and the strain change due to martensite reorientation are constant under various 2D stresses. These findings imply that FSMA under multi-axial stresses still keeps its advantages — low intrinsic dissipation and large reversible strain. In order to predict the material's behaviors under general multi-axial magneto-mechanical loadings for the practical use (especially in complex structures), 3D constitutive models of FSMA martensite reorientation are demanded.

4.1.1. Literature review of models

A number of constitutive models for FSMA martensite reorientation have been proposed, emphasizing different aspects of the material's behaviors. Micromagnetics models are focused on studying the fundamental mechanism of the material's behaviors in microscopic scale. James and Wuttig (1998) and DeSimone and James (2002) developed a constrained theory of magnetostriction, which can qualitatively predict the magnetic-field-induced strain in FSMA (Tickle et al., 1999). Phase-field models (e.g., Jin, 2009; Li et al., 2008, 2011; Mennerich et al., 2011; Zhang and Chen, 2005) have been developed by choosing different order

parameters, which provide elegant descriptions of the evolutions of magnetic domains and martensite microstructures.

Energy models aim at understanding the origin of martensite reorientation through energy analysis. O'Handley (1998) studied the magnetic-field-induced martensite reorientation between two variants separated by a single twin boundary. The driving force for the twin boundary motion is identified as the magnetic energy difference between the two variants. Later on, Murray et al. (2001) introduced the effect of uniaxial stress by adding a mechanical potential. The two variants abruptly switch to each other when the difference between the variants' energy (mechanical potential and magnetic energy) changes its sign. The model is limited by its assumption that the magnetization vector in each variant is always along the magnetic easy-axis (i.e., no magnetization rotation mechanism). In the model of Müllner et al. (2002), the magnetization vectors are free to rotate. During magnetic field rotation (without mechanical stress), variant switching takes place periodically when the magnetic energy difference between the two variants changes its sign. He et al. (2011, 2012) proposed a more systematic study of variant switching under multi-axial magneto-mechanical loadings, in which the hysteretic effect is also considered. The abrupt variant switching happens when the difference of variants' energy reaches a threshold. The model offers quantitative predictions of the switching field/stress/angle. In the model of Likhachev and Ullakko (2000), a magnetic driving force on twin boundaries is proposed as the ratio between the magnetic anisotropy energy difference of the two variants and the strain change due to the martensite reorientation. The macroscopic strain is assumed to be determined by the driving force (mechanical or magnetic), so the stress-strain curve from the test of compression-driven martensite reorientation can be used to predict the strain due to the martensite reorientation driven by a magnetic field (magnetic driving force). Based on this approach, several models have been

proposed to predict the martensite reorientation between two variants under different loading conditions (e.g., Kiang and Tong, 2005, 2007; Straka and Heczko, 2003a).

Statistical models, describing statistically the volume-fraction evolutions of the martensite variants, can predict macroscopic behaviors of the material. In the model of Glavatska et al. (2003), an effective stress (linear combination of mechanical stresses and magnetic-field-induced stress) is used to represent the magneto-mechanical loadings and the probability of variant switching at an effective stress level is described by a statistical distribution. The model, considering two martensite variants, provides quantitative predictions of the material's strain evolution in a magnetic field and its stress-strain behaviors under constant magnetic fields (Chernenko et al., 2004; Glavatska et al., 2003). Some other models are developed based on the assumption of thermally activated variant switching (Buchelnikov and Bosko, 2003; Krevet et al., 2008; O'Handley et al., 2006), where the rates of variant switchings are related to an energy barrier. By properly setting the model parameters, these models can show quantitative agreement with the experimental observations.

The approach based on thermodynamics of irreversible process is capable of describing the dissipative processes and the loading path effects on the material's behaviors. The so-built thermodynamics models, combining the macro-scale thermodynamics and the micro-scale ingredients by introducing the internal state variables, can give a better quantitative prediction of the material's macroscopic behaviors. Many models of this kind have been proposed for conventional shape memory alloys (e.g., Boyd and Lagoudas, 1996; Lcellent et al., 2000; Moumni et al., 2008; Zaki and Moumni, 2007 among many others). For FSMA, Hirsinger and Lcellent (2003b) first proposed a constitutive model of 1D (uniaxial stress with a perpendicular magnetic field) for martensite reorientation between two variants. In their model, the magnetization vectors of the variants are assumed to be fixed at the magnetic easy-axis. Later on, Creton and Hirsinger (2005) and Gauthier et al. (2007) proposed models where

the magnetization vectors are allowed to rotate. Kiefer and Lagoudas (2005, 2007, 2009) developed a more systematic model for martensite reorientation between two variants. The magnetic domain wall motion and the magnetization rotation mechanisms are considered by the internal state variables. The model is good in relating the macroscopic magneto-mechanical behaviors of the material to its micro-structural evolutions. Auricchio et al. (2011) proposed a 3D model with all the three martensite variants involved. An affine relation between the magnetization vector and the transformation strain tensor due to martensite reorientation is introduced. The model can give a qualitative prediction of the material's behaviors under certain loading conditions. Recently, Wang and Steinmann (2012) proposed a model by variational approach. Their model takes into consideration the geometry effect of the sample and captures most of the characteristic features of the material's behaviors in 1D loading conditions (uniaxial stress with/without a perpendicular magnetic field).

Generally speaking, in literature there is no multi-axial model which is able to predict the material's macroscopic behaviors in all the existing loading conditions and which is ready for use in 3D structural analysis. Most existing models are dealing with two martensite variants and limited to 2D loading conditions, because a mechanical stress or a magnetic field in the third direction will introduce the third martensite variant. There are models dealing with all the three tetragonal variants (e.g., Buchelnikov and Bosko, 2003; Gauthier, 2007; Krevet et al., 2008), but they have been developed in 1D configuration and they are not validated in more complex loading conditions (e.g., rotating magnetic field, biaxial compressions, magnetic field with biaxial stresses). Furthermore, most of the existing models are limited to static loadings. In high frequency magnetic loadings, temperature variation in the FSMA samples can be significant due to the mechanical intrinsic dissipation and the heat from eddy current (Henry, 2002; Lai, 2009). And FSMA martensite reorientation is sensitive to temperature (e.g., Heczko and Straka, 2003; Straka et al., 2006). However, few models in literature consider the

temperature effect on the FSMA martensite reorientation: in Gauthier (2007), two model parameters are expressed as a function of temperature and only qualitative predictions are given.

4.1.2. Outline of chapter

This chapter proposes a thermodynamics model to describe the martensite reorientations among the three (5M) tetragonal variants in Ni-Mn-Ga single crystals in 3D magneto-mechanical loading conditions. The model is built within the framework of generalized standard materials with internal constraints (Halphen and Nguyen, 1974; Moumni, 1995; Moumni et al., 2008). The temperature dependence of martensite reorientation is also taken into account. Containing a few state variables, the model can be easily incorporated into finite element analysis for 3D structural calculations.

The remaining parts of the chapter are organized as follows: Section 4.2 is devoted to a short introduction of the theoretical framework and the detailed development of the model. In Section 4.3, the material's behaviors under various loading conditions are simulated and compared with the experiments in literature. The temperature dependence of martensite reorientation is considered and simulated at the end of this section. In Section 4.4, the 3D constitutive model is incorporated into finite element analysis to predict the nonlinear bending behaviors of FSMA beams. The specimen-geometry effects and the material anisotropic effects are systematically studied. Finally, a general conclusion is given in Section 4.5.

Remark for the representation of the parameters: scalar parameter x ; vector parameter \underline{x} ; tensor parameter of order 2 $\underline{\underline{x}}$; tensor parameter of order 4 $\underline{\underline{\underline{\underline{x}}}}$.

4.2. Magneto-mechanical model of ferromagnetic shape memory alloys

4.2.1. Introduction of generalized standard materials with internal constraints

(Halphen and Nguyen, 1974; Moumni, 1995; Moumni et al., 2008)

The thermodynamic state of a material can be defined by a set of state variables: stress $\underline{\underline{\sigma}}$ (or strain $\underline{\underline{\varepsilon}}$), absolute temperature T , irreversible internal variables $\underline{\alpha}$ which are related to the dissipative mechanisms, and reversible internal variables $\underline{\beta}$ related to non-dissipative mechanisms. The material's Gibbs free energy density g is given by: $g = g(\underline{\underline{\sigma}}, T, \underline{\alpha}, \underline{\beta})$. The state variables are assumed to be subjected to the following internal constraints:

$$k_m(\underline{\underline{\sigma}}, \underline{\alpha}, \underline{\beta}) = 0 \quad \text{where } m = 1, 2, \dots, M \quad (66a)$$

$$h_n(\underline{\underline{\sigma}}, \underline{\alpha}, \underline{\beta}) \geq 0 \quad \text{where } n = 1, 2, \dots, N \quad (66b)$$

The perfect internal constraints (Eq. (66)) can be derived from a potential W_l :

$$W_l = -\sum_{m=1}^M \lambda_m k_m - \sum_{n=1}^N \mu_n h_n \quad (67)$$

where λ_m ($m = 1, 2, \dots, M$) and μ_n ($n = 1, 2, \dots, N$) are the Lagrange multipliers. μ_n , associated with the unilateral constraints (Eq. (66b)), must satisfy the following requirements:

$$\mu_n \geq 0, \quad \mu_n h_n = 0 \quad \text{where } n = 1, 2, \dots, N \quad (68)$$

Let the Lagrangian \mathcal{L} be: $\mathcal{L} = g + W_l$. Then the generalized forces associated with the state variables can be derived as:

$$\underline{\underline{\varepsilon}} = -\frac{\partial \mathcal{L}}{\partial \underline{\underline{\sigma}}} = -\frac{\partial g}{\partial \underline{\underline{\sigma}}} + \sum_{m=1}^M \lambda_m \frac{\partial k_m}{\partial \underline{\underline{\sigma}}} + \sum_{n=1}^N \mu_n \frac{\partial h_n}{\partial \underline{\underline{\sigma}}} \quad (69a)$$

$$\underline{\alpha} = -\frac{\partial \mathcal{L}}{\partial \underline{\alpha}} = -\frac{\partial g}{\partial \underline{\alpha}} + \sum_{m=1}^M \lambda_m \frac{\partial k_m}{\partial \underline{\alpha}} + \sum_{n=1}^N \mu_n \frac{\partial h_n}{\partial \underline{\alpha}} \quad (69b)$$

$$\underline{\beta} = -\frac{\partial \mathcal{L}}{\partial \underline{\beta}} = -\frac{\partial g}{\partial \underline{\beta}} + \sum_{m=1}^M \lambda_m \frac{\partial k_m}{\partial \underline{\beta}} + \sum_{n=1}^N \mu_n \frac{\partial h_n}{\partial \underline{\beta}} \quad (69c)$$

Then the intrinsic dissipation can be expressed as:

$$D = \underline{A} \cdot \dot{\underline{\alpha}} + \underline{B} \cdot \dot{\underline{\beta}} \quad (70)$$

where \underline{A} and \underline{B} are the thermodynamic forces associated with the internal state variables $\underline{\alpha}$ and $\underline{\beta}$, respectively. \underline{B} must be null because $\underline{\beta}$ is related to non-dissipative mechanisms. Therefore, the intrinsic dissipation (Eq. (70)) can be reduced to:

$$D = \underline{A} \cdot \dot{\underline{\alpha}} \quad (71)$$

For standard generalized materials (Halphen and Nguyen, 1974), there exists a convex non-negative function $\mathcal{D}(\underline{\alpha}, \dot{\underline{\alpha}})$, so-called pseudo-dissipation potential. The thermodynamic forces \underline{A} belongs to the sub-gradient of \mathcal{D} with respect to $\dot{\underline{\alpha}}$:

$$\underline{A} \in \partial_{\dot{\underline{\alpha}}} \mathcal{D} \quad (72)$$

For a pseudo-dissipation potential \mathcal{D} whose minimum ($\mathcal{D}_{min} = 0$) is at $\dot{\underline{\alpha}} = 0$, the requirement of non-negative intrinsic dissipation (Eq. (71)) is automatically satisfied. The directional derivatives of \mathcal{D} (Eq. (72)) define a yield surface limiting a convex domain of admissible forces. If \underline{A} is inside the domain, $\dot{\underline{\alpha}}$ is null; if \underline{A} is on the yield surface, the normality rule holds: $\dot{\underline{\alpha}}$ is proportional to the external normal of the domain.

4.2.2. State variables and internal constraints

The absolute temperature T , the Cauchy stress tensor $\underline{\sigma}$ and the internal magnetic field strength vector \underline{H} are the state variables. There are three martensite variants in 5M Ni-Mn-Ga single crystals (see Fig. 1 in Chapter 1), and their volume fractions are respectively denoted by z_1 , z_2 , z_3 , which are chosen as the internal state variables. The internal variables must satisfy the following physical constraints:

- The material is in the martensitic phase. So the sum of the volume fractions of all the martensite variants must be equal to 1 (100%).

$$z_1 + z_2 + z_3 - 1 = 0 \quad (73)$$

- Martensite variant volume fractions (z_1, z_2, z_3) cannot be negative:

$$z_i \geq 0 \quad \text{where } i = 1, 2, 3 \quad (74)$$

The constraints are assumed to be perfect. Therefore, they can be derived from a potential W_l defined as:

$$W_l = -\lambda(z_1 + z_2 + z_3 - 1) - \mu_1 z_1 - \mu_2 z_2 - \mu_3 z_3 \quad (75)$$

where λ, μ_1, μ_2 and μ_3 are Lagrange multipliers. By Eq. (68), μ_1, μ_2 and μ_3 must obey:

$$\mu_i \geq 0, \quad \mu_i z_i = 0 \quad \text{where } i = 1, 2, 3 \quad (76)$$

4.2.3. Formulation of Gibbs free energy density

The Gibbs free energy g has four contributions: thermal energy g_{the} , mechanical energy g_{mec} , magnetic energy g_{mag} and interaction energy g_{int} due to the incompatibility among the martensite variants.

$$g = g_{the} + g_{mec} + g_{mag} + g_{int} \quad (77)$$

4.2.3.1. Thermal energy

The thermal energy g_{the} is expressed as:

$$g_{the}(T) = \rho C_p \left(T - T_0 - T \ln\left(\frac{T}{T_0}\right) \right) \quad (78)$$

where ρ is the mass density; C_p is the specific heat capacity, which is assumed to be the same for all martensite variants; T_0 is a reference temperature, e.g., it can be the lowest temperature

where the magnetic-field-induced strain can be observed. The choice of T_0 has no influence on the constitutive equations.

4.2.3.2. Mechanical energy

The mechanical energy g_{mec} is composed of the elastic energy g_{elas} and the combination of the mechanical potentials g_{me-po}^{v1} , g_{me-po}^{v2} and g_{me-po}^{v3} of the variants (He et al., 2011, 2012):

$$g_{mec}(\underline{\underline{\sigma}}, z_1, z_2, z_3) = g_{elas}(\underline{\underline{\sigma}}) + z_1 g_{me-po}^{v1}(\underline{\underline{\sigma}}) + z_2 g_{me-po}^{v2}(\underline{\underline{\sigma}}) + z_3 g_{me-po}^{v3}(\underline{\underline{\sigma}}) \quad (79)$$

■ Elastic energy

The Gibbs free energy related to the elastic energy is:

$$g_{elas}(\underline{\underline{\sigma}}) = -\frac{1}{2} \underline{\underline{\sigma}} : \underline{\underline{S}} : \underline{\underline{\sigma}} \quad (80)$$

where $\underline{\underline{S}}$ is the elastic compliance tensor of the martensite.

■ Mechanical potentials

Based on the martensitic transformation from the cubic austenitic phase to the tetragonal martensitic phase, the transformation strain tensors $\underline{\underline{U}}_1$, $\underline{\underline{U}}_2$ and $\underline{\underline{U}}_3$ of the variants can be obtained as:

$$\underline{\underline{U}}_1 = -\varepsilon_c \underline{e}_x \otimes \underline{e}_x + \varepsilon_a \underline{e}_y \otimes \underline{e}_y + \varepsilon_a \underline{e}_z \otimes \underline{e}_z \quad \text{for variant 1} \quad (81a)$$

$$\underline{\underline{U}}_2 = \varepsilon_a \underline{e}_x \otimes \underline{e}_x - \varepsilon_c \underline{e}_y \otimes \underline{e}_y + \varepsilon_a \underline{e}_z \otimes \underline{e}_z \quad \text{for variant 2} \quad (81b)$$

$$\underline{\underline{U}}_3 = \varepsilon_a \underline{e}_x \otimes \underline{e}_x + \varepsilon_a \underline{e}_y \otimes \underline{e}_y - \varepsilon_c \underline{e}_z \otimes \underline{e}_z \quad \text{for variant 3} \quad (81c)$$

where \underline{e}_x , \underline{e}_y and \underline{e}_z are the unit vectors respectively along x -, y - and z -coordinate of the parent austenite lattice; ε_a and ε_c are expressed as:

$$\varepsilon_a = (a - a_0) / a_0 \quad (82a)$$

$$\varepsilon_c = (a_0 - c) / a_0 \quad (82b)$$

a_0 is the length of the cubic austenite unit cell; a and c are respectively the lengths of the long and short axes of the tetragonal martensite unit cell (see Fig. 1 in Chapter 1). The mechanical potentials g_{me-po}^{v1} , g_{me-po}^{v2} and g_{me-po}^{v3} of the variants are:

$$g_{me-po}^{v1}(\underline{\underline{\sigma}}) = -\underline{\underline{\sigma}} : \underline{\underline{U}}_1 = \sigma_{xx}\epsilon_c - \epsilon_a(\sigma_{yy} + \sigma_{zz}) \quad \text{for variant 1} \quad (83a)$$

$$g_{me-po}^{v2}(\underline{\underline{\sigma}}) = -\underline{\underline{\sigma}} : \underline{\underline{U}}_2 = \sigma_{yy}\epsilon_c - \epsilon_a(\sigma_{zz} + \sigma_{xx}) \quad \text{for variant 2} \quad (83b)$$

$$g_{me-po}^{v3}(\underline{\underline{\sigma}}) = -\underline{\underline{\sigma}} : \underline{\underline{U}}_3 = \sigma_{zz}\epsilon_c - \epsilon_a(\sigma_{xx} + \sigma_{yy}) \quad \text{for variant 3} \quad (83c)$$

From Eqs. (79), (80) and (83), the Gibbs free energy density of the mechanical part is:

$$\begin{aligned} g_{mec}(\underline{\underline{\sigma}}, z_1, z_2, z_3) = & -\frac{1}{2} \underline{\underline{\sigma}} : \underline{\underline{S}} : \underline{\underline{\sigma}} + z_1 (\sigma_{xx}\epsilon_c - \epsilon_a(\sigma_{yy} + \sigma_{zz})) + z_2 (\sigma_{yy}\epsilon_c - \epsilon_a(\sigma_{zz} + \sigma_{xx})) \\ & + z_3 (\sigma_{zz}\epsilon_c - \epsilon_a(\sigma_{xx} + \sigma_{yy})) \end{aligned} \quad (84)$$

4.2.3.3. Magnetic energy

The magnetic energy density E_{mag} stored in the material is (O'Handley, 2000):

$$E_{mag}(\underline{\mathcal{M}}) = \int_0^{\underline{\mathcal{M}}} \mu_0 \underline{H} \cdot d\underline{m} \quad (85)$$

where μ_0 is the vacuum permeability; $\underline{\mathcal{M}}$ is the magnetization vector. The dual-energy (Gibbs free energy part g_{mag} related to the magnetic energy) is obtained by the Legendre transformation:

$$g_{mag}(\underline{H}) = - \int_0^{\underline{H}} \mu_0 \underline{\mathcal{M}} \cdot d\underline{h} \quad (86)$$

The magnetization vector $\underline{\mathcal{M}}$ is an extensive variable (Maugin, 1999). At a generic material point, $\underline{\mathcal{M}}$ is the linear combination of the magnetizations $\underline{\mathcal{M}}_1$, $\underline{\mathcal{M}}_2$ and $\underline{\mathcal{M}}_3$ of the variants:

$$\underline{\mathcal{M}} = z_1 \underline{\mathcal{M}}_1 + z_2 \underline{\mathcal{M}}_2 + z_3 \underline{\mathcal{M}}_3 \quad (87)$$

With Eq. (87), Eq. (86) can be rewritten as:

$$g_{mag}(\underline{H}, z_1, z_2, z_3) = - \left(z_1 \int_0^{\underline{H}} \mu_0 \underline{\mathcal{M}}_1 \cdot d\underline{h} + z_2 \int_0^{\underline{H}} \mu_0 \underline{\mathcal{M}}_2 \cdot d\underline{h} + z_3 \int_0^{\underline{H}} \mu_0 \underline{\mathcal{M}}_3 \cdot d\underline{h} \right) \quad (88)$$

Let H be the magnitude of the magnetic field strength, M_1 , M_2 and M_3 be the magnetization components along the field for variant 1, 2 and 3, respectively. For the magnetization process (i.e., magnetize the material by the increase of the magnitude of a magnetic field in a fixed direction) of each variant i ($i = 1, 2, 3$), we have:

$$\int_0^H \mu_0 \mathcal{M}_i \cdot d\mathbf{h} = \int_0^H \mu_0 M_i dh \quad \text{where } i = 1, 2, 3 \quad (89)$$

The magnetization curve of each variant can be linearized as shown in Fig. 29, where the slope a_i ($i = 1, 2, 3$) of the approximated line is the magnetic susceptibility of variant i . Then the magnetization M_1 , M_2 and M_3 of the variants can be expressed as:

$$M_1(H) = \begin{cases} a_1 H & (0 \leq H < \frac{M_s}{a_1}) \\ M_s & (H \geq \frac{M_s}{a_1}) \end{cases} \quad \text{for variant 1} \quad (90a)$$

$$M_2(H) = \begin{cases} a_2 H & (0 \leq H < \frac{M_s}{a_2}) \\ M_s & (H \geq \frac{M_s}{a_2}) \end{cases} \quad \text{for variant 2} \quad (90b)$$

$$M_3(H) = \begin{cases} a_3 H & (0 \leq H < \frac{M_s}{a_3}) \\ M_s & (H \geq \frac{M_s}{a_3}) \end{cases} \quad \text{for variant 3} \quad (90c)$$

where M_s is the saturation magnetization. The magnetic susceptibility a_i ($i = 1, 2, 3$) reflects the overall effects of the magnetic-domain-wall motions and local magnetization rotations on the global magnetization process (Likhachev and Ullakko, 2000). The piecewise Eq. (90) can be rewritten as:

$$M_1(H) = a_1 H + \left\langle H - \frac{M_s}{a_1} \right\rangle (M_s - a_1 H) \quad \text{for variant 1} \quad (91a)$$

$$M_2(H) = a_2 H + \left\langle H - \frac{M_s}{a_2} \right\rangle (M_s - a_2 H) \quad \text{for variant 2} \quad (91b)$$

$$M_3(H) = a_3 H + \left\langle H - \frac{M_s}{a_3} \right\rangle (M_s - a_3 H) \quad \text{for variant 3} \quad (91c)$$

where $\langle x \rangle = \{0, \text{if } x < 0 ; 1, \text{if } x \geq 0\}$.

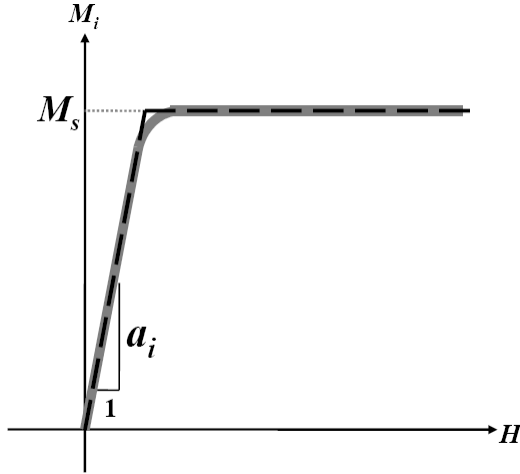


Fig. 29. Linear approximation (dashed line) of the magnetization curve (solid line) for martensite variant i ($i = 1, 2, 3$). The slope a_i of the approximated line is the magnetic susceptibility of variant i ; M_s is the saturation magnetization.

With Eqs. (89) and (91), the magnetic energy (Eq. (88)) can be calculated as:

$$g_{mag}(H, z_1, z_2, z_3) = - \left(\sum_{i=1}^3 z_i \left[\frac{\mu_0 a_i}{2} H^2 + \left\langle H - \frac{M_s}{a_i} \right\rangle \left(\mu_0 H M_s - \frac{\mu_0 a_i}{2} H^2 - \frac{\mu_0 M_s^2}{2 a_i} \right) \right] \right) \quad (92)$$

4.2.3.4. Interaction energy

The proposed expression of the interaction energy g_{int} is similar to the energy contribution due to the linear kinematic hardening of an elasto-plastic material:

$$g_{int}(z_1, z_2, z_3) = \frac{1}{2} k (z_1^2 + z_2^2 + z_3^2) \quad (93)$$

where k is the interaction parameter, whose detailed physical interpretation will be given in sub-section 4.2.6.

4.2.3.5. Expression of Gibbs free energy

With Eqs. (78), (84), (92) and (93), the final expression of the Gibbs free energy (Eq. (77)) is:

$$\begin{aligned}
g(T, \underline{\underline{\sigma}}, \underline{\underline{H}}, z_1, z_2, z_3) = & -\frac{1}{2} \underline{\underline{\sigma}} : \underline{\underline{S}} : \underline{\underline{\sigma}} \\
& - z_1 \left(-\sigma_{xx} \varepsilon_c + \varepsilon_a (\sigma_{yy} + \sigma_{zz}) + \left(\frac{\mu_0 a_1}{2} H^2 + \left\langle H - \frac{M_s}{a_1} \right\rangle \left(\mu_0 M_s H - \frac{\mu_0 a_1}{2} H^2 - \frac{\mu_0 M_s^2}{2 a_1} \right) \right) \right) \\
& - z_2 \left(-\sigma_{yy} \varepsilon_c + \varepsilon_a (\sigma_{zz} + \sigma_{xx}) + \left(\frac{\mu_0 a_2}{2} H^2 + \left\langle H - \frac{M_s}{a_2} \right\rangle \left(\mu_0 M_s H - \frac{\mu_0 a_2}{2} H^2 - \frac{\mu_0 M_s^2}{2 a_2} \right) \right) \right) \quad (94) \\
& - z_3 \left(-\sigma_{zz} \varepsilon_c + \varepsilon_a (\sigma_{xx} + \sigma_{yy}) + \left(\frac{\mu_0 a_3}{2} H^2 + \left\langle H - \frac{M_s}{a_3} \right\rangle \left(\mu_0 M_s H - \frac{\mu_0 a_3}{2} H^2 - \frac{\mu_0 M_s^2}{2 a_3} \right) \right) \right) \\
& + \frac{1}{2} k(z_1^2 + z_2^2 + z_3^2) + \rho C_p \left(T - T_0 - T \ln \left(\frac{T}{T_0} \right) \right)
\end{aligned}$$

4.2.3.6. Expression of Lagrangian

The Lagrangian \mathcal{L} of the material is composed of the Gibbs free energy density (Eq. (94)) and the potential related to the internal constraints (Eq. (75)):

$$\begin{aligned}
L(T, \underline{\underline{\sigma}}, \underline{\underline{H}}, z_1, z_2, z_3) = & -\frac{1}{2} \underline{\underline{\sigma}} : \underline{\underline{S}} : \underline{\underline{\sigma}} \\
& - z_1 \left(-\sigma_{xx} \varepsilon_c + \varepsilon_a (\sigma_{yy} + \sigma_{zz}) + \left(\frac{\mu_0 a_1}{2} H^2 + \left\langle H - \frac{M_s}{a_1} \right\rangle \left(\mu_0 M_s H - \frac{\mu_0 a_1}{2} H^2 - \frac{\mu_0 M_s^2}{2 a_1} \right) \right) \right) \\
& - z_2 \left(-\sigma_{yy} \varepsilon_c + \varepsilon_a (\sigma_{zz} + \sigma_{xx}) + \left(\frac{\mu_0 a_2}{2} H^2 + \left\langle H - \frac{M_s}{a_2} \right\rangle \left(\mu_0 M_s H - \frac{\mu_0 a_2}{2} H^2 - \frac{\mu_0 M_s^2}{2 a_2} \right) \right) \right) \quad (95) \\
& - z_3 \left(-\sigma_{zz} \varepsilon_c + \varepsilon_a (\sigma_{xx} + \sigma_{yy}) + \left(\frac{\mu_0 a_3}{2} H^2 + \left\langle H - \frac{M_s}{a_3} \right\rangle \left(\mu_0 M_s H - \frac{\mu_0 a_3}{2} H^2 - \frac{\mu_0 M_s^2}{2 a_3} \right) \right) \right) \\
& + \frac{1}{2} k(z_1^2 + z_2^2 + z_3^2) + \rho C_p \left(T - T_0 - T \ln \left(\frac{T}{T_0} \right) \right) - \lambda(z_1 + z_2 + z_3 - 1) - \mu_1 z_1 - \mu_2 z_2 - \mu_3 z_3
\end{aligned}$$

4.2.4. State equations

From the Lagrangian (Eq. (95)), we obtain the following state equations:

- Stress-strain relation

$$\begin{aligned}\underline{\underline{\varepsilon}}^*(\underline{\underline{\sigma}}, z_1, z_2, z_3) = & -\frac{\partial L}{\partial \underline{\underline{\sigma}}} = S : \underline{\underline{\sigma}} + z_1 (-\varepsilon_c \underline{e}_x \otimes \underline{e}_x + \varepsilon_a \underline{e}_y \otimes \underline{e}_y + \varepsilon_a \underline{e}_z \otimes \underline{e}_z) \\ & + z_2 (\varepsilon_a \underline{e}_x \otimes \underline{e}_x - \varepsilon_c \underline{e}_y \otimes \underline{e}_y + \varepsilon_a \underline{e}_z \otimes \underline{e}_z) \\ & + z_3 (\varepsilon_a \underline{e}_x \otimes \underline{e}_x + \varepsilon_a \underline{e}_y \otimes \underline{e}_y - \varepsilon_c \underline{e}_z \otimes \underline{e}_z)\end{aligned}\quad (96)$$

The martensitic phase is assumed to be elastically isotropic with Young's modulus E and Poisson's ratio ν . Then Eq. (96) can be rewritten as:

$$\begin{aligned}\underline{\underline{\varepsilon}}^*(\underline{\underline{\sigma}}, z_1, z_2, z_3) = & \frac{1+\nu}{E} \underline{\underline{\sigma}} - \frac{\nu}{E} (\text{tr} \underline{\underline{\sigma}}) \underline{\underline{I}} \\ & + z_1 (-\varepsilon_c \underline{e}_x \otimes \underline{e}_x + \varepsilon_a \underline{e}_y \otimes \underline{e}_y + \varepsilon_a \underline{e}_z \otimes \underline{e}_z) \\ & + z_2 (\varepsilon_a \underline{e}_x \otimes \underline{e}_x - \varepsilon_c \underline{e}_y \otimes \underline{e}_y + \varepsilon_a \underline{e}_z \otimes \underline{e}_z) \\ & + z_3 (\varepsilon_a \underline{e}_x \otimes \underline{e}_x + \varepsilon_a \underline{e}_y \otimes \underline{e}_y - \varepsilon_c \underline{e}_z \otimes \underline{e}_z)\end{aligned}\quad (97)$$

where $(\text{tr} \underline{\underline{\sigma}})$ is the trace of the stress tensor $\underline{\underline{\sigma}}$; $\underline{\underline{I}}$ is the identity tensor. Let $z_1^{(0)}$, $z_2^{(0)}$ and $z_3^{(0)}$ denote the initial volume fractions of the martensite variants. Then the initial strain $\underline{\underline{\varepsilon}}^{*(0)}$ is:

$$\begin{aligned}\underline{\underline{\varepsilon}}^{*(0)} (\underline{\underline{\sigma}}^{(0)} = \underline{\underline{0}}, z_1^{(0)}, z_2^{(0)}, z_3^{(0)}) = & z_1^{(0)} (-\varepsilon_c \underline{e}_x \otimes \underline{e}_x + \varepsilon_a \underline{e}_y \otimes \underline{e}_y + \varepsilon_a \underline{e}_z \otimes \underline{e}_z) \\ & + z_2^{(0)} (\varepsilon_a \underline{e}_x \otimes \underline{e}_x - \varepsilon_c \underline{e}_y \otimes \underline{e}_y + \varepsilon_a \underline{e}_z \otimes \underline{e}_z) \\ & + z_3^{(0)} (\varepsilon_a \underline{e}_x \otimes \underline{e}_x + \varepsilon_a \underline{e}_y \otimes \underline{e}_y - \varepsilon_c \underline{e}_z \otimes \underline{e}_z)\end{aligned}\quad (98)$$

In the small strain approximation, the strain change $\underline{\underline{\varepsilon}}$ during magneto-mechanical loadings can be calculated from Eqs. (97) and (98) as:

$$\begin{aligned}\underline{\underline{\varepsilon}}(\underline{\underline{\sigma}}, z_1, z_2, z_3) = \underline{\underline{\varepsilon}}^* - \underline{\underline{\varepsilon}}^{*(0)} = & \frac{1+\nu}{E} \underline{\underline{\sigma}} - \frac{\nu}{E} (\text{tr} \underline{\underline{\sigma}}) \underline{\underline{I}} \\ & + (z_1 - z_1^{(0)}) (-\varepsilon_c \underline{e}_x \otimes \underline{e}_x + \varepsilon_a \underline{e}_y \otimes \underline{e}_y + \varepsilon_a \underline{e}_z \otimes \underline{e}_z) \\ & + (z_2 - z_2^{(0)}) (\varepsilon_a \underline{e}_x \otimes \underline{e}_x - \varepsilon_c \underline{e}_y \otimes \underline{e}_y + \varepsilon_a \underline{e}_z \otimes \underline{e}_z) \\ & + (z_3 - z_3^{(0)}) (\varepsilon_a \underline{e}_x \otimes \underline{e}_x + \varepsilon_a \underline{e}_y \otimes \underline{e}_y - \varepsilon_c \underline{e}_z \otimes \underline{e}_z)\end{aligned}\quad (99)$$

Let z_{12} , z_{23} and z_{31} denote the volume-fraction transformations between the variants (see Fig. 30). Then the current volume fractions (z_1 , z_2 , z_3) are related to the initial volume fractions ($z_1^{(0)}$, $z_2^{(0)}$, $z_3^{(0)}$) by:

$$z_1 = z_1^{(0)} - z_{12} + z_{31} \quad \text{for variant 1} \quad (100a)$$

$$z_2 = z_2^{(0)} - z_{23} + z_{12} \quad \text{for variant 2} \quad (100\text{b})$$

$$z_3 = z_3^{(0)} - z_{31} + z_{23} \quad \text{for variant 3} \quad (100\text{c})$$

With Eq. (100), the strain tensor $\underline{\underline{\varepsilon}}$ (Eq. (99)) can be expressed as:

$$\begin{aligned} \underline{\underline{\varepsilon}}(\underline{\underline{\sigma}}, z_{12}, z_{23}, z_{31}) = & \frac{1+v}{E} \underline{\underline{\sigma}} - \frac{v}{E} (\text{tr} \underline{\underline{\sigma}}) \underline{\underline{I}} + z_{12} (\underline{\varepsilon}_0 \underline{e}_x \otimes \underline{e}_x - \underline{\varepsilon}_0 \underline{e}_y \otimes \underline{e}_y) \\ & + z_{23} (\underline{\varepsilon}_0 \underline{e}_y \otimes \underline{e}_y - \underline{\varepsilon}_0 \underline{e}_z \otimes \underline{e}_z) + z_{31} (\underline{\varepsilon}_0 \underline{e}_z \otimes \underline{e}_z - \underline{\varepsilon}_0 \underline{e}_x \otimes \underline{e}_x) \end{aligned} \quad (101)$$

where ε_0 is expressed as:

$$\varepsilon_0 = \varepsilon_a + \varepsilon_c = \frac{a - c}{a_0} \quad (102)$$

ε_0 is the strain change due to martensite reorientation (Karaca et al. 2006). The mathematical expressions of ε_a and ε_c are given in Eq. (82), and the lattices lengths a_0 , a and c are illustrated by Fig. 1 in Chapter 1.

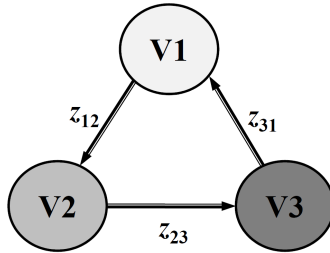


Fig. 30. Martensite reorientation among three variants (V1, V2, V3). z_{12} (z_{23} or z_{31}) denotes volume-fraction transformation from V1 (V2 or V3) to V2 (V3 or V1).

■ Magnetization–magnetic field relation

$$M(\underline{H}, z_1, z_2, z_3) = -\frac{1}{\mu_0} \frac{\partial L}{\partial H} = \sum_{i=1}^3 z_i \left(a_i H + \left\langle H - \frac{M_s}{a_i} \right\rangle (M_s - a_i H) \right) \quad (103)$$

■ Thermodynamic forces A_1 , A_2 and A_3 respectively related to the volume fractions z_1 , z_2 , z_3

The internal constraints (Eqs. (73) and (74)) only depend on the dissipative internal state variables (z_1, z_2, z_3), so the related thermodynamic forces (A_1, A_2, A_3) can be directly obtained from the Gibbs free energy (Moumni, 1995; Moumni et al., 2008):

$$A_1(\underline{\underline{\sigma}}, \underline{H}, z_1) = -\frac{\partial g}{\partial z_1} = -kz_1 - \sigma_{xx}\epsilon_c + \epsilon_a(\sigma_{yy} + \sigma_{zz}) + \left(\frac{\mu_0 a_1}{2} H^2 + \left\langle H - \frac{M_s}{a_1} \right\rangle \right) (\mu_0 M_s H - \frac{\mu_0 a_1}{2} H^2 - \frac{\mu_0 M_s^2}{2a_1}) \quad (104a)$$

$$A_2(\underline{\underline{\sigma}}, \underline{H}, z_2) = -\frac{\partial g}{\partial z_2} = -kz_2 - \sigma_{yy}\epsilon_c + \epsilon_a(\sigma_{zz} + \sigma_{xx}) + \left(\frac{\mu_0 a_2}{2} H^2 + \left\langle H - \frac{M_s}{a_2} \right\rangle \right) (\mu_0 M_s H - \frac{\mu_0 a_2}{2} H^2 - \frac{\mu_0 M_s^2}{2a_2}) \quad (104b)$$

$$A_3(\underline{\underline{\sigma}}, \underline{H}, z_3) = -\frac{\partial g}{\partial z_3} = -kz_3 - \sigma_{zz}\epsilon_c + \epsilon_a(\sigma_{xx} + \sigma_{yy}) + \left(\frac{\mu_0 a_3}{2} H^2 + \left\langle H - \frac{M_s}{a_3} \right\rangle \right) (\mu_0 M_s H - \frac{\mu_0 a_3}{2} H^2 - \frac{\mu_0 M_s^2}{2a_3}) \quad (104c)$$

4.2.5. Evolution laws of internal state variables

The martensite reorientation is assumed to be the only source of energy dissipation. So the intrinsic dissipation D can be expressed as:

$$D = A_1 \dot{z}_1 + A_2 \dot{z}_2 + A_3 \dot{z}_3 \quad (105)$$

where \dot{z}_1, \dot{z}_2 and \dot{z}_3 are the rates of the volume fractions. Let $\dot{z}_{12}, \dot{z}_{23}$ and \dot{z}_{31} denote the rates

of the volume-fraction transformations (see Fig. 30), then \dot{z}_1, \dot{z}_2 and \dot{z}_3 can be expressed as:

$$\dot{z}_1 = -\dot{z}_{12} + \dot{z}_{31} \quad (106a)$$

$$\dot{z}_2 = -\dot{z}_{23} + \dot{z}_{12} \quad (106b)$$

$$\dot{z}_3 = -\dot{z}_{31} + \dot{z}_{23} \quad (106c)$$

In Eq. (105), replace \dot{z}_1, \dot{z}_2 and \dot{z}_3 with Eq. (106) and we obtain:

$$D = (-A_1 + A_2) \dot{z}_{12} + (-A_2 + A_3) \dot{z}_{23} + (-A_3 + A_1) \dot{z}_{31} \quad (107)$$

We define A_{12} , A_{23} and A_{31} as the thermodynamic forces related to the martensite reorientations respectively between variants (1, 2), (2, 3) and (3, 1):

$$A_{12} = -A_1 + A_2 = k(z_1 - z_2) + \varepsilon_0(\sigma_{xx} - \sigma_{yy}) + E_{12}(\underline{H}) \quad (108a)$$

$$A_{23} = -A_2 + A_3 = k(z_2 - z_3) + \varepsilon_0(\sigma_{yy} - \sigma_{zz}) + E_{23}(\underline{H}) \quad (108b)$$

$$A_{31} = -A_3 + A_1 = k(z_3 - z_1) + \varepsilon_0(\sigma_{zz} - \sigma_{xx}) + E_{31}(\underline{H}) \quad (108c)$$

To obtain Eq. (108), Eq. (104) has been used for the expressions of A_1 , A_2 and A_3 . In Eq. (108), $E_{12}(\underline{H})$, $E_{23}(\underline{H})$ and $E_{31}(\underline{H})$ are the magnetic energy differences respectively between variants (1, 2), (2, 3) and (3, 1):

$$\begin{aligned} E_{12}(\underline{H}) &= -\left(\frac{\mu_0 a_1}{2} H^2 + \left\langle H - \frac{M_s}{a_1} \right\rangle \left(\mu_0 M_s H - \frac{\mu_0 a_1}{2} H^2 - \frac{\mu_0 M_s^2}{2a_1} \right)\right) \\ &\quad + \left(\frac{\mu_0 a_2}{2} H^2 + \left\langle H - \frac{M_s}{a_2} \right\rangle \left(\mu_0 M_s H - \frac{\mu_0 a_2}{2} H^2 - \frac{\mu_0 M_s^2}{2a_2} \right)\right) \end{aligned} \quad (109a)$$

$$\begin{aligned} E_{23}(\underline{H}) &= -\left(\frac{\mu_0 a_2}{2} H^2 + \left\langle H - \frac{M_s}{a_2} \right\rangle \left(\mu_0 M_s H - \frac{\mu_0 a_2}{2} H^2 - \frac{\mu_0 M_s^2}{2a_2} \right)\right) \\ &\quad + \left(\frac{\mu_0 a_3}{2} H^2 + \left\langle H - \frac{M_s}{a_3} \right\rangle \left(\mu_0 M_s H - \frac{\mu_0 a_3}{2} H^2 - \frac{\mu_0 M_s^2}{2a_3} \right)\right) \end{aligned} \quad (109b)$$

$$\begin{aligned} E_{31}(\underline{H}) &= -\left(\frac{\mu_0 a_3}{2} H^2 + \left\langle H - \frac{M_s}{a_3} \right\rangle \left(\mu_0 M_s H - \frac{\mu_0 a_3}{2} H^2 - \frac{\mu_0 M_s^2}{2a_3} \right)\right) \\ &\quad + \left(\frac{\mu_0 a_1}{2} H^2 + \left\langle H - \frac{M_s}{a_1} \right\rangle \left(\mu_0 M_s H - \frac{\mu_0 a_1}{2} H^2 - \frac{\mu_0 M_s^2}{2a_1} \right)\right) \end{aligned} \quad (109c)$$

With Eq. (108), the intrinsic dissipation D (Eq. (107)) can be rewritten as:

$$D = A_{12} \dot{z}_{12} + A_{23} \dot{z}_{23} + A_{31} \dot{z}_{31} \quad (110)$$

The martensite reorientation needs to overcome some internal frictional force, known as twinning stress σ_{tw} (Heczko, 2005; Heczko et al., 2006; Likhachev and Ullakko, 2000). So the pseudo-dissipation potential \mathcal{D} of the martensite reorientations among three variants can be proposed as:

$$\mathcal{D} = \sigma_{tw} \varepsilon_0 (|z_{12}| + |z_{23}| + |z_{31}|) \quad (111)$$

where $|x|$ denotes the absolute value of x ; ε_0 , the strain change due to martensite reorientation, is mathematically expressed by Eq. (102). By Eq. (72), the directional derivatives of \mathcal{D} define the yield surfaces for the thermodynamic forces A_{12} , A_{23} and A_{31} :

$$A_{12} \in \partial_{z_{12}} \mathcal{D} \Rightarrow |A_{12}| \leq \sigma_{tw} \varepsilon_0 \quad (112a)$$

$$A_{23} \in \partial_{z_{23}} \mathcal{D} \Rightarrow |A_{23}| \leq \sigma_{tw} \varepsilon_0 \quad (112b)$$

$$A_{31} \in \partial_{z_{31}} \mathcal{D} \Rightarrow |A_{31}| \leq \sigma_{tw} \varepsilon_0 \quad (112c)$$

Based on Eq. (112), the yield functions associated with the martensite reorientations between variants (1, 2), (2, 3) and (3, 1) are proposed as:

$$F_{ij} = |A_{ij}| - \sigma_{tw} \varepsilon_0 \quad \text{where } (i, j) = (1, 2), (2, 3), (3, 1)$$

- If $F_{ij} < 0$, no martensite reorientation between variant i and j . So $\dot{z}_{ij} = 0$.
- If $F_{ij} = 0$ and $\dot{F}_{ij} < 0$, no martensite reorientation between i and j . $\dot{z}_{ij} = 0$.
- If $F_{ij} = 0$ (i.e., $|A_{ij}| = \sigma_{tw} \varepsilon_0$) and $\dot{F}_{ij} = 0$ (i.e., $\dot{A}_{ij} = 0$), martensite reorientation between i and j exists. With Eqs. (106) and (108), \dot{z}_{ij} is given by the consistency condition of $\dot{F}_{ij} = 0$:

$$(i, j) = (1, 2): \dot{z}_{12} = \frac{1}{2k} (\varepsilon_0 (\dot{\sigma}_{xx} - \dot{\sigma}_{yy}) + \dot{E}_{12}(\underline{H})) \quad \text{martensite reorientation between V1, V2} \quad (113a)$$

$$(i, j) = (2, 3): \dot{z}_{23} = \frac{1}{2k} (\varepsilon_0 (\dot{\sigma}_{yy} - \dot{\sigma}_{zz}) + \dot{E}_{23}(\underline{H})) \quad \text{martensite reorientation between V2, V3} \quad (113b)$$

$$(i, j) = (3, 1): \dot{z}_{31} = \frac{1}{2k} (\varepsilon_0 (\dot{\sigma}_{zz} - \dot{\sigma}_{xx}) + \dot{E}_{31}(\underline{H})) \quad \text{martensite reorientation between V3, V1} \quad (113c)$$

Summary

The complete model consists of the following constitutive relations:

■ Stress-strain relation

$$\begin{aligned}\underline{\underline{\varepsilon}}(\underline{\underline{\sigma}}, z_{12}, z_{23}, z_{31}) = & \frac{1+\nu}{E} \underline{\underline{\sigma}} - \frac{\nu}{E} (\text{tr} \underline{\underline{\sigma}}) \underline{\underline{I}} + z_{12} (\underline{\varepsilon}_0 \underline{e}_x \otimes \underline{e}_x - \underline{\varepsilon}_0 \underline{e}_y \otimes \underline{e}_y) \\ & + z_{23} (\underline{\varepsilon}_0 \underline{e}_y \otimes \underline{e}_y - \underline{\varepsilon}_0 \underline{e}_z \otimes \underline{e}_z) + z_{31} (\underline{\varepsilon}_0 \underline{e}_z \otimes \underline{e}_z - \underline{\varepsilon}_0 \underline{e}_x \otimes \underline{e}_x)\end{aligned}$$

■ Magnetization-magnetic field relation

$$M(\underline{H}, z_1, z_2, z_3) = \sum_{i=1}^3 z_i \left(a_i H + \left\langle H - \frac{\underline{M}_s}{a_i} \right\rangle (M_s - a_i H) \right)$$

■ Thermodynamic driving forces for martensite reorientations

$$A_{12} = k(z_1 - z_2) + \varepsilon_0 (\sigma_{xx} - \sigma_{yy}) + E_{12}(\underline{H})$$

$$A_{23} = k(z_2 - z_3) + \varepsilon_0 (\sigma_{yy} - \sigma_{zz}) + E_{23}(\underline{H})$$

$$A_{31} = k(z_3 - z_1) + \varepsilon_0 (\sigma_{zz} - \sigma_{xx}) + E_{31}(\underline{H})$$

where:

$$\begin{aligned}E_{12}(\underline{H}) = & -\left(\frac{\mu_0 a_1}{2} H^2 + \left\langle H - \frac{\underline{M}_s}{a_1} \right\rangle \left(\mu_0 M_s H - \frac{\mu_0 a_1}{2} H^2 - \frac{\mu_0 M_s^2}{2a_1}\right)\right) \\ & + \left(\frac{\mu_0 a_2}{2} H^2 + \left\langle H - \frac{\underline{M}_s}{a_2} \right\rangle \left(\mu_0 M_s H - \frac{\mu_0 a_2}{2} H^2 - \frac{\mu_0 M_s^2}{2a_2}\right)\right)\end{aligned}$$

$$\begin{aligned}E_{23}(\underline{H}) = & -\left(\frac{\mu_0 a_2}{2} H^2 + \left\langle H - \frac{\underline{M}_s}{a_2} \right\rangle \left(\mu_0 M_s H - \frac{\mu_0 a_2}{2} H^2 - \frac{\mu_0 M_s^2}{2a_2}\right)\right) \\ & + \left(\frac{\mu_0 a_3}{2} H^2 + \left\langle H - \frac{\underline{M}_s}{a_3} \right\rangle \left(\mu_0 M_s H - \frac{\mu_0 a_3}{2} H^2 - \frac{\mu_0 M_s^2}{2a_3}\right)\right)\end{aligned}$$

$$\begin{aligned}E_{31}(\underline{H}) = & -\left(\frac{\mu_0 a_3}{2} H^2 + \left\langle H - \frac{\underline{M}_s}{a_3} \right\rangle \left(\mu_0 M_s H - \frac{\mu_0 a_3}{2} H^2 - \frac{\mu_0 M_s^2}{2a_3}\right)\right) \\ & + \left(\frac{\mu_0 a_1}{2} H^2 + \left\langle H - \frac{\underline{M}_s}{a_1} \right\rangle \left(\mu_0 M_s H - \frac{\mu_0 a_1}{2} H^2 - \frac{\mu_0 M_s^2}{2a_1}\right)\right)\end{aligned}$$

■ Evolution laws for the volume fractions of the variants

$$\text{When } |A_{12}| = \sigma_{tw} \varepsilon_0 \text{ and } \dot{A}_{12} = 0, \quad \dot{z}_{12} = \frac{1}{2k} (\varepsilon_0 (\dot{\sigma}_{xx} - \dot{\sigma}_{yy}) + \dot{E}_{12}(\underline{H}));$$

$$\text{When } |A_{23}| = \sigma_{tw} \varepsilon_0 \text{ and } \dot{A}_{23} = 0, \quad \dot{z}_{23} = \frac{1}{2k} (\varepsilon_0 (\dot{\sigma}_{yy} - \dot{\sigma}_{zz}) + \dot{E}_{23}(\underline{H}));$$

$$\text{When } |A_{31}| = \sigma_{tw} \varepsilon_0 \text{ and } \dot{A}_{31} = 0, \quad \dot{z}_{31} = \frac{1}{2k} (\varepsilon_0 (\dot{\sigma}_{zz} - \dot{\sigma}_{xx}) + \dot{E}_{31}(\underline{H})).$$

$$\dot{z}_1 = -\dot{z}_{12} + \dot{z}_{31}, \quad \dot{z}_2 = -\dot{z}_{23} + \dot{z}_{12}, \quad \dot{z}_3 = -\dot{z}_{31} + \dot{z}_{23}$$

$$z_1 \geq 0, \quad z_2 \geq 0, \quad z_3 \geq 0, \quad z_1 + z_2 + z_3 = 1$$

4.2.6. Identification of model parameters

The involved parameters in the model are listed below:

- E : Young's modulus.
- ν : Poisson's ratio which is assumed to be 0.3 (ν for commonly used metals is around 1/3).
- ε_0 : strain change due to martensite reorientation.
- k : interaction parameter representing the incompatibility among the martensite variants.
- σ_{tw} : twinning stress (considered as the internal frictional force or threshold driving force for martensite reorientation).
- M_s : saturation magnetization.
- a_1, a_2, a_3 : magnetic susceptibilities of the three martensite variants.

Three basic experiments are required to completely determine the model parameters above:
uniaxial compression test, magnetization tests along magnetic easy- and hard-axis.

4.2.6.1. Uniaxial compression test

This experiment is for identifying the Young's modulus E , the strain change ε_0 due to martensite reorientation, the interaction parameter k and the twinning stress σ_{tw} . The material in the initial state of V1 (with short-axis along x -coordinate) is under a uniaxial compressive stress σ_{yy} along y -coordinate (see Fig. 31(a)). Martensite reorientation from V1 to V2 (with short-axis along y -coordinate) is induced and the resulted stress-strain curve ($\sigma_{yy}-\varepsilon_{yy}$) is shown in Fig. 31(b).

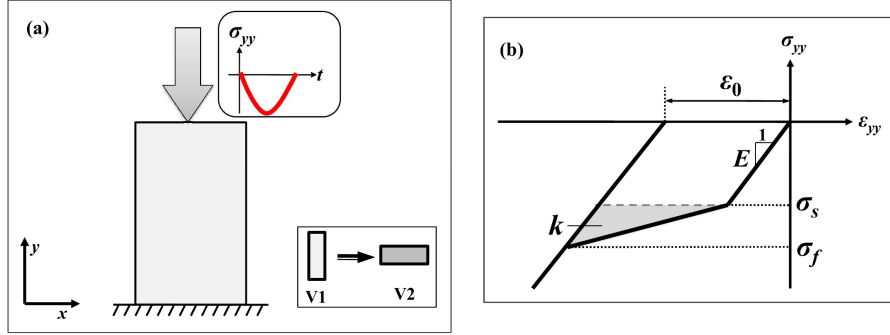


Fig. 31. (a) Martensite reorientation (from V1 to V2) induced by compressive stress σ_{yy} . (b) Stress-strain curve (σ_{yy} - ε_{yy}) of martensite reorientation under compression. Young's modulus E , strain change ε_0 due to martensite reorientation and interaction parameter k are illustrated on the figure. σ_s and σ_f are respectively the start and finish stresses for the martensite reorientation.

By linear approximation of the strain-stress curve before martensite reorientation, the Young's modulus E is obtained (see Fig. 31(b)). Furthermore, the strain change ε_0 due to martensite reorientation can be identified as the absolute value of the residual strain after unloading (Fig. 31(b)). By the evolution laws introduced in sub-section 4.2.5, during martensite reorientation from V1 to V2, the associated thermodynamic force A_{12} (Eq. (108a)) must be equal to $\sigma_{tw}\varepsilon_0$. Let σ_s and σ_f respectively be the start and finish stresses for the martensite reorientation (see Fig. 31(b)). Then we have:

- At the beginning of martensite reorientation, $\sigma = \sigma_s$, $z_1 = 1$, $z_2 = 0$:

$$A_{12} = k - \sigma_s \varepsilon_0 = \sigma_{tw} \varepsilon_0 \quad (114)$$

- At the end, $\sigma = \sigma_f$, $z_1 = 0$, $z_2 = 1$:

$$A_{12} = -k - \sigma_f \varepsilon_0 = \sigma_{tw} \varepsilon_0 \quad (115)$$

By solving Eqs. (114) and (115), we obtain:

$$k = \frac{1}{2} \varepsilon_0 (\sigma_s - \sigma_f) \quad (116)$$

$$\sigma_{tw} = -\frac{1}{2} (\sigma_f + \sigma_s) \quad (117)$$

Equation (116) shows that the interaction parameter k represents an area bounded by the strain-stress curve (see the shaded area in Fig. 31(b)). If the martensite variants are compatible ($\sigma_s = \sigma_f$), then the area $|\varepsilon_0(\sigma_s - \sigma_f)|/2$ is null (i.e., $k = 0$). If the two variants are incompatible ($\sigma_s \neq \sigma_f$), then the area is not zero. Therefore, such area ($= k$) can be viewed as the energy needed to overcome the incompatibility of the variants during martensite reorientation.

4.2.6.2. Magnetization tests

From the experiments in this sub-section, the saturation magnetization M_s can be directly obtained. Two other parameters (i.e., the magnetic anisotropic energy coefficient K_u and the magnetic susceptibility $a(0)$ for the magnetization along the magnetic easy-axis) are also obtained in order to calculate the magnetic susceptibilities a_1, a_2, a_3 of the variants.

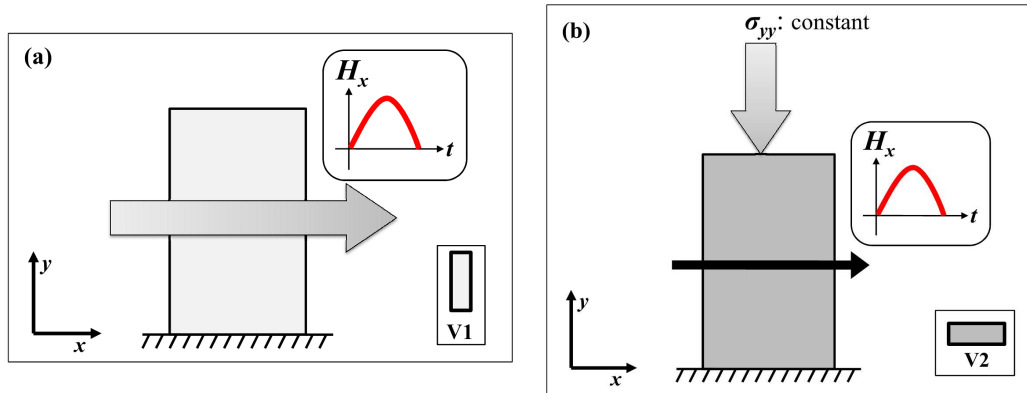


Fig. 32. (a) Magnetization test along magnetic easy-axis. (b) Magnetization test along magnetic hard-axis. A constant compressive stress σ_{yy} of large value is simultaneously applied to prevent martensite reorientation.

■ Magnetization along magnetic easy-axis

The material in the state of V1 (with magnetic easy-axis along x -coordinate) is put in a magnetic field H_x along x -coordinate (Fig. 32(a)). By linearization of the magnetization curve,

we can determine the saturation magnetization M_s , and the magnetic susceptibility $a(0)$ for the magnetization along the magnetic easy-axis (see Fig. 33).

■ Magnetization along magnetic hard-axis

The material in the state of V2 (with magnetic easy-axis along y -coordinate) is put in a magnetic field H_x perpendicular to the magnetic easy-axis of V2. To prevent martensite reorientation during the experiment, a constant compressive stress σ_{yy} (~ 10 MPa) is applied along y -coordinate (Fig. 32(b)). Following the same procedures as the previous experiment, the magnetization curve for the magnetization process along the magnetic hard-axis is obtained.

■ Calculation of a_1, a_2, a_3

The uniaxial magneto-crystalline anisotropy energy density u_a for Ni-Mn-Ga 5M martensite can be expressed as (O'Handley et al., 2000):

$$u_a(\theta) = K_u \sin^2 \theta \quad (118)$$

where K_u is the coefficient of magneto-crystalline anisotropy energy; θ is the equilibrium angle between the magnetic easy-axis of the martensite variant and its magnetization vector. $u_a(\theta)$ can be determined by the area between the magnetization curve along the easy-axis and that along the direction deviating by an angle θ from the easy-axis (see the shaded area in Fig. 33). For the magnetization along the magnetic hard-axis ($\theta = \pi/2$), we have $u_a = K_u$. So K_u can be directly obtained by the magnetization curves from the previous two magnetization tests.

From Fig. 33, $u_a(\theta)$ can be calculated as:

$$u_a(\theta) = \frac{1}{2} \mu_0 M_s^2 \left(\frac{1}{a(\theta)} - \frac{1}{a(0)} \right) \quad (119)$$

where $a(0)$ and $a(\theta)$ are respectively the magnetic susceptibilities of the magnetization along the magnetic easy-axis ($\theta = 0^\circ$) and that along the direction deviating by an angle θ from the easy-axis. With Eqs. (118) and (119), we can obtain the following expression of $a(\theta)$:

$$a(\theta) = \left(\frac{1}{a(0)} + \frac{2K_u(\sin^2 \theta)}{\mu_0 M_s^2} \right)^{-1} \quad (120)$$

The magnetic easy-axes for variants 1, 2 and 3 are respectively the x -, y - and z -coordinate. Let θ_1 , θ_2 and θ_3 be the angles between the magnetic field \underline{H} and the x -, y -, z -coordinate, respectively. By Eq. (120), the magnetic susceptibilities of the variants are:

$$a_1(\underline{H}) = a(\theta_1) = \left(\frac{1}{a(0)} + \frac{2K_u(\sin^2 \theta_1)}{\mu_0 M_s^2} \right)^{-1} \quad \text{for variant 1} \quad (121\text{a})$$

$$a_2(\underline{H}) = a(\theta_2) = \left(\frac{1}{a(0)} + \frac{2K_u(\sin^2 \theta_2)}{\mu_0 M_s^2} \right)^{-1} \quad \text{for variant 2} \quad (121\text{b})$$

$$a_3(\underline{H}) = a(\theta_3) = \left(\frac{1}{a(0)} + \frac{2K_u(\sin^2 \theta_3)}{\mu_0 M_s^2} \right)^{-1} \quad \text{for variant 3} \quad (121\text{c})$$

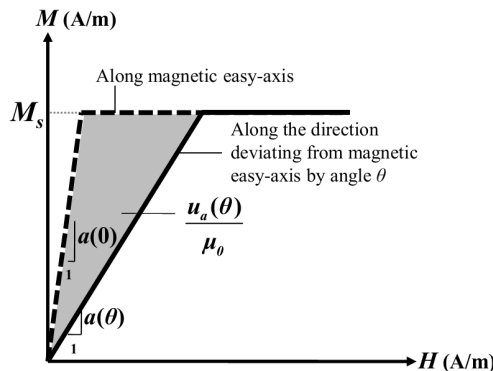


Fig. 33. Magnetization curves (after linear approximation) of the magnetization along the magnetic easy-axis (dashed line) and that along the direction deviating from the easy-axis by an angle θ (solid line). The uniaxial magneto-crystalline anisotropy energy $u_a(\theta)$ can be determined by the area between the two magnetization curves. The saturation magnetization M_s and the magnetic susceptibilities $a(0)$ and $a(\theta)$ are also illustrated.

4.3. Numerical simulations and model validations

Application of the constitutive model in simulating the material's behaviors (using Matlab) is reported in this section, while the structural simulations (using the finite element code Cast3M: <http://www-cast3m.cea.fr>) are reported in the next section (i.e., Section 4.4). The algorithm of the Matlab program is summarized in Table 2. Table 3 lists the values of the model parameters used for the simulations. Five kinds of the material's behaviors are simulated and compared with experiments in the following sub-sections: (1) Martensite reorientation induced by a non-rotating magnetic field (the direction of the magnetic field is fixed while its magnitude is changing); (2) Martensite reorientation induced by a rotating magnetic field (the magnitude of the magnetic field is fixed while its direction is changing); (3) Super-elasticity under biaxial compressions; (4) Super-elasticity under magneto-mechanical loadings (compressive stress plus a perpendicular magnetic field); (5) Thermo-magneto-mechanical behaviors of FSMA. For convenience, values of compressive stresses are positive in this section.

Table 2. Algorithm of simulation on material's behaviors.

Initialization of model parameters

Initialization of material state

Input: $\underline{\sigma}, \underline{H}$

Output: $\underline{\varepsilon}, M$

Start:

Equally divide the magneto-mechanical loading path into N intervals ($\Delta\underline{\sigma}, \Delta\underline{H}$)

Initialize the counter: $n = 1$

While $n < N + 1$:

1. $\underline{\underline{\sigma}}^{(n)} = \underline{\underline{\sigma}}^{(n-1)} + \Delta\underline{\underline{\sigma}}$, $\underline{H}^{(n)} = \underline{H}^{(n-1)} + \Delta\underline{H}$
2. Calculate $a_i^{(n)}$ ($i = 1, 2, 3$) by Eq. (121).
3. Calculate the thermodynamic forces $A_{ij}^{(n)}$ ($(i, j) = (1, 2), (2, 3), (3, 1)$) by Eqs. (108) and (109).
4. Detection of martensite reorientations:
 - If $A_{ij}^{(n)} > \sigma_{tw}\varepsilon_0$, $z_i^{(n-1)} > 0$ and $z_j^{(n-1)} < 1$, then martensite reorientation between variant i and j .
 - If $A_{ij}^{(n)} < -\sigma_{tw}\varepsilon_0$, $z_i^{(n-1)} < 1$ and $z_j^{(n-1)} > 0$, then martensite reorientation between variant i and j .
5. If there is martensite reorientation between variant i and j , then calculate the volume fraction transformation Δz_{ij} by Eq. (113); if not, $\Delta z_{ij} = 0$.
6. Update the volume fractions

$$z_{12}^{(n)} = z_{12}^{(n-1)} + \Delta z_{12}$$

$$z_{23}^{(n)} = z_{23}^{(n-1)} + \Delta z_{23}$$

$$z_{31}^{(n)} = z_{31}^{(n-1)} + \Delta z_{31}$$

$$z_1^{(n)} = z_1^{(n-1)} - \Delta z_{12} + \Delta z_{31}$$

$$z_2^{(n)} = z_2^{(n-1)} - \Delta z_{23} + \Delta z_{12}$$

$$z_3^{(n)} = z_3^{(n-1)} - \Delta z_{31} + \Delta z_{23}$$
7. Update the strain $\underline{\underline{\varepsilon}}^{(n)}$ and the magnetization $M^{(n)}$ by Eqs. (101) and (103).
8. Increase the counter: $n+1$.

End.

Table 3. Parameter values from the uniaxial compression test and the magnetization tests in (Heczko, 2005).

Model parameters

E (MPa)	100,000	M_s (A/m)	500,000
ε_0 (%)	5.8	$a(0)$	5
k (J/m ³)	10,900	K_u (J/m ³)	170,000
σ_{tw} (MPa)	1.2		

4.3.1. Martensite reorientation induced by a non-rotating magnetic field

Large reversible strain and high frequency response make FSMA a promising candidate for actuators. Actually, many simple actuators based on FSMA have already been proposed in literature (e.g., Gauthier et al., 2006; Suorsa et al., 2002; Tellinen et al., etc.). This sub-section is devoted to simulate the material's behavior as an actuator driven by a non-rotating magnetic field.

4.3.1.1. Non-rotating magnetic field with a uniaxial stress

The material in the initial state of V2 is under a magnetic field H_x (along x -coordinate) and a constant compressive stress σ_{yy} (along y -coordinate) (see Fig. 34). Magnetic loading (H_x increases) can induce the martensite reorientation from V2 to V1 (with magnetic easy-axis along the field), while during unloading (H_x decreases to 0), reverse martensite reorientation from V1 to V2 can be induced by the compressive stress. The magneto-mechanical responses of the material from the experiments (Heczko, 2005) and simulations are compared in Fig. 35.

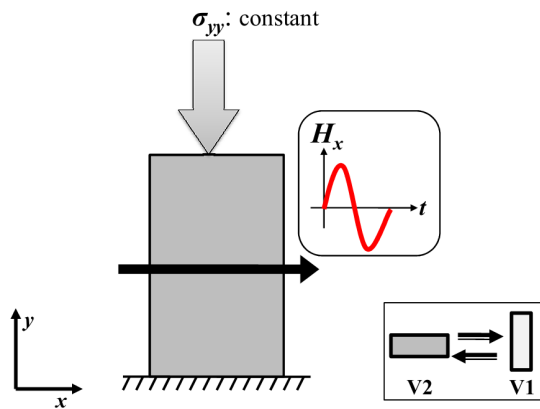
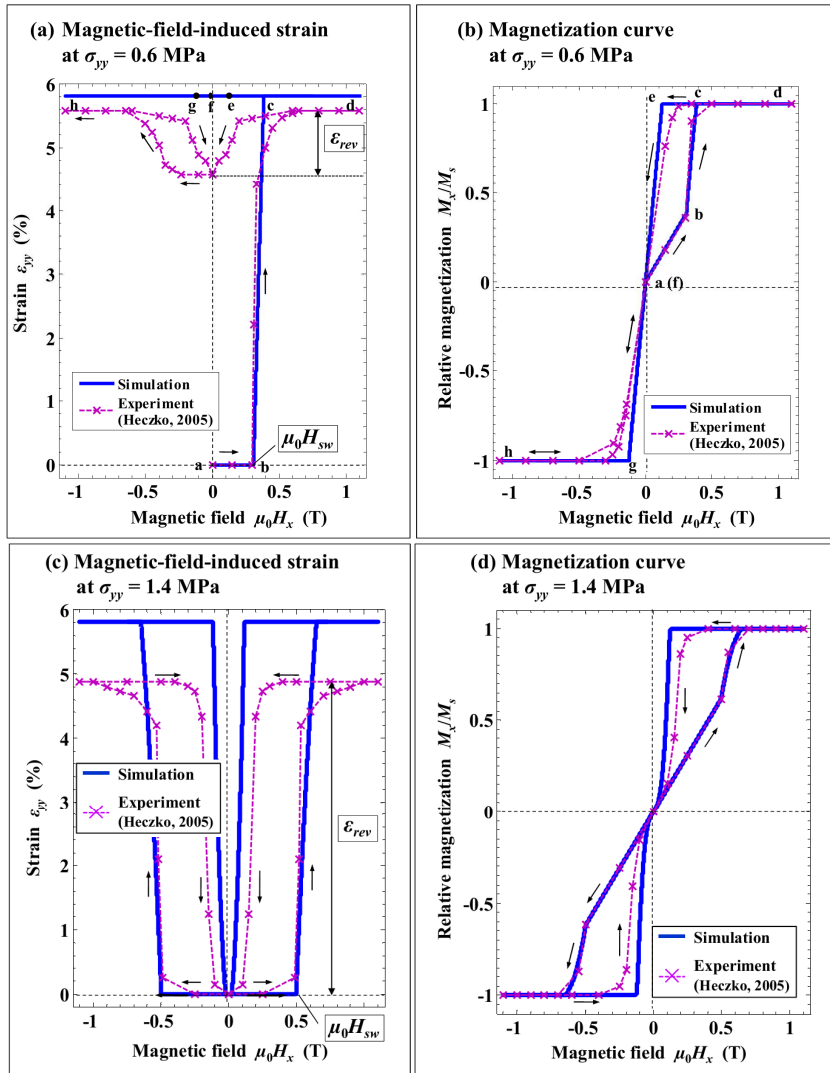


Fig. 34. FSMA used as an actuator driven by a non-rotating magnetic field (1D case: uniaxial stress). During magnetic loading-unloading (the magnitude of the field increases and decreases), martensite reorientations between V2 and V1 are induced, which lead to the reversible strain of FSMA actuator.

Figures 35(a) and 35(b) are, respectively, the magnetic-field-induced strain and the magnetization curve obtained for the case of small compressive stress σ_{yy} (0.6 MPa). The points (a, b, c, d, e, f, g, h) on the figures indicate the sequences of the material's responses. Path $a \rightarrow b \rightarrow c \rightarrow d \rightarrow e \rightarrow f$ corresponds to the first magnetic loading-unloading cycle, and path $f \rightarrow g \rightarrow h \rightarrow g \rightarrow f$ corresponds to the second cycle. At the beginning of the first cycle, the strain ε_{yy} remains 0 and the magnetization increases slowly ($a \rightarrow b$ in Figs. 35(a) and 35(b)) until the switching field $\mu_0 H_{sw}$ (≈ 0.3 T in Fig. 35(a)) is reached, where the martensite reorientation starts and a rapid increase of both strain and magnetization is observed ($b \rightarrow c$). For the small values of σ_{yy} (0.6 MPa here), the martensite reorientation is almost complete (i.e., all variant 2 has transferred to variant 1 during magnetic loading), so the strain change ε_0 ($\approx 5.8\%$) due to martensite reorientation is obtained at the end of loading (point d in Fig. 35(a)). During the magnetic unloading (magnetic field decreases to 0), the small stress cannot induce the reverse martensite reorientation, so the material remains in the state of V1 and no reversible strain is predicted. But in the experiment, a small reversible strain ($\varepsilon_{rev}/\varepsilon_0 < 20\%$) is observed. The simulation is performed on a material point while the experiment gives a structural response, where the stress and the magnetic field are not strictly uniform. For the second magnetic loading-unloading cycle (magnetic field in the negative direction of x -coordinate), no martensite reorientation is induced and no strain change is predicted. The material's response of the first cycle is quite different from that of the second cycle. Such phenomenon is called first cycle effect.

For a larger constant compressive stress σ_{yy} (e.g., 1.4 MPa in Figs. 35(c) and 35(d)), martensite reorientation during loading begins at a larger switching field ($\mu_0 H_{sw} \approx 0.5$ T in Fig. 35(c)), because σ_{yy} hinders the martensite reorientation process. During unloading, reverse martensite reorientation is induced by σ_{yy} and a rapid decrease of strain ε_{yy} is observed in Fig. 35(c). At the end of unloading, the material returns to its initial variant state, so a large

reversible strain is obtained. The material's behaviors are repeated in the following magnetic loading-unloading cycles. If the compressive stress σ_{yy} is too large (e.g., 3 MPa in Figs. 35(e) and 35(f)), martensite reorientation is totally blocked and no strain is observed. The compressive stress over which the martensite reorientation is blocked is defined as blocking stress σ_b . To obtain the magnetic-field-induced strain in the 1D case (uniaxial stress with a magnetic field), the applied compressive stress σ_{yy} cannot exceed σ_b . However, σ_b is only a few MPa (Heczko et al., 2000; Murray et al., 2000). To obtain a larger output stress σ_{yy} (larger than σ_b), FSMA must work in multi-axial loadings (multi-axial stress with a magnetic field), which is the topic of the following sub-section.



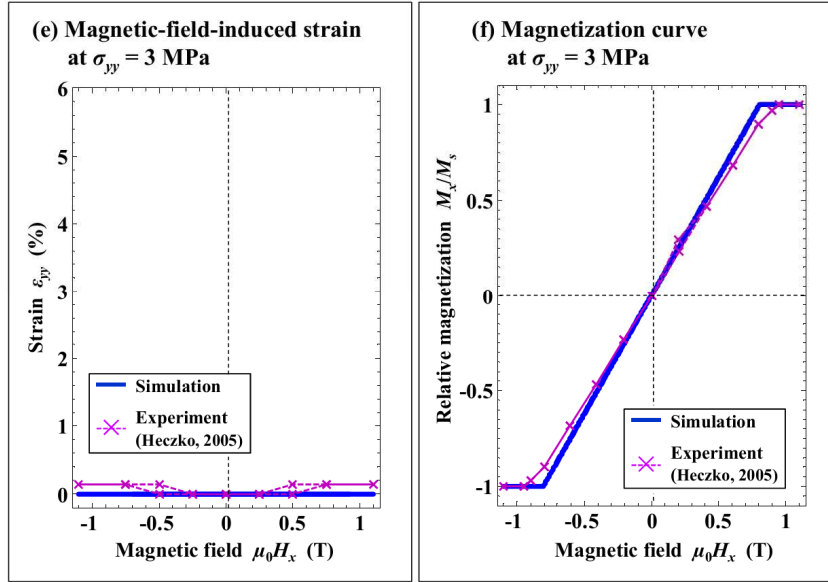


Fig. 35. Comparison between simulations and experiments (Heczko, 2005) of the material's magneto-mechanical responses at different levels of compressive stress σ_{yy} : (a) and (b) for $\sigma_{yy} = 0.6$ MPa, (c) and (d) for $\sigma_{yy} = 1.4$ MPa, (e) and (f) for $\sigma_{yy} = 3$ MPa. Figures on the left-hand side represent the magnetic-field-induced strain and those on the right-hand side are the magnetization curves.

4.3.1.2. Non-rotating magnetic field with biaxial stresses

Magnetic field H_x (along x -coordinate) and constant biaxial compressions σ_{xx} and σ_{yy} (along x - and y - coordinate, respectively) are applied to the material in the initial state of V2 (see Fig. 36). The material can switch to V1 during the magnetic loading and switch back during unloading depending on the stress levels. As indicated by Eq. (108a), the thermodynamic driving force A_{12} for the martensite reorientation between variant 1 and 2 depends on the stress difference $(\sigma_{yy} - \sigma_{xx})$, so the key parameters in the biaxial loading conditions are not the two stresses themselves, but their difference $(\sigma_{yy} - \sigma_{xx})$. Fig. 37 shows the effects of the stress difference $(\sigma_{yy} - \sigma_{xx})$ on the material's magneto-mechanical responses predicted by the model.

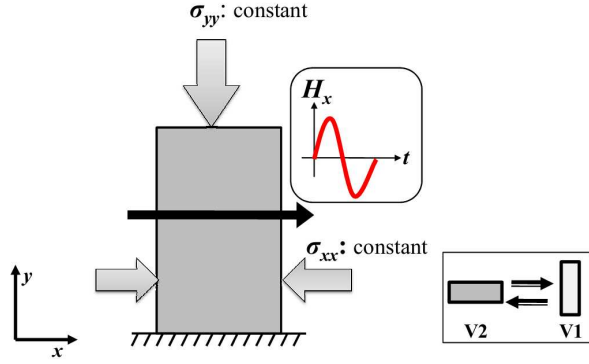


Fig. 36. FSMA used as an actuator driven by a non-rotating magnetic field (2D case: biaxial compressions). During magnetic loading-unloading, martensite reorientations between V2 and V1 are induced.

For the cases of small and large stress differences (e.g., $\sigma_{yy} - \sigma_{xx} = 0$ MPa and 3 MPa in Fig. 37(a)), martensite reorientation is blocked either during magnetic loading ($\sigma_{yy} - \sigma_{xx} = 3$ MPa) or unloading ($\sigma_{yy} - \sigma_{xx} = 0$ MPa), so no reversible strain is observed. To obtain a large reversible strain, medium levels of the stress difference are needed (e.g., $\sigma_{yy} - \sigma_{xx} = 1.3$ MPa and 1.6 MPa in Fig. 37(a)). It is noted that the effect of the biaxial stresses (σ_{xx}^{2D} and σ_{yy}^{2D}) on the material's behaviors is identical to that of a uniaxial stress σ_{yy}^{1D} in 1D configuration: $\sigma_{yy}^{1D} \sim (\sigma_{yy}^{2D} - \sigma_{xx}^{2D})$. So the applied compressive stress σ_{yy}^{2D} in 2D configurations can be larger than the blocking stress σ_b (stress limit in the uniaxial loading conditions, see sub-section 4.3.1.1), as long as the stress difference ($\sigma_{yy}^{2D} - \sigma_{xx}^{2D}$) is less than the blocking stress. Similar discussions can also be found in (He et al., 2011, 2012).

The simulation results (Figs. 35 and 37) of the martensite reorientation induced by the non-rotating magnetic field demonstrate that the model is able to describe most of the characteristic features of the material's behaviors: hysteresis, influence of the compressive stress on the switching field, blocking of martensite reorientation at high stress levels, first cycle effect at low stress levels, etc.

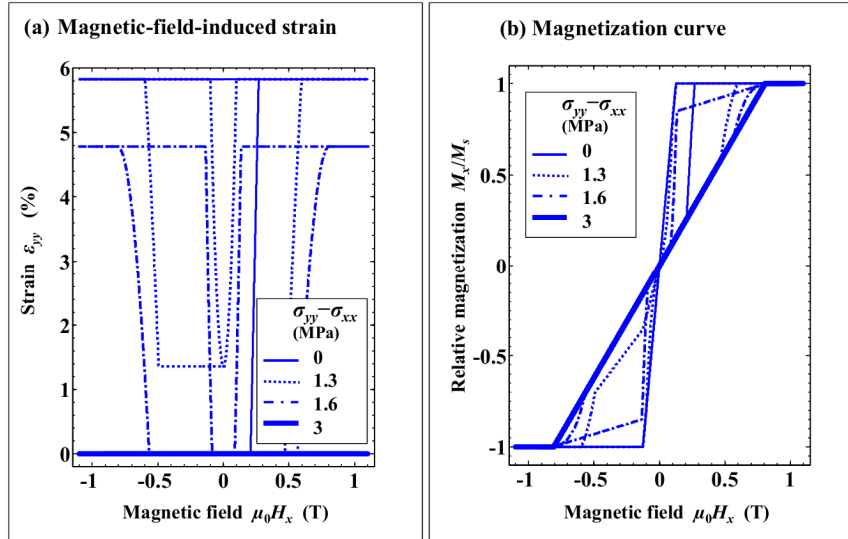


Fig. 37. Model predictions of the material's magneto-mechanical responses at different levels of compressive stress difference ($\sigma_{yy} - \sigma_{xx}$): (a) for magnetic-field-induced strain, (b) for magnetization curves.

4.3.2. Martensite reorientation induced by a rotating magnetic field

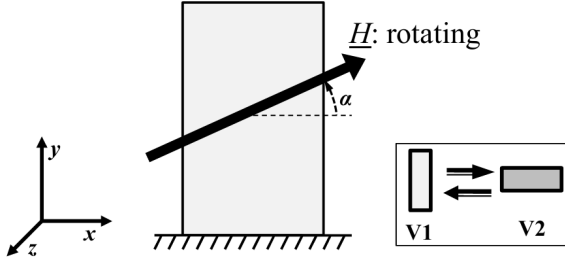


Fig. 38. FSMA used as an actuator driven by a rotating magnetic field. α is the rotation angle. Periodical martensite reorientations between V1 and V2 lead to reversible strain during the rotation of the magnetic field.

FSMA-based actuators can also be driven by a rotating magnetic field (see Fig. 38). The material's behavior in a rotating magnetic field is simulated and compared with experiments (Müllner et al., 2002) in Fig. 39. The rotation starts with the field along x -coordinate (rotation angle $\alpha = 0^\circ$) and the material's initial state V1. During the first half-cycle ($\alpha: 0^\circ \rightarrow 180^\circ$), the

material changes from V1 to V2 at a switching angle α_1 ($\approx 54^\circ$ in Fig. 39) with a rapid decrease in strain ε_{yy} . The strain is recovered when V2 switches back to V1 at another switching angle α_2 ($\approx 144^\circ$ in Fig. 39). Such process is repeated in further rotations. The strain change during the martensite reorientations is smaller in experiment than in simulation, because simulation is done with $\varepsilon_0 = 5.8\%$ while ε_0 of the material used in experiment is 1.9% (Müllner et al., 2002). In the first half-cycle, the material is in the state of V2 for the angle range of $[\alpha_1, \alpha_2]$. Considering a rotating field of constant rate, the time fraction of variant 2 is: $(\alpha_2 - \alpha_1)/180^\circ = 50\%$, which means that both variants occupy the same time fraction in a rotation cycle.

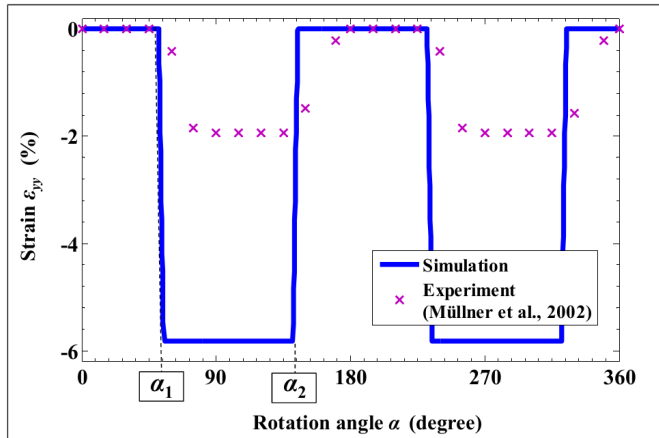


Fig. 39. Evolution of strain ε_{yy} with the rotation of the magnetic field (with constant magnitude $\mu_0H = 2$ T): results from the simulation (solid line) and experiment (crosses) are compared. α_1 and α_2 are the switching angles where the martensite reorientations take place during the first half-cycle of rotation.

The time fractions of the variants can be changed by applying certain compressions (e.g., σ_{xx} and σ_{yy} respectively along x - and y -coordinate, see Fig. 40(a)). The simulation results in Fig. 40(b) indicate that both the time fractions of the variants and the field-induced reversible strain of the material depend on the stress difference ($\sigma_{xx} - \sigma_{yy}$). When σ_{xx} and σ_{yy} are equal, the time fractions of the two variants in a rotation cycle are equal ($\sigma_{xx} - \sigma_{yy} = 0$ in Fig. 40(b)). When σ_{xx} is larger, V1 occupies a larger time fraction (e.g., $\sigma_{xx} - \sigma_{yy} = 1$ MPa); when σ_{xx} is too

large, martensite reorientation is blocked and the material is always in the state of V1 (e.g., $\sigma_{xx} - \sigma_{yy} = 3$ MPa). An analytic relation between the stress difference and the time fractions of the variants can be found in (He et al., 2011). For the part of the reversible strain, when the stress difference $|\sigma_{xx} - \sigma_{yy}|$ is small (e.g., $\sigma_{xx} - \sigma_{yy} = 0$ or 1 MPa in Fig. 40(b)), the martensite reorientations between V1 and V2 are complete so that the maximum reversible strain of 5.8% ($= \varepsilon_0$) is obtained. When $|\sigma_{xx} - \sigma_{yy}|$ is medium (e.g., $\sigma_{xx} - \sigma_{yy} = 1.7$ MPa in Fig. 40(b)), martensite reorientations are incomplete due to hardening effects (interaction parameter $k > 0$). So a smaller reversible strain (< ε_0) is obtained. When $|\sigma_{xx} - \sigma_{yy}|$ is large (e.g., $\sigma_{xx} - \sigma_{yy} = 3$ MPa in Fig. 40(b)), martensite reorientation is blocked and no strain change is observed.

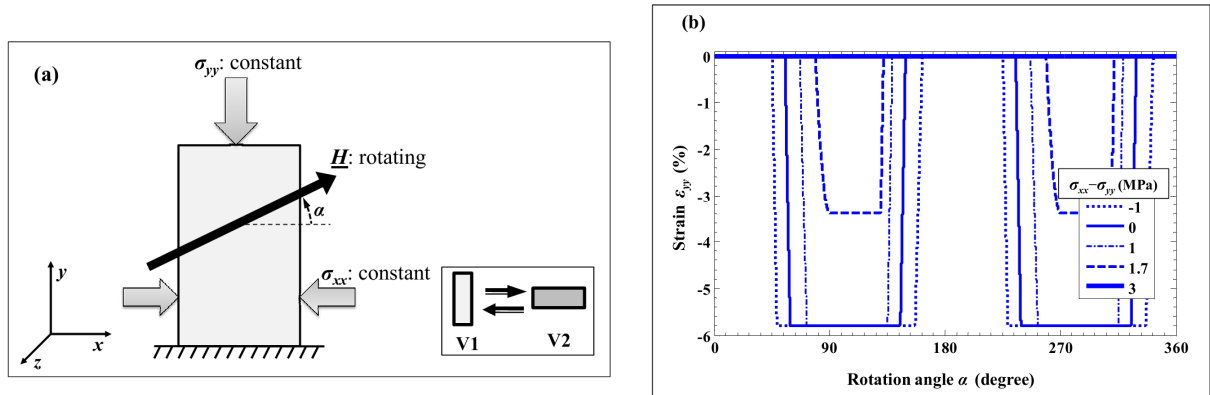


Fig. 40. (a) FSMA in a rotating magnetic field H and constant biaxial compressions σ_{xx} and σ_{yy} . (b) Model predictions of rotating-field-induced strain ε_{yy} at various levels of stress difference ($\sigma_{xx} - \sigma_{yy}$).

4.3.3. Super-elasticity under biaxial compressions

Before discussing the simulation results for biaxial compressions, we first report our recent 2D compression tests (for comparison with simulations) since all of the existing experiments on FSMA are done in 1D configurations (i.e., a magnetic field with a uniaxial stress of a few MPa). Our 2D compression tests in this sub-section aim to explore the possibility of using FSMA in multi-axial stresses of high levels. Fig. 41(a) shows the schematic diagram of the

experimental setup: the material in the initial state of martensite variant 1 is under a constant compressive stress σ_{xx} along x -coordinate and a varying compressive stress σ_{yy} along y -coordinate. Variant 1 switches to variant 2 during the loading of σ_{yy} , and switches back during unloading. Compressive strains are positive in this sub-section and in the following sub-section 4.3.4.

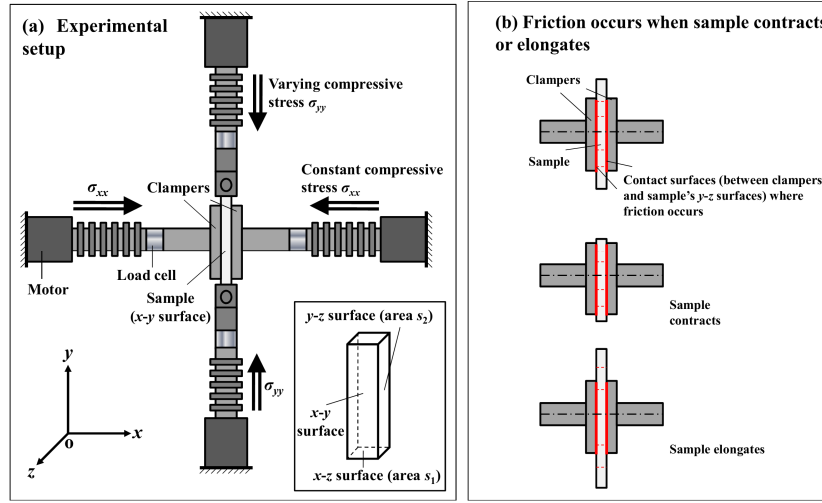


Fig. 41. (a) Schematic diagram of the experimental setup for symmetric biaxial compression tests. (b) Friction occurs on the contact surfaces between the clampers and the sample's y - z surfaces. Dotted lines are marked on the sample for reference showing the relative motion between the sample and the clampers.

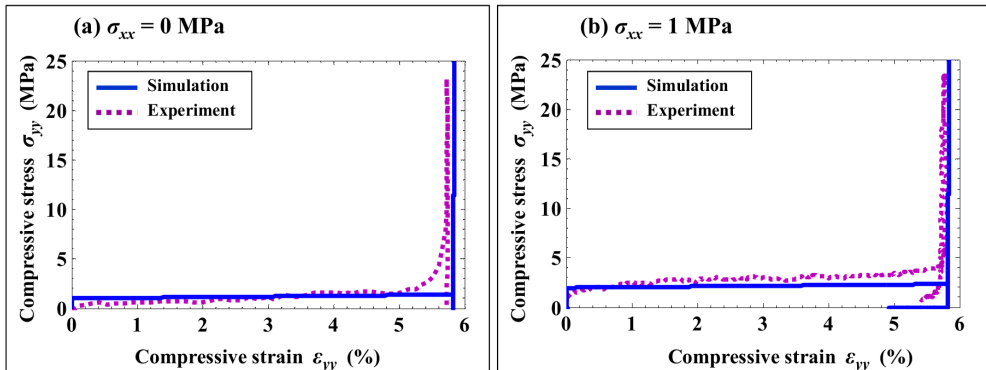
During the experiments, the sample contracts or elongates, leading to the external friction between the clampers and the sample's surfaces (see Fig. 41(b)). The effects of the external friction are removed from the nominal stress σ_{yy}^0 to get the effective stress σ_{yy} (details about the external friction can be found in Chapter 3 – sub-section 3.1.3):

$$\sigma_{yy} = \sigma_{yy}^0 - \mu \sigma_{xx} s_2 / s_1 \quad \text{during loading} \quad (122a)$$

$$\sigma_{yy} = \sigma_{yy}^0 + \mu \sigma_{xx} s_2 / s_1 \quad \text{during unloading} \quad (122b)$$

where μ is the friction coefficient (measured to be 0.095); s_1 is the cross section area of x - z surface ($1 \times 2.5 \text{ mm}^2$, see the insert of Fig. 41(a)); s_2 is the contact area of y - z surface between the sample and the clampers ($1 \times 10 \text{ mm}^2$ with the clammer length of 10 mm, see Fig. 41(a)).

Figure 42 shows four stress-strain curves (σ_{yy} - ε_{yy}) at different levels of σ_{xx} ($0 \sim 9 \text{ MPa}$). For the case of uniaxial compression test ($\sigma_{xx} = 0$ in Fig. 42(a)), after a very small elastic loading, martensite reorientation from variant 1 to variant 2 begins. During the reorientation, with compressive strain ε_{yy} increasing, the compressive stress σ_{yy} remains nearly constant (so-called stress plateau). After the reorientation, the elastic deformation of variant 2 leads to significant stress increase. During unloading (compressive stress σ_{yy} decreases to 0), only the small elastic deformation is recovered. Residual strain as large as 5.7% appears because the material is in the state of variant 2 rather than variant 1 (initial state) at the end of unloading. For biaxial compressions ($\sigma_{xx} \neq 0$ in Figs. 42(b), 42(c) and 42(d)), the residual strain decreases significantly with increasing σ_{xx} , because reverse martensite reorientation from variant 2 to variant 1 is induced during unloading. At high levels of σ_{xx} (e.g., 6.5 MPa in Fig. 42(c), 9 MPa in Fig. 42(d)), super-elasticity is obtained (zero residual strain). The biaxial compression tests show that the intrinsic dissipation and the transformation strain related to the martensite reorientation are constant in all the tested 2D stress states, which imply the possibility of using FSMA in high levels of multi-axial stresses while keeping their advantages — low intrinsic dissipation and large reversible strain (Chen et al., 2013).



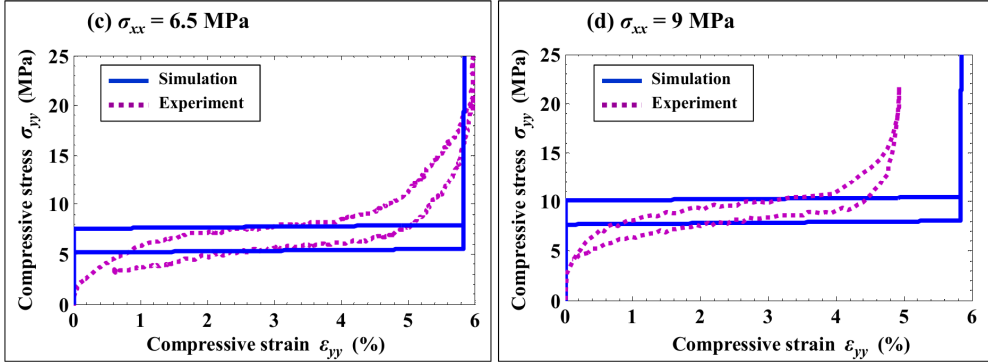


Fig. 42. Compressive stress-strain curves (σ_{yy} - ε_{yy}) at different levels of σ_{xx} : (a) $\sigma_{xx} = 0$ MPa, (b) $\sigma_{xx} = 1$ MPa, (c) $\sigma_{xx} = 6.5$ MPa, (d) $\sigma_{xx} = 9$ MPa. Simulations (solid lines) and experiments (dotted lines, after removing the effects of the external friction by Eq. (122)) are compared.

Model simulations are also shown in Fig. 42 to compare with the experiments. It is seen that the model can capture the important effects of the auxiliary stress σ_{xx} on the material's mechanical behaviors (σ_{yy} - ε_{yy} curves): super-elasticity at high σ_{xx} , and dependence of the plateau stresses on σ_{xx} . In the experiments, hardening increases with the increase of σ_{xx} . The increasing hardening is due to the fact that under biaxial stresses, the martensite reorientations are realized by the motion of many fine twin boundaries, in contrast to the motion of single or a few twin boundaries under uniaxial stress (Chen et al., 2013). Although the model assumes constant hardening (constant interaction parameter k) for all stress states, the simulated plateau stresses are close to the average plateau stresses observed in the experiments (see Figs. 42(c) and 42(d)).

4.3.4. Field-assisted super-elasticity

Besides actuators, FSMA can also be used as a sensor or voltage generator or magnetically controlled damper (e.g., Stephan et al., 2011; Suorsa et al., 2004). Fig. 43 shows a schematic diagram of the loading conditions for FSMA sensor/generator/damper: the material in the initial state of V1 is under a compressive stress σ_{yy} along y-coordinate and a constant magnetic

field H_x along x -coordinate. During the mechanical loading-unloading of σ_{yy} , martensite reorientations between V1 and V2 are induced. Comparisons between simulation predictions and experimental observations (Heczko, 2005) are shown in Fig. 44.

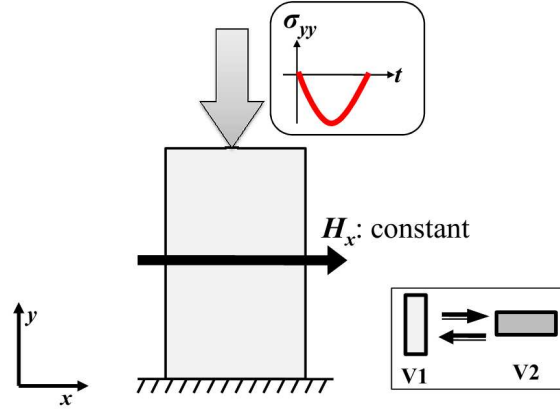


Fig. 43. FSMA used as a sensor/generator/damper. During the mechanical loading-unloading, martensite reorientations between V1 and V2 are induced.

Figure 44(a) is the stress-strain curve ($\sigma_{yy}-\varepsilon_{yy}$) of martensite reorientation under uniaxial compression σ_{yy} ($\mu_0 H_x = 0$), which is the same as Fig. 42(a). For the magnetization evolutions (Fig. 44(b)), no net magnetization is observed without the magnetic field H_x . In the moderate magnetic fields (e.g., $\mu_0 H_x = 0.4$ T), rapid magnetization changes are observed during the martensite reorientations (Fig. 44(d)), and such stress-induced magnetization change can be used for sensors or voltage generators. In the strong magnetic fields (e.g., $\mu_0 H_x = 1.1$ T), magnetization remains at the saturation level (Fig. 44(f)), because both variants arrive at saturation magnetization along the field. It is also seen that super-elasticity is obtained in the medium and strong fields (Figs. 44(c) and 44(e)). The intrinsic dissipation in the hysteresis loop of the stress-strain curves can be used for dampers.

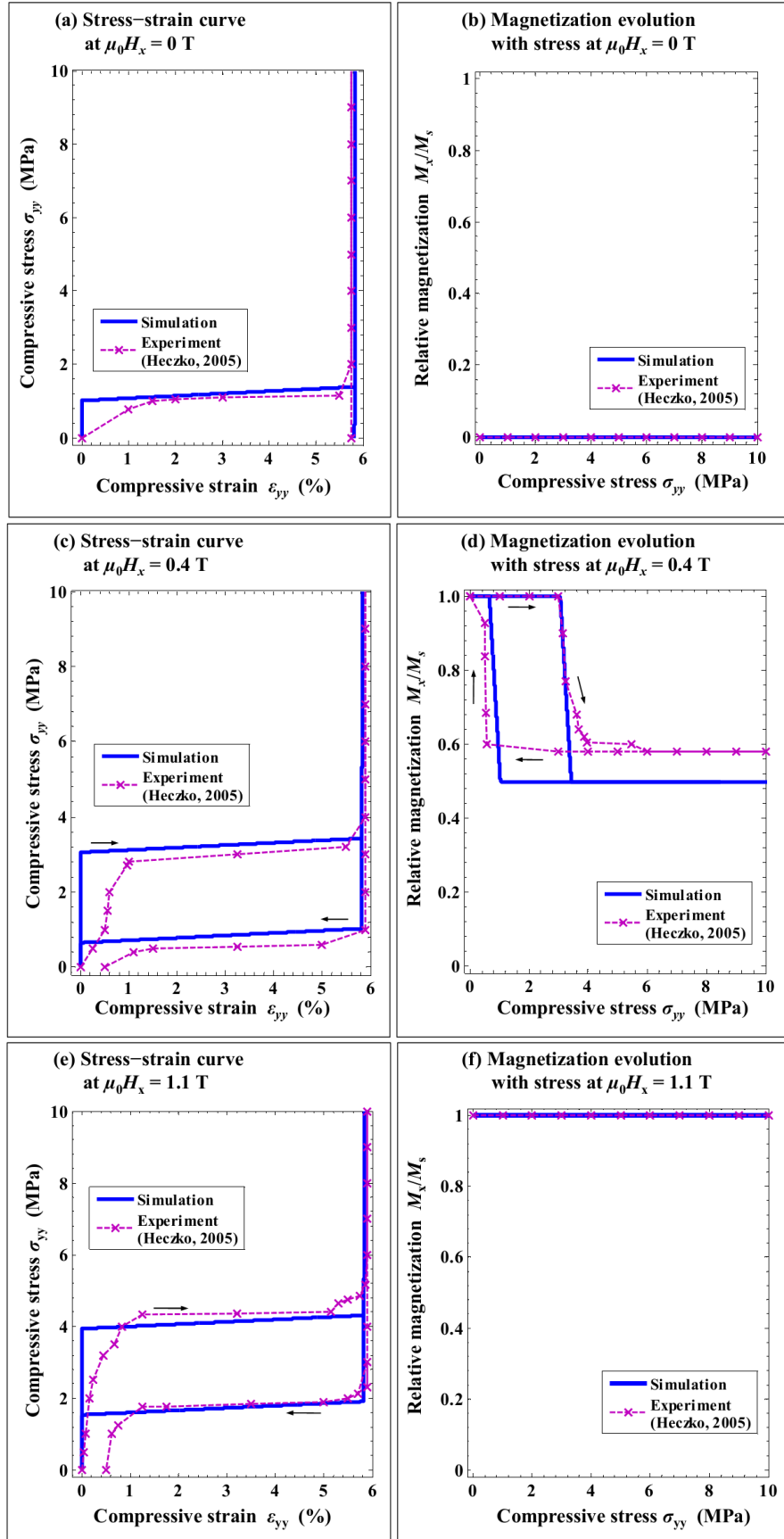


Fig. 44. Comparison between simulations and experiments (Heczko, 2005) of the material's magneto-mechanical responses at different levels of magnetic field $\mu_0 H_x$: (a) and (b) for $\mu_0 H_x = 0$ T, (c) and (d)

for $\mu_0 H_x = 0.4$ T, (e) and (f) for $\mu_0 H_x = 1.1$ T. Figures on the left-hand side are stress–strain curves (σ_{yy} – ε_{yy}) and those on the right-hand side represent the magnetization evolution with the applied stress σ_{yy} .

Comparing Figs. 44(a), 44(c) and 44(e), it is seen that the stress plateaus for forward and reverse martensite reorientations increase with increasing H_x . The effect of H_x on the material’s mechanical behaviors (σ_{yy} – ε_{yy} curves) is similar to that of σ_{xx} in the case of biaxial compressions (see sub-section 4.3.3). In fact, we can calculate the equivalent stress of H_x (so-called magneto-stress $\sigma_{mag}(H_x)$) by the increase of the plateau stress in the magnetic field (shown in Fig. 45(a)). The model well predicts the dependence of σ_{mag} on H_x : σ_{mag} increases with increasing H_x and saturates at a certain level where both variants reach the saturation magnetization (Fig. 45(b)).

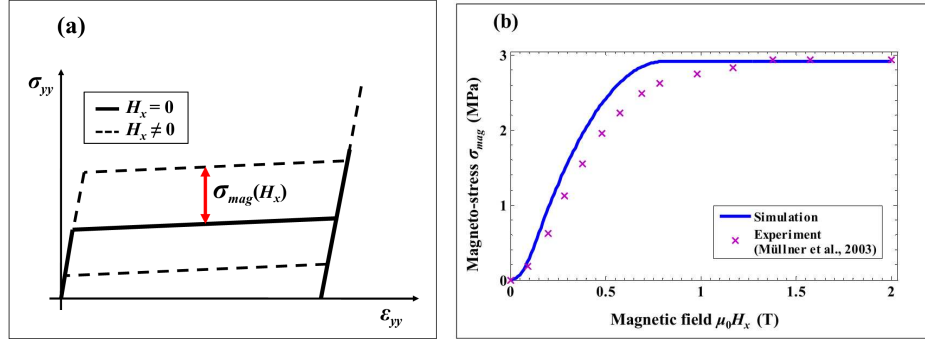


Fig. 45. (a) Illustration of the magneto-stress $\sigma_{mag}(H_x)$. (b) Magneto-stress σ_{mag} obtained from simulations and experiments (Müllner et al., 2003).

The model quantitatively predicts the characteristic features of the material’s behaviors in the experiments: hysteresis, magneto-stress evolutions, magnetization change in moderate magnetic fields, super-elasticity in strong magnetic fields, etc.

4.3.5. Thermo-magneto-mechanical behaviors of ferromagnetic shape memory alloys

Several parameters (i.e., ε_0 , σ_{tw} , M_s , K_u) governing the material's behaviors are temperature dependent (Glavatska et al., 2002; Heczko and Straka, 2003; Heczko and Ullakko, 2001; Jiang et al., 2005; Okamoto et al., 2006; Straka and Heczko, 2003b; Straka et al., 2006, 2011a). Although the temperature-dependence of these parameters are generally non-linear in a wide temperature range, the material's working temperature range is not large, i.e., around 10 K ~ 120 K below the martensitic transformation temperature, where the field-induced martensite reorientation exists (O'Handley et al., 2006). In this regard, we can make linear approximations for a rough estimation of the material parameters in the working temperature range:

$$\varepsilon_0(T) = c_1 T + c_2 \quad (123a)$$

$$\sigma_{tw}(T) = c_3 T + c_4 \quad (123b)$$

$$M_s(T) = c_5 T + c_6 \quad (123c)$$

$$K_u(T) = c_7 T + c_8 \quad (123d)$$

where the coefficients c_i ($i = 1, 2, \dots, 8$) can be determined from experiments. By fitting the experimental results of ε_0 , σ_{tw} , M_s and K_u at different temperatures (see Fig. 46), we can obtain:

$$\varepsilon_0(T) = -0.012T + 9.33 \quad (124a)$$

$$\sigma_{tw}(T) = -0.0093T + 3.67 \quad (124b)$$

$$M_s(T) = -960T + 840000 \quad (124c)$$

$$K_u(T) = -760T + 390000 \quad (124d)$$

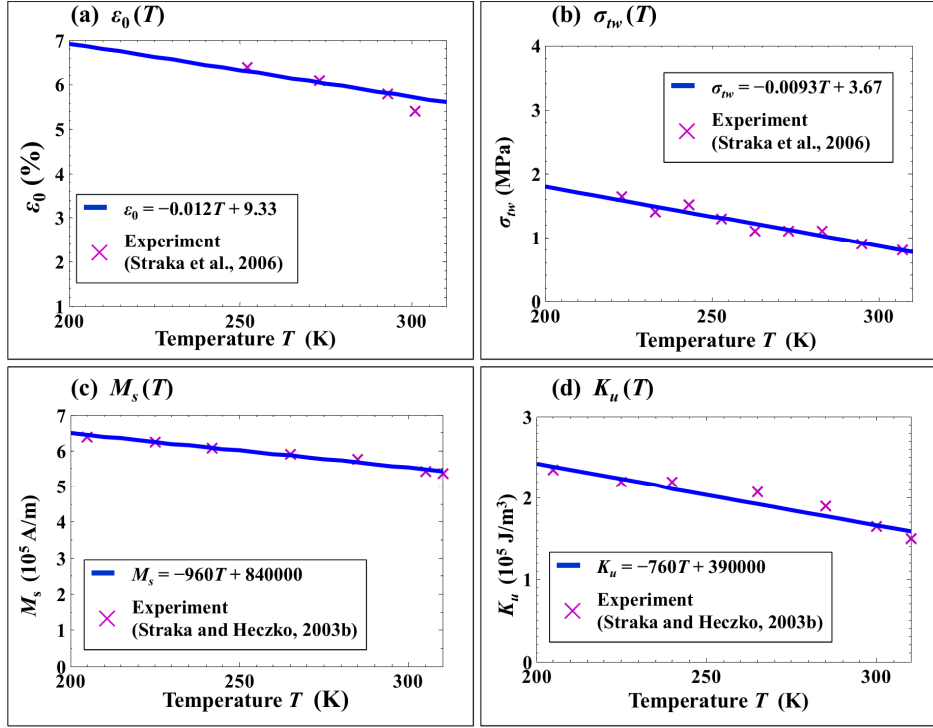
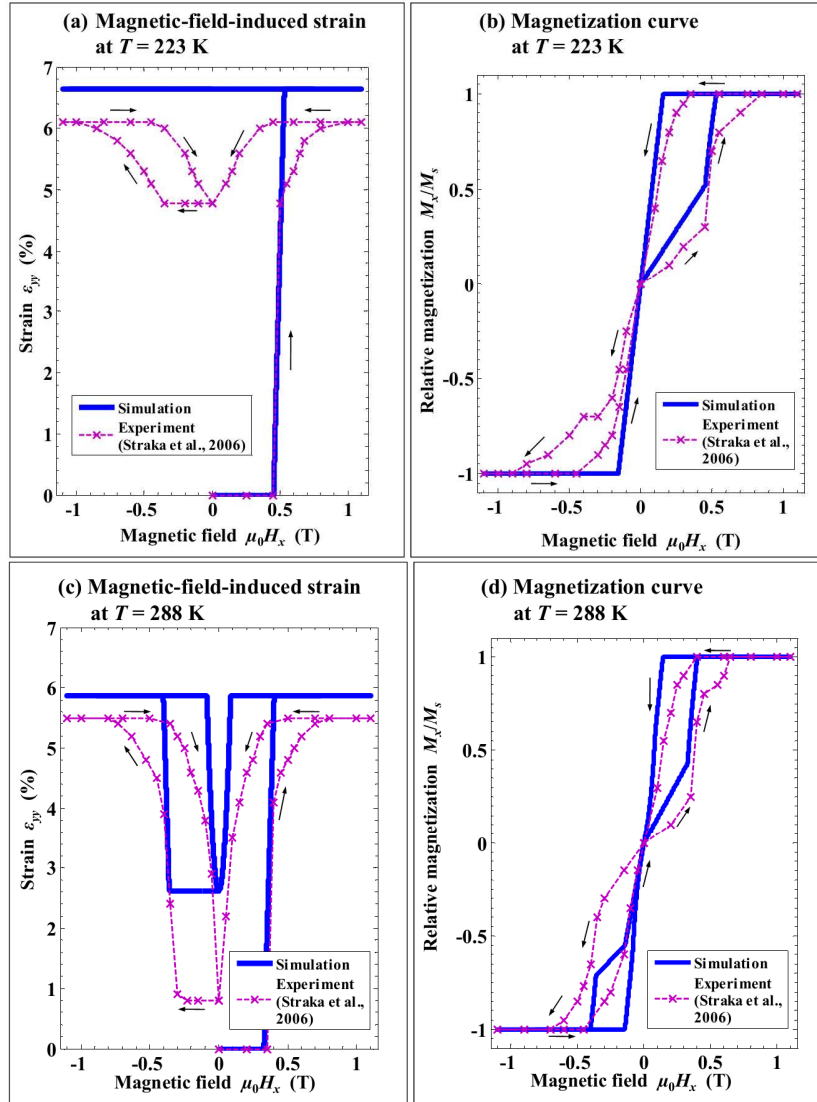


Fig. 46. Linear approximations of the temperature-dependence of the material parameters ($\varepsilon_0(T)$, $\sigma_{tw}(T)$, $M_s(T)$ and $K_u(T)$) in the working temperature range.

Equation (124) (for calculating ε_0 , σ_{tw} , M_s , K_u) and Table 3 (for other model parameters) are used in the simulations of temperature-dependent behaviors of FSMA. Model predictions of field-induced martensite reorientation under the constant compressive stress σ_{yy} of 1 MPa (see Fig. 34 for the experimental set-up) at different temperatures are compared with the experimental results in Fig. 47. It is seen from Figs. 47(a), 47(c) and 47(e) that the forward martensite reorientations during magnetic loading are complete, while the reverse martensite reorientations during unloading depend on the temperatures. At low temperatures where the applied compressive stress σ_{yy} ($= 1$ MPa) is smaller than σ_{tw} , reverse martensite reorientation cannot be induced by σ_{yy} during magnetic unloading, so no reversible strain is predicted (e.g., $T = 223$ K in Fig. 47(a)). A small reversible strain observed in the experiment is possibly due to the structural response (some stress concentration in corners or clamping end, etc.). When the temperature increases, σ_{tw} decreases (see Fig. 46(b)), leading to partial reverse martensite reorientation (e.g., $\sigma_{tw} \approx 1$ MPa at $T = 288$ K in Fig. 47(c)). Complete reverse martensite

reorientation is obtained at higher temperatures where $\sigma_{tw} < 1$ MPa (e.g., $T = 307$ K in Fig. 47(e)).



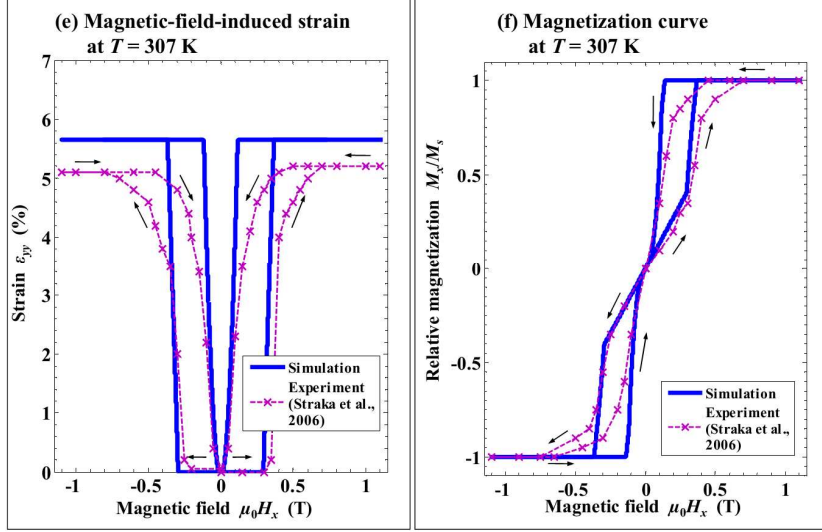


Fig. 47. Material's magneto-mechanical behaviors at different temperatures T : (a) and (b) for $T = 223$ K, (c) and (d) for $T = 288$ K, (e) and (f) for $T = 307$ K. Figures on the left-hand side represent the magnetic-field-induced strain and those on the right-hand side are the magnetization curves.

In the previous case, σ_{yy} is small, so the magnetic field can conquer σ_{yy} and σ_{tw} to induce the complete forward martensite reorientation in the working temperature range. In another case where σ_{yy} is relatively large (e.g., $\sigma_{yy} = 1.9$ MPa $> \sigma_{tw}(T)$ in Fig. 48), the reverse martensite reorientation (induced by σ_{yy} during magnetic unloading) is complete, while the forward martensite reorientation (induced by the magnetic field during magnetic loading) depends on the temperatures. At low temperatures, martensite reorientation is totally blocked because σ_{tw} is too large for the magnetic field to induce martensite reorientation (e.g., $T = 220$ K in Fig. 48). With the temperature increase, σ_{tw} decreases and the forward martensite reorientation is induced, so more and more strain is observed (see the magnetic-field-induced strain at $T = 250$ K, 280 K and 310 K in Fig. 48).

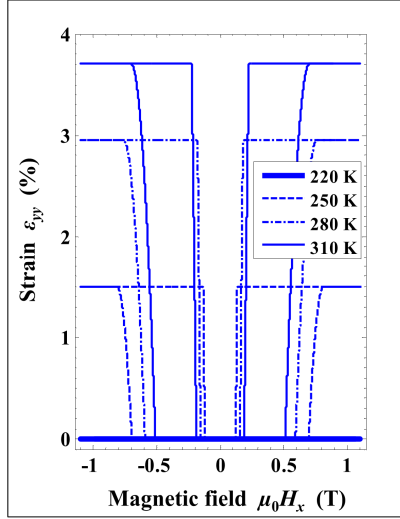


Fig. 48. Model predictions of magnetic-field-induced strain under the constant compressive stress of 1.9 MPa at different temperatures.

In quasi-static loadings (the frequency of the magnetic field is low), temperature variation is negligible. However, in dynamic loadings (the frequency of the magnetic field is larger than 100 Hz), temperature variation in the material can be important due to the mechanical intrinsic dissipation and the heat from eddy current: Henry (2002) analytically calculated a temperature increase of 13 K in 5 s in the magnetic field of 500 Hz; Lai (2009) observed, in the magnetic field of 400 Hz, a temperature increase of 7 K in 35 s and this increase was not saturated. The temperature increase of the material in dynamic loadings will influence its behaviors. Take an example of a dynamic test in the magnetic field of 500 Hz with the predicted temperature increase of 13 K in 5 s by (Henry, 2002): At the beginning, the material's behavior is similar to that in Fig. 47(c). After 10 seconds, the temperature can rise to 307 K and the material's behavior can change to Fig. 47(e). After another 10 seconds, there can be no strain change due to the martensite reorientation, because the temperature is higher than the austenite finish temperature. A rough estimation of the evolutions of the material's response is shown in Fig. 49. Therefore, temperature effects should be taken into account in

high frequency dynamic analysis. In this case, the constitutive model with temperature effects can be extended for the dynamic problems of thermo-magneto-mechanical coupling.

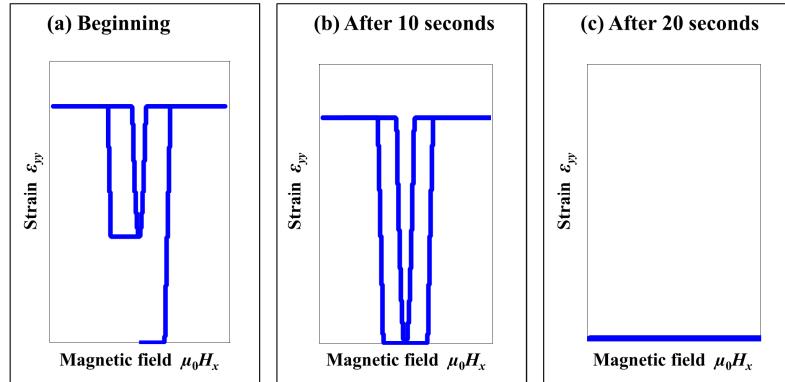


Fig. 49. Rough estimations of the magnetic-field-induced strain under high-frequency dynamic loading. (a) Beginning. (b) After 10 seconds the material's temperature rises. (c) After 20 seconds the temperature is so high that the material is in the austenitic phase.

4.4. Structural analysis of ferromagnetic shape memory beams

In literature, besides the linear FSMA actuators and sensors, some FSMA bending actuators and dampers have also been proposed (e.g., Kohl et al., 2004, 2007; Zeng et al., 2010). To predict the nonlinear bending behaviors of FSMA beams, our 3D constitutive model is incorporated into finite element analysis in this section. The simulated beam is fixed at one end (no displacement or rotation) and a vertical force ($F_y = 0.1$ N) is applied at another end (see Fig. 50). Structural calculations are done using the finite element code Cast3M with the model parameters in Table 3 and simulation algorithm in Table 4.

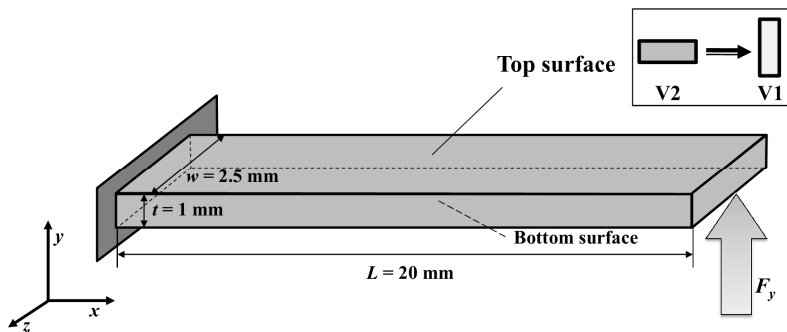


Fig. 50. Clamped FSMA beam for numerical analysis of bending behaviors.

Table 4. Algorithm of structural calculations.

Initialization of model parameters

Initialization of structure state

Input: applied force \underline{F}

Output: displacement field \underline{u}

Start:

Equally divide the mechanical loading path into N steps ($\Delta \underline{F}$)

Initialize the step: $n = 1$.

While $n < N + 1$:

$$1. \underline{F}^{(n)} = \underline{F}^{(n-1)} + \Delta \underline{F}.$$

2. Initialization of the iteration:

- Set iteration number $l = 1$.

$$\blacksquare \underline{\underline{\varepsilon}}^{(n)(l=0)} = \underline{\underline{\varepsilon}}^{(n-1)}; \quad z_{ij}^{(n)(l=0)} = z_{ij}^{(n-1)} \quad ((i,j)=(1,2), (2,3), (3,1)); \quad z_i^{(n)(l=0)} = z_i^{(n-1)} \quad (i = 1, 2, 3).$$

3. With applied force $\underline{F}^{(n)}$ and $z_{12}^{(n)(l-1)}, z_{23}^{(n)(l-1)}, z_{31}^{(n)(l-1)}$, compute the displacement field $\underline{u}^{(n)(l)}$:

- Solve the governing equation with boundary condition considered in the finite element formulation for the nodal displacement $\{u\}$, and the nodal traction $\{T\}$ on the surface of imposed displacement:

$$\begin{bmatrix} [K] & -[G] \\ {}'[G] & 0 \end{bmatrix} \begin{Bmatrix} \{u\} \\ \{T\} \end{Bmatrix} = \begin{Bmatrix} \{F^n\} + \{ZZ(z_{12}^{(n)(l-1)}, z_{23}^{(n)(l-1)}, z_{31}^{(n)(l-1)})\} \\ \{u^*\} \end{Bmatrix}$$

where $[K]$ is the stiffness matrix; $[G]$ is the localization matrix related to the boundary condition of imposed displacement (Bonnet and Frangi, 2006); $\{F^n\}$ is the applied nodal force; $\{ZZ\}$ is the supplementary effort related to the volume-fraction transformations between the variants; $\{u^*\}$ is the imposed nodal displacement. The detailed presentations of the finite element formulations are given in Appendix B.

- Calculate the displacement field $\underline{u}^{(n)(l)}$ by displacement discretization:

$$\underline{u}^{(n)(l)} = [N]\{u\}$$

where $[N]$ is a matrix composed of the shape functions related to all the nodes in the structure (see Appendix B.3).

4. Compute the strain field with small strain approximation: $\underline{\underline{\varepsilon}}^{(n)(l)} = \frac{1}{2}(\nabla \underline{u}^{(n)(l)} + {}' \nabla \underline{u}^{(n)(l)})$.

5. Compute the stress field by elastic loading increase: $\underline{\underline{\sigma}}^{(n)(l)} = \underline{\underline{\sigma}}^{(n)(l-1)} + \underline{\underline{C}} : (\underline{\underline{\varepsilon}}^{(n)(l)} - \underline{\underline{\varepsilon}}^{(n)(l-1)})$,

where $\underline{\underline{C}}$ is the elastic stiffness tensor of the FSMA martensite.

6. Compute the thermodynamic forces $A_{ij}^{(n)(l)}$ ($(i,j)=(1,2), (2,3), (3,1)$) by Eqs. (108).

7. Detection of martensite reorientations:

- If $A_{ij}^{(n)(l)} > \sigma_{tw}\varepsilon_0$, $z_i^{(n)(l-1)} > 0$ and $z_j^{(n)(l-1)} < 1$, then martensite reorientation between variant i and j .
- If $A_{ij}^{(n)(l-1)} < -\sigma_{tw}\varepsilon_0$, $z_i^{(n)(l-1)} < 1$ and $z_j^{(n)(l-1)} > 0$, then martensite reorientation between variant i and j .

8. ■ If there is martensite reorientation between variant i and j , then calculate the volume fraction transformation Δz_{ij} :

$$\Delta z_{ij} = -\frac{(\underline{\underline{U}}_i - \underline{\underline{U}}_j) : \underline{\underline{C}} : (\underline{\underline{\varepsilon}}^{(n)(l)} - \underline{\underline{\varepsilon}}^{(n)(l-1)})}{2k + (\underline{\underline{U}}_i - \underline{\underline{U}}_j) : \underline{\underline{C}} : (\underline{\underline{U}}_i - \underline{\underline{U}}_j)} \quad \text{where } \underline{\underline{U}}_i \text{ and } \underline{\underline{U}}_j \text{ are transformation strain tensors}$$

respectively for variant i and j (see Eq. (81) for the mathematical expressions).

- If there is no martensite reorientation between variant i and j , then $\Delta z_{ij} = 0$.

9. Update the volume fractions

$$z_{12}^{(n)(l)} = z_{12}^{(n)(l-1)} + \Delta z_{12}$$

$$z_{23}^{(n)(l)} = z_{23}^{(n)(l-1)} + \Delta z_{23}$$

$$z_{31}^{(n)(l)} = z_{31}^{(n)(l-1)} + \Delta z_{31}$$

$$z_1^{(n)(l)} = z_1^{(n)(l-1)} - \Delta z_{12} + \Delta z_{31}$$

$$z_2^{(n)(l)} = z_2^{(n)(l-1)} - \Delta z_{23} + \Delta z_{12}$$

$$z_3^{(n)(l)} = z_3^{(n)(l-1)} - \Delta z_{31} + \Delta z_{23}$$

10. Check the governing equation with the updated $z_{12}^{(n)(l)}$, $z_{23}^{(n)(l)}$, $z_{31}^{(n)(l)}$:

$$[K]\{u\} - [G]\{T\} = \{F^n\} + \{ZZ(z_{12}^{(n)(l)}, z_{23}^{(n)(l)}, z_{31}^{(n)(l)})\}$$

- If the governing equation stands within the defined tolerance, then the iteration stops:

Update the results of the structural calculations for the current loading step n and then go to

11.

$$\underline{\underline{u}}^{(n)} = \underline{\underline{u}}^{(n)(l)}; \quad \underline{\underline{\varepsilon}}^{(n)} = \underline{\underline{\varepsilon}}^{(n)(l)}; \quad z_{ij}^{(n)} = z_{ij}^{(n)(l)} \quad ((i, j) = (1, 2), (2, 3), (3, 1)); \quad z_i^{(n)} = z_i^{(n)(l)} \quad (i = 1, 2, 3).$$

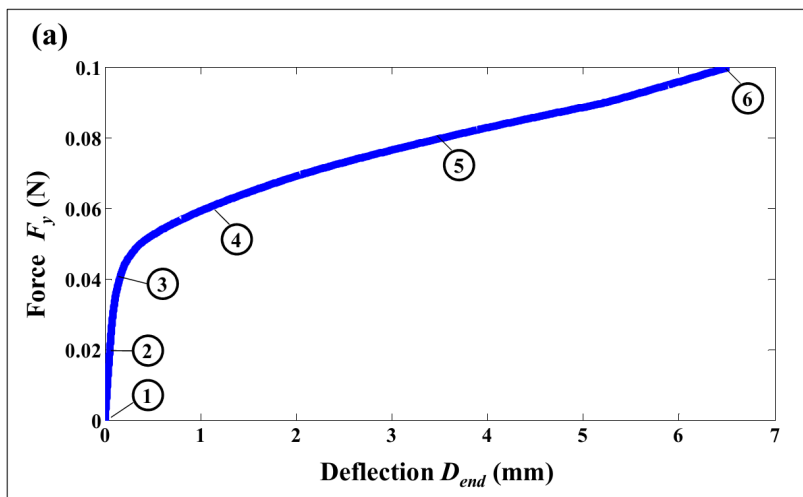
- If the equation does not stand, continue the iteration: $l = l+1$, go back to 3.

11. Increase the counter for the structural calculations of the next loading step: $n+1$.

End.

4.4.1. Simulation results

The material is assumed to be in the initial state of V2 with short axis along y-coordinate. The application of the force F_y (see Fig. 50) introduces a compression (along x-coordinate) on the top surface of the FSMA beam and a traction (along x-coordinate) on its bottom surface. As a result, variant switching from V2 to V1 (with short axis along x-coordinate) is induced by the compression on the top surface, while no variant switching happens on the bottom surface. Fig. 51 shows the simulated force-deflection curve with typical deformed shapes of the FSMA beam and the variants' distributions at different levels of F_y ($0 \sim 0.1$ N). It is seen that after an initial elastic loading ($\textcircled{1} \rightarrow \textcircled{2}$: $F_y = 0 \sim 0.02$ N), martensite reorientation from V2 to V1 takes place (see the variants' distributions in Figs. 51(c) and 51(d) at $F_y = 0.04$ N ($\textcircled{3}$), 0.06 N ($\textcircled{4}$), 0.08 N ($\textcircled{5}$) and 0.1 N ($\textcircled{6}$)). During the reorientation, deflection increases significantly while the force F_y increases slowly (so-called force plateau, see the section $\textcircled{4} \rightarrow \textcircled{6}$ in Fig. 51(a)). The deformed FSMA beam (Fig. 51(b)) and the corresponding variants' distributions (Figs. 51(c) and 51(d)) demonstrate that the large deflection in the FSMA beam is due to the FSMA martensite reorientation.



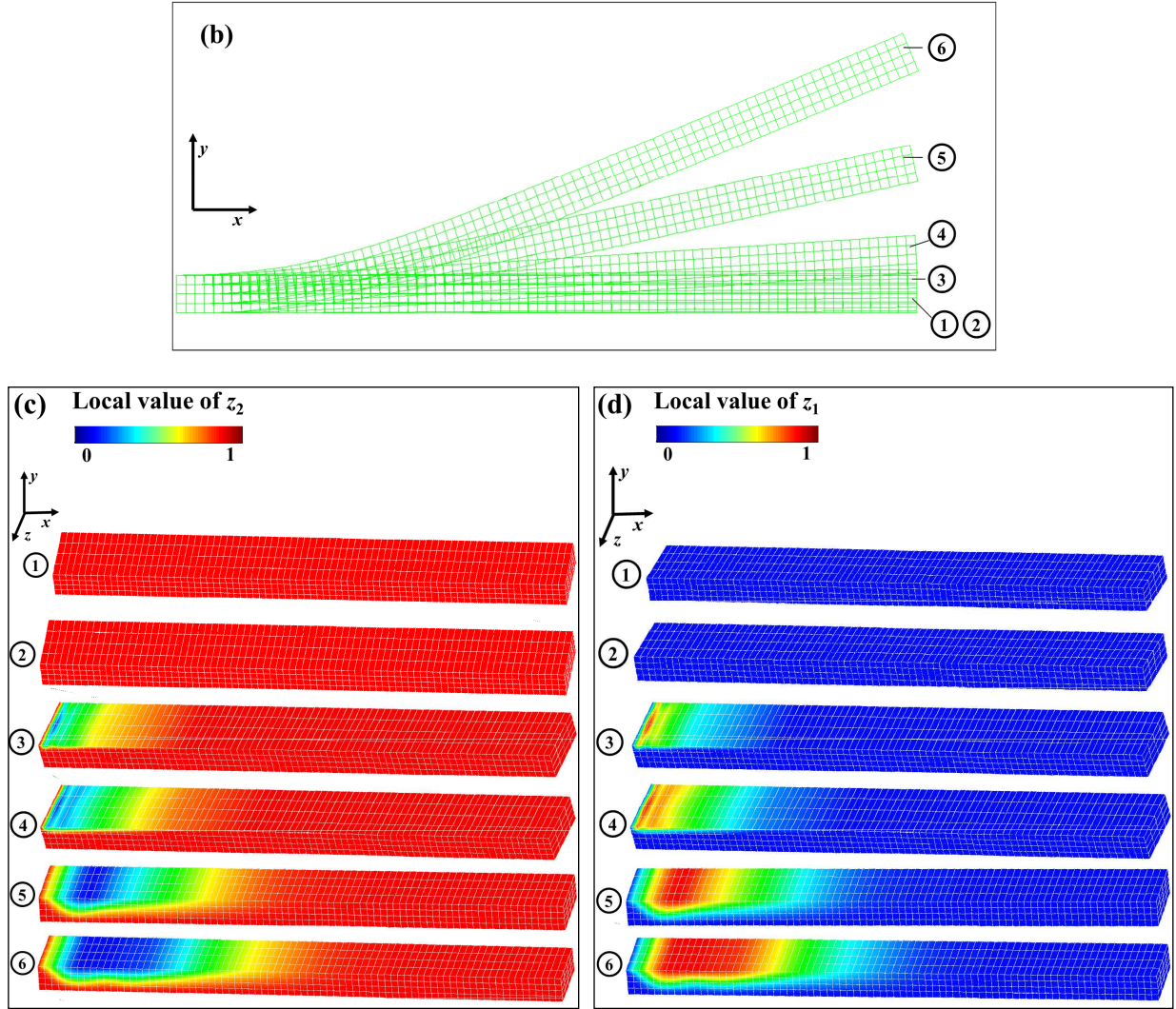


Fig. 51. (a) Force–deflection curve of FSMA beam. D_{end} is the deflection at the free end of the beam. (b), (c) and (d) respectively show the evolutions of the deformed FSMA beam and the volume-fraction distributions for V2 (z_2) and V1 (z_1).

4.4.2. Specimen-geometry effect on bending deflection

To study the specimen-geometry effect on the deflection D_{end} (deflection at the free end of the beam), simulations are done for the beams with different cross sections. The thickness of the cross section is denoted by t (along the same direction as the applied force F_y) and the width is denoted by w (see Fig. 50). Both t and w are varied while the second moment of area

I_z ($= \frac{1}{12}t^3w$) is kept constant so that all the simulated beams have the same elastic response

(i.e., if the beams are elastic without martensite reorientation, they will give the same deflection). Thus, the simulated deflection difference is only related to the geometry effect on FSMA martensite reorientation. The constant I_z is given by the cross section $t = 1 \text{ mm}$ and $w = 2.5 \text{ mm}$ (dimensions of the FSMA samples provided by Adaptamat Ltd. is usually $1 \times 2.5 \times 20 \text{ mm}^3$). Since $I_z (= \frac{1}{12}t^3w)$ is constant in the simulations, only one of t and w is independent. Here, t is chosen as the independent variable to plot the geometric effect on D_{end} (at $F_y = 0.1 \text{ N}$) in Fig. 52.

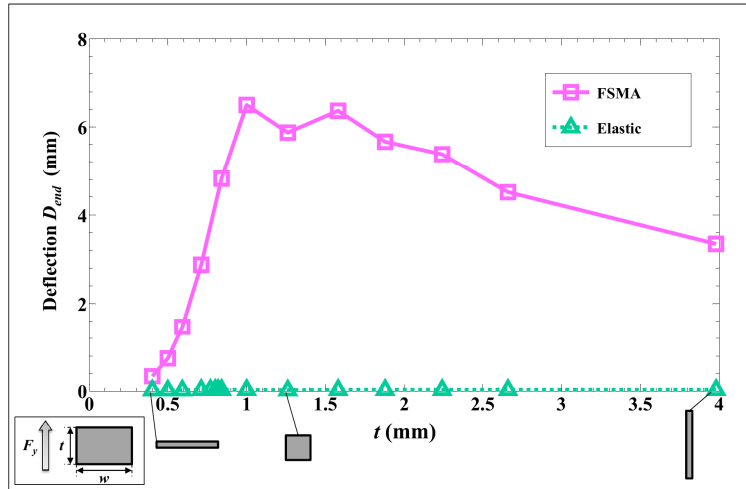


Fig. 52. Geometric effect on deflection D_{end} . The responses of the elastic beams (represented by triangles) without martensite reorientations (i.e., fixed $z_2 = 1$, $z_1=z_3=0$) are shown for reference here.

Contrary to the common sense that a thicker beam (with a larger thickness t) will give a smaller deflection, the deflection D_{end} of the FSMA beam shows a non-monotonic variation with the thickness t : when t increases, D_{end} first increases to a maximum value, and then decreases (see Fig. 52). From Euler-Bernoulli beam theory, the absolute value of the compression σ_{xx} induced by the applied force F_y on the top surface of an elastic beam is:

$$\sigma_{xx}(x) = \frac{F_y \cdot t}{2I_z} (L - x) \quad (125)$$

where L is the length of the beam, x is the position along the beam (see Fig. 53).

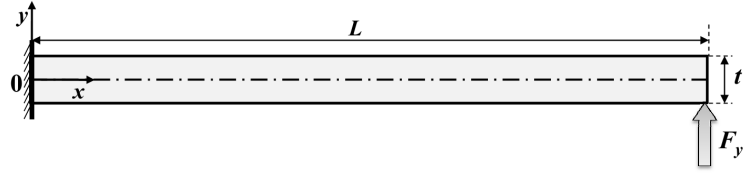


Fig. 53. Bending of an elastic beam.

From Eqs. (108a) and (112a), $\sigma_{xx}(x)$ must reach the twinning stress σ_{tw} (hardening is ignored: $k = 0$) in order to trigger the martensite reorientation from V2 to V1. Eq. (125) shows that $\sigma_{xx}(x)$ is proportional to the thickness t . So if t is small, then $\sigma_{xx}(x)$ will not be large enough (larger than σ_{tw}) to trigger martensite reorientation. For the extreme case where t is too small, even the maximum $\sigma_{xx}(x=0)$ is not large enough, then the FSMA beam will give an elastic response (see the force–deflection curve for $t = 0.4$ mm in Fig. 54). With the increase of t , $\sigma_{xx}(x)$ increases and martensite reorientation takes place in more and more parts of the beam, which leads to the significant increase of deflection in Fig. 52. A typical force–deflection curve for $t = 1$ mm is shown in Fig. 54, where the martensite reorientation can be identified by a force plateau. When the martensite reorientation is completed, the maximum strain ε_{xx}^{\max} ($= \varepsilon_0$) is reached on the top surface, so the displacement u_x ($= \varepsilon_{xx} \cdot x$) on the top surface also reaches its maximum value u_x^{\max} . For the fixed displacement u_x^{\max} on the top surface, the increase of the thickness t will reduce the slope of the beam (see a schematic diagram in Fig. 55), which leads to the decrease in deflection with further increasing t in Fig. 52. Typical force–deflection curves for $t = 2.2$ mm and 4 mm are shown in Fig. 54: the end of martensite reorientation is indicated by a significant force increase after the force plateau.

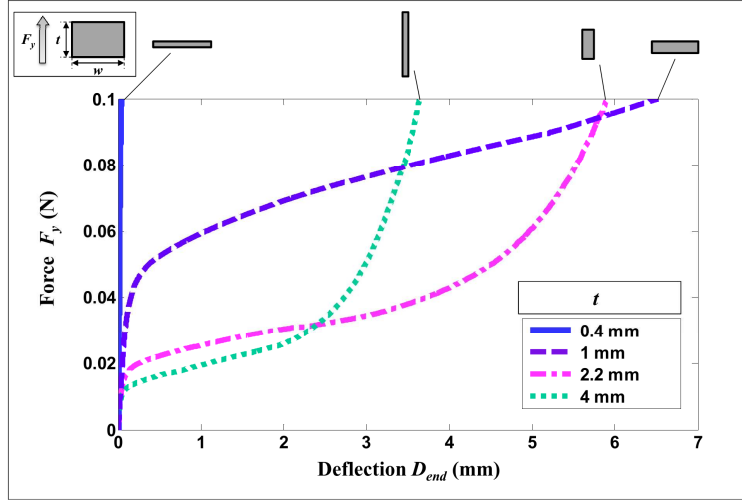


Fig. 54. Force–deflection curves at different values of the beam thickness t . The presented deflection (D_{end}) is the deflection at the free end of the beam.

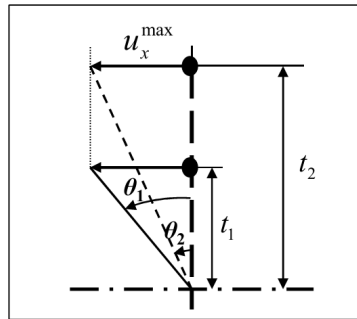


Fig. 55. Illustration showing that for a fixed displacement u_x^{\max} on the top surface of the beam, the increase in the beam thickness from t_1 to t_2 reduces the slope of the beam from θ_1 to θ_2 . Compared with the strain ε_0 (5.8%) due to martensite reorientation on the top surface of the FSMA beam, the elastic strain (around 0.001%) on the bottom surface is very small. So the neutral axis of the FSMA beam is near the bottom surface. Here for the convenience of illustration, the neutral axis is assumed to lie on the bottom surface.

4.4.3. Material anisotropic effect on bending deflection

This sub-section studies the material anisotropic effects (i.e., initial states of martensite variants in the material) on the bending behaviors of the FSMA beams. Simulations are done for the FSMA beams in the initial state of V1 or V3. For each initial state (V1 or V3), a series of cross sections are used (varied thickness t and width w with constant second moment of

area I_z ($= \frac{1}{12} t^3 w$), similar to the simulations done in sub-section 4.4.2 for the initial state of V2). The deflection D_{end} at different thickness of t for the initial states of V1, V2 and V3 are compared in Fig. 56.

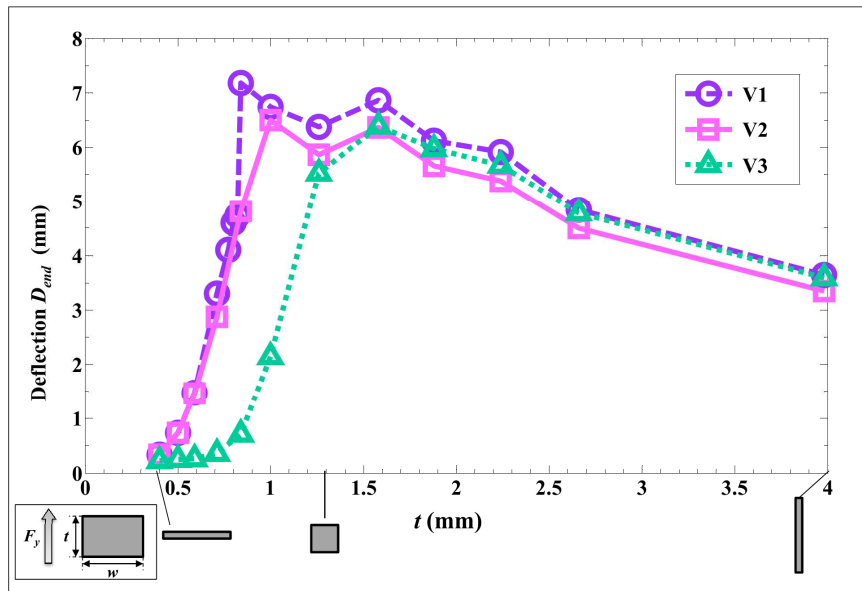


Fig. 56. Geometric effect on deflection D_{end} for the FSMA beams in the initial states of martensite variant 1(V1), variant 2 (V2) and variant 3 (V3).

It is seen from Fig. 56 that the behaviors of the FSMA beams in the initial state of V3 are different from those in the initial states of V1 and V2: When the thickness t is small (< 1 mm), the bending deflections of the FSMA beams in the initial state of V3 are much smaller than those in V1 and V2. For the FSMA beam in the initial state of V3, the V3 \rightarrow V1 switching is induced on the top surface of the beam by the compression σ_{xx} , while on the bottom surface the material responses elastically to the tension along x -coordinate, i.e., it is expanded in x direction and compressed in y and z directions (see Fig. 57(a)). The shrinkage of the bottom surface along z -coordinate introduces a compression σ_{zz} on the top surface (see a schematic diagram in Fig. 57(b))). σ_{zz} energetically prefers V3 and hinders V3 \rightarrow V1 switching. Therefore, compared with the FSMA beams in the initial states of V1 and V2, the FSMA beam in the

initial state of V3 has less martensite reorientation, leading to smaller deflection. Experiments on damping behaviors of FSMA beams (with thickness $t = 1.1$ mm) show the same material anisotropic effects: the FSMA beams in the initial of V1 and V2 have much larger loss factors than the FSMA beam in the initial state of V3, because the latter one has less martensite reorientation (Zeng et al., 2010). σ_{xx} is proportional to the beam thickness t (see Eq. (125)), so when t is large enough (> 1.5 mm in Fig. 56), martensite reorientation induced by σ_{xx} can be completed in all the FSMA beams (with the initial state of any variant). Therefore, the same level of deflection is obtained at large t .

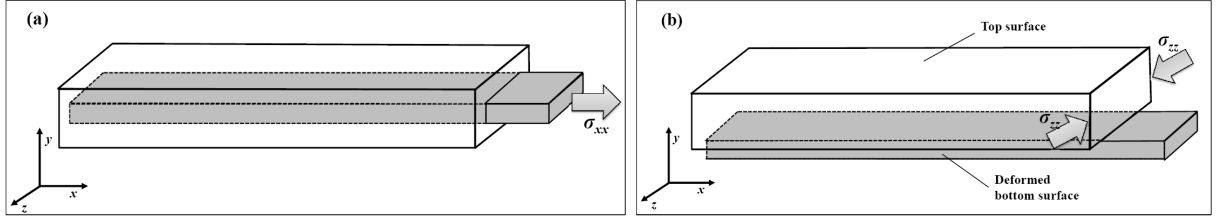


Fig. 57. (a) The bottom surface is expanded in x direction and compressed in y and z directions. The white and grey areas respectively represent the initial and the deformed shapes of the bottom surface. The deformation is exaggerated in the schematic diagram. (b) The shrinkage of the bottom surface along z -coordinate introduces a compression σ_{zz} on the top surface.

4.5. Conclusions

A 3D constitutive model of martensite reorientation in Ferromagnetic Shape Memory Alloys (FSMA) is developed within the framework of thermodynamics of irreversible processes with internal variables. Compared with the existing models, the model has the following advantages:

- (1) The model is able to quantitatively describe all the existing magneto-mechanical behaviors of FSMA: e.g., rotating/non-rotating magnetic-field-induced martensite reorientation and field-assisted super-elasticity. Moreover, experimental results of biaxial

loadings are reported, which agree well with the model simulations. The model, considering all the martensite variants and validated by 2D experiments, is ready for use in the general 3D magneto-mechanical loading conditions.

(2) Only a few internal state variables are involved in the model and the model parameters can be easily identified by simple experiments, which facilitate the practical use of the model.

(3) The temperature effect on the material's constitutive behaviors is considered in the model by taking several material properties as linear functions of temperature. In high-frequency dynamic loadings where the temperature variation of the material can be important, the model can be extended for the study of thermo-magneto-mechanical couplings.

(4) The model is incorporated into finite element analysis to predict the nonlinear bending behaviors of FSMA beams. Both the sample-geometry effect and the material anisotropic effect are systematically studied and found to be important when designing the FSMA-based bending actuators.

The behavior of a material point can be different from that of a structure due to the demagnetization effect (depending on the geometry of the sample) and the presence of the magnetic body force, body couple and surface force. In Appendix B, the finite element formulations for structural analysis are developed.

Chapter 5 General conclusion and future work

In this dissertation, we theoretically and experimentally study the martensite reorientation in Ni-Mn-Ga (5M martensite) Ferromagnetic Shape Memory Alloys (FSMA). A 2D/3D magneto-mechanical energy analysis is presented and incorporated into phase diagrams in order to study the path-dependent martensite reorientation of FSMA in general 3D loadings. The criteria and the material requirements for obtaining reversible strain in cyclic loadings are derived, which provide design guidelines for FSMA-based actuators. Furthermore, the energy analysis reveals the advantages of using FSMA in multi-axial configurations: e.g., high output stress, tunable switching field/angle where martensite reorientation takes place. To validate the predictions of energy analysis, martensite reorientation of FSMA in multi-axial loadings is experimentally studied. It is found that the intrinsic dissipation and the transformation strain due to martensite reorientation are constant in all tested 2D stress states. Moreover, preliminary results of 2D magneto-mechanical tests show that the output stress of FSMA can be increased by the increase of the auxiliary stress. All these findings imply the possibility of using FSMA in multi-axial loading conditions. In order to predict the magneto-mechanical behaviors of FSMA in 3D loadings, a constitutive model is developed within the framework of thermodynamics of irreversible processes. All the three tetragonal martensite variants are considered in the model and the temperature effects on martensite reorientation are also taken into account. The model is further incorporated into finite element analysis to study the non-linear bending behaviors of FSMA beams. The sample-geometry effect and the material anisotropic effect are found to be important for designing the FSMA-based bending actuators. The proposed 3D constitutive model, validated by the existing 1D and 2D experiments, is

ready for practical use in analyzing the material's behaviors in general multi-axial magneto-mechanical loadings.

The work will be continued with multi-axial experimental studies on FSMA containing Type II twin. Furthermore, experiments have shown that the deformation of FSMA during martensite reorientation is inhomogeneous (see the DIC images of strain localization in Fig. 23). However, the constitutive model developed in this dissertation is just for describing the macroscopic behaviors of FSMA. New model will be developed to study the material instability and to simulate the strain pattern evolutions during martensite reorientation.

Appendix A. Supplementary document for multi-axial experiments on ferromagnetic shape memory alloys

-
- A.1. Biaxial compression tests 154
 - A.2. Biaxial magneto-mechanical tests 156
-

A.1. Biaxial compression tests

The photos of the experimental setup are shown in Fig. A.1. Fig. A.2 shows the nominal stress–strain curves (σ_{yy} – ε_{yy}) at different levels of σ_{xx} (0 ~ 9 MPa).

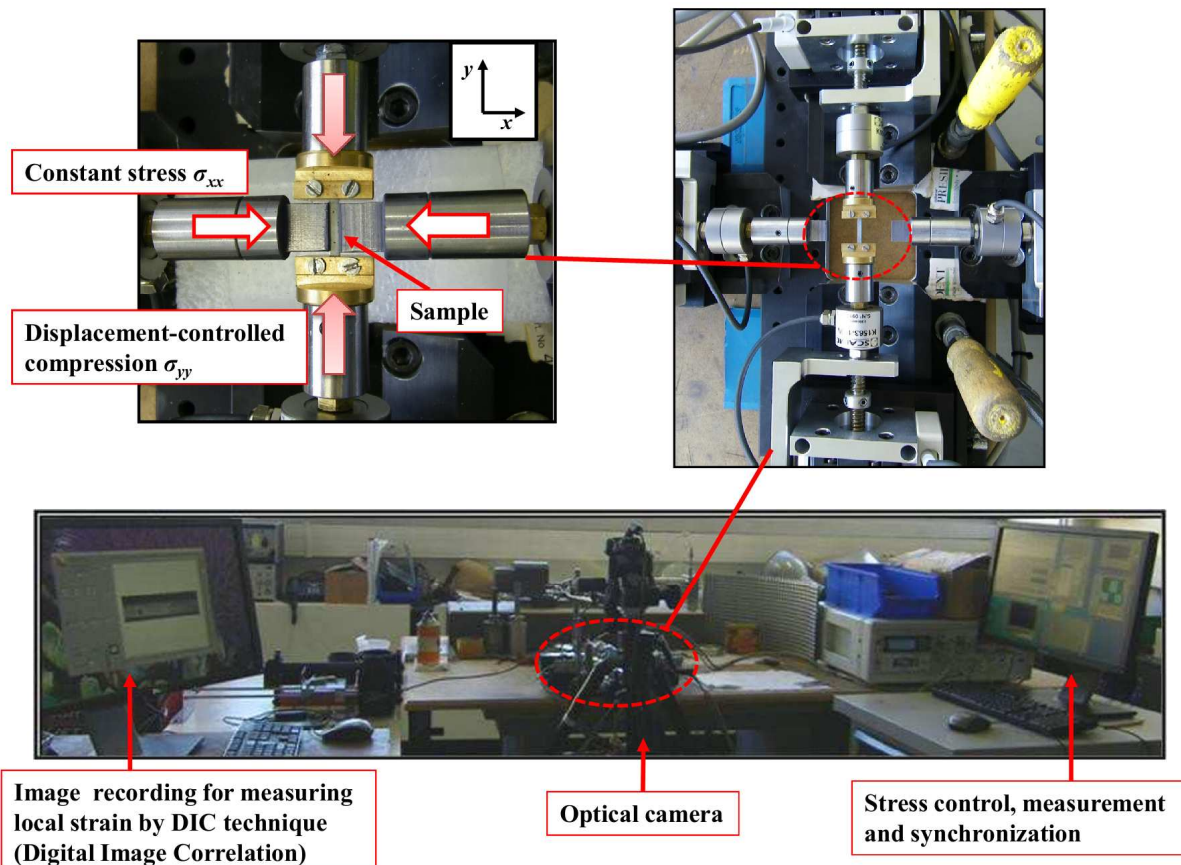


Fig. A.1. Photos of the experimental setup for symmetric biaxial compression tests.

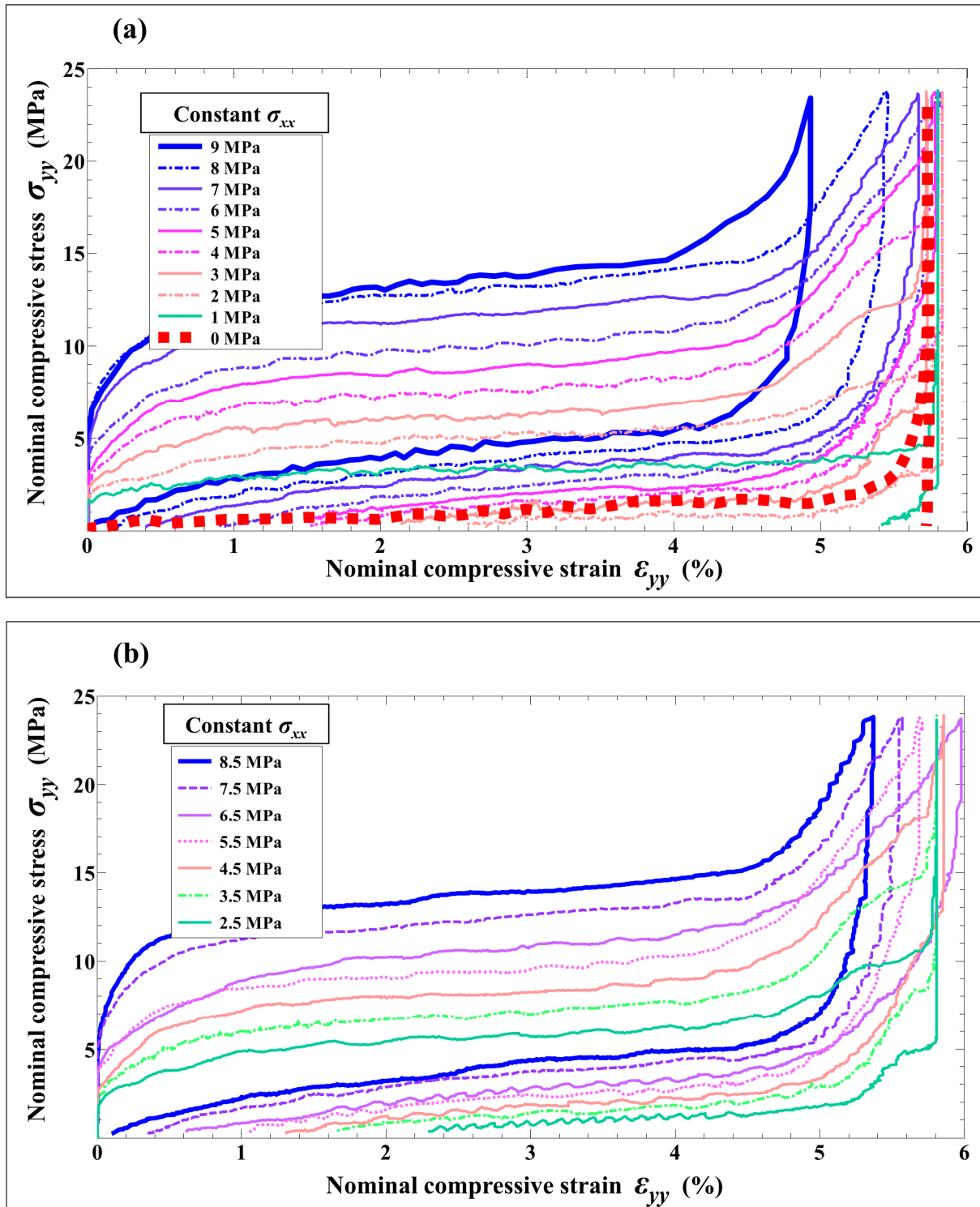


Fig. A.2. Nominal stress–strain curves (σ_{yy} – ε_{yy}) at different levels of σ_{xx} (0 ~ 9 MPa).

A.2. Biaxial magneto-mechanical tests

The photos of the experimental setup are shown in Fig. A.3.

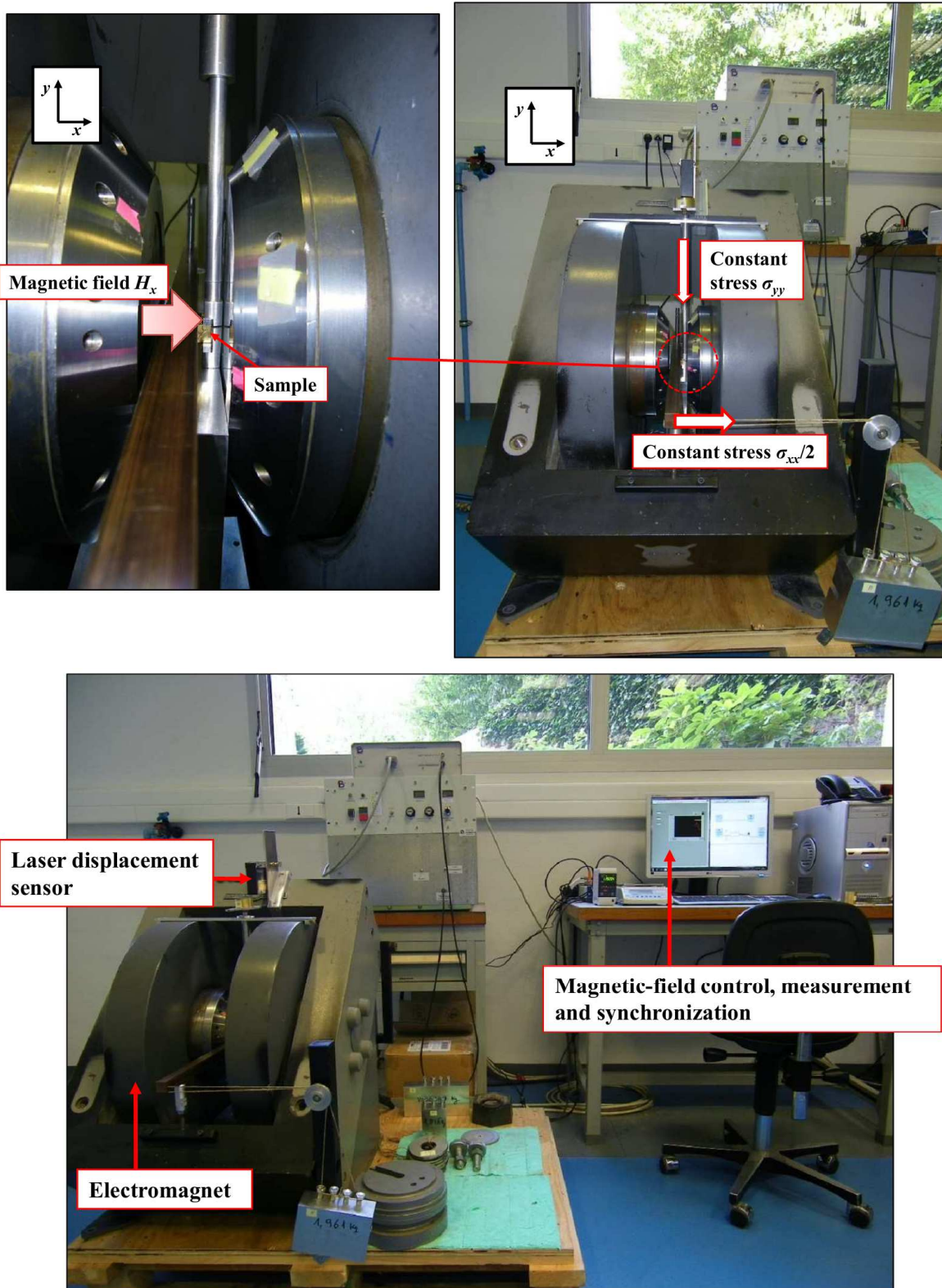


Fig. A.3. Photos of 2D magneto-mechanical setup.

Appendix B. Finite element formulation for magneto-mechanical analysis of Ferromagnetic Shape Memory Alloys (FSMA)

B.1. Governing equations and boundary conditions for general magneto-mechanical analysis	157
B.1.1. Magnetic part	157
B.1.2. Mechanical part	159
B.1.3. Summary of fully coupled dynamic magneto-mechanical analysis	161
B.2. Weak form formulations	162
B.2.1. Magnetic part	164
B.2.2. Mechanical part	164
B.3. Finite element formulations	165
B.3.1. Magnetic part	165
B.3.2. Mechanical part	168
B.4. Summary	171

B.1. Governing equations and boundary conditions for general magneto-mechanical analysis

B.1.1. Magnetic part

The total Maxwell's equations are composed of four laws: Gauss' law, Gauss-Faraday law, Ampère's law and Faraday's law. In the stationary frame, their global forms are:

$$\oint_{\partial\Omega} \underline{D} \cdot \underline{n} \, ds = \int_{\Omega} \rho_e \, d\Omega \quad (\text{B.1a})$$

$$\oint_{\partial\Omega} \underline{B} \cdot \underline{n} \, ds = 0 \quad (\text{B.1b})$$

$$\oint_L \underline{H} \cdot d\underline{l} = \int_S (\underline{J} + \frac{\partial \underline{D}}{\partial t}) \cdot \underline{n} \, ds \quad (\text{B.1c})$$

$$\oint_L \underline{E} \cdot d\underline{l} = - \int_S \frac{\partial \underline{B}}{\partial t} \cdot \underline{n} \, ds \quad (\text{B.1d})$$

Where Ω is the domain occupied by the material body with boundary surface $\partial\Omega$ and outward unit normal \underline{n} ; S is the boundary surface with closed curve L and unit normal \underline{n} ; \underline{B} is the magnetic flux density and \underline{H} is the magnetic field strength; \underline{D} is the electric displacement field, \underline{E} is the electric field strength, ρ_e is the free electric charge density and \underline{J} is the free electric current density. After applying the divergence theorem or Stokes' theorem, we arrive at the local forms of the equations:

$$\nabla \cdot \underline{D} = \rho_e \quad (\text{B.2a})$$

$$\nabla \cdot \underline{B} = 0 \quad (\text{B.2b})$$

$$\nabla \times \underline{H} = \underline{J} + \frac{\partial \underline{D}}{\partial t} \quad (\text{B.2c})$$

$$\nabla \times \underline{E} = -\frac{\partial \underline{B}}{\partial t} \quad (\text{B.2d})$$

The Maxwell's equations are supplemented by the following constitutive relations:

$$\underline{D} = \epsilon_0 \underline{E} + \underline{P} \quad (\text{B.3a})$$

$$\underline{B} = \mu_0 (\underline{H} + \underline{M}) \quad (\text{B.3b})$$

$$\underline{J} = \tau \underline{E} + \underline{J}_e \quad (\text{B.3c})$$

where ϵ_0 is the vacuum permittivity and μ_0 is the vacuum permeability; \underline{M} is the magnetization density; τ is the electrical conductivity of the material; \underline{P} is the polarization density and \underline{J}_e is the externally generated current density.

For the analysis of non-polarizable materials ($\underline{P} = 0$) like FSMA, Eq. (B.2a) can be neglected from the Maxwell's equations, and the electric constitutive relation (Eq. (B.3a)) can be reduced to:

$$\underline{D} = \epsilon_0 \underline{E} \quad (\text{B.4})$$

Moreover, as no external current is applied ($\underline{J}_e = 0$), Eq. (B.3c) can be rewritten as:

$$\underline{J} = \tau \underline{E} \quad (\text{B.5})$$

For relatively low frequencies ($\ll 1$ GHz), the time variation of the electric displacement ($\frac{\partial \underline{D}}{\partial t} = \epsilon_0 \frac{\partial \underline{E}}{\partial t}$) is negligible with respect to the induced current density ($\underline{J} = \tau \underline{E}$), so the Ampère's law (Eq. (B.2c)) becomes:

$$\nabla \times \underline{H} = \underline{J} \quad (\text{B.6})$$

To further reduce the Maxwell's equations, a magnetic vector potential \underline{A} is introduced as

$$\underline{B} = \nabla \times \underline{A} \quad (\text{B.7})$$

So that the Gauss-Faraday law (Eq. (B.2b)) is automatically satisfied: $\nabla \cdot \underline{B} = \nabla \cdot (\nabla \times \underline{A}) \equiv 0$.

Replace the magnetic flux density \underline{B} by the magnetic vector potential \underline{A} in Eq. (B.2d):

$$\nabla \times \underline{E} = -\frac{\partial \underline{B}}{\partial t} = -\frac{\partial(\nabla \times \underline{A})}{\partial t} = -\nabla \times \frac{\partial \underline{A}}{\partial t} \Rightarrow \underline{E} = -\frac{\partial \underline{A}}{\partial t} \quad (\text{B.8})$$

Equation (B.8) represents the relationship between the electric field strength and the time variation of the magnetic vector potential.

In summary, the necessary equations for the magnetic analysis are:

■ Maxwell's equation – Ampère's law: $\nabla \times \underline{H} = \underline{J}$

■ Useful relations:

$$\underline{B} = \nabla \times \underline{A}, \quad \underline{B} = \mu_0(\underline{H} + \underline{M})$$

$$\underline{E} = -\frac{\partial \underline{A}}{\partial t}, \quad \underline{J} = \tau \underline{E}$$

Boundary conditions and initial conditions

The two types of boundary conditions are: (1) imposed magnetic vector potential \underline{A}^* on the surface $\partial\Omega_A$, and (2) imposed magnetic field strength \underline{H}^* parallel to the surface $\partial\Omega_H$. The intersection of the two surfaces is empty and their union is the total surface of the material body. Mathematically, the boundary conditions can be expressed as:

$$\underline{A} = \underline{A}^* \text{ on } \partial\Omega_A \quad (\text{B.9a})$$

$$\underline{H} \times \underline{n} = \underline{H}^* \times \underline{n} \text{ on } \partial\Omega_H \quad (\text{B.9b})$$

where $\partial\Omega_A \cap \partial\Omega_H = \emptyset$, $\partial\Omega_A \cup \partial\Omega_H = \partial\Omega_t$.

The initial magnetic vector potential is given by the initial condition:

$$\underline{A}(\underline{x}, t=0) = \underline{A}_0(\underline{x}) \quad (\text{B.10})$$

B.1.2. Mechanical part

Balance of linear momentum: The time rate of momentum change of a material body is equal to the resultant force acting upon the body (Eringen and Maugin, 1990). The global form of this balance is:

$$\frac{d}{dt} \int_{\Omega_t} \rho \frac{\partial \underline{u}}{\partial t} d\Omega = \oint_{\partial\Omega_t} \underline{T} ds + \int_{\Omega_t} \underline{f} d\Omega \quad (\text{B.11})$$

where ρ is the mass density; Ω_t is the domain occupied by the material body at the instant t ; \underline{u} is the displacement vector; \underline{T} is the traction on the boundary surface $\partial\Omega_t$ of the material body; \underline{f} is the body force density (including mechanical and electro-magnetic parts). By introducing the Cauchy stress tensor $\underline{\underline{\sigma}}$ ($\underline{\underline{\sigma}} \cdot \underline{n} = \underline{T}$, where \underline{n} is the outward unit normal of the body surface), and using the conservation of mass and the divergence theorem, the local form of the balance equation can be obtained as:

$$\nabla \cdot \underline{\underline{\sigma}} + \underline{f} = \rho \frac{\partial^2 \underline{u}}{\partial t^2} \quad (\text{B.12})$$

No mechanical body force is considered in the material. Since FSMA is only magnetizable, we have (Pérez-Aparicio and Sosa, 2004)

$$\underline{f} = \underline{J} \times \underline{B} + \nabla(\mu_0 \underline{H}) \cdot \underline{M} \quad (\text{B.13})$$

The 1st part on the right-hand side of Eq. (B.13) is the Lorentz force density, and the 2nd part is the force density due to the gradient of magnetic field. Then Eq. (B.12) can be rewritten as:

$$\nabla \cdot \underline{\underline{\sigma}} + \underline{f} = \rho \frac{\partial^2 \underline{u}}{\partial t^2} \Rightarrow \nabla \cdot \underline{\underline{\sigma}} + \underline{J} \times \underline{B} + \nabla(\mu_0 \underline{H}) \cdot \underline{M} = \rho \frac{\partial^2 \underline{u}}{\partial t^2} \quad (\text{B.14})$$

Balance of angular momentum: The time rate of angular momentum change of a material body is equal to the resultant moment of all forces and the resultant of couples acting upon the body (Eringen and Maugin, 1990). The mathematical expression is:

$$\frac{d}{dt} \int_{\Omega_t} \underline{x} \times \rho \frac{\partial \underline{u}}{\partial t} d\Omega = \oint_{\partial\Omega_t} \underline{x} \times \underline{T} ds + \int_{\Omega_t} [\underline{x} \times \underline{f} + \underline{C}^m] d\Omega \quad (\text{B.15})$$

where \underline{x} is the position in the material body; \underline{C}^m is the magnetic couple density:

$$\underline{C}^m = \underline{M} \times (\mu_0 \underline{H}) \quad (\text{B.16})$$

After several calculations (see details in Appendix C.1), the local form can be reached:

$$skw\underline{\underline{\sigma}} = skw(\underline{M} \otimes (\mu_0 \underline{H})) \quad (\text{B.17})$$

where the definition $skw\underline{\underline{\sigma}} := \frac{1}{2}(\underline{\underline{\sigma}} - {}^t \underline{\underline{\sigma}})$. Due to the presence of the magnetic body couple,

the mechanical stress tensor $\underline{\underline{\sigma}}$ is not symmetric.

There are two boundary conditions: imposed displacement \underline{u}^* on the surface $\partial\Omega_u$ and applied traction \underline{T}^* on the surface $\partial\Omega_T$. The intersection of these two surfaces is empty and their union is the total surface of the material body. Mathematically, we have

$$\underline{u} = \underline{u}^* \text{ on } \partial\Omega_u \quad (\text{B.18a})$$

$$\underline{\underline{\sigma}} \cdot \underline{n} = \underline{T}^* \text{ on } \partial\Omega_T \quad (\text{B.18b})$$

where $\partial\Omega_u \cap \partial\Omega_T = \emptyset$, $\partial\Omega_u \cup \partial\Omega_T = \partial\Omega_t$.

One important thing to point out: The surface force \underline{T}^* has two contributions, i.e., \underline{T}^{mech} of mechanical origin and \underline{T}^{mag} of magnetic origin. \underline{T}^{mag} is defined as the jump of the Maxwell stress tensor $\underline{\underline{\sigma}}^{MW}$, i.e., $\underline{T}^{mag} := \|\underline{\underline{\sigma}}^{MW}\| \cdot \underline{n}$ (Hirsinger and Billardon, 1995). For magnetizable and non-polarizable materials, the general expression of the Maxwell stress $\underline{\underline{\sigma}}^{MW}$ is:

$\underline{\underline{\sigma}}^{MW} = \underline{H} \otimes \underline{B} - \frac{1}{2} \mu_0 (\underline{H} \cdot \underline{H}) \underline{\underline{I}}$, where $\underline{\underline{I}}$ is the identity tensor. In magneto-static case (no electric current), we have: $\|\underline{\underline{\sigma}}^{MW}\| \cdot \underline{n} = \frac{1}{2} \mu_0 (\underline{M} \cdot \underline{n})^2 \underline{n}$ (Kankanala and Triantafyllidis, 2004; Haldar et al., 2011).

The initial displacement and velocity are given by the initial conditions:

$$\underline{u}(\underline{x}, t=0) = \underline{u}_0(\underline{x}) \quad (\text{B.19a})$$

$$\frac{\partial \underline{u}}{\partial t}(\underline{x}, t=0) = \underline{v}_0(\underline{x}) \quad (\text{B.19b})$$

B.1.3. Summary of fully coupled dynamic magneto-mechanical analysis

A summary of variables, equations and boundary conditions concerned in the general magneto-mechanical analysis is given below:

Magnetic part

- Variables: \underline{A} , \underline{B} , \underline{H} , \underline{M} , \underline{E}
- Governing equation: $\nabla \times \underline{H} = \underline{J}$
- Useful relations

$$\underline{B} = \nabla \times \underline{A}, \quad \underline{B} = \mu_0 (\underline{H} + \underline{M})$$

$$\underline{E} = -\frac{\partial \underline{A}}{\partial t}, \quad \underline{J} = \tau \underline{E}$$

- Boundary conditions

$$\underline{A} = \underline{A}^* \text{ on } \partial\Omega_A$$

$$\underline{H} \times \underline{n} = \underline{H}^* \times \underline{n} \text{ on } \partial\Omega_H$$

- Initial condition: $\underline{A}(\underline{x}, t=0) = \underline{A}_0(\underline{x})$

Mechanical part

- Variables: \underline{u} , $\underline{\varepsilon}$, $\underline{\sigma}$, $\underline{\sigma}^s$

Due to the presence of the magnetic body couple, the mechanical stress tensor $\underline{\sigma}$ is generally non-symmetric. In this case, the symmetric stress tensor $\underline{\sigma}^s$ (related to $\underline{\sigma}$ by Eq. (B. 20) is generally chosen as the state variable used in the constitutive equations.

- Governing equations

$$\nabla \cdot \underline{\sigma} + \underline{f} = 0$$

$$skw\underline{\sigma} = skw(\underline{M} \otimes (\mu_0 \underline{H}))$$

The body force \underline{f} includes mechanical and electro-magnetic body forces.

- Compatibility equation: $\underline{\varepsilon} = \frac{1}{2}(\nabla \underline{u} + {}^t(\nabla \underline{u}))$

Small strain and negligible rotation approximation is applied.

- Useful relation: $\underline{\sigma}^s = \underline{\sigma} + (\mu_0 \underline{H}) \otimes \underline{M}$ (B.20)

We take the expression of $\underline{\sigma}^s$ from (Haldar et al., 2011). Similar expression can also be found in (Hirsinger and Billardon, 1995).

- Boundary conditions

$$\underline{u} = \underline{u}^* \text{ on } \partial\Omega_u$$

$$\underline{\sigma} \cdot \underline{n} = \underline{T}^* \text{ on } \partial\Omega_T$$

The surface force \underline{T}^* includes the mechanical surface force and the magnetic surface force.

- Initial conditions: $\underline{u}(\underline{x}, t=0) = \underline{u}_0(\underline{x})$, $\frac{\partial \underline{u}}{\partial t}(\underline{x}, t=0) = \underline{v}_0(\underline{x})$.

Coupled constitutive equations: $\underline{\varepsilon} = \underline{\varepsilon}(\underline{\sigma}^s, \underline{H})$, $\underline{M} = \underline{M}(\underline{\sigma}^s, \underline{H})$

Note 1: If the magnetic body couple is zero (the magnetization \underline{M} is co-linear with the magnetic field \underline{H}), the mechanical stress tensor $\underline{\sigma}$ is symmetric. In this case, $\underline{\sigma}$ is directly used as a state variable in the constitutive equations, and there is no need to calculate $\underline{\sigma}^s$ or

consider the balance law of angular momentum (i.e., Eq. (B.17): $\operatorname{skw}\underline{\underline{\sigma}} = \operatorname{skw}(\underline{M} \otimes (\mu_0 \underline{H})) \equiv 0$).

Note 2: Static analysis (special case in dynamic analysis)

In static case, the magnetic flux density \underline{B} does not change with time. So there is no electric field \underline{E} (induced by the time-variation of \underline{B}) or electric current \underline{J} . Therefore, the magnetic analysis part can be simplified as follows:

- Variables: $\underline{A}, \underline{B}, \underline{H}, \underline{M}$
- Governing equation: $\nabla \times \underline{H} = \underline{0}$
- Useful relations: $\underline{B} = \nabla \times \underline{A}, \underline{B} = \mu_0(\underline{H} + \underline{M})$
- Boundary conditions

$$\underline{A} = \underline{A}^* \text{ on } \partial\Omega_A$$

$$\underline{H} \times \underline{n} = \underline{H}^* \times \underline{n} \text{ on } \partial\Omega_H$$

B.2. Weak form formulations

The weak form formulations developed in this sub-section and the finite element formulations in the following are for the constitutive model proposed in Chapter 4. In the constitutive model, the magnetization is co-linear with the magnetic field (the constitutive model gives the magnetization along the magnetic field). Therefore, the magnetic body couple is zero. The symmetric stress tensor $\underline{\underline{\sigma}}$ directly enters the constitutive model as a state variable. Appendix C.2 verifies that the magnetic body couple due to the magnetization part perpendicular to the magnetic field can be neglected. The formulations can be applied to all cases where there is no or negligible magnetic body couple.

The displacement \underline{u} and the magnetic vector potential \underline{A} are the unknowns that the mechanical and magnetic governing equations should solve respectively. So there are six nodal unknowns of the magneto-mechanical analysis: ${}^t\{\underline{u}, \underline{A}\} = {}^t\{u^x, u^y, u^z, A^x, A^y, A^z\}$.

B.2.1. Magnetic part

The magnetic governing equation (Eq. (B.6)) is weighted by virtual variation of the magnetic vector potential $\underline{\omega}_A(x)$, and then integrated over the material domain Ω . With boundary condition and constitutive relations (Eqs. (B.5), (B.8) and (B.9b)), we obtain the weak form formulation after several calculations:

$$\int_{\Omega} (\nabla \times \underline{\omega}_A) \cdot \underline{H}(A) d\Omega + \int_{\Omega} \tau \frac{\partial A}{\partial t} \cdot \underline{\omega}_A d\Omega - \int_{\partial\Omega_A} (\underline{H} \times \underline{n}) \cdot \underline{\omega}_A ds = \int_{\partial\Omega_H} (\underline{H}^* \times \underline{n}) \cdot \underline{\omega}_A ds \quad (\forall \underline{\omega}_A \in D) \quad (B.21)$$

where D is a collection of admissible magnetic vector potentials in the domain Ω without considering the boundary condition of imposed A^* (Eq. (B.9a)). Eq. (B.9a) is multiplied by an admissible magnetic field \underline{H}' and then integrated over the surface $\partial\Omega_A$

$$\int_{\partial\Omega_A} (\underline{H} \times \underline{n}) \cdot \underline{A} ds = \int_{\partial\Omega_A} (\underline{H} \times \underline{n}) \cdot \underline{A}^* ds \quad (\underline{H}' \in D'[\partial\Omega_A]) \quad (B.22)$$

where $D'[\partial\Omega_A]$ is a collection of admissible magnetic field strength on the boundary $\partial\Omega_A$.

B.2.2. Mechanical part

The governing equation (Eq. (B.14)) is weighted by virtual variation of the displacement vector $\underline{\omega}_u(x)$ and then integrated over the material domain Ω . By considering the boundary condition of applied traction (Eq. (B.18b)), we arrive at the weak form formulation of the governing equation after several calculations:

$$\int_{\Omega} \underline{\underline{\sigma}}(x) : \underline{\underline{\epsilon}}(\underline{\omega}_u) d\Omega + \int_{\Omega} \rho \frac{\partial^2 \underline{u}}{\partial t^2} \cdot \underline{\omega}_u d\Omega - \int_{\partial\Omega_u} \underline{T} \cdot \underline{\omega}_u ds = \int_{\Omega} \underline{f} \cdot \underline{\omega}_u d\Omega + \int_{\partial\Omega_T} \underline{T}^* \cdot \underline{\omega}_u ds \quad (\forall \underline{\omega}_u \in C) \quad (B.23)$$

where C is a set of admissible displacements in the domain Ω without considering the boundary condition of imposed displacement (Eq. (B.18a)). To obtain the weak form formulation of Eq. (B.18a), the right-hand and left-hand sides of this equation are multiplied by an admissible traction \underline{T}' and then integrated over the surface $\partial\Omega_u$:

$$\int_{\partial\Omega_u} \underline{u} \cdot \underline{T}' ds = \int_{\partial\Omega_u} \underline{u}^* \cdot \underline{T}' ds \quad (\underline{T}' \in C'[\partial\Omega_u]) \quad (B.24)$$

where $C'[\partial\Omega_u]$ is a collection of admissible tractions on the surface $\partial\Omega_u$.

B.3. Finite element formulations

B.3.1. Magnetic part

The magnetic vector potential $\underline{A}(\underline{x})$ is discretized as:

$$\underline{A}(\underline{x}, t) = \sum_{k=1}^{n_p} N_k(\underline{x}) \underline{A}_k(t) = [N(\underline{x})] \{A(t)\} \quad (\text{B.25})$$

where n_p is the total number of nodes in the material domain; $\underline{A}_k(t)$ and $N_k(\underline{x})$ are respectively the magnetic vector potential and the shape function on node k . In matrix expression, $[N(\underline{x})]$ is composed of all the shape functions and $\{A(t)\}$ is composed of all the nodal magnetic vector potentials:

$$[N(\underline{x})] = \begin{bmatrix} N_1(\underline{x}) & 0 & 0 & \dots & N_{n_p}(\underline{x}) & 0 & 0 \\ 0 & N_1(\underline{x}) & 0 & \dots & 0 & N_{n_p}(\underline{x}) & 0 \\ 0 & 0 & N_1(\underline{x}) & \dots & 0 & 0 & N_{n_p}(\underline{x}) \end{bmatrix} \quad (\text{B.26})$$

$$\{A(t)\} = {}^t \left\{ A_1^x(t), A_1^y(t), A_1^z(t), \dots, A_{n_p}^x(t), A_{n_p}^y(t), A_{n_p}^z(t) \right\} \quad (\text{B.27})$$

Similarly, the virtual variation of magnetic vector potential $\underline{\omega}_A$ can also be expressed as:

$$\underline{\omega}_A(\underline{x}) = [N(\underline{x})] \{\omega_A\} \quad (\text{B.28})$$

$$\text{where } \{\omega_A\} = {}^t \left\{ \omega_{A,1}^x, \omega_{A,1}^y, \omega_{A,1}^z, \dots, \omega_{A,n_p}^x, \omega_{A,n_p}^y, \omega_{A,n_p}^z \right\}.$$

With Eqs. (B.25) and (B.28), we can make following calculations for each term in the weak form magnetic governing equations (Eqs. (B.21) and (B.22)):

- Time variation term (2nd term on the left-hand side of Eq. (B.21))

$$\int_{\Omega} \tau \frac{\partial \underline{A}}{\partial t} \cdot \underline{\omega}_A d\Omega = {}^t \{\omega_A\} [MC] \{\dot{A}(t)\} \quad (\text{B.29})$$

where $\dot{A}(t)$ is the first order partial derivative of A with respect to time t ; $[MC]$ is the electrical conductivity matrix: $[MC] = \int_{\Omega} \tau {}^t [N(\underline{x})] [N(\underline{x})] d\Omega$.

- Unknown surface magnetic field (3rd term on the left-hand side of Eq. (B.21))

$$\int_{\partial\Omega_A} (\underline{H} \times \underline{n}) \cdot \underline{\omega}_A ds = {}^t \{\omega_A\} [GM] \{H(t)\} \quad (\text{B.30})$$

$[GM]$ is the localization matrix [Bonnet and Frangi, 2006] ; $\{H(t)\}$ is the nodal magnetic field ($\underline{H} \times \underline{n}$) parallel to the boundary $\partial\Omega_A$.

■ Applied magnetic field term (right-hand side of Eq. (B.21))

$$\int_{\partial\Omega_H} (\underline{H}^* \times \underline{n}) \cdot \underline{\omega}_A \, ds = {}^t \{\omega_A\} \{FM(t)\} \quad (B.31)$$

where the nodal applied magnetic field strength is: $\{FM(t)\} = \int_{\partial\Omega_H} {}^t [N(t)] (\underline{H}^*(\underline{x}, t) \times \underline{n}) \, ds$.

■ Internal effort term (1st term on the left-hand side of Eq. (B.21))

We have:

$$\nabla \times \underline{\omega}_A = [J_c(\underline{x})] \{\omega_A\} \quad (B.32)$$

where:

$$[J_c(\underline{x})] = \begin{bmatrix} 0 & -\frac{\partial}{\partial z} N_1(\underline{x}) & \frac{\partial}{\partial y} N_1(\underline{x}) & 0 & -\frac{\partial}{\partial z} N_{n_p}(\underline{x}) & \frac{\partial}{\partial y} N_{n_p}(\underline{x}) \\ \frac{\partial}{\partial z} N_1(\underline{x}) & 0 & -\frac{\partial}{\partial x} N_1(\underline{x}), \dots, \frac{\partial}{\partial z} N_{n_p}(\underline{x}) & 0 & -\frac{\partial}{\partial x} N_{n_p}(\underline{x}) & \\ -\frac{\partial}{\partial y} N_1(\underline{x}) & \frac{\partial}{\partial x} N_1(\underline{x}) & 0 & -\frac{\partial}{\partial y} N_{n_p}(\underline{x}) & \frac{\partial}{\partial x} N_{n_p}(\underline{x}) & 0 \end{bmatrix} \quad (B.33)$$

Similarly, we have:

$$\nabla \times \underline{A} = [J_c(\underline{x})] \{A\} \quad (B.34)$$

With Eqs. (B.7) and (B.34), we have:

$$\underline{B} = [J_c(\underline{x})] \{A\} \quad (B.35)$$

Moreover, by Eq. (B.3b) and the constitutive equation for magnetization density \underline{M} (Eq. (103)), we obtain:

$$\underline{B} = \mu_0 \left(H + \sum_{i=1}^3 z_i \left(a_i H + \left\langle H - \frac{M_s}{a_i} \right\rangle (M_s - a_i H) \right) \right) \hat{H} = C(\underline{H}, z_1, z_2, z_3) \underline{H} \quad (B.36)$$

where $C(\underline{H}, z_1, z_2, z_3) = \mu_0 \left((1 + z_1 a_1 |_{H \in S_{11}} + z_2 a_2 |_{H \in S_{21}} + z_3 a_3 |_{H \in S_{31}}) + \frac{M_s}{H} (z_1 |_{H \in S_{12}} + z_2 |_{H \in S_{22}} + z_3 |_{H \in S_{32}}) \right)$.

The six domains (i.e., S_{11} , S_{12} , S_{21} , S_{22} , S_{31} , S_{32}) are defined for the magnitude H of the magnetic field strength in Table B.1, where M_s is the saturation magnetization, a_1 , a_2 and a_3

are magnetic susceptibilities respectively for martensite variant 1, 2 and 3 (see Chapter 4 – sub-section 4.2.3.3).

From Eqs. (B.35) and (B.36), we obtain:

$$\underline{H} = \frac{1}{C(\underline{H}, z_1, z_2, z_3)} [J_c(\underline{x})] \{A\} \quad (\text{B.37})$$

By introducing Eqs. (B.32) and (B.37), we have:

$$\int_{\Omega} (\nabla \times \underline{\omega}_A) \cdot \underline{H} (\underline{A}) d\Omega = {}^t \{\omega_A\} [KM(\underline{H}, z_1, z_2, z_3)] \{A(t)\} \quad (\text{B.38})$$

$$\text{where } [KM(\underline{H}, z_1, z_2, z_3)] = \int_{\Omega} \frac{1}{C(\underline{H}, z_1, z_2, z_3)} {}^t [J_c(\underline{x})] [J_c(\underline{x})] d\Omega.$$

With Eqs. (B.29), (B.30), (B.31) and (B.38), Eq. (B.21) can be reduced to:

$$\begin{aligned} {}^t \{\omega_A\} [KM(\underline{H}, z_1, z_2, z_3)] \{A(t)\} + {}^t \{\omega_A\} [MC] \dot{\{A(t)\}} - {}^t \{\omega_A\} [GM] \{H(t)\} &= {}^t \{\omega_A\} \{FM(t)\} \\ \Rightarrow [MC] \dot{\{A(t)\}} + [KM(\underline{H}, z_1, z_2, z_3)] \{A(t)\} - [GM] \{H(t)\} &= \{FM(t)\} \end{aligned} \quad (\text{B.39})$$

Table B.1. Domains for magnetic field strength.

Domains for Variant 1		Domains for Variant 2		Domains for Variant 3	
S_{11}	$H \leq \frac{M_s}{a_1}$	S_{21}	$H \leq \frac{M_s}{a_2}$	S_{31}	$H \leq \frac{M_s}{a_3}$
S_{12}	$H > \frac{M_s}{a_1}$	S_{22}	$H > \frac{M_s}{a_2}$	S_{32}	$H > \frac{M_s}{a_3}$

■ Boundary condition (Eq. (B.22))

With the discretization of the magnetic vector potential (Eq. (B.25)), the left-hand and right-hand sides of Eq. (B.22) can be written as (Bonnet and Frangi, 2006):

$$\int_{\partial\Omega_A} (\underline{H} \times \underline{n}) \cdot \underline{A} ds = {}^t \{H\} {}^t [GM] \{A(t)\} \quad (\text{B.40a})$$

$$\int_{\partial\Omega_A} (\underline{H} \times \underline{n}) \cdot \underline{A}^* ds = {}^t \{H\} \{A^*(t)\} \quad (\text{B.40b})$$

Where \underline{H}' and $\{A^*\}$ are respectively the virtual nodal magnetic field ($\underline{H} \times \underline{n}$) and the nodal imposed magnetic vector potential on the boundary $\partial\Omega_A$. Therefore, Eq. (B.22) can be reduced to:

$${}^t [GM] \{A(t)\} = \{A^*(t)\} \quad (\text{B.41})$$

In summary, the final discretized equations for magnetic analysis are:

$$[MC] \{\dot{A}(t)\} + [KM(\underline{H}, z_1, z_2, z_3)] \{A(t)\} - [GM] \{H(t)\} = \{FM(t)\}$$

$${}^t [GM] \{A(t)\} = \{A^*(t)\}$$

B.3.2. Mechanical part

The displacement field $\underline{u}(\underline{x})$ can be discretized using the same nodes and shape functions as those used in the previous magnetic part (i.e., sub-section B.3.1):

$$\underline{u}(\underline{x}, t) = \sum_{k=1}^{n_p} N_k(\underline{x}) \underline{u}_k = [N(\underline{x})] \{u(t)\} \quad (\text{B.42})$$

where

$$\{u(t)\} = {}^t \left\{ u_1^x(t), u_1^y(t), u_1^z(t), \dots, u_{n_p}^x(t), u_{n_p}^y(t), u_{n_p}^z(t) \right\} \quad (\text{B.43})$$

Similarly, the virtual variation of displacement $\underline{\omega}_u$ can be expressed as:

$$\underline{\omega}_u(\underline{x}) = [N(\underline{x})] \{\omega_u\} \quad (\text{B.44})$$

$$\text{where } \{\omega_u\} = {}^t \left\{ \omega_{u,1}^x, \omega_{u,1}^y, \omega_{u,1}^z, \dots, \omega_{u,n_p}^x, \omega_{u,n_p}^y, \omega_{u,n_p}^z \right\}.$$

With Eqs. (B.42) and (B.44), the following calculations are made successively for each term in the weak form formulations (Eqs. (B.23) and (B.24)):

- Inertial term (2nd term on the left-hand side of Eq. (B.23))

$$\int_{\Omega} \rho \frac{\partial^2 \underline{u}}{\partial t^2} \cdot \underline{\omega}_u \, d\Omega = {}^t \{\omega_u\} [M] \{\ddot{u}(t)\} \quad (\text{B.45})$$

where $\ddot{u}(t)$ is the partial derivative of order 2 of u with respect to time t ; $[M]$ is the mass matrix: $[M] = \int_{\Omega} \rho {}^t [N(\underline{x})] [N(\underline{x})] \, d\Omega$.

- Unknown surface traction (3rd term on the left-hand side of Eq. (B.23))

$$\int_{\partial\Omega_u} \underline{T} \cdot \underline{\omega}_u \, ds = {}^t \{ \omega_u \} [G] \{ T \} \quad (\text{B.46})$$

where $[G]$ is the localization matrix (Bonnet and Frangi, 2006); $\{T\}$ is the nodal force on the surface $\partial\Omega_u$.

■ External effort (right-hand side of Eq. (B.23))

$$\int_{\Omega} \underline{f} \cdot \underline{\omega}_u \, d\Omega + \int_{\partial\Omega_T} \underline{T}^* \cdot \underline{\omega}_u \, ds = \{ \omega_u \}^T \{ F(t) \} \quad (\text{B.47})$$

where the nodal external force is: $\{ F(t) \} = \int_{\Omega} [N(\underline{x})]^T \underline{f}(\underline{x}, t) \, d\Omega + \int_{\partial\Omega_T} {}^t [N(\underline{x})] \underline{T}^*(\underline{x}) \, ds$.

■ Internal effort term (1st term on the left-hand side of Eq. (B.23))

The infinitesimal strain tensor $\underline{\varepsilon}$ is related to the displacement $\underline{u}(\underline{x}, t)$ by:

$\underline{\varepsilon}(\underline{u}) = \frac{1}{2} (\nabla \underline{u}(\underline{x}, t) + {}^t \nabla \underline{u}(\underline{x}, t))$. So the strain vector $\{ \varepsilon(\underline{u}) \} = {}^t \{ \varepsilon_{xx}, \varepsilon_{yy}, \varepsilon_{zz}, 2\varepsilon_{xy}, 2\varepsilon_{xz}, 2\varepsilon_{yz} \}$

can be expressed as:

$$\{ \varepsilon(\underline{u}) \} = [J_s(\underline{x})] \{ u(\underline{x}, t) \} \quad (\text{B.48})$$

Where

$$[J_s(\underline{x})] = \begin{bmatrix} \frac{\partial N_1}{\partial x} & 0 & 0 & \frac{\partial N_{n_p}}{\partial x} & 0 & 0 \\ 0 & \frac{\partial N_1}{\partial y} & 0 & , \dots, & 0 & \frac{\partial N_{n_p}}{\partial y} \\ 0 & 0 & \frac{\partial N_1}{\partial z} & & 0 & \frac{\partial N_{n_p}}{\partial z} \\ \frac{\partial N_1}{\partial y} & \frac{\partial N_1}{\partial x} & 0 & \frac{\partial N_{n_p}}{\partial y} & \frac{\partial N_{n_p}}{\partial x} & 0 \\ \frac{\partial N_1}{\partial z} & 0 & \frac{\partial N_1}{\partial x}, \dots, & \frac{\partial N_{n_p}}{\partial z} & 0 & \frac{\partial N_{n_p}}{\partial x} \\ 0 & \frac{\partial N_1}{\partial z} & \frac{\partial N_1}{\partial y} & 0 & \frac{\partial N_{n_p}}{\partial z} & \frac{\partial N_{n_p}}{\partial y} \end{bmatrix} \quad (\text{B.49})$$

Similarly, the strain vector $\{ \varepsilon(\underline{\omega}_u) \}$ related to the virtual displacement variation $\underline{\omega}_u(\underline{x})$ can be expressed as:

$$\{\varepsilon(\underline{\omega}_u)\} = [J_s(\underline{x})]\{\omega_u\} \quad (\text{B.50})$$

The state equation for strain tensor (Eq. (101)) can be changed to the state equation for the stress vector $\{\sigma(\underline{x}, t)\} = {}^t \{\sigma_{xx}(\underline{x}, t), \sigma_{yy}(\underline{x}, t), \sigma_{zz}(\underline{x}, t), \sigma_{xy}(\underline{x}, t), \sigma_{xz}(\underline{x}, t), \sigma_{yz}(\underline{x}, t)\}$:

$$\begin{aligned} \{\sigma(\underline{x}, t)\} &= [R][J_s(\underline{x})]\{u(\underline{x}, t)\} \\ &\quad - [R]((\{U_2\} - \{U_1\})z_{12} + (\{U_3\} - \{U_2\})z_{23} + (\{U_1\} - \{U_3\})z_{31}) \end{aligned} \quad (\text{B.51})$$

where $[R]$ is the elastic rigidity matrix of FSMA martensite; $\{U_i\}$ ($i = 1, 2, 3$) is the strain vector corresponding to the transformation strain tensor $\underline{\underline{U}}_i$ for variant i (see Eq. (81) in Chapter 4).

With Eqs. (B.50) and (B.51), we have:

$$\int_{\Omega} \underline{\underline{\sigma}}(\underline{x}) : \underline{\underline{\varepsilon}}(\underline{\omega}_u) d\Omega = {}^t \{\omega_u\}[K]\{u\} - {}^t \{\omega_u\}\{ZZ(z_{12}, z_{23}, z_{31})\} \quad (\text{B.52})$$

where $[K]$ is the stiffness matrix and $\{ZZ(z_{12}, z_{23}, z_{31})\}$ is a supplementary effort related to the volume-fraction transformations between the variants:

$$\begin{aligned} [K] &= \int_{\Omega} {}^t [J_s(\underline{x})][R][J_s(\underline{x})] d\Omega \\ &\{ZZ(z_{12}, z_{23}, z_{31})\} \\ &= \int_{\Omega} {}^t [J_s(\underline{x})][R]((\{U_2\} - \{U_1\})z_{12}(\underline{x}) + (\{U_3\} - \{U_2\})z_{23}(\underline{x}) + (\{U_1\} - \{U_3\})z_{31}(\underline{x})) d\Omega \end{aligned}$$

With Eqs. (B.45), (B.46), (B.47) and (B.52), Eq. (B.23) can be changed to the following finite element formulation:

$$\begin{aligned} {}^t \{\omega_u\}[K]\{u(t)\} + {}^t \{\omega_u\}[M]\{\ddot{u}(t)\} - {}^t \{\omega_u\}\{ZZ(z_{12}, z_{23}, z_{31})\} - {}^t \{\omega_u\}[G]\{T(t)\} &= {}^t \{\omega_u\}\{F(t)\} \\ \Rightarrow [M]\{\ddot{u}(t)\} + [K]\{u(t)\} - \{ZZ(z_{12}, z_{23}, z_{31})\} - [G]\{T(t)\} &= \{F(t)\} \end{aligned} \quad (\text{B.53})$$

■ Boundary condition of imposed displacement (Eq. (B.24))

With the displacement discretization (Eq. (B.42)), the left-hand and right-hand sides of Eq. (B.24) can be respectively rewritten as (Bonnet and Frangi, 2006):

$$\int_{\partial\Omega_u} \underline{u} \cdot \underline{T}' ds = {}^t \{T'\} {}^t [G]\{u(t)\} \quad (\text{B.54a})$$

$$\int_{\partial\Omega_u} \underline{u}^* \cdot \underline{T}' ds = {}^t \{T'\} \{u^*(t)\} \quad (\text{B.54b})$$

where $\{T'\}$ and $\{u^*\}$ are respectively the virtual nodal force and the imposed nodal displacement on the surface $\partial\Omega_u$. With Eq. (B.54), Eq. (B.24) can be reduced to:

$${}^t [G] \{u(t)\} = \{u^*(t)\} \quad (\text{B.55})$$

In summary, the final discretized equations for mechanical analysis are:

$$[M] \{\ddot{u}(t)\} + [K] \{u(t)\} - \{ZZ(z_{12}, z_{23}, z_{31})\} - [G] \{T(t)\} = \{F(t)\}$$

$${}^t [G] \{u(t)\} = \{u^*(t)\}$$

B.4. Summary

In this section, the finite element formulations for fully coupled magneto-mechanical analysis of FSMA are derived. They are:

- For magnetic analysis

$$[MC] \{\dot{A}(t)\} + [KM](\underline{H}, z_1, z_2, z_3) \{A(t)\} - [GM] \{H(t)\} = \{FM(t)\}$$

$${}^t [GM] \{A(t)\} = \{A^*(t)\}$$

- For mechanical analysis

$$[M] \{\ddot{u}(t)\} + [K] \{u(t)\} - \{ZZ(z_{12}, z_{23}, z_{31})\} - [G] \{T(t)\} = \{F(t)\}$$

$${}^t [G] \{u(t)\} = \{u^*(t)\}$$

The iterative decoupled approach of structural analysis can be used (see the flowchart in Fig. B.1): magnetic and mechanical analyses are made successively, and then pass on to the ‘martensite reorientation’ process where the volume fractions of the martensite variants can be updated. An equilibrium check (check of magnetic and mechanical governing equations) is made at the end of the iteration.

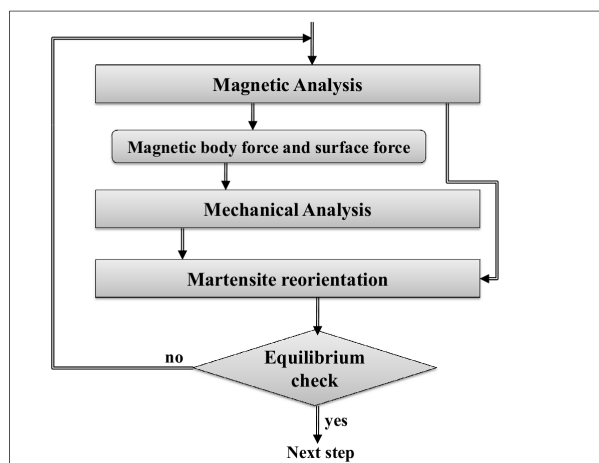


Fig. B.1. Iteration of magneto-mechanical analysis.

Appendix C. Non-symmetric stress tensor of magnetic materials in magnetic field

C.1. Introduction — origin of the non-symmetric stress tensor for magnetic materials 172

C.2. Non-symmetric stress tensor in ferromagnetic shape memory alloys 174

C.1. Introduction — origin of the non-symmetric stress tensor for magnetic materials

When a magnetic material is placed in the magnetic field, magnetic body couple is generally induced in the material, which leads to the non-symmetric stress tensor of the material. In this section, the relation between the magnetic body couple and the non-symmetric stress tensor is derived. Similar deductions can be found in Kiefer (2006).

Balance of angular momentum: The time rate of angular momentum change of a material body is equal to the resultant moment of all forces and the resultant of couples acting upon the body (Eringen and Maugin, 1990). It is mathematically expressed as:

$$\frac{d}{dt} \int_{\Omega_t} \underline{x} \times \rho \frac{\partial \underline{u}}{\partial t} d\Omega = \oint_{\partial\Omega_t} \underline{x} \times \underline{T} ds + \int_{\Omega_t} [\underline{x} \times (\underline{f} + \underline{f}^m) + \underline{C}^m] d\Omega \quad (C.1)$$

where Ω_t is the domain occupied by the material body at the instant t ; $\partial\Omega_t$ is the boundary surface of the material body; \underline{x} is the position in the material body; \underline{u} is the displacement vector; \underline{T} is the traction on the boundary surface; \underline{f} and \underline{f}^m are respectively the mechanical and magnetic body force densities; \underline{C}^m is the magnetic couple density, which is expressed as

$$\underline{C}^m = \underline{M} \times (\mu_0 \underline{H}) \quad (C.2)$$

where $\mu_0 (= 4\pi \times 10^{-7} \text{ T} \cdot \text{m/A})$ is the vacuum permeability; \underline{H} is the magnetic field strength and \underline{M} is the magnetization of the material. If \underline{H} and \underline{M} are in the same direction, there is no

magnetic couple ($\underline{C}^m = \underline{0}$); if not, due to the presence of the magnetic couple \underline{C}^m , the Cauchy stress tensor $\underline{\underline{\sigma}}$ is generally not symmetric.

For the convenience of deriving the relation between \underline{C}^m and the non-symmetry of $\underline{\underline{\sigma}}$, Eq. (C.1) is rewritten by index notation for Cartesian coordinates:

$$\frac{d}{dt} \int_{\Omega_t} \rho \epsilon_{ijk} x_i \frac{\partial u_j}{\partial t} d\Omega = \oint_{\partial\Omega_t} \epsilon_{ijk} x_i T_j ds + \int_{\Omega_t} [\epsilon_{ijk} x_i (f_j + f_j^m) + C_k^m] d\Omega \quad (\text{C.3})$$

where ϵ_{ijk} is the Levi-Civita symbol. The term on the left-hand side of Eq. (C.3) can be rewritten as:

$$\begin{aligned} & \frac{d}{dt} \int_{\Omega_t} \rho \epsilon_{ijk} x_i \frac{\partial u_j}{\partial t} d\Omega \\ &= \int_{\Omega_t} \frac{d}{dt} \left(\rho \epsilon_{ijk} x_i \frac{\partial u_j}{\partial t} \right) d\Omega + \int_{\Omega_t} \left(\rho \epsilon_{ijk} x_i \frac{\partial u_j}{\partial t} \right) v_{l,l} d\Omega \\ &= \int_{\Omega_t} \rho \frac{d}{dt} \left(\epsilon_{ijk} x_i \frac{\partial u_j}{\partial t} \right) d\Omega + \int_{\Omega_t} \left(\epsilon_{ijk} x_i \frac{\partial u_j}{\partial t} \right) \left(\frac{d\rho}{dt} + \rho v_{l,l} \right) d\Omega \\ &= \int_{\Omega_t} \rho \epsilon_{ijk} x_i \left(\frac{\partial^2 u_j}{\partial t^2} \right) d\Omega + \int_{\Omega_t} \rho \epsilon_{ijk} \left(\frac{\partial x_i}{\partial t} \right) \left(\frac{\partial u_j}{\partial t} \right) d\Omega + \int_{\Omega_t} \left(\epsilon_{ijk} x_i \frac{\partial u_j}{\partial t} \right) \left(\frac{d\rho}{dt} + \rho v_{l,l} \right) d\Omega \\ &= \int_{\Omega_t} \rho \epsilon_{ijk} x_i \left(\frac{\partial^2 u_j}{\partial t^2} \right) d\Omega + \int_{\Omega_t} \rho \epsilon_{ijk} v_i v_j d\Omega + \int_{\Omega_t} \left(\epsilon_{ijk} x_i \frac{\partial u_j}{\partial t} \right) \left(\frac{d\rho}{dt} + \rho v_{l,l} \right) d\Omega \\ &= \int_{\Omega_t} \rho \epsilon_{ijk} x_i \left(\frac{\partial^2 u_j}{\partial t^2} \right) d\Omega + \int_{\Omega_t} \left(\epsilon_{ijk} x_i \frac{\partial u_j}{\partial t} \right) \left(\frac{d\rho}{dt} + \rho v_{l,l} \right) d\Omega \end{aligned} \quad (\text{C.4})$$

By conservation of mass ($\frac{d\rho}{dt} + \rho v_{l,l} = 0$), the second term on the right-hand side of Eq. (C.4)

is zero and we finally obtain:

$$\frac{d}{dt} \int_{\Omega_t} \rho \epsilon_{ijk} x_i \frac{\partial u_j}{\partial t} d\Omega = \int_{\Omega_t} \rho \epsilon_{ijk} x_i \left(\frac{\partial^2 u_j}{\partial t^2} \right) d\Omega \quad (\text{C.5})$$

In the first term on the right-hand side of Eq. (C.3), replace the traction \underline{T} with the Cauchy stress tensor $\underline{\underline{\sigma}}$ and use the divergence theorem:

$$\begin{aligned} \oint_{\partial\Omega_t} \epsilon_{ijk} x_i T_j ds &= \oint_{\partial\Omega_t} \epsilon_{ijk} x_i \sigma_{jl} n_l ds \\ &= \int_{\Omega_t} \epsilon_{ijk} (x_{i,l} \sigma_{jl} + x_i \sigma_{jl,l}) d\Omega \end{aligned}$$

$$= \int_{\Omega_t} \varepsilon_{ijk} \sigma_{ji} d\Omega + \int_{\Omega_t} \varepsilon_{ijk} x_i \sigma_{jl,l} d\Omega \quad (\text{C.6})$$

Introducing Eqs. (C.5) and (C.6) into Eq. (C.3), we obtain:

$$\begin{aligned} \int_{\Omega_t} \rho \varepsilon_{ijk} x_i \left(\frac{\partial^2 u_j}{\partial t^2} \right) d\Omega &= \int_{\Omega_t} \varepsilon_{ijk} \sigma_{ji} d\Omega + \int_{\Omega_t} \varepsilon_{ijk} x_i \sigma_{jl,l} d\Omega + \int_{\Omega_t} [\varepsilon_{ijk} x_i (f_j + f_j^m) + C_k^m] d\Omega \\ \Rightarrow \int_{\Omega_t} \varepsilon_{ijk} x_i \left(\sigma_{jl,l} + f_j + f_j^m - \rho \frac{\partial^2 u_j}{\partial t^2} \right) d\Omega + \int_{\Omega_t} (\varepsilon_{ijk} \sigma_{ji} + C_k^m) d\Omega &= 0 \end{aligned} \quad (\text{C.7})$$

By the balance of linear momentum ($\sigma_{jl,l} + f_j + f_j^m = \rho \frac{\partial^2 u_j}{\partial t^2}$), the first term on the left-hand side of Eq. (C.7) is zero and we obtain:

$$\begin{aligned} \int_{\Omega_t} (\varepsilon_{ijk} \sigma_{ji} + C_k^m) d\Omega &= 0 \\ \Rightarrow \varepsilon_{ijk} \sigma_{ji} + C_k^m &= 0 \\ \Rightarrow \varepsilon_{ijk} \sigma_{ji} &= -C_k^m \end{aligned}$$

which means:

$$\sigma_{12} - \sigma_{21} = C_3^m \quad (\text{C.8a})$$

$$\sigma_{23} - \sigma_{32} = C_1^m \quad (\text{C.8b})$$

$$\sigma_{31} - \sigma_{13} = C_2^m \quad (\text{C.8c})$$

C.2. Non-symmetric stress tensor in ferromagnetic shape memory alloys

In this section, we calculate the maximum difference ($\sigma_{ij} - \sigma_{ji}, i \neq j$) due to the magnetic body couple in Ni-Mn-Ga ferromagnetic shape memory alloys. The material is assumed to be in the state of martensite variant II (with short axis along x_2 -coordinate) consisting of a single magnetic domain. A magnetic field H_1 along x_1 -coordinate is applied (see Fig. C.1(a)). By Eq. (C.2), the magnetic body couple \underline{C}^m is calculated as: $\underline{C}^m = (0, 0, -\mu_0 H_1 M_2)$, where M_2 is the magnetization component of the material along x_2 -coordinate (shown in Fig. C.1(a)). So in \underline{C}^m , only the component $C_3^m (= -\mu_0 H_1 M_2)$ is non-zero. By Eq. (C.8a), we have:

$$\sigma_{21} - \sigma_{12} = \mu_0 H_1 M_2 \quad (\text{C.9})$$

For variant II's magnetization curve (M_1 – H_1 , where M_1 is magnetization component along the magnetic field, shown in Fig. C.1(a)), we can make linear approximations as shown in Fig. 1(b), where a is the magnetic susceptibility of variant II. Then we have:

$$M_1(H_1) = \begin{cases} aH_1 & (0 \leq H_1 < \frac{M_s}{a}) \\ M_s & (H_1 \geq \frac{M_s}{a}) \end{cases} \quad (\text{C.10})$$

where M_s is the saturation magnetization. By the relation between M_1 and M_2 ($M_1^2 + M_2^2 = M_s^2$), we have:

$$M_2(H_1) = \begin{cases} \sqrt{M_s^2 - a^2 H_1^2} & (0 \leq H_1 < \frac{M_s}{a}) \\ 0 & (H_1 \geq \frac{M_s}{a}) \end{cases} \quad (\text{C.11})$$

With Eqs. (C.9) and (C.11), we obtain:

$$\sigma_{21} - \sigma_{12} = \begin{cases} \mu_0 H_1 \sqrt{M_s^2 - a^2 H_1^2} & (0 \leq H_1 < \frac{M_s}{a}) \\ 0 & (H_1 \geq \frac{M_s}{a}) \end{cases} \quad (\text{C.12})$$

The maximum ($\sigma_{21} - \sigma_{12}$) is obtained at the critical magnetic field H_c defined by:

$$\left. \begin{aligned} \frac{\partial(\mu_0 H_1 \sqrt{M_s^2 - a^2 H_1^2})}{\partial H_1} \Bigg|_{H_1=H_c} &= 0 \\ \frac{\partial^2(\mu_0 H_1 \sqrt{M_s^2 - a^2 H_1^2})}{\partial H_1^2} \Bigg|_{H_1=H_c} &> 0 \end{aligned} \right\} \Rightarrow H_c = \frac{M_s}{\sqrt{2}a} \quad (\text{C.13})$$

Therefore, the maximum $(\sigma_{21} - \sigma_{12})_{\max}$ is:

$$(\sigma_{21} - \sigma_{12})_{\max} = \frac{\mu_0 M_s^2}{2a} \quad (\text{C.14})$$

For Ni-Mn-Ga ferromagnetic shape memory alloys, we have: $M_s = 500,000$ A/m, $a = 1.1$ (Heczko, 2005). With these values, Eqs. (C.13) and (C.14) are calculated as:

$$(\sigma_{21} - \sigma_{12})_{\max} = 0.14 \text{ MPa} \quad \text{at} \quad \mu_0 H_c = 0.4 \text{ T} \quad (\text{C.15})$$

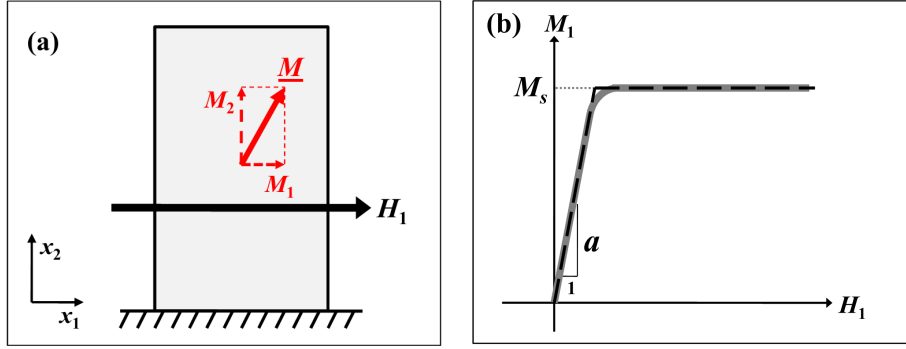


Fig. C.1. (a) Ni-Mn-Ga sample (single magnetic domain is assumed) in the magnetic field H_1 along x_1 -coordinate. \underline{M} is the magnetization vector in the sample; M_1 and M_2 are magnetization components respectively along x_1 - and x_2 -coordinate. (b) Linear approximation (dashed line) of the magnetization curve (solid line) for martensite variant II (with short axis along x_2 -coordinate). a is the magnetic susceptibility; M_s is the saturation magnetization.

The twinning stress for type I twin boundary motion is around $1 \sim 2$ MPa, which is almost ten times $(\sigma_{21}-\sigma_{12})_{\max}$ from the magnetic body couple. So the magnetic body couple has little influence on the type I twin boundary motion.

For the type II twin boundary motion (Straka et al., 2011b), its twinning stress ($0.05 \sim 0.3$ MPa) is comparable with $(\sigma_{21}-\sigma_{12})_{\max}$. So the magnetic body couple might influence the type II twin boundary motion. However, long before reaching the critical magnetic field $\mu_0 H_c = 0.4$ T, the twin boundary motion (due to the magnetic anisotropic energy difference) has already completed at such a low twinning stress, and the material is composed of single martensite variant whose easy-axis of magnetization is along the magnetic field. Therefore, there is no magnetic couple in the material (magnetization and magnetic field are in the same direction, so the magnetic couple is zero by Eq. (C.2)).

In conclusion, for both type I and II twin boundary motions in the magnetic field, there is no need to consider the effects of the magnetic body couple and the stress tensor of the material can be assumed to be symmetric. In literature, the magnetic body couples are always negligible in soft magnetic materials (zero magnetization without magnetic field) and only in hard magnets (large permanent magnetization) are considered the magnetic body couples (Eringen and Maugin, 1990; Hirsinger and Billardon, 1995).

References

- Auernhammer, D., Schmitt, M., Ohtsuka, M., Kohl, M., 2008. NiMnGa nanostructures produced by electron beam lithography and Ar-ion etching. *The European Physical Journal Special Topics* 158, 249–254.
- Auricchio, F., Bessoud, A.-L., Reali, A., Stefanelli, U., 2011. A three-dimensional phenomenological model for magnetic shape memory alloys. *GAMM-Mitteilungen* 34, 90–96.
- Bonnet, M., Frangi, A., 2006. Analyse des solides déformables par la méthode des éléments finis. Edition de l’Ecole Polytechnique, Palaiseau.
- Boonyongmaneerat, Y., Chmielus, M., Dunand, D.C., Müllner, P., 2007. Increasing magnetoplasticity in polycrystalline Ni-Mn-Ga by reducing internal constraints through porosity. *Physical Review Letters* 99, 247201.
- Boyd, J.G., Lagoudas, D.C., 1996. A thermodynamical constitutive model for shape memory materials. Part I. The monolithic shape memory alloy. *International Journal of Plasticity* 12, 805–842.
- Buchelnikov, V.D., Bosko, S.I., 2003. The kinetics of phase transformations in ferromagnetic shape memory alloys Ni–Mn–Ga. *Journal of Magnetism and Magnetic Materials* 258–259, 497–499.
- Chen, X., He, Y.J., Moumni, Z., 2013. Twin boundary motion in NiMnGa single crystals under biaxial compression. *Materials Letters* 90, 72–75.
- Chernenko, V.A., L’vov, V.A., Müllner, P., Kostorz, G., Takagi, T., 2004. Magnetic-field-induced superelasticity of ferromagnetic thermoelastic martensites: Experiment and modeling. *Physical Review B* 69, 134410.
- Chernenko, V.A., Zagorodnyuk, S.P., L’vov, V.A., O’Handley, R.C., Kono, Y., 2006. Magnetization curves for tetragonal martensites: experiments and modeling. *Journal of Applied Physics* 99, 103906.
- Chmielus, M., Chernenko, V.A., Knowlton, W.B., Kostorz, G., Müllner, P., 2008. Training, constraints and high-cycle magneto-mechanical properties of NiMnGa magnetic shape-memory alloys. *The European Physical Journal Special Topics* 158, 79–85.
- Chmielus, M., Glavatskyy, I., Hoffmann, J.-U., Chernenko, V.A., Schneider, R., Müllner, P., 2011a. Influence of constraints and twinning stress on magnetic field-induced strain of magnetic shape-memory alloys. *Scripta Materialia* 64, 888–891.

- Chmielus, M., Rolfs, K., Wimpory, R., Reimers, W., Müllner, P., Schneider, R., 2010a. Effects of surface roughness and training on the twinning stress of Ni-Mn-Ga single crystals. *Acta Materialia* 58, 3952–3962.
- Chmielus, M., Witherspoon, C., Ullakko, K., Müllner, P., Schneider, R., 2011b. Effects of surface damage on twinning stress and the stability of twin microstructures of magnetic shape memory alloys. *Acta Materialia* 59, 2948–2956.
- Chmielus, M., Witherspoon, C., Wimpory, R.C., Paulke, A., Hilger, A., Zhang, X., Dunand, D.C., Müllner, P., 2010b. Magnetic-field-induced recovery strain in polycrystalline Ni-Mn-Ga foam. *Journal of Applied Physics* 108, 123526.
- Chopra, H.D., Ji, C., Kokorin, V.V., 2000. Magnetic-field-induced twin boundary motion in magnetic shape-memory alloys. *Physical Review B* 61, R14913–R14915.
- Chulist, R., Böhm, A., Lippmann, T., Skrotzki, W., Drossel, W.-G., Neugebauer, R., 2010a. Twinning behaviour of textured polycrystalline Ni-Mn-Ga alloy after hot extrusion by high-pressure torsion. *Materials Science Forum* 635, 195–199.
- Chulist, R., Skrotzki, W., Oertel, C.-G., Böhm, A., Lippmann, T., Rybacki, E., 2010b. Microstructure and texture in $\text{Ni}_{50}\text{Mn}_{29}\text{Ga}_{21}$ deformed by high-pressure torsion. *Scripta Materialia* 62, 650–653.
- Chulist, R., Skrotzki, W., Oertel, C.-G., Böhm, A., Pötschke, M., 2010c. Change in microstructure during training of a $\text{Ni}_{50}\text{Mn}_{29}\text{Ga}_{21}$ bicrystal. *Scripta Materialia* 63, 548–551.
- Chulist, R., Sozinov, A., Straka, L., Lanska, N., Soroka, A., Lippmann, T., Oertel, C.-G., Skrotzki, W., 2012. Diffraction study of bending-induced polysynthetic twins in 10M modulated Ni-Mn-Ga martensite. *Journal of Applied Physics* 112, 063517.
- Chulist, R., Straka, L., Lanska, N., Soroka, A., Sozinov, A., Skrotzki, W., 2013. Characterization of mobile type I and type II twin boundaries in 10M modulated Ni–Mn–Ga martensite by electron backscatter diffraction. *Acta Materialia* 61, 1913–1920.
- Creton, N., Hirsinger, L., 2005. Rearrangement surfaces under magnetic field and/or stress in Ni–Mn–Ga. *Journal of Magnetism and Magnetic Materials* 290–291, 832–835.
- Cui, J., Shield, T.W., James, R.D., 2004. Phase transformation and magnetic anisotropy of an iron-palladium ferromagnetic shape-memory alloy. *Acta Materialia* 52, 35–47.
- DeSimone, A., James, R.D., 2002. A constrained theory of magnetoelasticity. *Journal of the Mechanics and Physics of Solids* 50, 283–320.
- Dong, J.W., Xie, J.Q., Lu, J., Adelmann, C., Palmstrøm, C.J., Cui, J., Pan, Q., Shield, T.W., James, R.D., McKernan, S., 2004. Shape memory and ferromagnetic shape memory effects in single-crystal Ni_2MnGa thin films. *Journal of Applied Physics* 95, 2593–2600.

- Eringen, A.C., Maugin, G.A., 1990. Electrodynamics of continua I: foundations and solid media. Springer-Verlag, New York.
- Faran, E., Shilo, D., 2011. The kinetic relation for twin wall motion in NiMnGa. *Journal of the Mechanics and Physics of Solids* 59, 975–987.
- Feuchtwanger, J., Michael, S., Juang, J., Bono, D., O'Handle, R.C., Allen, S.M., Jenkins, C., Goldie, J., Berkowitz, A., 2003. Energy absorption in Ni-Mn-Ga-polymer composites. *Journal of Applied Physics* 93, 8528–8530.
- Gaitzsch, U., Pötschke, M., Roth, S., Rellinghaus, B., Schultz, L., 2007. Mechanical training of polycrystalline 7 M Ni₅₀Mn₃₀Ga₂₀ magnetic shape memory alloy. *Scripta Materialia* 57, 493–495.
- Gaitzsch, U., Pötschke, M., Roth, S., Rellinghaus, B., Schultz, L., 2009. A 1% magnetostrain in polycrystalline 5M Ni-Mn-Ga. *Acta Materialia* 57, 365–370.
- Ganor, Y., Shilo, D., Shield, W., James, R.D., 2008. Breaching the work output limitation of ferromagnetic shape memory alloys. *Applied Physics Letters* 93, 122509.
- Ganor, Y., Shilo, D., Zarrouati, N., James, R.D., 2009. Ferromagnetic shape memory flapper. *Sensors and Actuators A* 150, 277–279.
- Gans, E., Henry, C., Carman, G.P., 2004. Reduction in required magnetic field to induce twin-boundary motion in ferromagnetic shape memory alloys. *Journal of Applied Physics* 95, 6965–6967.
- Gauthier, J.Y., 2007. Modélisation des alliages à mémoire de forme magnétiques pour la conversion d'énergie dans les actionneurs et leur commande. Ph.D. Thesis, Université de Franche-Comté, France.
- Gauthier, J.Y., Hubert, A., Abadie, J., Lexcellent, C., Chaillet, N., 2006. Multistable actuator based on magnetic shape memory alloy. In: Proceedings of the 10th International Conference on New Actuators. Bremen, Germany, pp. 787–790.
- Gauthier, J.Y., Lexcellent, C., Hubert, A., Abadie, J., Chaillet, N., 2007. Modelling rearrangement process of martensite platelets in a magnetic shape memory alloy Ni₂MnGa single crystal under magnetic field and (or) stress action. *Journal of Intelligent Material Systems and Structures* 18, 289–299.
- Gavriljuk, V.G., Söderberg, O., Bliznuk, V.V., Glavatska, N.I., Lindroos, V.K., 2003. Martensitic transformations and mobility of twin boundaries in Ni₂MnGa alloys studied by using internal friction. *Scripta Materialia* 49, 803–809.

- Ge, Y., Heczko, O., Söderberg, O., Lindroos, V.K., 2004. Various magnetic domain structures in a Ni-Mn-Ga martensite exhibiting magnetic shape memory effect. *Journal of Applied Physics* 96, 2159–2163.
- Ge, Y., Jiang, H., Sozinov, A., Söderberg, O., Lanska, N., Keränen, J., Kauppinen, E.I., Lindroos, V.K., Hannula, S.-P., 2006. Crystal structure and macrotwin interface of five-layered martensite in Ni-Mn-Ga magnetic shape memory alloy. *Materials Science and Engineering A* 438–440, 961–964.
- Glavatska, N., Mogylny, G., Glavatskiy, I., Gavriljuk, V., 2002. Temperature stability of martensite and magnetic field induced strain in Ni–Mn–Ga. *Scripta Materialia* 46, 605–610.
- Glavatska, N.I., Rudenko, A.A., Glavatskiy, I.N., L'vov, V.A., 2003. Statistical model of magnetostrain effect in martensite. *Journal of Magnetism and Magnetic Materials* 265, 142–151.
- Haldar, K., Kiefer, B., Lagoudas, D.C., 2011. Finite element analysis of the demagnetization effect and stress inhomogeneities in magnetic shape memory alloy samples. *Philosophical Magazine* 91, 4126–4157.
- Halphen, B., Nguyen, Q.S., 1974. Plastic and visco-plastic materials with generalized potential. *Mechanics Research Communications* 1, 43–47.
- Hamilton, R.F., Efstathiou, C., Sehitoglu, H., Chumlyakov, Y., 2006. Thermal and stress-induced martensitic transformations in NiFeGa single crystals under tension and compression. *Scripta Materialia* 54, 465–469.
- He, Y.J., Chen, X., Moumni, Z., 2011. Two-dimensional analysis to improve the output stress in ferromagnetic shape memory alloys. *Journal of Applied Physics* 110, 063905.
- He, Y.J., Chen, X., Moumni, Z., 2012. Reversible-strain criteria of ferromagnetic shape memory alloys under cyclic 3D magneto-mechanical loadings. *Journal of Applied Physics* 112, 033902.
- He, Y.J., Sun, Q.P., 2010. Macroscopic equilibrium domain structure and geometric compatibility in elastic phase transition of thin plates. *International Journal of Mechanical Sciences* 52, 198–211.
- Heczko, O., 2005. Magnetic shape memory effect and magnetization reversal. *Journal of Magnetism and Magnetic Materials* 290–291, 787–794.
- Heczko, O., Jurek, K., Ullakko, K., 2001. Magnetic properties and domain structure of magnetic shape memory Ni-Mn-Ga alloy. *Journal of Magnetism and Magnetic Materials* 226–230, 996–998.
- Heczko, O., Soroka, A., Hannula, S.-P., 2008. Magnetic shape memory effect in thin foils. *Applied Physics Letters* 93, 022503.
- Heczko, O., Sozinov, A., Ullakko, K., 2000. Giant field-induced reversible strain in magnetic shape memory NiMnGa alloy. *IEEE Transactions on Magnetics* 36, 3266–3268.

- Heczko, O., Straka, L., 2003. Temperature dependence and temperature limits of magnetic shape memory effect. *Journal of Applied Physics* 94, 7139–7143.
- Heczko, O., Straka, L., Hannula, S.P., 2006. Stress dependence of magnetic shape memory effect and its model. *Materials and Science and Engineering A* 438–440, 1003–1006.
- Heczko, O., Straka, L., Lanska, N., Ullakko, K., 2002. Temperature dependence of magnetic anisotropy in Ni-Mn-Ga alloys exhibiting giant field-induced strain. *Journal of Applied Physics* 91, 8228–8230.
- Heczko, O., Straka, L., Seiner, H., 2013. Different microstructures of mobile twin boundaries in 10 M modulated Ni-Mn-Ga martensite. *Acta Materialia* 61, 622–631.
- Heczko, O., Ullakko, K., 2001. Effect of temperature on magnetic properties of Ni–Mn–Ga magnetic shape memory (MSM) alloys. *IEEE Transactions on Magnetics* 37, 2672–2674.
- Henry, C.P., 2002. Dynamic actuation properties of Ni–Mn–Ga ferromagnetic shape memory alloys. Ph.D. Thesis, Massachusetts Institute of Technology, USA.
- Henry, C.P., Bono, D., Feuchtwanger, J., Allen, S.M., O’Handley, R.C., 2002. AC field-induced actuation of single crystal Ni–Mn–Ga. *Journal of Applied Physics* 91, 7810–7811.
- Hirsinger, L., Billardon, R., 1995. Magneto-elastic finite element analysis including magnetic forces and magnetostriction effects. *IEEE Transactions on Magnetics* 31, 1877–1879.
- Hirsinger, L., Lexcellent, C., 2003a. Modelling detwinning of martensite platelets under magnetic and (or) stress actions on Ni-Mn-Ga alloys. *Journal of Magnetism and Magnetic Materials* 254–255, 275–277.
- Hirsinger, L., Lexcellent, C., 2003b. Internal variable model for magneto-mechanical behaviour of ferromagnetic shape memory alloys Ni-Mn-Ga. *Journal de Physique IV France* 112, 977–980.
- Hosoda, H., Takeuchi, S., Inamura, T., Wakashima, K., 2004. Material design and shape memory properties of smart composites composed of polymer and ferromagnetic shape memory alloy particles. *Science and Technology of Advanced Materials* 5, 503–509.
- Hu, F., Shen, B., Sun, J., Wu, G., 2001. Large magnetic entropy change in a Heusler alloy $\text{Ni}_{52.6}\text{Mn}_{23.1}\text{Ga}_{24.3}$ single crystal. *Physical Review B* 64, 132412.
- James, R.D., Wuttig, M., 1998. Magnetostriction of martensite. *Philosophical Magazine A* 77, 1273–1299.
- Jaswon, M.A., Dove, D.B., 1960. The crystallography of deformation twinning. *Acta Crystallographica* 13, 232–240.

- Jeong, S., Inoue, K., Inoue, S., Kotera, K., Taya, M., Inoue, K., 2003. Effect of magnetic field on martensite transformation in a polycrystalline Ni₂MnGa. *Materials and Engineering A* 359, 253–260.
- Jiang, C., Wang, J., Xu, H., 2005. Temperature dependence of the giant magnetostrain in a NiMnGa magnetic shape memory alloy. *Applied Physics Letters* 86, 252508.
- Jin, Y.M., 2009. Domain microstructure evolution in magnetic shape memory alloys: phase-field model and simulation. *Acta Materialia* 57, 2488–2495.
- Kainuma, R., Imano, Y., Ito, W., Morito, H., Sutou, Y., Oikawa, K., Fujita, A., Ishida, K., Okamoto, S., Kitakami, O., Kanomata, T., 2006a. Metamagnetic shape memory effect in a Heusler-type Ni₄₃Co₇Mn₃₉Sn₁₁ polycrystalline alloy. *Applied Physics Letters* 88, 192513.
- Kainuma, R., Imano, Y., Ito, W., Sutou, Y., Morito, H., Okamoto, Kitakami, O., S., Oikawa, K., Fujita, A., Kanomata, T., Ishida, K., 2006b. Magnetic-field-induced shape recovery by reverse phase transformation. *Nature* 439, 957–960.
- Kakeshita, T., Takeuchi, T., Fukuda, T., Tsujiguchi, M., Saburi, T., Oshima, R., Muto, S., 2000. Giant magnetostriction in an ordered Fe₃Pt single crystal exhibiting a martensitic transformation. *Applied Physics Letters* 77, 1502–1504.
- Kankanala, S.V., Triantafyllidis, N., 2004. On finitely strained magnetorheological elastomers. *Journal of the Mechanics and Physics of Solids* 52, 2869–2908.
- Karaca, H.E., Karaman, I., Basaran, B., Chumlyakov, Y.I., Maier, H.J., 2006. Magnetic field and stress induced martensite reorientation in NiMnGa ferromagnetic shape memory alloy single crystals. *Acta Materialia* 54, 233–245.
- Karaca, H.E., Karaman, I., Lagoudas, D.C., Maier, H.J., Chumlyakov, Y.I., 2003. Recoverable stress-induced martensitic transformation in a ferromagnetic CoNiAl alloy. *Scripta Materialia* 49, 831–836.
- Karaman, I., Basaran, B., Karaca, H.E., Karsilayan, A.I., Chumlyakov, Y.I., 2007. Energy harvesting using martensite variant reorientation mechanism in a NiMnGa magnetic shape memory alloy. *Applied Physics Letters* 90, 172505.
- Khan, M., Ali, N., Stadler, S., 2007. Inverse magnetocaloric effect in ferromagnetic Ni₅₀Mn_{37+x}Sb_{13-x} Heusler alloys. *Journal of Applied Physics* 101, 053919.
- Khelfaoui, F., Kohl, M., Buschbeck, J., Heczko, O., Fähler, S., Schultz, L., 2008. A fabrication technology for epitaxial Ni-Mn-Ga microactuators. *The European Physical Journal Special Topics* 158, 167–172.

- Kiang, J., Tong, L., 2005. Modelling of magneto-mechanical behaviour of Ni–Mn–Ga single crystals. *Journal of Magnetism and Magnetic Materials* 292, 394–412.
- Kiang, J., Tong, L., 2007. Three-dimensional constitutive equations for Ni–Mn–Ga single crystals. *Journal of Magnetism and Magnetic Materials* 313, 214–229.
- Kiefer, B., 2006. A phenomenological constitutive model for magnetic shape memory alloys. Ph.D. Theis, Texas A&M University, USA.
- Kiefer, B., Karaca, H.E., Lagoudas, D.C., Karaman, I., 2007. Characterization and modeling of the magnetic field-induced strain and work output in Ni₂MnGa magnetic shape memory alloys. *Journal of Magnetism and Magnetic Materials* 312, 164–175.
- Kiefer, B., Lagoudas, D.C., 2005. Magnetic field-induced martensitic variant reorientation in magnetic shape memory alloys. *Philosophical Magazine* 85, 4289–4329.
- Kiefer, B., Lagoudas, D.C., 2009. Modeling the coupled strain and magnetization response of magnetic shape memory alloys under magnetomechanical loading. *Journal of Intelligent Material Systems and Structures* 20, 143–170.
- Kohl, M., Brugger, D., Ohtsuka, M., Krevet, B., 2007. A ferromagnetic shape memory actuator designed for large 2D optical scanning. *Sensors and Actuators A* 135, 92–98.
- Kohl, M., Brugger, D., Ohtsuka, M., Takagi, T., 2004. A novel actuation mechanism on the basis of ferromagnetic SMA thin films. *Sensors and Actuators A* 114, 445–450.
- Kohl, M., Srinivasa Reddy, Y., Khelfaoui, F., Krevet, B., Backen, A., Fähler, S., Eichhorn, T., Jakob, G., Mecklenburg, A., 2010. Recent progress in FSMA microactuator developments. *Materials Science Forum* 635, 145–154.
- Kohl, M., Yin, R., Pinneker, V., Ezer, Y., Sozinov, A., 2013. A miniature energy harvesting device using martensite variant reorientation. *Materials Science Forum* 738–739, 411–415.
- Krenke, T., Duman, E., Acet, M., Wassermann, E.F., 2007. Magnetic superelasticity and inverse magnetocaloric effect in Ni-Mn-In. *Physical Review B* 75, 104414.
- Krevet, B., Kohl, M., Morrison, P., Seelecke, S., 2008. Magnetization- and strain-dependent free energy model for FEM simulation of magnetic shape memory alloys. *The European Physical Journal Special Topics* 158, 205–211.
- Lai, Y.W., 2009. Magnetic microstructure and actuation dynamics of NiMnGa magnetic shape memory materials. Ph.D. Thesis, Technische Universität Dresden, Germany.
- Lai, Y.-W., Schäfer, R., Schultz, L., McCord, J., 2008. Direct observation of AC field-induced twin-boundary dynamics in bulk NiMnGa. *Acta Materialia* 56, 5130–5137.

- Lexcellent, C., Leclercq, S., Gabry, B., Bourbon, G., 2000. The two way shape memory effect of shape memory alloys: an experimental study and a phenomenological model. International Journal of Plasticity 16, 1155–1168.
- Levitas, V.I., Preston, D.L., 2002a. Three-dimensional Landau theory for multivariant stress-induced martensitic phase transformations. I. Austenite \leftrightarrow martensite. Physical Review B 66, 134206.
- Levitas, V.I., Preston, D.L., 2002b. Three-dimensional Landau theory for multivariant stress-induced martensitic phase transformations. II. Multivariant phase transformations and stress space analysis. Physical Review B 66, 134207.
- Li, Y., Jiang, C., Liang, T., Ma, Y., Xu, H., 2003. Martensitic transformation and magnetization of Ni-Fe-Ga ferromagnetic shape memory alloys. Scripta Materialia 48, 1255–1258.
- Li, L.J., Lei, C.H., Shu, Y.C., Li, J.Y., 2011. Phase-field simulation of magnetoelastic couplings in ferromagnetic shape memory alloys. Acta Materialia 59, 2648–2655.
- Li, L.J., Li, J.Y., Shu, Y.C., Chen, H.Z., Yen, J.H., 2008. Magnetoelastic domains and magnetic field-induced strains in ferromagnetic shape memory alloys by phase-field simulation. Applied Physics Letters 92, 172504.
- Liang, Y., Sutou, Y., Wada, T., Lee, C.-C., Taya, M., Mori, T., 2003. Magnetic field-induced reversible actuation using ferromagnetic shape memory alloys. Scripta Materialia 48, 1415–1419.
- Likhachev, A.A., Sozinov, A., Ullakko, K., 2004. Different modeling concepts of magnetic shape memory and their comparison with some experimental results obtained in Ni-Mn-Ga. Materials Science and Engineering A 378, 513–518.
- Likhachev, A.A., Ullakko, K., 2000. Magnetic-field-controlled twin boundaries motion and giant magneto-mechanical effects in Ni–Mn–Ga shape memory alloy. Physics Letters A 275, 142–151.
- L'vov, V.A., Zagorodnyuk, S.P., Chernenko, V.A., 2002. A phenomenological theory of giant magnetoelastic response in martensite. The European Physical Journal B 27, 57–62.
- Mahendran, M., Feuchtwanger, J., Techapiesancharoenkij, R., Bono, D., O'Handley, R.C., 2011. Acoustic energy absorption in Ni-Mn-Ga/polymer composites. Journal of Magnetism and Magnetic Materials 323, 1098–1100.
- Marcos, J., Planes, A., Mañosa, L., Casanova, F., Batlle, X., Labarta, A., Martínez, B., 2002. Magnetic field induced entropy change and magnetoelasticity in Ni-Mn-Ga alloys. Physical Review B 66, 224413.
- Marioni, M.A., O'Handley, R.C., Allen, S.M., 2002. Analytical model for field-induced strain in ferromagnetic shape-memory alloy polycrystals. Journal of Applied Physics 91, 7807–7809.

- Marioni, M.A., O'Handley, R.C., Allen, S.M., 2003. Pulsed magnetic field-induced actuation of Ni–Mn–Ga single crystals. *Applied Physics Letters* 83, 3966–3968.
- Martynov, V.V., Kokorin, V.V., 1992. The crystal structure of thermally- and stress-induced martensites in Ni₂MnGa single crystals. *Journal de Physique III France* 2, 739–749.
- Maugin, G.A., 1999. The thermomechanics of nonlinear irreversible behaviours. World Scientific Publishing, Singapore.
- Mennerich, C., Wendler, F., Jainta, M., Nestler, B., 2011. A phase-field model for the magnetic shape memory effect. *Archives of Mechanics* 63, 549–571.
- Morito, H., Fujita, A., Fukamichi, K., Kainuma, R., Ishida, K., Oikawa, K., 2002. Magnetocrystalline anisotropy in single-crystal Co-Ni-Al ferromagnetic shape-memory alloy. *Applied Physics Letters* 81, 1657–1659.
- Morito, H., Fujita, A., Oikawa, K., Ishida, K., Fukamichi, K., Kainuma, R., 2007. Stress-assisted magnetic-field-induced strain in Ni-Fe-Ga-Co ferromagnetic shape memory alloys. *Applied Physics Letters* 90, 062505.
- Morito, H., Oikawa, K., Fujita, A., Fukamichi, K., Kainuma, R., Ishida, K., 2009. Stress-assisted large magnetic-field-induced strain in single-variant Co-Ni-Ga ferromagnetic shape memory alloy. *Journal of Physics: Condensed Matter* 21, 256002.
- Morito, H., Oikawa, K., Fujita, A., Fukamichi, K., Kainuma, R., Ishida, K., 2010. Large magnetic-field-induced strain in Co-Ni-Al single-variant ferromagnetic shape memory alloy. *Scripta Materialia* 63, 379–382.
- Moumni, Z., 1995. Sur la modélisation du changement de phase à l'état solide. Ph.D. Thesis, Ecole Nationale Supérieure des Ponts et Chaussées, France.
- Moumni, Z., Zaki, W., Nguyen, Q.S., 2008. Theoretical and numerical modeling of solid–solid phase change: application to the description of the thermomechanical behavior of shape memory alloys. *International Journal of Plasticity* 24, 614–645.
- Moya, X., Mañosa, L., Planes, A., Aksoy, S., Acet, M., Wassermann, E.F., Krenke, T., 2007. Cooling and heating by adiabatic magnetization in the Ni₅₀Mn₃₄In₁₆ magnetic shape-memory alloy. *Physical Review B* 75, 184412.
- Müllner, P., Chernenko, V.A., Kostorz, G., 2003. A microscopic approach to the magnetic-field-induced deformation of martensite (magnetoplasticity). *Journal of Magnetism and Magnetic Materials* 267, 325–334.
- Müllner, P., Chernenko, V.A., Kostorz, G., 2004. Large cyclic magnetic-field-induced deformation in orthorhombic (14M) Ni-Mn-Ga martensite. *Journal of Applied Physics* 95, 1531–1536.

- Müllner, P., Chernenko, V.A., Wollgarten, M., Kostorz, G., 2002. Large cyclic deformation of a Ni-Mn-Ga shape memory alloy induced by magnetic fields. *Journal of Applied Physics* 92, 6708–6713.
- Murray, S.J., Marioni, M., Allen, S.M., O’Handley, R.C., Lograsso, T.A., 2000. 6% magnetic-field-induced strain by twin-boundary motion in ferromagnetic Ni–Mn–Ga. *Applied Physics Letters* 77, 886–888.
- Murray, S.J., O’Handley, R.C., Allen, S.M., 2001. Model for discontinuous actuation of ferromagnetic shape memory alloy under stress. *Journal of Applied Physics* 89, 1295–1301.
- O’Handley, R.C., 1998. Model for strain and magnetization in magnetic shape-memory alloys. *Journal of Applied Physics* 83, 3263–3270.
- O’Handley, R.C., 2000. Modern magnetic materials: principles and applications. John Wiley & Sons, Inc., USA.
- O’Handley, R.C., Murray, S.J., Marioni, M., Nembach, H., Allen, S.M., 2000. Phenomenology of giant magnetic-field-induced strain in ferromagnetic shape-memory materials. *Journal of Applied Physics* 87, 4712–4717.
- O’Handley, R.C., Paul, D.I., Allen, S.M., Richard, M., Feuchtwanger, J., Peterson, B., Techapiesancharoenkij, R., Barandiaran, M., Lazpita P., 2006. Model for temperature dependence of field-induced strain in ferromagnetic shape memory alloys. *Materials Science and Engineering A* 438–440, 445–449.
- Ohtsukaa, M., Matsumoto, M., Koike, K., Takagi, T., Itagaki, K., 2007. Martensitic transformation and shape memory effect of Ni-rich Ni₂MnGa sputtered films under magnetic field. *Journal of Magnetism and Magnetic Materials* 310, 2782–2784.
- Ohtsuka, M., Sekino, J., Koyama, K., Takagi, T., Itagaki, K., 2008. Magnetostructural phase transformation and shape memory effect of Fe-added Ni₂MnGa films. *The European Physical Journal Special Topics* 158, 173–178.
- Oikawa, K., Ito, W., Imano, Y., Sutou, Y., Kainuma, R., Ishida, K., Okamoto, S., Kitakami, O., 2006. Effect of magnetic field on martensitic transition of Ni₄₆Mn₄₁In₁₃ Heusler alloy. *Applied Physics Letters* 88, 122507.
- Oikawa, K., Ota, T., Ohmori, T., Tanaka, Y., Morito, H., Fujita, A., Kainuma, R., Fukamichi, K., Ishida, K., 2002. Magnetic and martensitic phase transitions in ferromagnetic Ni-Ga-Fe shape memory alloys. *Applied Physics Letters* 81, 5201–5203.
- Oikawa, K., Wulff, L., Iijima, T., Gejima, F., Ishida, K., 2001. Promising ferromagnetic Ni-Co-Al shape memory alloy system. *Applied Physics Letters* 79, 3290–3292.

- Okamoto, N., Fukuda, T., Kakeshita, T., 2006. Magnetocrystalline anisotropy and twinning stress in Ni-Mn-Ga ferromagnetic shape memory alloys. *Journal of Physics: Conference Series* 51, 315–318.
- Pareti, L., Solzi, M., Albertini, F., Paoluzi, A., 2003. Giant entropy change at the co-occurrence of structural and magnetic transitions in the $\text{Ni}_{2.19}\text{Mn}_{0.81}\text{Ga}$ Heusler alloy. *The European Physical Journal B* 32, 303–307.
- Paul, D.I., McGehee, W., O'Handley, R.C., Richard, M., 2007. Ferromagnetic shape memory alloys: a theoretical approach. *Journal of Applied Physics* 101, 123917.
- Pecharsky, V.K., Gschneidner, K.A., 1997. Giant magnetocaloric effect in $\text{Gd}_5(\text{Si}_2\text{Ge}_2)$. *Physical Review Letters* 78, 4494–4497.
- Pérez-Aparicio, J.L., Sosa, H., 2004. A continuum three-dimensional, fully coupled, dynamic, non-linear finite element formulation for magnetostrictive materials. *Smart Materials and Structures* 13, 493–502.
- Planes, A., Mañosa, L., Acet, M., 2009. Magnetocaloric effect and its relation to shape-memory properties in ferromagnetic Heusler alloys. *Journal of Physics: Condensed Matter* 21, 233201.
- Reinhold, M., Kiener, D., Knowlton, W.B., Dehm, G., Müllner, P., 2009. Deformation twinning in Ni-Mn-Ga micropillars with 10M martensite. *Journal of Applied Physics* 106, 053906.
- Sakamoto, T., Fukuda, T., Kakeshita, T., Takeuchi, T., Kishio, K., 2003. Magnetic field-induced strain in iron-based ferromagnetic shape memory alloys. *Journal of Applied Physics* 93, 8647–8649.
- Sasso, C.P., L'vov, V.A., Chernenko, V.A., Barandiaran, J.M., Pasquale, M., Kono, Y., 2010. Transformation of twinned $\text{Ni}_{52.0}\text{Mn}_{24.4}\text{Ga}_{23.6}$ martensite in a rotating magnetic field: theory and experiment. *Physical Review B* 81, 224428.
- Söderberg, O., Ge, Y., Sozinov, A., Hannula, S.-P., Lindroos, V. K., 2005. Recent breakthrough development of the magnetic shape memory effect in Ni-Mn-Ga alloys. *Smart Materials and Structures* 14, S223–S235.
- Sozinov, A., Lanska, N., Soroka, A., Straka, L., 2011. Highly mobile type II twin boundary in Ni-Mn-Ga five-layered martensite. *Applied Physics Letters* 99, 124103.
- Sozinov, A., Likhachev, A.A., Lanska, N., Ullakko, K., 2002. Giant magnetic-field-induced strain in NiMnGa seven-layered martensitic phase. *Applied Physics Letters* 80, 1746–1748.
- Stephan, J.M., Pagounis, E., Laufenberg, M., Paul, O., Ruther, P., 2011. A novel concept for strain sensing based on the ferromagnetic shape memory alloy NiMnGa. *IEEE Sensors Journal* 11, 2683–2689.
- Straka, L., Hänninen, H., Heczko, O., 2011a. Temperature dependence of single twin boundary motion in Ni–Mn–Ga martensite. *Applied Physics Letters* 98, 141902.

- Straka, L., Heczko, O., 2003a. Superelastic response of Ni–Mn–Ga martensite in magnetic fields and a simple model. *IEEE Transactions on Magnetics* 39, 3402–3404.
- Straka, L., Heczko, O., 2003b. Magnetic anisotropy in Ni–Mn–Ga martensites. *Journal of Applied Physics* 93, 8636–8638.
- Straka, L., Heczko, O., 2005. Reversible 6% strain of Ni-Mn-Ga martensite using opposing external stress in static and variable magnetic fields. *Journal of Magnetism and Magnetic Materials* 290-291, 829–831.
- Straka, L., Heczko, O., Hänninen, H., 2008. Activation of magnetic shape memory effect in Ni-Mn-Ga alloys by mechanical and magnetic treatment. *Acta Materialia* 56, 5492–5499.
- Straka, L., Heczko, O., Hannula, S.-P., 2006. Temperature dependence of reversible field-induced strain in Ni–Mn–Ga single crystal. *Scripta Materialia* 54, 1497–1500.
- Straka, L., Heczko, O., Seiner, H., Lanska, N., Drahokoupil, J., Soroka, A., Fähler, S., Hänninen, H., Sozinov, A., 2011b. Highly mobile twinned interface in 10 M modulated Ni-Mn-Ga martensite: Analysis beyond the tetragonal approximation of lattice. *Acta Materialia* 59, 7450–7463.
- Straka, L., Lanska, N., Ullakko, K., Sozinov, A., 2010. Twin microstructure dependent mechanical response in Ni-Mn-Ga single crystals. *Applied Physics Letters* 96, 131903.
- Straka, L., Soroka, A., Seiner, H., Hänninen, H., Sozinov, A., 2012. Temperature dependence of twinning stress of Type I and Type II twins in 10M modulated Ni-Mn-Ga martensite. *Scripta Materialia* 67, 25–28.
- Sullivan, M.R., Chopra, H.D., 2004. Temperature- and field-dependent evolution of micromagnetic structure in ferromagnetic shape-memory alloys. *Physical Review B* 70, 094427.
- Suorsa, I., Tellinen, J., Pagounis, E., Aaltio, I., Ullakko, K., 2002. Applications of magnetic shape memory actuators. In: Proceedings of the 8th International Conference on New Actuators. Bremen, Germany, pp. 158–161.
- Suorsa, I., Tellinen, J., Ullakko, K., Pagounis, E., 2004. Voltage generation induced by mechanical straining in magnetic shape memory materials. *Journal of Applied Physics* 95, 8054–8058.
- Sutou, Y., Imano, Y., Koeda, N., Omori, T., Kainuma, R., Ishida, K., Oikawa, K., 2004a. Magnetic and martensitic transformations of NiMnX (X = In, Sn, Sb) ferromagnetic shape memory alloys. *Applied Physics Letters* 85, 4358–4360.
- Sutou, Y., Kamiya, N., Omori, T., Kainuma, R., Ishida, K., Oikawa, K., 2004b. Stress-strain characteristics in Ni-Ga-Fe ferromagnetic shape memory alloys. *Applied Physics Letters* 84, 1275–1277.

- Techapiesancharoenkij, R., Kostamo, J., Allen, S.M., O'Handley, R.C., 2009. Frequency response of acoustic-assisted Ni–Mn–Ga ferromagnetic-shape-memory-alloy actuator. *Journal of Applied Physics* 105, 093923.
- Tellinen, J., Suorsa, I., Jääskeläinen, A., Aaltio, I., Ullakko, K., 2002. Basic properties of magnetic shape memory actuators. In: Proceedings of the 8th International Conference on New Actuators. Bremen, Germany, pp. 566–569.
- Thomas, M., Heczko, O., Buschbeck, J., Rößler, U.K., McCord, J., Scheerbaum, N., Schultz, L., Fähler, S., 2008. Magnetically induced reorientation of martensite variants in constrained epitaxial Ni-Mn-Ga films grown on MgO(001). *New Journal of Physics* 10, 023040.
- Tickle, R., James, R.D., 1999. Magnetic and magnetomechanical properties of Ni₂MnGa. *Journal of Magnetism and Magnetic Materials* 195, 627–638.
- Tickle, R., James, R.D., Shield, T., Wuttig, M., Kokorin, V.V., 1999. Ferromagnetic shape memory in the NiMnGa system. *IEEE Transactions on Magnetics* 35, 4301–4310.
- Ullakko, K., Ezer, Y., Sozinov, A., Kimmel, G., Yakovenko, P., Lindroos, V.K., 2001. Magnetic-field-induced strains in polycrystalline Ni-Mn-Ga at room temperature. *Scripta materialia* 44, 475–480.
- Ullakko, K., Huang, J.K., Kantner, C., O'Handley, R.C., Kokorin, V.V., 1996. Large magnetic-field-induced strains in Ni₂MnGa single crystals. *Applied Physics Letters* 69, 1966–1968.
- Wada, T., Liang, Y., Kato, H., Tagawa, T., Taya, M., Mori, T., 2003. Structural change and straining in Fe-Pd polycrystals by magnetic field. *Materials Science and Engineering A* 361, 75–82.
- Wang, W.H., Liu, G.D., Wu, G.H., 2006. Magnetically controlled high damping in ferromagnetic Ni₅₂Mn₂₄Ga₂₄ single crystal. *Applied Physics Letters* 89, 101911.
- Wang, J., Steinmann, P., 2012. A variational approach towards the modeling of magnetic field-induced strains in magnetic shape memory alloys. *Journal of the Mechanics and Physics of Solids* 60, 1179–1200.
- Webster, P.J., Ziebeck, K.R.A., Town, S.L., Peak, M.S., 1984. Magnetic order and phase transformation in Ni₂MnGa. *Philosophical Magazine B* 49, 295–310.
- Wuttig, M., Li, J., Craciunescu, C., 2001. A new ferromagnetic shape memory alloy system. *Scripta materialia* 44, 2393–2397.
- Yamamoto, T., Taya, M., Sutou, Y., Liang, Y., Wada, T., Sorensen, L., 2004. Magnetic field-induced reversible variant rearrangement in Fe-Pd single crystals. *Acta Materialia* 52, 5083–5091.
- Yu, S.Y., Ma, L., Liu, G.D., Liu, Z.H., Chen, J.L., Cao, Z.X., Wu, G.H., Zhang, B., Zhang, X. X., 2007. Magnetic field-induced martensitic transformation and large magnetoresistance in NiCoMnSb alloys. *Applied Physics Letters* 90, 242501.

- Zaki, W., Moumni, Z., 2007. A three-dimensional model of the thermomechanical behavior of shape memory alloys. *Journal of the Mechanics and Physics of Solids* 55, 2455–2490.
- Zasimchuk, I.K., Kokorin, V.V., Martynov, V.V., Tkachenko, A.V., Chernenko, V.A., 1990. Crystal structure of martensite in Heusler alloy Ni₂MnGa. *Phys. Met. Metall.* 69, 104–108.
- Zeng, M., Or, S.W., Chan, H.L.W., 2010. Ultrahigh anisotropic damping in ferromagnetic shape memory Ni-Mn-Ga single crystal. *Journal of Alloys and Compounds* 493, 565–568.
- Zhang, J.X., Chen, L.Q., 2005. Phase-field model for ferromagnetic shape-memory alloys. *Philosophical Magazine Letters* 85, 533–541.
- Zhang, X.X., Witherspoon, C., Müllner, P., Dunand, D.C., 2011. Effect of pore architecture on magnetic-field-induced strain in polycrystalline Ni-Mn-Ga. *Acta Materialia* 59, 2229–2239.